Modeling Dust Evolution in Hydrodynamic Simulations of Protoplanetary Disks

—New Methods and Applications—

Thomas Pfeil

München 2024

Modeling Dust Evolution in Hydrodynamic Simulations of Protoplanetary Disks

—New Methods and Applications—

Thomas Pfeil

Dissertation
der Fakultät für Physik
der Ludwig-Maximilians-Universität
München

vorgelegt von
Thomas Pfeil
geboren in Leinefelde, jetzt Leinefelde-Worbis

München, den 01.02.2024

Erstgutachter:	Prof. Dr. Tilman Birnstiel
Zweitgutachter:	Prof. Dr. H. Hubertus Klahr
Tag der mündlichen Prüfung:	18.03.2024

ZUSAMMENFASSUNG

Unser Verständnis der Planetenentstehung in Gas- und Staubscheiben, welche neugeborene Sterne umgeben, hängt entscheidend von der Genauigkeit und Komplexität numerischer Modelle ab. Gas und Staub interagieren auf verschiedene Art und Weise, sowohl aerodynamisch als auch thermodynamisch. Dieses Zusammenspiel führt zur Entwicklung von Instabilitäten und zur Bildung von Substrukturen in protoplaneteren Scheiben. Es muss außerdem verstanden werden, um deren beobachtete Erscheinung zu erklären.

Im ersten Teil dieser Dissertation wird die Signifikanz der thermischen Kopplung von Staub und Gas für die Entwicklung der vertikalen Scherinstabilität (VSI) demonstriert. Diese, rein hydrodynamische, Instabilität führt zur Entstehung von Turbulenz und Substrukturen in protoplanetaren Scheiben. Zudem spricht ihr Einfluss auf die vertikale Dispersion des Staubes für eine bedeutende Rolle bei der Interpretation von Beobachtungsdaten. Voraussetzung für die Entstehung der VSI ist eine hinreichend kurze thermische Ankoppelzeit von Gas und Staub, welche für eine effiziente Kühlung des Gases sorgt. Ob sich die VSI entwickeln kann, hängt daher von den Details der Staubgrößenverteilung ab. Die Ergebnisse der hier präsentierten numerischen Simulationen legen nahe, dass die VSI in den äußeren Bereichen von protoplanetaren Scheiben (jenseits von ~70 au) unterdrückt sein kann wenn die Staubpartikel bereits stark angewachsen sind. Der Grund hierfür ist die reduzierte Menge kleinen Staubes, welcher maßgeblich an der Kühlung des Gases beteiligt ist. Im Anschluss an diese Studien wird die entsprechende Methodik verfeinert und die thermische Ankoppelzeit dynamisch, auf Basis der vorhanden Staubverteilung in weiteren Simulationen berechnet. Es zeigt sich, dass eine protoplanetare Scheibe nur VSI entwickeln und aufrechterhalten kann, wenn ausreichend kleiner Staub ($\lesssim 10\,\mu m$) vorhanden ist, welcher für hinreichend schnelle thermische Relaxation sorgt. Dies verdeutlicht die Notwendigkeit den Koagulationsprozess in Modellen protoplanetarer Scheiben zu berücksichtigen.

Der Einbindung moderner Staubkoagulationsmodelle in großskaligen hydrodynamischen Simulation steht jedoch deren enormer Rechenaufwand entgegen. Daher beschäftigt sich der weitere Teil dieser Arbeit mit der Entwicklung zweier neuer, approximativer und daher effizienterer Sub-Grid-Modelle des Staubwachstum. Beide Methoden basieren auf der Darstellung der Größenverteilung als Potenzgesetz mit nur zwei Populationen und vermeiden daher die übliche, numerisch aufwendige, Verwendung hochaufgelöster Massengitter. Das erste Modell ist halb-analytisch. Die Wachstums- und Massenaustauschraten der Staubpopulationen sind analytisch definiert und werden numerisch integriert. Da es sich bei den Entwicklungsraten um Approximationen handelt, beinhalten sie diverse freie Parameter. Das Modell wird daher kalibriert, um eine gute Übereinstimmung mit vollwertigen Staubkoagulationsmodellen zu erreichen. Die Genauigkeit dieses Ansatzes zeigt sich in verschiedenen Testsimulationen. Als mögliches Anwendungsbeispiel wird zudem eine zweidimensionale Simulation einer protoplanetaren Scheibe demonstriert, welche durch das Gravitationspotential eines Planeten gestört wird. Zuletzt wird die Verwendung von Techniken des maschinellen Lernens als Alternative zum halb-analytischen Ansatz diskutiert. Dafür werden die analytischen Entwicklungsraten durch ein künstliches neuronales Netzwerk ersetzt, welches mit Hilfe der Daten von vollwertigen Staubkoagulationssimulationen trainiert wird. Dieses Modell wurde lokal, also unter Vernachlässigung des Staubtransportes, getestet. Es zeigt sich, dass die lokale Staubentwicklung mit hoher Präzision von künstlichen neuronalen Netzwerken vorhergesagt werden kann.

ABSTRACT

Our understanding of planet formation in the gas and dust disks surrounding newborn stars is crucially dependent on the accuracy and complexity of numerical models. Gas and dust interact in different ways, both aerodynamically and thermodynamically. This interaction leads to the development of structure-forming instabilities and must be understood to explain the observed appearance of protoplanetary disks.

In the first part of this dissertation, we demonstrate that efficient thermal coupling of dust and gas is essential for the development of the vertical shear instability (VSI). This purely hydrodynamic instability leads to the formation of turbulence and substructures in protoplanetary disks. VSI furthermore contributes to the vertical dispersion of dust and might thus play an essential role in the interpretation of observational data. A prerequisite for its development is a sufficiently short thermal coupling time of the gas and dust, which ensures efficient cooling of the gas. Whether the VSI can develop is therefore influenced by the subtleties of the dust size distribution. The results of our numerical simulations suggest that the VSI could be suppressed in the outer regions of protoplanetary disks (beyond $\sim$70 au) if the dust particles have undergone significant growth. The reason for this is the depletion of small grains, which are necessary for the cooling process. Following these studies, we refine our methodology and conduct simulations in which the thermal coupling time is calculated dynamically, based on the evolving dust distribution. We show that a protoplanetary disk can only develop and maintain VSI if sufficient amounts of small dust ($\lesssim 10\,\mu$m) are present to ensure the necessary fast thermal relaxation. This illustrates the necessity of considering the coagulation process in simulations of protoplanetary disks.

However, the integration of modern dust coagulation models into large-scale hydrodynamic simulations is hindered by their enormous computational cost. In the remaining part of this thesis, we therefore develop two new, approximate and, therefore, more efficient sub-grid models of dust growth. Both methods are based on the representation of the size distribution as a power law with only two populations and thus avoid the usual, time-consuming use of high-resolution mass grids. The first model is semi-analytic. The growth and mass exchange rates of the dust populations are analytically defined and numerically integrated. Since these rates are approximations, they contain various free parameters. Therefore, the model is calibrated to achieve good agreement with full-fledged dust coagulation models. We demonstrate the accuracy of this approach in various test simulations. As a possible application example, we present a two-dimensional simulation of a protoplanetary disk that is perturbed by the gravitational potential of a planet. Finally, we discuss the use of a machine-learning-based technique as an alternative to the semi-analytical approach. For this purpose, we replace the analytical evolution rates with an artificial neural network, which is trained using data from full dust coagulation simulations. This model has so far only been tested locally, i.e., without considering the dust transport. We show that the local dust evolution can be predicted by artificial neural networks with high precision.

CONTENTS

CHAPTER 1

INTRODUCTION

"Kol-Ut-Shan"
"Infinite Diversity in Infinite Combinations."

— Principle of Vulcan Philosophy
Star Trek

How Can We Explain the Diversity of Exoplanets?

Historical Remarks on Planet Formation Theory

In 1995 Mayor and Queloz reported the first detection of a planetary companion to a solar-type star, leading to their reception of the Nobel Prize in physics in 2019 (Mayor & Queloz, 1995). Since then, an astounding multitude of planets has been discovered in alien star systems[1]. Even the earliest detections raised new questions about the origins of these systems. They were incompatible with the classical paradigms in planet formation theory which were conceptualized with only the Solar system in mind. High-mass planets in extremely close orbits, such as the one detected in 1995, were simply not known.

The earliest models of planet formation were developed in the 18^{th} century. In *Universal Natural History and Theory of the Heavens*, Immanuel Kant—inspired by the coplanar trajectories of the Solar system planets—hypothesized that the celestial objects in orbit of the Sun must have formed from a disk-like gas and dust cloud. Kant's idea, however, was not further pursued for almost two centuries. Alternative concepts emerged in the early 20^{th} century. Chamberlin & Moulton (1909) investigated the possibility of tidal ejection of matter from the Sun, which would have then condensed into *planetesimals*—their term for an infinitesimal version of a planet. However, no upcoming theory proved to be as plausible as the almost forgotten *Nebular Hypothesis*.

In 1943, von Weizsäcker resurrected Kant's approach and for the first time supported it with a basic mathematical framework. His formulations became the prototype of modern planet formation theory (Weizsäcker, 1943). They could explain the coplanar orbits of the Solar system bodies, the angular momentum distribution in the Solar system, and the origins of the planets as a natural consequence of star formation. The extreme Reynolds numbers within the proposed protoplanetary disk are so large ($\sim 10^7$), that von Weizsäcker assumed the disk to be highly turbulent. Turbulence would lead to the formation of vortices, which collect solid particles which would condense into planets. Driven by turbulent angular momentum transport, the gaseous disk would accrete onto the central star—a process von Weizäcker formalized later (Weizsäcker, 1948). His equation was first solved by Lüst (1952) and became a standard model for the evolution of accretion disks. Further developed by Lynden-Bell & Pringle (1974), it can be used to predict the evolution and structure of

[1] see `https://exoplanets.nasa.gov/`

viscously evolving circumstellar disks. The theory of viscous accretion and the respective disk structure model are still widely used in theoretical studies of planet formation today.

In parallel to the aforementioned advancements in the physical understanding of the gaseous disk, theories for the evolution of solids and the formation of planets were further developed. Safronov (1969) and Goldreich & Ward (1973) independently developed a theory on planetesimal formation in which solids accumulate in the protoplanetary disk's midplane to form a dense, gravitationally unstable layer. The local collapse of this dust layer would then lead to the formation of the planetesimals. Even low levels of turbulence, however, prevent a thin enough layer from forming in the first place. It became clear that direct gravitational collapse of the particle layer in turbulent protoplanetary disks is probably not occurring (Weidenschilling, 1980; Cuzzi et al., 1993).

Nowadays, it is believed that a single physical mechanism for planetesimal formation does not exist. Instead, a number of physical processes are likely occurring simultaneously or in sequence, that lead to the emergence of larger bodies (see Drążkowska et al., 2023). Many details of this picture remain elusive. Micrometer-sized dust grains, as present in interstellar space, must grow several orders of magnitude in size until they can undergo significant settling. Even then, further accumulation in large-scale structures—so-called dust traps—must likely occur to facilitate high-enough concentrations to trigger planetesimal formation. The origins of such high-pressure regions are ambiguous even in contemporary theories (see Bae et al., 2023). Modern-day studies of planet-forming disks thus involve hydrodynamic simulations of the gas and dust flows on large scales (several 10^{11} m), as well as modeling of the microphysics of dust (from µm to m). Both aspects are necessary to better understand the origins of our world and the diversity of exoplanets that we observe today.

1.1 From Clouds to Disks and Stars

The formation of a protostar is the necessary first step toward the formation of a planetary system. Star formation occurs in the cold phase of the *interstellar medium* (ISM) within *Giant Molecular Clouds* (GMCs). These structures have typical temperatures of ∼10 K and masses of 10^4–10^6 $M_\odot$—about 1 % of which is made up of heavy elements in the form of solids, referred to as dust (see Chevance et al., 2023). Stellar feedback and supernova shock fronts create bubbles and filamentary substructures within molecular clouds.

An especially spectacular example of such a substructure is the Local Bubble—an underdense region of space with a size of ∼100 pc (1 pc=3.086×10^{18} cm) our Sun is passing through (Cox & Reynolds, 1987). Recent studies by Zucker et al. (2022) could for the first time show that the surface of this bubble is a site of active star formation. Overdense cloud cores can be formed along the surfaces of these substructures.

If they reach the critical Bonnor-Ebert mass (Ebert, 1955; Bonnor, 1956), exterior pressure perturbations can no longer be counteracted by an internal increase in gas pressure and the core begins to collapse (see Figure 1.1). At first, this collapse is continuing almost isothermally, as the gas is optically thin and can cool on a short timescale. But as densities increase in its center, the structure becomes optically thick and thus heats up. The increasing internal pressure leads to the formation of a first hydrostatic structure in the center, the so-called first Larson core (Larson, 1969).

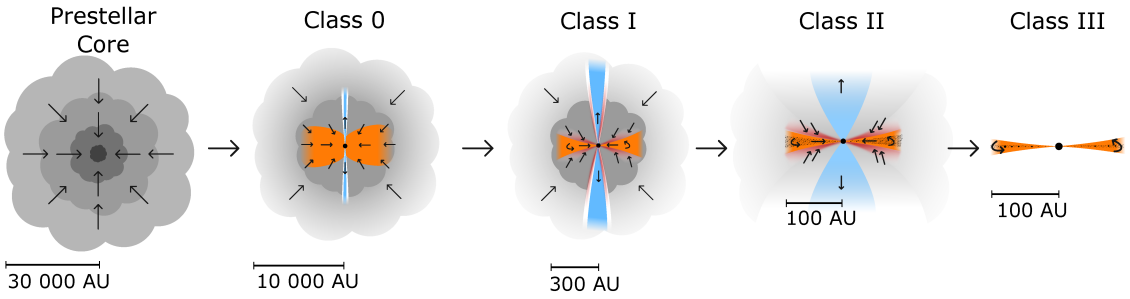

Figure 1.1
Overview of the star and disk formation process. Stellar feedback leads to the formation of substructures in the cold ISM. Individual molecular cloud cores can undergo gravitational collapse. The infalling material has non-zero angular momentum and thus forms a disk-shaped structure around the embedded protostar (class 0/I). After the main accretion phase, the pre-main-sequence star and the protoplanetary disk are directly observable (class II/III) (figure adapted from Persson (2013), originally licensed under CC BY 4.0).

As material is continuously added from the surrounding layers, the core undergoes an adiabatic contraction phase, which increases the central temperature (Masunaga et al., 1998; Bhandare et al., 2018). Cooling remains inefficient until the temperatures surpass ~2000 K. At this point, the main constituent of the structure, molecular hydrogen, begins to dissociate. Thermal energy stemming from the continuous compression of the core is no longer increasing the temperature but is absorbed by the dissociation of the H_2 molecules. A second collapse phase sets in, which persists until all molecular hydrogen has been dissociated and a stable adiabatic core composed of atomic hydrogen is formed. This second core is what is referred to as a protostar or the second Larson core (Masunaga & Inutsuka, 2000; Bhandare et al., 2020). It is still deeply embedded in the accreting cloud envelope and the central object can thus not be observed directly. Such a system is referred to as a class 0/I *young stellar object* (YSO).

The accreting material has non-zero angular momentum due to the large-scale motion of the cloud core. Therefore, gas parcels cannot directly fall onto the emerging protostar but settle into a disk-shaped structure. Given the typical angular momentum of a molecular cloud code of size $\ell_{\rm core}$, mass $M_{\rm core}$, and angular frequency $\Omega_{\rm core}$, we can estimate the size of the emerging disk by assuming angular momentum conservation. In the emerging disk, centrifugal and gravitation forces are balanced, which gives us the Keplerian angular frequency $\Omega_{\rm K} = \sqrt{GM_\star/R^3}$, where G is the gravitational constant, $M_\star$ is the mass of the central star and R is the distance to the star. From angular momentum conservation $R^2_{\rm disk}\Omega_{\rm K,disk} = \ell^2_{\rm core}\Omega_{\rm core}$, we then find

$$R_{\rm disk} = \frac{\ell^4_{\rm core}\Omega^2_{\rm core}}{GM_{\rm core}} \sim 100\,{\rm au}\,, \tag{1.1}$$

(1 au=1.496×10^{13} cm) where $R_{\rm disk}$ is the radius at which the cloud material ends up in a centrifugally balanced disk. It is also referred to as the *centrifugal radius* (e.g., Terebey et al., 1984). This is of course only an order of magnitude estimate and disk of larger and smaller sizes have been observed (see Miotello et al., 2023).

1.2 Unresolved Observations of Young Stellar Objects

As even the closest star-forming regions are hundreds of pc away, it was not possible to even spatially resolve YSO's until the era of space-borne observatories (O'dell et al., 1993). A technique that only requires unresolved observations to determine whether an object is a YSO is the analysis of the object's *spectral energy distribution* (SED), i.e., the distribution of observed flux F_λ across wavelengths λ. The logarithmic slope of the SED in the infrared, referred to as the *spectral index*, is a commonly used measure to distinguish between the different evolutionary stages and is defined as

$$\alpha_{\mathrm{IR}} = \frac{\partial \log(\lambda F_\lambda)}{\partial \log(\lambda)} \,.$$

For this, the slope is usually measured in the near to mid-infrared from ∼2 µm to ∼10 µm. In the following, I refer to the standard classification scheme as summarized by Armitage (2020). A class 0 YSO is still deeply embedded in a cold envelope. No radiation from the central object is directly visible, which means all detected radiation was processed by the dusty envelope and the SED peaks in the far-infrared. Since no detectable radiation is emitted in the near-infrared at this stage, the spectral slope is not defined for such objects.

In these earliest phases of its lifetime, the protoplanetary disk is still embedded in an optically thick envelope. First signs of disk formation may show up, such as jets which carve cavities at the poles of the cloud. The SED is typically rising or flat in the region between near-infrared and mid-infrared and the object is called a class I YSO. A very simple model of such an object is shown in Figure 1.2, where it is simulated as a spherical envelope with a parabolic polar cavity surrounding a protostar. The main accretion phase ends after $\sim 10^6$ yr, and the resulting central body, which has almost reached its final mass, is called a pre-main-sequence star. It is still surrounded by the geometrically thin circumstellar disk which has a typical size of 100 au. The system is now referred to as a class II pre-main-sequence star with the surrounding protoplanetary disk. The SED in the near-infrared is essentially the SED of the central pre-main-sequence star. The surrounding gas and dust disk, however, scatters short wavelength radiation from the star or absorbs it and re-emit in the mid to far-infrared which causes an infrared excess. This sets a class II YSO apart from the spectrum of a class III object that has accreted almost all mass and is essentially the spectrum of a pre-main-sequence star.

The identification of class II YSOs from their SEDs makes it possible to determine how frequent protoplanetary disks are (Haisch et al., 2001). Alternatively, ultraviolet observations can reveal the signatures of ongoing mass accretion, as they track the hot shocks of material reaching the central star (Hartmann et al., 1998). Determining the numbers of class II YSO in star formation regions of different ages with these methods therefore allows us to deduce the average lifetimes of these objects. In general, one finds that almost all stars in clusters of ages $\lesssim 10^6$ yr have protoplanetary disks. Clusters older than 3×10^6 yr have a disk fraction of $\sim 5\,\%$. Disk lifetimes are thus generally assumed to be in the range of a few 10^6 yr (Manara et al., 2023).

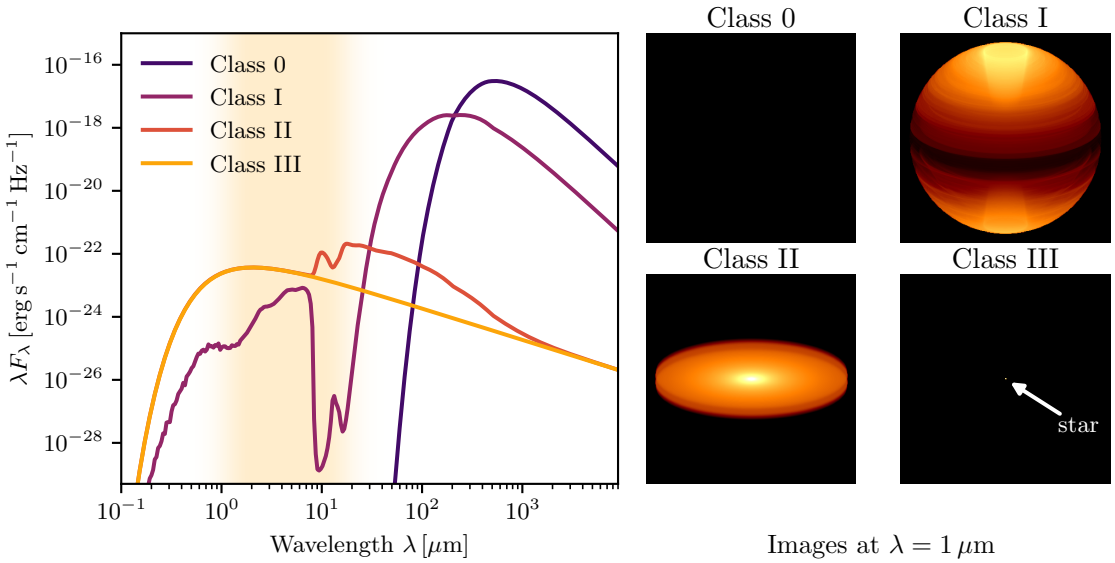

Figure 1.2
Simple radiative transfer modeling of SEDs and infrared pictures of YSO models at $\lambda = 1\,\mu$m and at an inclination of 70°. The yellow shaded area marks the wavelength region in which the spectral slope is typically calculated. All objects have the same stellar model in the center and are only distinguished by their dusty envelopes. Class 0 has a high-density spherical envelope, which completely obscures the central object. It cannot be observed in the near IR. Class I is modeled as a spherical envelope with lower density and a parabolic cavity. Here, some near IR flux can be detected and the spectral slope is increasing or nearly flat. The class II object is modeled as a much smaller, flaring disk. The stellar spectrum is present but a strong infrared excess can be seen, stemming from the reprocessed stellar light from the disk. Class III is a non-obscured pre-main-sequence star with a typical black body spectrum. Spectra and images were modeled with `RADMC-3D` (Dullemond et al., 2012).

1.3 Resolved Observations of Protoplanetary Disks

In observations at optical wavelengths, edge-on protoplanetary disks show up as dark shadows, blocking the light from the central pe-main-sequence star, as seen by the *Hubble Space Telescope* in the Orion star-forming region (Figure 1.3).

These images also reveal that protoplanetary disks are not isolated structures. They are subject to radiation from nearby stars, as well as streamers of gas from the surrounding star-forming region. The spatial resolution necessary for the observation of an object of 100 au radius in the Orion nebular at a distance of 414 pc is only $\sim 0.48''$. The protoplanetary disk images in Figure 1.3 combine broadband and narrowband observations with the *Wide Field Channel* of the *Advanced Camera for Surveys* (ACS/WFC), installed on Hubble (Ricci et al., 2008). This instrument allows for spatial resolutions of $\sim 0.1''$[2]. The resolution of such space-borne observatories is only limited by diffraction at the aperture and can be calculated via

$$\theta_{\text{lim}} \approx 1.22 \frac{\lambda}{D}, \tag{1.2}$$

where D is the size of the aperture of the telescope (Rayleigh, 1879). Larger telescopes or

[2] from the ACS user handbook.

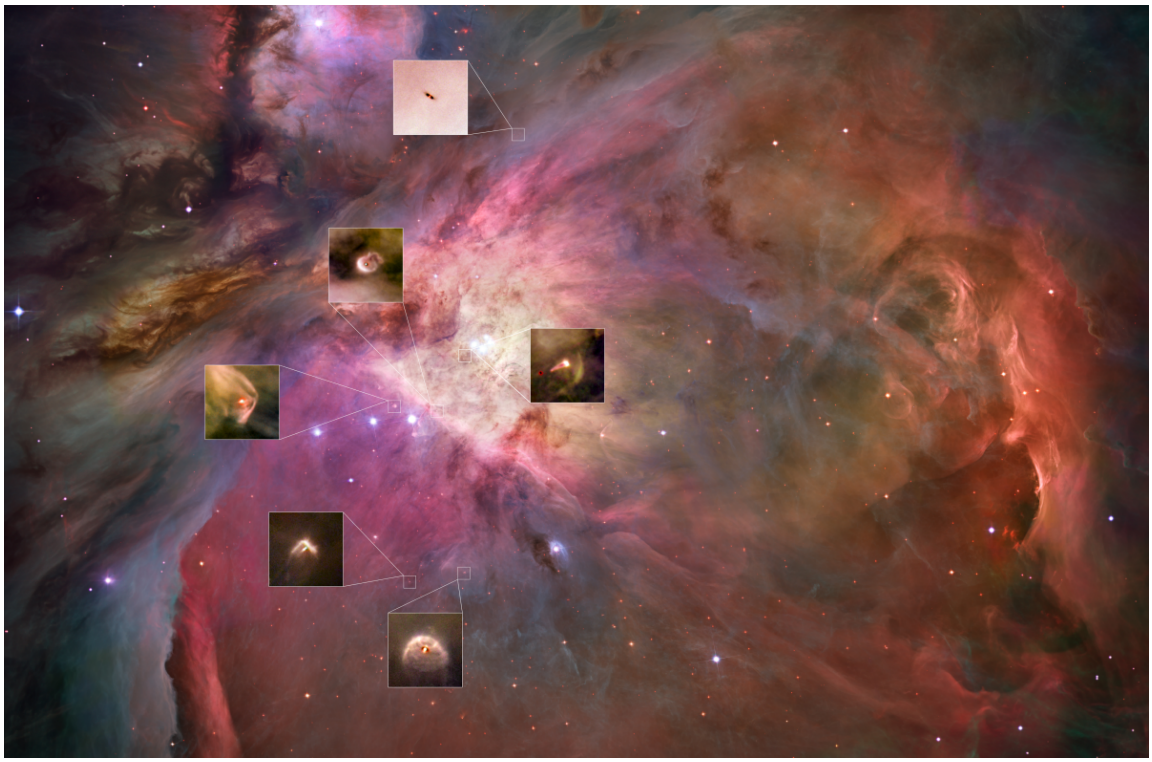

Figure 1.3
Protoplanetary disks in the Orion nebular. The base image was taken with the ground-based 2.2 m ESO telescope at La Silla. The inserted pictures of protoplanetary disks were obtained with the *Wide Field Channel of the Advanced Camera for Surveys* (ACS/WFC) of Hubble at various wavelengths (Ricci et al., 2008). (figure by NASA, ESA, M. Robberto (Space Telescope Science Institute/ESA), the Hubble Space Telescope Orion Treasury Project Team and L. Ricci (ESO), licensed under CC BY 4.0)

observations at shorter wavelength thus allow for higher angular resolution.

Observations targeting the dust or objects that are obscured by it however rely on the use of longer wavelengths. Radio interferometers, like the *Atacama Large Millimeter/Submillimeter Array* (ALMA) and adaptive optics systems in combination with coronographs, like the *Spectro-Polarimetric High-contrast Exoplanet REsearch* (SPHERE) instrument at the *Very Large Telescope* (VLT) make observations at spatial resolutions possible that were unheard of only 10 years ago. ALMA's longest baseline configuration with a maximum separation of 16 km, for example, can reach spatial resolutions of up to $0.02''$[3]. Going to longer wavelengths and utilizing interferometric techniques not only influences the resolution of the observations but also *what* is observed. Infrared and millimeter-wavelength observations allow for an in-depth look at protoplanetary disks, while in the optical wavelength range light is almost completely blocked or scattered by the dust.

Figure 1.4 depicts a representative example of how the use of different wavelengths influences what we see. Shown is the protoplanetary disk around the pre-main-sequence star IM Lup in the Lupus 2 molecular cloud[4]. In the millimeter-wavelength observation on

[3] from the ALMA technical handbook.
[4] `https://simbad.cds.unistra.fr/simbad/sim-id?Ident=IM+Lup`

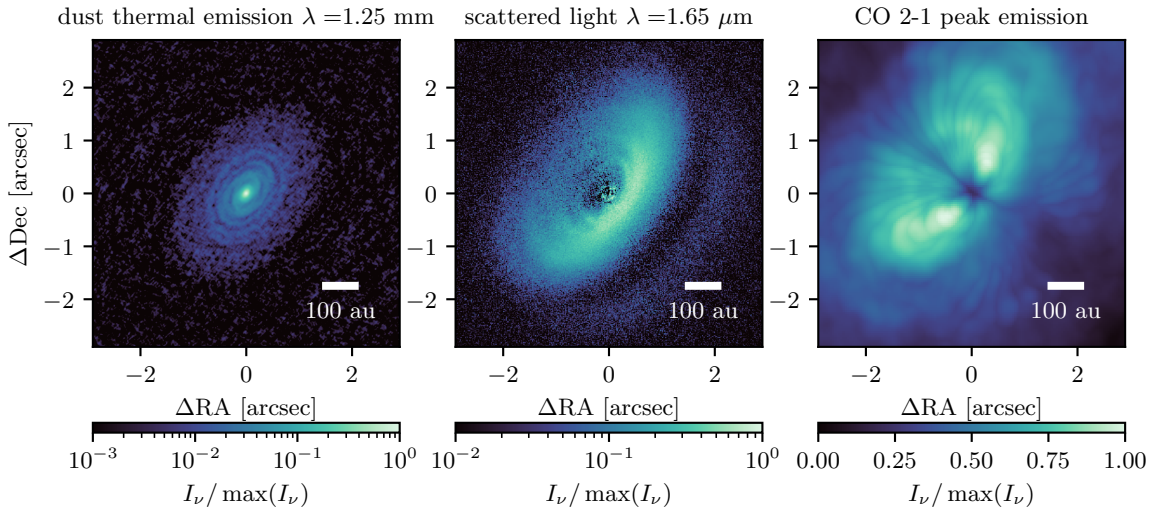

Figure 1.4
Views of the protoplanetary disk around IM Lup at different wavelengths, obtained with different instruments. Millimeter-wavelength observations, obtained by Andrews et al. (2018) with ALMA reveal the thermal emission of larger dust grains that form a thin layer in the midplane of the disk. In the near-infrared image, obtained by Avenhaus et al. (2018) with the SPHERE instrument at the VLT, one can see the surface of the disk, where small dust grains scatter the infrared radiation from the central star. ALMA can also be used to study molecular line emission, as in the data presented in the right panel obtained by the MAPS collaboration (Öberg et al., 2021). Here, the 2-1 rotational transition of CO molecules is probed which can be found in a molecular layer above the disk midplane.

the left, obtained at $\lambda = 1.25\,\mathrm{mm}$ by Andrews et al. (2018), we can see the thermal emission of mostly larger dust grains. Larger particles appear to exist close to the midplane of the disk. Substructure is visible in the form of two spiral arms close to the central star. Smaller particles scatter shorter-wavelength infrared and optical light from the star, which can be seen in the central panel of Figure 1.4, observed with the SPHERE instrument by Avenhaus et al. (2018). The disk appears much larger and vertically extended in these observations, which means that the smaller dust particles do not form a thin structure but are kept at larger height above the disk's midplane. With ALMA, molecular line observations offer another way to study disk structure as done by Öberg et al. (2021), who probe the 2-1 rotational transition of the CO molecule, shown in the right panel of Figure 1.4.

These examples show that there must be processes in protoplanetary disks that separate dust grains of different sizes and the gas component. To understand how this works, we need to consider the overall physical structure of the gaseous disk, the gasflows therein, and the aerodynamic properties of the dust grains. To further explain how substantial amounts of larger grains can exist in a disk that is formed from material that contains predominantly micrometer-sized particles, we must also consider the physics of particle collisions that lead to coagulation and fragmentation. Bringing these aspects together in hydrodynamic models of protoplanetary disks is the main topic of this thesis.

CHAPTER 2

THEORETICAL BACKGROUND

2.1 Hydrodynamics of Protoplanetary Disks

Protoplanetary disks are predominantly made up of gas in the form of molecular hydrogen. The large scale of the system ($\sim 10^{13}$ cm) and the comparably short mean free path of the gas molecules ($\sim$10 cm)[1], make it possible to describe the evolution of the gas with the laws of hydrodynamics, i.e., through the Navier-Stokes equations (see, e.g., Shu, 1992)

$$\frac{\partial \rho_\mathrm{g}}{\partial t} + \boldsymbol{\nabla} \cdot (\rho_\mathrm{g} \boldsymbol{v}) = 0 \tag{2.1}$$

$$\frac{\partial \rho_\mathrm{g} \boldsymbol{v}}{\partial t} + \boldsymbol{\nabla} \cdot (\rho_\mathrm{g}\, \boldsymbol{v} \otimes \boldsymbol{v}) = -\boldsymbol{\nabla} P - \rho_\mathrm{g} \boldsymbol{\nabla} \Phi + \boldsymbol{\nabla} \cdot \mathbf{T} + \rho_\mathrm{g} \boldsymbol{f}\,, \tag{2.2}$$

where ρ_g refers to the gas density, $\boldsymbol{v}$ is the gas velocity vector, P is the the pressure, Φ is the gravitational potential, $\mathbf{T}$ is called the viscous stress tensor, and $\boldsymbol{f}$ is a vector containing all other specific external forces. A similar conservation law holds for the total energy per unit volume of the fluid $E = \rho_\mathrm{g} \left(1/2\, \boldsymbol{v}^2 + e\right)$, where the first term is the specific kinetic energy and the second term is the specific internal energy. The energy equation reads

$$\frac{\partial E}{\partial t} + \boldsymbol{\nabla} \cdot [(E + P)\boldsymbol{v}] = \boldsymbol{\nabla} \cdot (\boldsymbol{v} \cdot \mathbf{T}) - \rho_\mathrm{g} \boldsymbol{v} \cdot \boldsymbol{\nabla} \Phi + \boldsymbol{\nabla} \cdot \boldsymbol{F}\,, \tag{2.3}$$

where $\boldsymbol{F}$ refers to the heat flux. Solving this system of equations analytically is only possible for a few fringe cases and numerical methods usually have to be applied (see Section 3.1). In any case, a closure relation is necessary that links pressure and density. Throughout this thesis, I use the ideal equation of state

$$P = \rho_\mathrm{g} \frac{k_\mathrm{B} T}{\mu m_\mathrm{P}} = \rho_\mathrm{g} c_\mathrm{s}^2\,, \tag{2.4}$$

where k_B is the Boltzmann constant, T is the gas temperature, and μm_P is the mean molecular mass. This also defines the isothermal speed of sound c_s. In the following sections, I give an overview of different applications of the Navier-Stokes equations in the context of protoplanetary disks, often in a simplified form, or with focus on specific terms of the equations.

[1] number density of molecules $n \sim 10^{14}\,\mathrm{cm}^{-3}$ (Armitage, 2020), collisional cross-section $\sim 10^{-15}\,\mathrm{cm}^2$ (Chapman & Cowling, 1991)

2.1.1 Hydrostatic Disk Structure

Protoplanetary disks are rotationally supported structures. Due to their lifetimes of a few 10^6 yr and the comparably short dynamical timescales of the gas motion, they can be seen as quasi-stationary and thus in hydrostatic equilibrium. Deriving their structure in the gravitational potential of their central star is most convenient in cylindrical coordinates R and z. In this coordinate system, the central star's gravitational potential is given by $\Phi = {}^{GM_\star}/\sqrt{R^2+z^2}$, with G referring to the gravitational constant and $M_\star$ being the mass of the central star. Assuming the disk to be axisymmetric and inviscid, hydrostatic equilibrium in Equation 2.2 gives

$$\frac{1}{\rho_\mathrm{g}}\frac{\partial P}{\partial z} = -\frac{GM_\star z}{(R^2+z^2)^{3/2}} \qquad \text{for vertical hydrostatic balance and}$$

$$\frac{1}{\rho_\mathrm{g}}\frac{\partial P}{\partial R} = -\frac{GM_\star R}{(R^2+z^2)^{3/2}} + \Omega^2 R \qquad \text{for radial hydrostatic balance.}$$

Here Ω is the angular frequency with $\Omega^2 R$ being the centrifugal acceleration of the gas. The equation for vertical hydrostatic equilibrium can readily be solved for ρ_g, which results in the standard form for the vertical stratification of a circumstellar disk

$$\rho_\mathrm{g}(R,z) = \rho_\mathrm{g,mid}(R)\exp\left[\frac{R^2}{H_\mathrm{g}^2}\left(\frac{R}{\sqrt{R^2+z^2}}-1\right)\right], \tag{2.5}$$

where $\rho_\mathrm{g,mid}$ is the density at $z = 0$ (the *disk midplane*) and H_g is referred to as the pressure scale height, defined as

$$H_\mathrm{g} = \frac{c_\mathrm{s} R^{3/2}}{\sqrt{GM_\star}} = \frac{c_\mathrm{s}}{\Omega_\mathrm{K}}\,. \tag{2.6}$$

The pressure scale height is a measure of the thickness of the gaseous disk and a typical aspect ratio observed in protoplanetary disks is ${}^{H_\mathrm{g}}/_R = 0.05$. It has essentially the same meaning as the pressure scale height of a planetary atmosphere (on Earth typically $H_\mathrm{g} \approx 8\,\mathrm{km}$, Holton & Hakim, 2012), which is why the vertical disk structure is occasionally referred to as *the atmosphere* of the protoplanetary disk—an analogy that I will further use in the overview of turbulence and hydrodynamic instabilities in Section 2.1.4.

The radial hydrostatic balance equation cannot be solved for the density structure so easily. Nonetheless, we can learn about the dynamics of the disk from it. Rearranging the equation gives

$$\left(\frac{\Omega}{\Omega_\mathrm{K}}\right)^2 = \left(\frac{H_\mathrm{g}}{R}\right)^2 \frac{\partial \log(P)}{\partial \log(R)} + \frac{R^3}{(R^2+z^2)^{3/2}}\,. \tag{2.7}$$

With the typical value for the aspect ratio of a protoplanetary disk and assuming that the logarithmic pressure gradient is negative, we can see that the gas will orbit the star at slightly sub-Keplerian velocity. The reason for this is the inward-pointing pressure gradient. Above the midplane of the disk, we find that the azimuthal gas velocity has a dependency on z. A hydrostatic disk atmosphere will thus be subject to a vertical shear. Deducing the radial density structure is not possible from just hydrostatic equilibrium. For this, we have to consider the evolution of the disk as a consequence of viscosity.

However, it is commonly assumed that the radial structure in density and temperature follows power laws, i.e., $T(R) \propto R^{\beta_T}$ and $\rho_{\mathrm{g,mid}}(R) \propto R^{\beta_\rho}$. The angular frequency thus follows as

$$\left(\frac{\Omega}{\Omega_\mathrm{K}}\right)^2 = \left(\frac{H_\mathrm{g}}{R}\right)^2 (\beta_T + \beta_\rho) - \frac{\beta_T R}{\sqrt{R^2+z^2}} + \beta_T + 1\,. \tag{2.8}$$

2.1.2 Viscous Evolution

The evolution of a protoplanetary disk requires some sort of dissipation of kinetic energy, which leads to the evolution of a gas parcel's orbit. In the Navier-Stokes equations, this dissipation is described with the viscous stress tensor $\mathbf{T}$ and is the consequence of the stress arising between shearing fluid parcels. If no shear is present, no dissipation is to be expected, which means that the viscous stress tensor cannot contain terms that are independent of $\partial v_i/\partial x_k$. This must of course also be true for a fluid in solid body rotation. The most general form that fulfills these conditions is

$$T_{ij} = \rho_\mathrm{g}\nu\left(\frac{\partial v_i}{\partial x_j} + \frac{\partial v_j}{\partial x_i} - \frac{2}{3}\delta_{ij}\frac{\partial v_k}{\partial x_k}\right) + \xi\delta_{ij}\frac{\partial v_k}{\partial x_k}\,, \tag{2.9}$$

where ν is called the kinematic viscosity and ξ is called the bulk viscosity. Both are inherent properties of a fluid (e.g., Landau & Lifschitz, 1987). The bulk viscosity can usually be ignored in astrophysical flows as long as they are sub-sonic. We thus set $\xi = 0$ in the following considerations (Clarke & Carswell, 2007). With these definitions, we can write the Navier-Stokes equation as

$$\frac{\partial \boldsymbol{v}}{\partial t} + (\boldsymbol{v}\cdot\boldsymbol{\nabla})\boldsymbol{v} = -\frac{1}{\rho_\mathrm{g}}\boldsymbol{\nabla}P - \boldsymbol{\nabla}\Phi + \nu\boldsymbol{\Delta}\boldsymbol{v} + \frac{\nu}{3}\boldsymbol{\nabla}(\boldsymbol{\nabla}\cdot\boldsymbol{v})\,, \tag{2.10}$$

where $\boldsymbol{\Delta} = \boldsymbol{\nabla}\cdot\boldsymbol{\nabla}$. Weizsäcker (1943) and Lüst (1952) were the first to analytically study the evolution of circumstellar disks under the influence of viscosity. Lynden-Bell & Pringle (1974) presented the derivations in a form that is commonly referred to nowadays. They assumed the disk to be thin and thus used the Navier-Stokes Equation 2.10 in a vertically integrated form with the gas column density $\Sigma_\mathrm{g} = \int_{-\infty}^{\infty}\rho_\mathrm{g}\,\mathrm{d}z$. Further assuming axisymmetry ($\partial_\varphi = 0$) and $v_z = 0$, the only non-zero component of the stress tensor in cylindrical coordinates is

$$T_{R\varphi} = \rho_\mathrm{g}\nu R\frac{\partial\Omega_\mathrm{K}}{\partial R}\,. \tag{2.11}$$

Using this definition, Lynden-Bell & Pringle (1974) derived the evolution equation of a Keplerian disk as

$$\frac{\partial\Sigma_\mathrm{g}}{\partial t} = \frac{3}{R}\frac{\partial}{\partial R}\left[R^{1/2}\frac{\partial}{\partial R}\left(\nu\Sigma_\mathrm{g}R^{1/2}\right)\right]\,. \tag{2.12}$$

This equation has a self-similar solution that illustrates the effect of viscosity on a differentially rotating circumstellar disk if viscosity follows a radial power law $\nu \propto R^{-\beta_\Sigma}$. For an

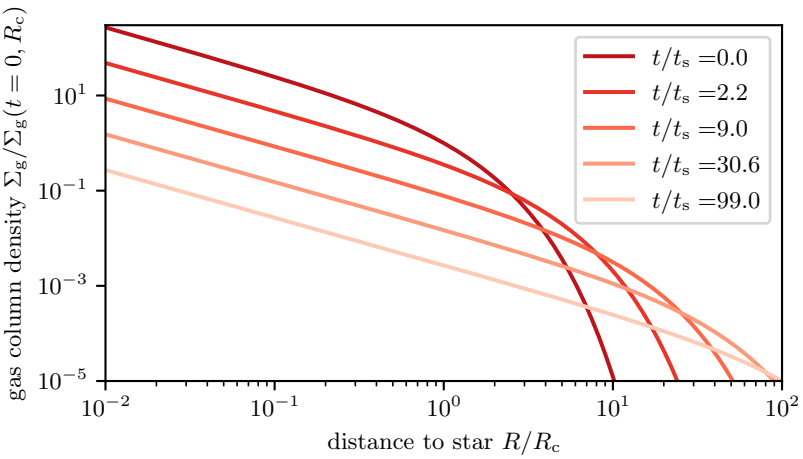

Figure 2.1
Solutions to the disk evolution equation for different evolution times. As angular momentum is transported outwards, the disk is expanding. The bulk of the mass is moving inwards, as a small mass fraction takes away the angular momentum.

initial condition given by

$$\Sigma_g(t=0,R) = \frac{C}{3\pi\nu_c}\left(\frac{R}{R_c}\right)^{\beta_\Sigma} \exp\left[-\left(\frac{R}{R_c}\right)^{\beta_\Sigma+2}\right], \tag{2.13}$$

with the characteristic radius R_c, and the viscosity $\nu_c = \nu(R_c)$, Lynden-Bell & Pringle (1974) derived

$$\Sigma_g(t,R) = \frac{C}{3\pi\nu_c}\left(\frac{R}{R_c}\right)^{\beta_\Sigma} \mathcal{T}^{\frac{5/2+\beta_\Sigma}{2+\beta_\Sigma}} \exp\left[-\frac{1}{\mathcal{T}}\left(\frac{R}{R_c}\right)^{\beta_\Sigma+2}\right], \tag{2.14}$$

where $\mathcal{T}$ is a dimensionless time variable (see also Armitage, 2020).

Figure 2.1 depicts the time evolution of such a truncated power-law disk. As an effect of viscosity, angular momentum is transported away from the central star by a small fraction of the disk's gas mass. In the process, the disk expands with time. Most mass moves inwards and is accreted onto the central object. Equation 2.12 can be brought into the form of a classic diffusion equation $\partial_t f - D\partial_R^2 f = 0$, which allows us to estimate the timescale of this process. The related diffusion timescale is simply $\tau_\nu \approx R_{\rm disk}^2/\nu$, where $R_{\rm disk}$ is the size of the disk, which we know is typically $R_{\rm disk} \sim 100\,\mathrm{au}$. We can estimate the diffusion coefficient by assuming that diffusivity is given by the random molecular velocity times the respective mean-free path, which we have already estimated to be $\sim 10\,\mathrm{cm}$. The typical velocity of gas molecules with a Maxwellian velocity distribution is given by $v_g = \sqrt{8/\pi}c_s$. The speed of sound can be obtained from the typical pressure scale height of a disk by using $H_g/R = c_s/v_K \approx 0.05$, where we set $v_K(R_{\rm disk}) = \Omega_K(R_{\rm disk})R_{\rm disk}$. With these estimates, we arrive at $v_g \approx 2.4\times10^4\,\mathrm{cm\,s^{-1}}$ and

$$t_\nu \approx 3\times10^{17}\,\mathrm{yr}\,.$$

This means that an accretion disk under the influence of molecular viscosity would have an evolutionary timescale longer than the age of the universe and about 10^{11} times longer than the observationally estimated lifetime of class II YSOs. Molecular viscosity can thus not be the driver of accretion in protoplanetary disks. Weizsäcker (1943) and Lüst (1952)

were already aware of this circumstance and therefore proposed an anomalous source of viscosity that could drive the evolution of protoplanetary disks: turbulence.

2.1.3 Turbulence

Turbulent flows are characterized by unsteady, irregular, and chaotic motions that transport and mix the fluid (e.g., Pope, 2000). In particular, turbulence is characterized by an evolving field of eddy motions of various sizes and velocities. The time evolution of this vorticity field $\boldsymbol{\omega} = \boldsymbol{\nabla} \times \boldsymbol{v}$ can be directly deduced from the Navier-Stokes equations. Gas motions in protoplanetary disks—turbulent or not—are generally sub-sonic and can thus be treated as incompressible (Lyra & Umurhan, 2019). Under this assumption, the density of a moving gas parcel is constant, which results in the condition $\boldsymbol{\nabla} \cdot \boldsymbol{v} = 0$ from Equation 2.1 and we get the incompressible Navier-Stokes equation

$$\frac{\partial \boldsymbol{v}}{\partial t} + (\boldsymbol{v} \cdot \boldsymbol{\nabla})\boldsymbol{v} = -\frac{1}{\rho_\mathrm{g}} \boldsymbol{\nabla} P - \boldsymbol{\nabla}\Phi + \frac{1}{\rho_\mathrm{g}} \boldsymbol{\nabla} \cdot \boldsymbol{T} = -\frac{1}{\rho_\mathrm{g}} \boldsymbol{\nabla} P - \boldsymbol{\nabla}\Phi + \nu \boldsymbol{\Delta} \boldsymbol{v} \,. \tag{2.15}$$

using the vector identity $(\boldsymbol{v} \cdot \boldsymbol{\nabla})\boldsymbol{v} = \boldsymbol{\nabla}(v^2/2) - \boldsymbol{v} \times \boldsymbol{\omega}$ and taking the curl leads to the vorticity equation

$$\frac{\partial \boldsymbol{\omega}}{\partial t} + (\boldsymbol{v} \cdot \boldsymbol{\nabla})\boldsymbol{\omega} = (\boldsymbol{\omega} \cdot \boldsymbol{\nabla})\boldsymbol{v} + \frac{\boldsymbol{\nabla}\rho_\mathrm{g} \times \boldsymbol{\nabla} P}{\rho_\mathrm{g}^2} + \nu \Delta \boldsymbol{\omega} \,, \tag{2.16}$$

(e.g., Davidson, 2015) where we have used that for a scalar function f, $\boldsymbol{\nabla} \times (\boldsymbol{\nabla} f) = 0$. The first term on the right-hand side is responsible for *vortex stretching*—if the velocity field deforms a vortex, it will either spin up or spin down depending on how the moment of inertia changes as a result of the deformation. The second term is the *baroclinic* term. It vanishes if the iso-surfaces of density and pressure are aligned, which is called *barotropic* stratification. The last term tells us that vorticity can be diffused through a medium via viscosity. If we have a look at a two-dimensional, barotropic flow, we find

$$\frac{\partial \boldsymbol{\omega}}{\partial t} + (\boldsymbol{v} \cdot \boldsymbol{\nabla})\boldsymbol{\omega} = \nu \Delta \boldsymbol{\omega} \,, \tag{2.17}$$

which means that vorticity, unlike velocity or momentum, can only change under the influence of viscosity or external body forces (which we have ignored here). While perturbations in pressure can change the velocity field of an incompressible fluid instantaneously and everywhere in the disk through sound waves, vorticity can only change incrementally and localized (Davidson, 2010).

The influence of the randomly fluctuating velocity field can be explored statistically. For this, we assume that the gas velocity and the other variables are the sum of an average component $\langle \boldsymbol{v} \rangle$ and a fluctuating component $\boldsymbol{v}'$. This technique is called Reynolds decomposition (Reynolds, 1895). By applying the chain rule in combination with this condition to the incompressible Navier-Stokes Equation 2.15 and ignoring the gravitational potential for the moment, we get

$$\frac{\partial(\langle v_i \rangle + v_i')}{\partial t} + \frac{\partial}{\partial x_j}(\langle v_j \rangle \langle v_i \rangle + \langle v_j \rangle v_i' + v_j' \langle v_i \rangle + v_i' v_j') = -\frac{1}{\rho_\mathrm{g}} \frac{\partial(\langle P \rangle + P')}{\partial x_i} - \frac{1}{\rho_\mathrm{g}} \frac{\partial(\langle T_{ij} \rangle + T_{ij}')}{\partial x_j} \,.$$

To investigate what effect the fluctuations have in the long run, we apply a time average to this equation, which eliminates all single fluctuating quantities and multiples of them, to arrive at the so-called Reynolds-averaged Navier-Stokes equation, also known as the *mean flow equation* (Reynolds, 1895)

$$\frac{\partial\langle v_i\rangle}{\partial t} + \langle v_j\rangle\frac{\partial\langle v_i\rangle}{\partial x_j} = -\frac{1}{\rho_\mathrm{g}}\frac{\partial\langle P\rangle}{\partial x_i} + \frac{1}{\rho_\mathrm{g}}\frac{\partial}{\partial x_j}\left(\langle T_{ij}\rangle - \rho_\mathrm{g}\langle v_i' v_j'\rangle\right). \tag{2.18}$$

As we can see, this equation contains the new term $-\rho_\mathrm{g}\langle v_i' v_j'\rangle \coloneqq T_{ij}^\mathrm{RS}$, called the Reynolds stress. It describes the momentum transport due to random fluctuations in the gas velocity, i.e., the chaotic mixing that characterizes turbulent flows. This leaves us with a new problem: an additional variable in the Navier-Stokes equation for which we do not have a closure relation.

The closure problem is a long-standing issue in science and engineering and no real solution has been found so far. In the context of accretion disks, an often applied workaround is the use of the *turbulent viscosity* hypothesis in combination with *mixing length* models to describe the long-term effects of turbulence. Boussinesq (1877) introduced the idea that the transport of momentum due to turbulent eddies could have the same effect as conventional viscosity. In this model, the action of turbulence would be proportional to the shear strain. Note, that only the anisotropic components of the Reynolds stresses can transport momentum, which is why the isotropic components are separated in an extra term (e.g., Pope, 2000)

$$-\rho_\mathrm{g}\langle v_i' v_j'\rangle \coloneqq \rho_\mathrm{g}\nu_\mathrm{T}\left(\frac{\partial\langle v_i\rangle}{\partial x_j} + \frac{\partial\langle v_j\rangle}{\partial x_i}\right) - \frac{\rho_\mathrm{g}}{3}\langle v_k' v_k'\rangle\delta_{ij}\,, \tag{2.19}$$

where ν_T is called the *turbulent viscosity* or *eddy viscosity*. If we assume the thin circumstellar disk from Section 2.1.2 we know that the Reynolds stress tensor's only non-zero component in cylindrical coordinates is $T_{R\varphi}^\mathrm{RS}$ (Equation 2.11).

This model leaves us with the question of how to determine the new turbulent viscosity. Mixing length models are a family of methods in which the turbulent viscosity is assumed to scale as $\nu_\mathrm{T} \propto \lambda_\mathrm{mix} v$, where λ_mix is the mixing length, along which turbulent momentum transfer occurs and v is the typical velocity of that transport (Prandtl, 1925). Shakura & Sunyaev (1973) applied this method in the context of accretion disks, assuming that the turbulent velocities would scale with the speed of sound. Since the corresponding length scale on which momentum transfer through an eddy occurs cannot be larger than the disk's vertical extend given by the pressure scale height H_g, they postulated

$$\nu_\mathrm{T} = \alpha c_\mathrm{s} H_\mathrm{g} \tag{2.20}$$

with $\alpha < 1$, which is a parameter characterizing the strength of the angular momentum transport associated with the turbulence. This simple prescription is frequently used in studies of protoplanetary disks, e.g., in models of radial and vertical disk structure (e.g., Meyer & Meyer-Hofmeister, 1982; D'Alessio et al., 1998; Bell & Lin, 1994; Woitke et al., 2009; Pfeil & Klahr, 2019), disk-population synthesis (e.g., Zormpas et al., 2022; Appelgren et al., 2023), planet population synthesis (e.g., Mordasini et al., 2009; Emsenhuber et al., 2021), and in models of dust coagulation (e.g., Birnstiel et al., 2010; Stammler & Birnstiel,

2022). From the same timescale considerations as in Section 2.1.2, we find that α must be in the order of 10^{-3}–10^{-2} to explain the observed disk lifetimes of a few 10^6 yr. By using Equation 2.11, we can relate this variable to the actual turbulent velocity correlations

$$\alpha = \frac{2}{3}\frac{\langle v'_R v'_\varphi \rangle}{c_s^2} \,. \tag{2.21}$$

Again, we have averted the actual problem and arrived at a new question. Is there even a mechanism that can drive turbulent velocity fluctuations in a protoplanetary disk at the required level?

2.1.4 Flow Instabilities

The simplest possible model for the hydrodynamics in a protoplanetary disks is a two-dimensional, unstratified shear flow with Keplerian rotation. A flow is generally considered stable if an arbitrary infinitesimal disturbance decays in time. If the disturbance grows, the flow is unstable (Pope, 2000).

Rayleigh (1917) found that a rotating flow is linearly stable if the condition

$$\frac{1}{R^3}\frac{\mathrm{d}(R^2\Omega)^2}{\mathrm{d}R} \geq 0 \tag{2.22}$$

is met. For a disk with Keplerian rotation $\Omega = \Omega_\mathrm{K}$, this condition is fulfilled, which means Keplerian shear flows are linearly stable. Thus, many other potential sources of instability and turbulence have been researched since the 1970s (Lyra & Umurhan, 2019). The introduction of a weak magnetic field to the ionized shear flow was deemed a possible solution. Interplay of magnetic tension and shear motion results in the *Magnetorotational Instability* (e.g., Balbus & Hawley, 1991) which creates Reynolds and Maxwell stresses strong enough to explain the evolutionary timescale of a perfectly ionized circumstellar disk. It was however soon realized that the low degree of ionization in a protoplanetary disk is a substantial hurdle for the MRI (Blaes & Balbus, 1994). Non-ideal magneto-hydrodynamic effects like *Ohmic resistivity* (Sano & Miyama, 1999) and *ambipolar diffusion* (Desch, 2004) quench the MRI in most regions of protoplanetary disks except for the very hot inner regions and the outer regions, far away from the star (e.g., Jankovic et al., 2021; Lesur et al., 2023). The resulting MRI-inactive region is referred to as the *dead zone*. Its extend is still the subject of current research, but recent studies that combined gas and dust evolution hint towards an outer limit between 10 au and 50 au, depending on the evolutionary stage (Delage et al., 2023).

Instabilities that are independent of the magnetic field and ionization degree have thus come into focus in recent years. They originate from the radial and vertical stratification of the disk itself, often in combination with a certain mode of thermal relaxation. This in combination with the strong impact of rotation makes many of them conceptually similar to instabilities in planetary or stellar atmospheres (Lyra & Umurhan, 2019; Lesur et al., 2023). If an arbitrary stratification is considered (but no thermal relaxation), the linear stability condition is given by the Solberg-Høiland criteria (e.g., Tassoul, 1978; Drazin &

Reid, 2004). Using the definitions of the buoyancy frequencies

$$N_R^2 = -\frac{1}{\rho_g C_P}\frac{\partial P}{\partial R}\frac{\partial S}{\partial R} \tag{2.23}$$

$$N_z^2 = -\frac{1}{\rho_g C_P}\frac{\partial P}{\partial z}\frac{\partial S}{\partial z}, \tag{2.24}$$

where $S = C_V \log\left(P/\rho_g^\gamma\right)$ is the specific entropy of the gas with the ratio of specific heats at constant pressure C_P and at constant volume C_V, $\gamma = c_P/c_V$, these conditions are

$$\frac{1}{C_V}\frac{\partial P}{\partial z}\left(\frac{1}{R^3}\frac{\partial (R^2\Omega)^2}{\partial R}\frac{\partial S}{\partial z} - R\frac{\partial \Omega^2}{\partial z}\frac{\partial S}{\partial R}\right) < 0 \tag{2.25}$$

$$\frac{1}{R^3}\frac{\partial (R^2\Omega)^2}{\partial R} + N_R^2 + N_z^2 > 0 \tag{2.26}$$

(Rüdiger et al., 2002). Both conditions have to be fulfilled for the flow to be stable. The interpretation of Equation 2.25 is a modified version of the classical Schwarzschild criterion and defines the onset of *convection*. Vertical convection ($N_z^2 < 0$) was discussed as a source of turbulent viscosity in the 1970s and 1980s (Cameron, 1978; Lin & Papaloizou, 1980). Fulfilling this condition in protoplanetary disks is however difficult as it requires a strong enough source of heat in the disk's midplane (Held & Latter, 2018; Pavlyuchenkov et al., 2020). Convection in the radial direction of a shear flow with Keplerian rotation is only possible if the radial temperature gradient overcomes the stabilizing effect of rotation. Also this condition is hardly fulfilled in protoplanetary disks, which have radial temperature gradients that are mostly determined by stellar irradiation and are thus not steep enough. The second criterion also takes the vertical shear and the effect of the vertical buoyancy into account. If a vertical shear is present, instability can be hindered by a stable vertical stratification.

Both criteria suggest stability for most protoplanetary disks, as the stratification is usually not strong enough to overcome the stabilizing effects of rotation or buoyancy. This, however, changes if cooling or energy transport are taken into account. I will introduce the radiative processes which make cooling in protoplanetary disks possible in the next sections. For now, we simply assume that temperature perturbations with respect to some equilibrium state can be thermally relaxed on a timescale t_{cool}.

GSF Instability and Vertical Shear Instability

The vertical shear in a protoplanetary disks is maintained by the spherical gravitational potential and the radial pressure gradient of the disk (Equation 2.8). This makes it possible for mostly vertical perturbations with wavenumbers $k_z \ll k_R$ to circumvent the Solberg-Høiland stability criterion (Equation 2.25). Gas parcels can move up-outwards under conservation of their angular momentum, into regions where a stable orbit would have lower kinetic energy than their own, which is illustrated in Figure 2.2. The gas parcel is thus further accelerating up-outwards. This mechanism was first studied in the context of rotating stars by Goldreich & Schubert (1967), and Fricke (1968) (GSF instability) as part of a class of *thermal instabilities*. Its possible application to circumstellar accretion disks

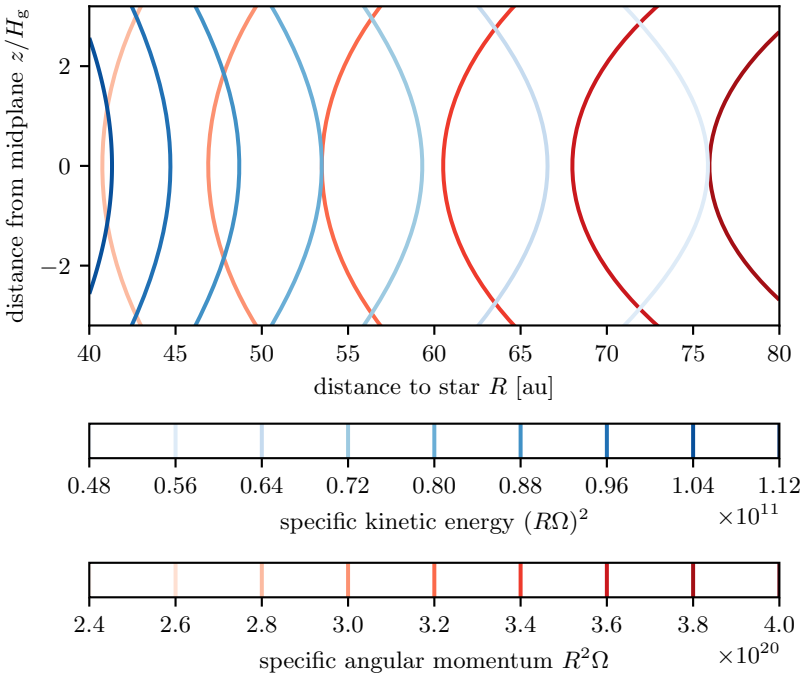

Figure 2.2
Contours of specific angular momentum (red) and specific kinetic energy (blue) in a circumstellar disk model with $\beta_T = -1$, $\beta_\rho = -2.1$ and $H_g/R = 0.05$. Gas parcels can be perturbed along the red contours, thus entering areas where a stable orbit has lower kinetic energy. This causes them to accelerate and create turbulence through the VSI if the cooling time is sufficiently short to diminish the effect of buoyancy.

was recognized by Urpin & Brandenburg (1998), who conducted a local stability analysis for a thin disk and rediscovered the original instability. Urpin (2003) discussed the strong dependency of the instability's growth rate on the cooling timescale. Many following works investigated the vertically global modes of this instability and coined the term *vertical shear instability* (VSI) (Klahr et al., 2023). The cooling time restriction for both versions are nonetheless similar and arise from the vertical stratification of the disk. A vertically moving gas parcel is subject to the vertical component of gravity and can only become buoyant if its entropy adjusts to the background entropy on a sufficiently short timescale. Otherwise, it would undergo a stable oscillation around its equilibrium position. Thermal relaxation is thus ideally instantaneous, which is the regime studied in the first simulations of VSI in protoplanetary disk models with radial and vertical stratification by Nelson et al. (2013). For vertically global VSI modes, Lin & Youdin (2015) found a critical cooling time at which the growth rates begin to decline

$$t_{\mathrm{VSI,\,crit}} = \frac{H_g}{R}\frac{|\beta_T|}{\gamma - 1}\Omega_K^{-1}, \tag{2.27}$$

which was recovered in recent numerical studies by Klahr et al. (2023). At lower numerical resolution, VSI can even be completely absent at cooling times exceeding Equation 2.27, as shown by Manger et al. (2021). Studies of the VSI in three-dimensional hydrodynamic simulations have also shown its ability to form large and long-lived vortices (Richard et al., 2016; Manger & Klahr, 2018). Figure 2.3 shows the three-dimensional protoplanetary disk simulation from Pfeil & Klahr (2021) in which large-scale vortices have formed. These structures emerge as a result of secondary instability in the non-linear velocity field of a VSI-active disk which was found to be the Kelvin-Helmholtz instability by Latter &

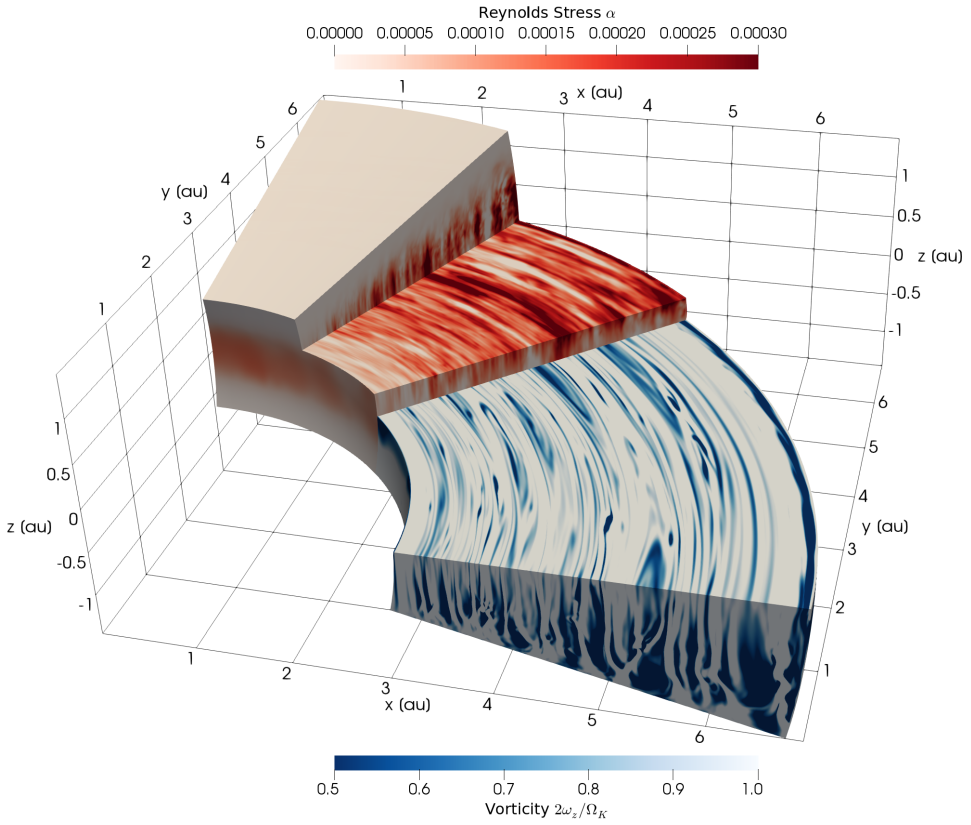

Figure 2.3
Three-dimensional hydrodynamic simulation of a VSI-active protoplanetary disk from Pfeil & Klahr (2021) with the PLUTO code (Mignone et al., 2007). The up and down moving VSI flow structures are initially axisymmetric, then experience a secondary instability, break up and form long-lived anticyclonic vortices.

Papaloizou (2018). Another possible mechanism of vortex formation from VSI turbulence is the Rossby-Wave instability, which was suggested by Richard et al. (2016) and Manger & Klahr (2018).

Convective Overstability and Subcritical Baroclinic Instability

From the Solberg-Høiland criteria, we know that convection in the radial direction of a protoplanetary disk (usually characterized by $N_R^2 < 0$) is stabilized by the angular momentum stratification of the disk. Radial perturbations in an adiabatic gas thus result in stable oscillations called epicycles, which are only slightly modified by a super-adiabatic stratification. Introducing a finite cooling time or some mean of energy transfer, however, changes this situation. Petersen et al. (2007a,b), first explained the resulting baroclinic amplification of vortices, known as the *Subcritical Baroclinic Instability* (SBI). Through vortical motion, a gas parcel is transported outwards in a protoplanetary disk. If the disk's stratification is superadiabatic, the moving gas parcel cannot expand fast enough to adjust to the lower surrounding entropy (see Figure 2.4). Buoyancy accelerates the warm gas parcel outwards. On its way, it thermally relaxes towards the entropy of its new surroundings—in the pro-

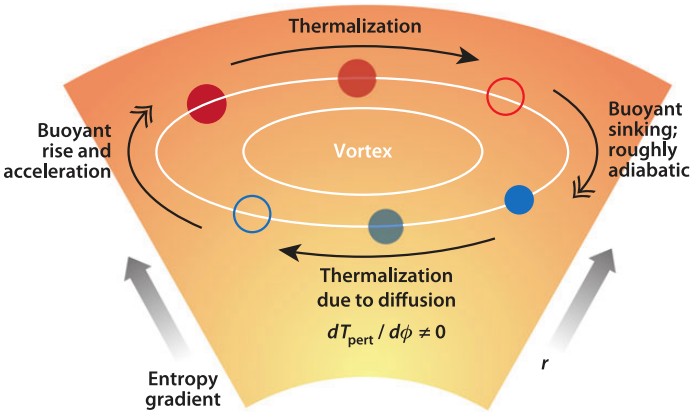

Figure 2.4
Baroclinic amplification of a vortex in the plane of a protoplanetary disk through the SBI mechanism. The general principle is identical for the COS, although the vortex must be exchanged for an epicycle that is not restricted to the disks R-φ plane, but can also contain a vertical perturbation. (used with permission of Annual Reviews, Inc., from Armitage, 2011, Annu. Rev. Astron. Astrophys., 49, 195; permission conveyed through Copyright Clearance Center, Inc.)

cess reducing its own entropy and establishing an entropy gradient in the surrounding gas. Once the gas parcel arrives back at the original distance to the star, it has a lower entropy than in the beginning. Having a lower entropy than the surrounding on its way through the inner disk regions, buoyancy now acts in the different direction, pushing the gas parcel further inside. On its way, it heats up and gains entropy. In that way the vortex creates an azimuthal gradient in temperature around itself, which drives the baroclinic term in the vorticity Equation 2.16 and amplifies the vortex motion. As buoyancy amplifies the cyclic vortex motion in the direction of the oscillation's restoring force, this mechanism can be describes as an *overstability*. A very similar, but linear, mechanism was discovered by Klahr & Hubbard (2014). The vortex is exchanged by an infinitesimal epicycle, which can also move in the vertical direction instead of the azimuthal direction. The same buoyancy gain and loss which is achieved by thermal relaxation amplifies the epicyclic motion and leads to a linear overstability that drives turbulence, called the *convective overstability* (COS). The ideal cooling timescale for this instability in a Keplerian disk is given for radially elongated modes as

$$t_{\mathrm{COS,\,max}} = \frac{1}{\gamma \Omega_{\mathrm{K}}}\,, \tag{2.28}$$

which means that VSI and COS reach their maximum growth rates in completely different cooling time regimes. Three-dimensional hydrodynamic simulations have shown that the SBI is in fact the saturated state of COS, where the small scale turbulence develops into large vortices (Lyra, 2014).

Zombie Vortex Instability

Marcus et al. (2013, 2015, 2016) first studied the non-linear instability of baroclinic layers in protoplanetary disks, called the *zombie vortex instability* (ZVI). ZVI, in contrast to VSI and COS, requires a finite amplitude perturbation. Given an already existing vortex filament, Rossby waves are launched, which are in resonance with buoyant oscillations in the direct vicinity. This critical layer surrounding the filament is made possible by the Doppler shift of the launched Rossby waves due to the Keplerian shear of the disk. The enhanced buoyant oscillations create a new vortex filament and the process is propagating through the disk, leading to turbulence. Since the mechanism relies on the existence of

buoyant oscillations, a buoyantly stable stratification and long cooling times are requires, which have to be longer than ten orbital timescales (see Lyra & Umurhan, 2019).

2.1.5 The Effect of Hydrodynamic Turbulence in Protoplanetary Disks

Advancements in numerical modeling and observational techniques have shed new light on the question whether protoplanetary disks are actually turbulent and what the effect of turbulence really is. For once, simulations suggest that the stress exerted by purely hydrodynamic turbulence is likely not the driving force of accretion in the disk that was discussed in Section 2.1.3 (Lyra & Umurhan, 2019; Lesur et al., 2023). Instead, focus has shifted towards photoevaporation and magnetic disk winds as causes for the dispersal of protoplanetary disks (see Pascucci et al., 2023). Planet and disk population synthesis models also show that very high levels of turbulence are probably not in agreement with our current understanding of the planet formation process and observations (Chambers, 2018; Zormpas et al., 2022). Gas kinematics also hint towards weak turbulence in some protoplanetary disks (e.g., Flaherty et al., 2018), but stronger turbulence in others (e.g., Paneque-Carreño et al., 2023). Another method to determine the level of turbulence measuring of the thickness of the dust layer (see Rosotti, 2023, for an overview of possible oservational techniques to constrain turbulence). These observations show different levels of turbulence in different disks (Villenave et al., 2020; Pizzati et al., 2023) and even within single disks (Doi & Kataoka, 2021). It seems to become clear that the strength in turbulence in protoplanetary disks has no universal value. Instead, the individual environmental conditions might determine whether a disk becomes turbulent, where it becomes turbulent, and at what level. Furthermore, not every form of turbulence leads to strong radial angular momentum transport (Lesur et al., 2023). The VSI for instance is highly anisotriopic (Stoll et al., 2017) and mostly transports angular momentum vertically. It therefore also contributes to the vertical dispersal of dust particles and thus influences the observational appearance of protoplanetary disks (see Chapters 4 and 5, Pfeil et al., 2023).

The influence of hydrodynamic instabilities on the evolution of dust particles (Section 2.2) and the formation of substructures (Section 2.3) should not be underestimated. Weak turbulence still contributes to the coagulation and fragmentation of dust particles and may create the necessary substructures for planet formation, such as vortices (Barge & Sommeria, 1995; Manger & Klahr, 2018; Raettig et al., 2021).

2.2 Dust Evolution

Dust grains are present throughout the ISM and comprise $\approx 1\,\%$ of its mass budget (Weingartner & Draine, 2001). Since protoplanetary disks form out of interstellar molecular gas clouds, they also contain these grains, which, in the ISM, are typically micrometer-sized. The higher densities and temperatures, and the strong rotation of the disk influence the dust evolution—leading to aerodynamic drag and a strongly enhanced grain-grain collision frequency. The higher dust densities mean that in most parts of protoplanetary disks, dust can be considered a fluid, similar to the gas. Dust fluids are however treated as pressureless since changes in the grain's internal energy mostly influence their surface temperatures, but not their movement (Garaud et al., 2004). The classic definition of pressure as a result

of elastic collisions, derived from a Boltzmann distribution, does also not hold for the dust fluid, as collisions under astrophysical conditions are oftentimes inelastic (for an overview of experimental results, see Blum, 2018). In the following section, I give an overview of some aspects of dust dynamics and evolution in protoplanetary disks.

2.2.1 Dust Dynamics

Relative velocities between dust and gas cause friction forces, which lead to a relative drag between both fluids. The respective force, coupling the fluid equations of dust and gas is

$$\boldsymbol{f}_{\mathrm{fric}} = -\frac{C_{\mathrm{drag}}\pi a^2 \rho_{\mathrm{g}} |\boldsymbol{v}_{\mathrm{d}} - \boldsymbol{v}_{\mathrm{g}}|}{2} (\boldsymbol{v}_{\mathrm{d}} - \boldsymbol{v}_{\mathrm{g}}) \,, \tag{2.29}$$

with the particle size a and the dimensionless drag coefficient C_{drag} (e.g., Weidenschilling, 1977). The value of C_{drag} depends on the aerodynamics of the problem. If the mean free path between dust particles and and gas molecules is larger than the grain's radius, which is the case in most parts of protoplanetary disks, we can apply the so-called Epstein regime (Epstein, 1924), in which the drag coefficient is given by

$$C_{\mathrm{drag}} = \frac{8\overline{v}_{\mathrm{mol}}}{3|\boldsymbol{v}_{\mathrm{d}} - \boldsymbol{v}_{\mathrm{g}}|} \,, \tag{2.30}$$

where $\overline{v}_{\mathrm{mol}}$ is the average gas molecule velocity. The strength of the coupling is characterized by the friction time $t_{\mathrm{fric}} = {}^{m_{\mathrm{d}}|\boldsymbol{v}_{\mathrm{d}} - \boldsymbol{v}_{\mathrm{g}}|}/_{|\boldsymbol{f}_{\mathrm{fric}}|}$, where $m_{\mathrm{d}} = {}^{4}/_{3}\,\pi \rho_{\mathrm{m}} a^3$ is the mass of an individual spherical particle with material density ρ_{m}. Expressing the friction time in terms of the local dynamical timescale of the disk gives us a useful measure for the effectiveness of the dust-gas coupling. The resulting quantity is called the *Stokes number* $\mathrm{St} = t_{\mathrm{fric}}\Omega_{\mathrm{K}}$. If we consider the vertically integrated disk structure, we can express it as

$$\mathrm{St} = \frac{\pi}{2} \frac{a \rho_{\mathrm{m}}}{\Sigma_{\mathrm{g}}} \,. \tag{2.31}$$

Stokes numbers larger than one correspond to a dust fluid that is mostly decoupled from the gas. Dust particles and gas molecules couple quickly if the Stokes number is much smaller than one. Using this definition, the coupled inviscid Navier-Stokes equations in terms of the friction time follow as

$$\frac{\partial \boldsymbol{v}_{\mathrm{d}}}{\partial t} + (\boldsymbol{\nabla} \cdot \boldsymbol{v}_{\mathrm{d}}) \boldsymbol{v}_{\mathrm{d}} = -\boldsymbol{\nabla}\Phi - \frac{\boldsymbol{v}_{\mathrm{d}} - \boldsymbol{v}_{\mathrm{g}}}{t_{\mathrm{fric}}} \tag{2.32}$$

$$\frac{\partial \boldsymbol{v}_{\mathrm{g}}}{\partial t} + (\boldsymbol{\nabla} \cdot \boldsymbol{v}_{\mathrm{g}}) \boldsymbol{v}_{\mathrm{g}} = -\boldsymbol{\nabla}\Phi + \varepsilon \frac{\boldsymbol{v}_{\mathrm{d}} - \boldsymbol{v}_{\mathrm{g}}}{t_{\mathrm{fric}}} - \frac{1}{\rho_{\mathrm{g}}} \boldsymbol{\nabla} P \,, \tag{2.33}$$

where we have introduced the dust-to-gas density ratio ε. If the friction time is short, gas and dust will be in an approximate force equilibrium at all times, where the drag force is balanced by gravity and pressure forces. Ignoring the advective terms in the coupled

dust-gas equations and setting $\partial_t = 0$ results in

$$\boldsymbol{v}_\mathrm{d} - \boldsymbol{v}_\mathrm{g} = \frac{t_\mathrm{fric}}{\rho_\mathrm{g}(1+\varepsilon)} \boldsymbol{\nabla} P \,, \tag{2.34}$$

which is referred to as the *terminal velocity* approximation (Youdin & Goodman, 2005). Thus, dust particles drift along the pressure gradient of the gas. In a protoplanetary disk, pressure is decreasing with distance to the central star, which means that particles drift towards the central star. Nakagawa et al. (1986) derived the steady state of the coupled equations under consideration of the advective terms for an axisymmetric disk in cylindrical coordinates and found for the radial and azimuthal components of the equilibrium velocity vector

$$(\boldsymbol{v}_\mathrm{d} - \boldsymbol{v}_\mathrm{g})|_R = \frac{\mathrm{St}(1+\varepsilon)}{\mathrm{St}^2 + (1+\varepsilon)^2} \frac{1}{\Omega_\mathrm{K} \rho_\mathrm{g}} \frac{\partial P}{\partial R} \tag{2.35}$$

$$(\boldsymbol{v}_\mathrm{d} - \boldsymbol{v}_\mathrm{g})|_\varphi = -\frac{1}{2} \frac{\mathrm{St}^2}{\mathrm{St}^2 + (1+\varepsilon)^2} \frac{1}{\Omega_\mathrm{K} \rho_\mathrm{g}} \frac{\partial P}{\partial R} \,. \tag{2.36}$$

For small Stokes numbers, the radial component can be expanded in a Taylor series to second order which is identical to the terminal velocity Equation 2.34. Drag forces also act on dust particles on inclined orbits, which perform one vertical oscillation per orbit and thus experience the effect of the vertical pressure gradient. Particles thus undergo vertical settling, where the terminal velocity is exactly given by Equation 2.34

$$(\boldsymbol{v}_\mathrm{d} - \boldsymbol{v}_\mathrm{g})|_z = \frac{\mathrm{St}}{\rho_\mathrm{g} \Omega_\mathrm{K} (1+\varepsilon)} \frac{\partial P}{\partial z} \,. \tag{2.37}$$

In a hydrostatic disk, this also allows for a different interpretation. Since $\partial_z P / \rho_\mathrm{g} \approx -\Omega_\mathrm{K}^2 z$, we could argue that a particle at height z feels the vertical component of the gravitational force, pulling it towards the midplane of the disk. Drag counteracts the free fall and limits it to the terminal velocity

$$(\boldsymbol{v}_\mathrm{d} - \boldsymbol{v}_\mathrm{g})|_z \approx -\mathrm{St} \Omega_\mathrm{K} z = t_\mathrm{fric} g_z \,, \tag{2.38}$$

where $\varepsilon \ll 1$ was assumed and g_z is the gravitational acceleration in z direction. This is identical to the terminal velocity of a falling particle in a planetary atmosphere.

Turbulent Diffusion

In the previous section, we have discussed the effect of turbulence on the gas flow and that it is oftentimes approximated as an additional viscosity $\nu_\mathrm{T} = \alpha c_\mathrm{s} H_\mathrm{g}$. Similar to the diffusive effect on the gas, turbulence can also mix the dust particles. To describe this process, it is often assumed that gradients in the dust density are flattened by turbulence, which means the diffusive flux takes the form

$$\boldsymbol{F}_\mathrm{diff} = -D_\mathrm{d} \rho_\mathrm{g} \boldsymbol{\nabla} \varepsilon \,, \tag{2.39}$$

(Dubrulle et al., 1995), where D_d is the dust diffusivity. Following the same considerations as for the gas viscosity, we set $D_\mathrm{d} = \delta c_\mathrm{s} H_\mathrm{g}$, where $\delta < 0$ is a parameter determining the strength of the diffusion. Adding this flux-component to the dust's continuity equation gives

$$\frac{\partial \rho_\mathrm{d}}{\partial t} + \boldsymbol{\nabla} \cdot (\rho_\mathrm{d} \boldsymbol{v}) = \boldsymbol{\nabla} \cdot \left(D_\mathrm{d} \rho_\mathrm{g} \boldsymbol{\nabla} \varepsilon \right) \,. \tag{2.40}$$

Different prescription for gradient dust diffusion exist. Some take the gradient of the dust density into account, others the gradient in ε, which is the mostly used variant in the protoplanetary disk community (see Binkert, 2023, for a comprehensive introduction to the treatment of dust diffusion in protoplanetary disks). Assuming that terminal velocity is reached, we can set $\partial_t = 0$ and $v_z = -\mathrm{St}(z)\Omega_\mathrm{K} z$ for the vertical component of Equation 2.40. Integrating the resulting equation in z gives a steady-state dust distribution, where vertical settling is exactly balanced by turbulent mixing

$$\rho_\mathrm{d}(R, z) = \rho_\mathrm{d,mid}(R) \exp\left[-\frac{\mathrm{St}_\mathrm{mid}}{\delta} \left(\exp\left(\frac{z^2}{2H_\mathrm{g}^2} \right) - 1 \right) - \frac{z^2}{2H_\mathrm{g}^2} \right], \tag{2.41}$$

where St_mid is the Stokes number in the disk midplane ($z = 0$) (Takeuchi & Lin, 2002). If it is assumed that the stopping time of the particles is constant with distance to the midplane, we can also find a much simpler vertical profile

$$\rho_\mathrm{d}(R, z) \approx \rho_\mathrm{d,mid}(R) \exp\left(-\frac{z^2}{2H_\mathrm{d}^2} \right), \tag{2.42}$$

where we have introduced the dust scale height

$$H_\mathrm{d} = H_\mathrm{g} \sqrt{\frac{\delta}{\delta + \mathrm{St}}} \,. \tag{2.43}$$

For large δ or small St, we see that the dust scale height approaches the gas scale height. From these considerations, we now have a possible explanation for why the geometrical appearance of the dust structure of a protoplanetary disks is so different in different wavelength regions. Infrared observations trace the light scattered by tiny dust particles (central panel of Figure 1.4), which, according to to Equation 2.43 have a much wider vertical distribution than larger particles, which we mostly see in the thermal millimeter radiation (left panel of Figure 1.4). These results have, however various limitations stemming from the underlying assumption. For once, turbulence was assumed to be isotropic throughout the disk, which is not given in protoplanetary disks, as will also be shown in the coming chapters. Furthermore, the terminal velocity approximation might not hold in the upper atmosphere of the disk, where the Strokes numbers can become much larger than one due to the low gas densities.

Streaming Instability

If enough dust is present, friction forces can also have a significant effect on the gas velocities. A radially drifting dust clump then drags the gas radially with it. The gas experiences

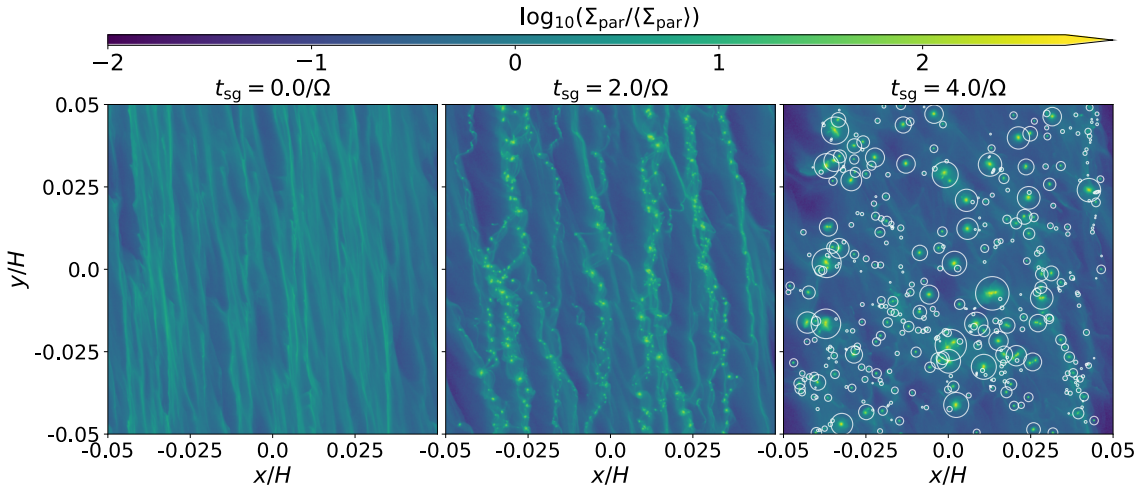

Figure 2.5
Local shearing box simulation of a protoplanetary disk with streaming instability by Nesvorný et al. (2019). The last snapshot shows that gravitationally bound planetesimals have formed, marked by the white circles (used with permission of Springer Nature BV, from Nesvorný et al., 2019, Nat. Astron. 3, 808–812 (2019); permission conveyed through Copyright Clearance Center, Inc.).

Coriolis forces that let it undergo an epicyclic motion. This azimuthal deflection again drags dust particles in the azimuthal direction causing them to accelerate to super-Keplerian velocities and move outwards into the original inwards drifting clump. This self enhancing cycle was first studied as a linear instability by Youdin & Goodman (2005) and named *streaming instability* (SI). Squire & Hopkins (2018a,b) later classified it as a resonant drag instability since the radial dust drift is in resonance with the epicylcic frequency of the gas.

SI is a particularly interesting mechanism in the context of planetesimal formation, as it leads to the formation of dense clumps that can undergo gravitational collapse if the right conditions are met (Schreiber & Klahr, 2018; Klahr & Schreiber, 2020; Gerbig et al., 2020). Nesvorný et al. (2019) showed that planetesimals formed out of these clumps reproduce the binary fraction of trans-Neptunian objects in our own Solar system (see Figure 2.5), which is seen as a strong indicator for the importance of SI in planet formation. However, SI requires enhanced dust densities to start in the first place. Some other mechanism thus has to concentrate the dust before SI can kick in and form planetesimals. Since dust trapping and concentration is more effective for larger particles, coagulation has to proceed before the onset of SI.

2.2.2 Dust Coagulation

The constituent particles of interstellar dust grains are called monomers and have typical sizes of 0.1 µm (Tazaki & Dominik, 2022). In order to form an Earth-sized planetary body out of these particles, 16 order of magnitude in radius and 42 order of magnitude in mass have to be bridged. The first step in this evolution is characterized by hit and stick collisions between the smallest constituents, i.e., *coagulation*. Sticking is facilitated by surface forces. At this lowest end of the mass scale of planet formation, Brownian

motion causes the relative particle velocities that lead to collisions. Particle encounters can, however, also lead to the break-up of larger aggregates, referred to as *fragmentation*, which produces a size spectrum of smaller grains. Coagulation and fragmentation therefore create a continuum number density distribution $n(m)$, whose time evolution is described by the integro-differential Smoluchowski equation (Smoluchowski, 1916)—in its most general form given as

$$\frac{\partial n(m)}{\partial t} = \int_0^\infty \int_0^\infty \mathcal{M}(m, m_1, m_2) n(m_1) n(m_2) \, \mathrm{d}m_1 \, \mathrm{d}m_2 \,, \tag{2.44}$$

where m is the particle mass (see Birnstiel et al., 2010). The quantity $\mathcal{M}$ is called the *kernel* and contains all information about the possible collision outcomes. If particle collisions only lead to perfect sticking, Equation 2.44 takes the form of the coagulation equation

$$\begin{aligned} \mathcal{M}(m, m_1, m_2) &= \frac{1}{2} C(m_1, m_2) \cdot \delta(m_1 + m_2 - m) - C(m_1, m_2) \cdot \delta(m_2 - m) \\ \frac{\partial n(m)}{\partial t} &= \frac{1}{2} \int_0^\infty C(m_1, m - m_1) n(m_1) n(m - m_1) \, \mathrm{d}m_1 - n(m) \int_0^\infty C(m_1, m) n(m_1) \, \mathrm{d}m_1 \,, \end{aligned} \tag{2.45}$$

where C is called the *coagulation kernel*. It can be written in terms of the *collision frequency function* $\mathcal{R}(m_1, m_2) = \Delta v(m_1, m_2) \sigma(m_1, m_2)$, and the coagulation probability $\mathcal{P}_\mathrm{c}$.

$$C(m_1, m_2) = \mathcal{P}_\mathrm{c}(m_1, m_2) \mathcal{R}(m_1, m_2) \,. \tag{2.46}$$

Here, we have the relative velocity Δv and the collision cross section σ. The equation's first right-hand side term accounts for the effect of coagulation on the particle number density of mass m, where the factor $1/2$ removes double counted collisions. The second term corresponds to the particles of mass m which are lost due to continued growth. Analytic solutions of this equation exist for some simple forms of the kernel, e.g., a constant or linear form (e.g., Silk & Takahashi, 1979; Wetherill, 1990). In most cases, however, the kernel is non-linear and the fragmentation process has to be considered. This makes the use of numerical methods necessary. Kornet et al. (2001) gave an estimate for the growth rate of dust particles in a monodisperse distribution. If every collision leads to growth, the particle mass should approximately change as

$$\frac{\mathrm{d}m_\mathrm{d}}{\mathrm{d}t} \approx \frac{m_\mathrm{d}}{t_\mathrm{coll}} = \sigma \, \Delta v \, n_\mathrm{d} \, m_\mathrm{d} \,, \tag{2.47}$$

where n_d is the the total number density of particles. For spherical particles, this can be expressed in terms of the particle radius as

$$\frac{\mathrm{d}a}{\mathrm{d}t} = \frac{\rho_\mathrm{d}}{\rho_\mathrm{m}} \Delta v \,. \tag{2.48}$$

This very simple estimation holds surprisingly well when compared to simulations of grain growth (see Section 3.2).

Laboratory experiments and molecular dynamics simulations have shown that collisions between similarly sized particles with velocity larger than a few $\mathrm{m\,s^{-1}}$ lead to the fragmen-

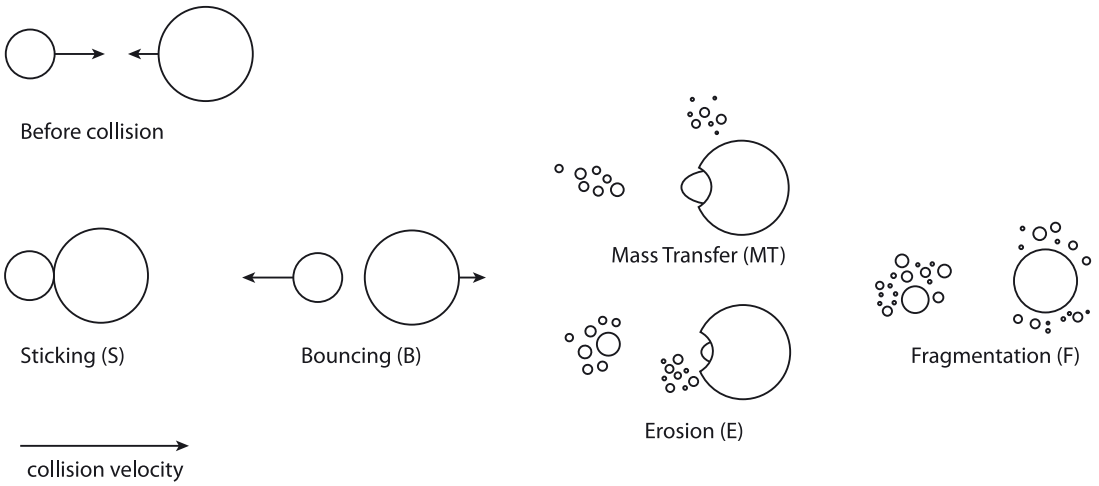

Figure 2.6
The different outcomes of grain collisions, sorted by relative grain velocities (figure by Windmark et al. (2012), licensed under CC BY 4.0).

tation of the colliders (Güttler et al., 2010). Furthermore, bouncing of particles, fragmentation with mass transfer, and erosion can play a role (see Blum, 2018; Birnstiel, 2023, for overviews). Figure 2.6 depicts the different possible outcomes of particles collisions sorted by impact speed. The collision speed's dependency on particle size is controlling many details of the resulting size distribution's shape (Birnstiel et al., 2011).

Particle Collision Velocities

The aerodynamic coupling of dust and gas depends on the size of the particles, expressed through the Stokes number. Differently-sized particles with Stokes numbers St_i and St_j (assuming $\mathrm{St}_i > \mathrm{St}_j$) thus have different terminal velocity which can be calculated with Equation 2.35 and Equation 2.36, where we assume a small dust-to-gas ratio

$$\Delta v_{ij}^{\mathrm{drift,R}} = \left| \frac{\mathrm{St}_i}{\mathrm{St}_i^2 + 1} - \frac{\mathrm{St}_j}{\mathrm{St}_j^2 + 1} \right| \frac{1}{\Omega_\mathrm{K} \rho_\mathrm{g}} \frac{\partial P}{\partial R} , \tag{2.49}$$

$$\Delta v_{ij}^{\mathrm{drift},\varphi} = \left| \frac{\mathrm{St}_i^2}{\mathrm{St}_i^2 + 1} - \frac{\mathrm{St}_j^2}{\mathrm{St}_j^2 + 1} \right| \frac{1}{2\Omega_\mathrm{K} \rho_\mathrm{g}} \frac{\partial P}{\partial R} . \tag{2.50}$$

Similarly, a differential settling velocity can be calculated. Assuming the dust to be in settling-mixing equilibrium, we set $z = H_\mathrm{d}$ in Equation 2.38 and obtain

$$\Delta v_{ij}^{\mathrm{set}} = \left| \mathrm{St}_i H_{\mathrm{d},i} - \mathrm{St}_j H_{\mathrm{d},j} \right| \Omega_\mathrm{K} . \tag{2.51}$$

It can be seen that these systemic contributions to the collision speeds vanish for equally-sized particles. Relative radial drift velocities become largest for $\mathrm{St} = 1$ and increase with the size difference between the colliders. Brownian motion is another size-dependent source of relative velocities between particles. For two particles with masses m_i and m_j, Brownian

motion leads to a relative velocity

$$\Delta v_{ij}^{\mathrm{Brown}} = \sqrt{\frac{8 k_{\mathrm{B}} T (m_i + m_j)}{\pi m_i m_j}}\,, \tag{2.52}$$

(Einstein, 1905; Otto & Fissan, 1999). In addition, turbulent eddies of different size and velocity preferentially couple to differently-sized particles. These effects lead to collisions between the particles of equal and different sizes. Ormel & Cuzzi (2007) assumed isotropic turbulence and derived closed-form expressions for the relative velocities in different regimes. They depend on the flow's Reynolds number

$$\mathfrak{Re} = \frac{\nu_{\mathrm{T}}}{\nu_{\mathrm{mol}}} = \frac{2\alpha H_{\mathrm{g}}}{\lambda_{\mathrm{mfp}}}\,, \tag{2.53}$$

where λ_{mfp} is the mean free path of the gas molecules, and the turnover time of the largest and smallest eddies are defined by

$$t_{\mathrm{S}} = \mathfrak{Re}^{-1/2} t_{\mathrm{L}} \qquad t_{\mathrm{L}} = \Omega_{\mathrm{K}}^{-1}\,. \tag{2.54}$$

The largest eddies thus have a similar turnover time as the disk itself. The turbulent relative velocities then follow as

$$\frac{\Delta v_{ij}^{\mathrm{turb}}}{v_{\mathrm{turb}}} = \begin{cases} \mathfrak{Re}^{1/4}(\mathrm{St}_i - \mathrm{St}_j) & \text{for } \mathrm{St}_i/\Omega_{\mathrm{K}} < t_s \quad (2.55) \\ \sqrt{\mathrm{St}_i}\left[2y_a^* - (1+\epsilon) + \dfrac{2}{1+\epsilon}\left(\dfrac{1}{1+y_a^*} + \dfrac{\epsilon^3}{y_a^*+\epsilon}\right)\right]^{1/2} & \text{for } 5t_{\mathrm{S}} \simeq \mathrm{St}_i/\Omega_{\mathrm{K}} \lesssim t_{\mathrm{L}} \quad (2.56) \\ \left(\dfrac{1}{1+\mathrm{St}_i} + \dfrac{1}{1+\mathrm{St}_j}\right)^{1/2} & \text{for } \mathrm{St}_i/\Omega_{\mathrm{K}} \geq t_{\mathrm{L}}\,, \quad (2.57) \end{cases}$$

(Ormel et al., 2008), where $v_{\mathrm{turb}} = c_{\mathrm{s}}\sqrt{3/2\,\alpha}$, $\epsilon = \mathrm{St}_i/\mathrm{St}_j$, and $y_a^* \approx 1.6$ is a numerical constant determined by Ormel & Cuzzi (2007).
The total collision velocity of the grains is then given by

$$\Delta v_{ij}^{\mathrm{rms}} = \sqrt{\left(\Delta v_{ij}^{\mathrm{turb}}\right)^2 + \left(\Delta v_{ij}^{\mathrm{set}}\right)^2 + \left(\Delta v_{ij}^{\mathrm{drift},R}\right)^2 + \left(\Delta v_{ij}^{\mathrm{drift},\varphi}\right)^2 + \left(\Delta v_{ij}^{\mathrm{Brown}}\right)^2}\,. \tag{2.58}$$

All sources of relative grain velocities increase with the particles' size, except for Brownian motion which is only relevant for small particles. Figure 2.7 shows the relative velocity contributions of the different processes as a function of the particle sizes. For larger particles, turbulence dominates much of the size spectrum. The fact that all relative velocities (except Brownian motion) increase with the size of the colliding particles means that collisions will naturally limit particles growth when a critical collision speed is reached at which sticking is no longer effective and erosive or destructive outcomes become likely. At what point the transition between positive and negative collision outcomes occurs is subject to ongoing numerical and experimental research. However, most studies point towards critical velocities in the range of a few $\mathrm{m\,s^{-1}}$ (e.g., Güttler et al., 2010; Wada et al., 2013). In the

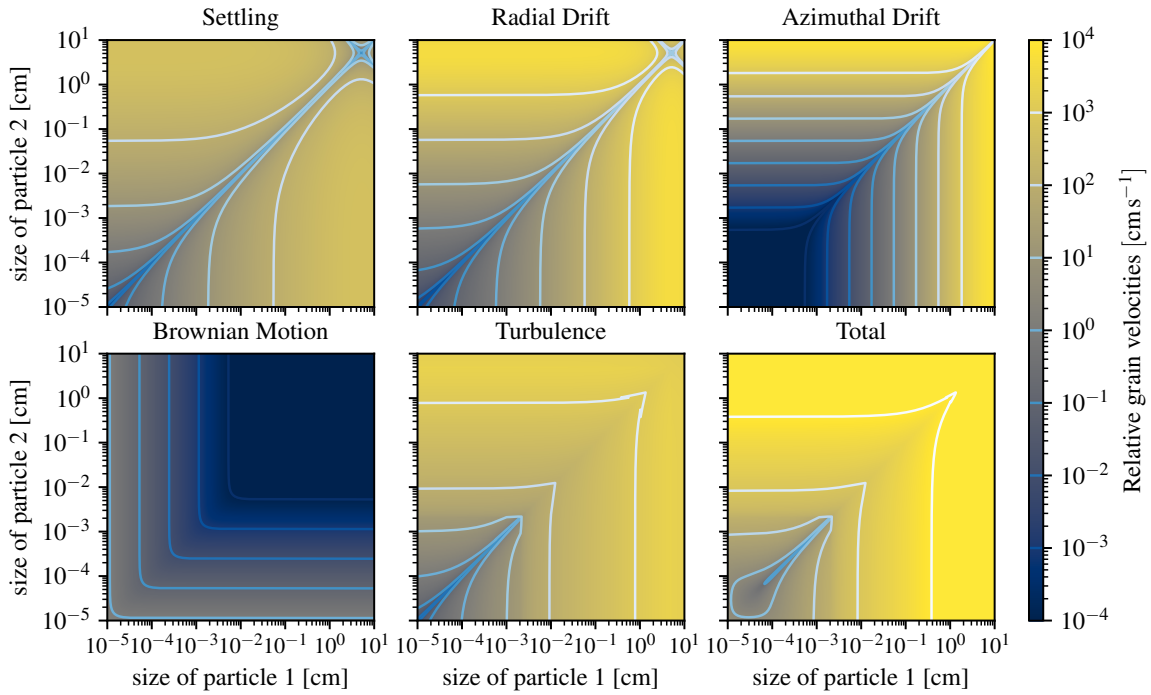

Figure 2.7
Relative particle velocity as a function of the colliding particles' sizes. Turbulent relative velocities are the largest component for most sizes. For very small particles, Brownian motion is a significant contribution and causes most collisions between monomers.

following, I will refer to the critical velocity specifically as the velocity corresponding to the onset of fragmentation.

Growth Limits

Birnstiel et al. (2012) derived the most important limits to particle growth. For particles $\gtrsim 1\,\mu\text{m}$, turbulence is the dominating source of grain collision velocities. If the particles are in the so-called fully-intermediate regime, collision speeds between equally-sized grains can be approximated as

$$\Delta v^{\text{turb}} \approx \sqrt{3\alpha \text{St}} c_\text{s} \tag{2.59}$$

$$a_\text{frag} = \frac{2}{3\pi} \frac{\Sigma_\text{g}}{\rho_\text{m} \alpha} \left(\frac{v_\text{frag}}{c_\text{s}} \right)^2 , \tag{2.60}$$

which is called the *fragmentation limit*. For large particles, or at low gas densities, differential drift can become a significant source of grain collision velocities too. Relative velocities between particles of Stokes numbers St and $N \cdot \text{St}$, with $N < 1$, are defined via

$$\Delta v^{\text{drift}} = \frac{c_\text{s}^2}{v_\text{K}} \text{St}(1 - N) \left| \frac{\partial \log(P)}{\partial \log(R)} \right| . \tag{2.61}$$

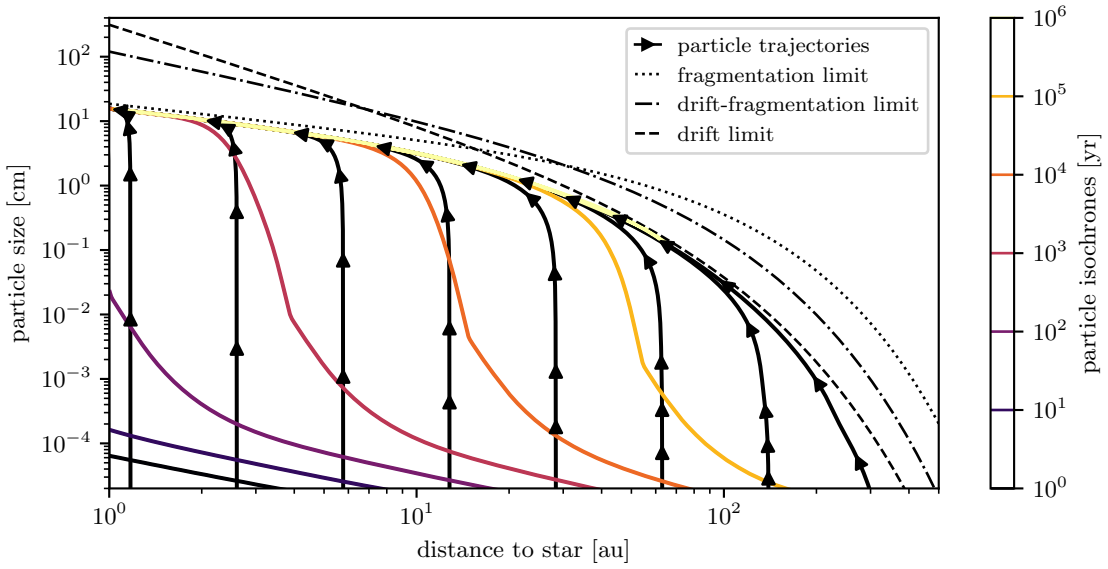

Figure 2.8
Global picture of dust growth and transport in a protoplanetary disk model. Black lines show the trajectories of particles with initial sizes of 0.1 µm. Colored contours indicate the particle locations at different evolution times. Each trajectory is evolved over 500 local dynamical timescales, meaning that the particles in the outer disk evolve over several 10^6 yr. In the inner disk regions, particles grow until they reach the fragmentation barrier. Radial drift limits the growth in the outer regions.

Setting this expression equal to the fragmentation velocity and using the definition of the Stokes number, we obtain the *drift-fragmentation limit*, which describes the particle size at which collisions due to differential drift lead to fragmentation

$$a_{\mathrm{drift-frag}} = \frac{2}{\pi}\frac{\Sigma_{\mathrm{g}}}{\rho_{\mathrm{m}}}\left|\frac{\partial \log(P)}{\partial \log(R)}\right|^{-1}\frac{v_{\mathrm{frag}}v_{\mathrm{K}}}{(1-N)c_{\mathrm{s}}^2}\,. \tag{2.62}$$

Finally, large grains are also effectively removed from the local size distribution by radial drift if they cannot be replenished quickly enough by growth of smaller particles. By comparing the respective timescales of growth and drift, we can get an estimate for the so-called *drift limit*. For the timescale of drift we can estimate $v_{\mathrm{dr}} \approx (\boldsymbol{v}_{\mathrm{d}} - \boldsymbol{v}_{\mathrm{g}})|_R$ and get

$$t_{\mathrm{drift}} = \frac{R}{|v_{\mathrm{dr}}|} \approx \frac{Rv_{\mathrm{K}}}{\mathrm{St}c_{\mathrm{s}}^2}\left|\frac{\partial \log(P)}{\partial \log(R)}\right|^{-1}\,. \tag{2.63}$$

Brauer et al. (2008) took the Kornet et al. (2001) estimate of the particle growth rate (Equation 2.48) to derive the particle growth timescale in the fully-intermediate regime of turbulence (Equation 2.59) and found

$$t_{\mathrm{growth}} = \frac{a}{\dot{a}} \approx \frac{1}{\Omega_{\mathrm{K}}\varepsilon}\,. \tag{2.64}$$

Equating both expressions gives the *drift limit*

$$a_{\mathrm{drift}} = \frac{2}{\pi} \frac{\varepsilon \Sigma_{\mathrm{g}}}{\rho_{\mathrm{m}}} \left(\frac{v_{\mathrm{K}}}{c_{\mathrm{s}}} \right)^2 \left| \frac{\partial \log(P)}{\partial \log(R)} \right|^{-1} . \tag{2.65}$$

Numerical simulations have shown that these growth barriers are good estimates for the maximum particle size in protoplanetary disks. They are used to get quick estimates for the particle sizes in hydrodynamic simulations (e.g., Tamfal et al., 2018) and disk models (e.g., Emsenhuber et al., 2021; Zormpas et al., 2022), and estimates for the interpretation of observations (e.g., Leiendecker et al., 2022; Bergez-Casalou et al., 2022; Antonellini et al., 2023). Figure 2.8 shows the trajectories of initially sub-micron-sized particles in the size-distance plane and for a steady gas disk, based on the radial drift velocity (Equation 2.35) and the monodisperse particle growth rate (Equation 2.48), which is limited by fragmentation. In the inner disk, particles grow to the fragmentation limit, whereas grains in the outer disk are drift-limited. Each location evolves on its local growth timescale, meaning that the growth and drift process in the very outer regions takes millions of years, while the particles in the inner disk reach their maximum size in a few thousand years. Based on our current knowledge of protoplanetary disk structure, reasonable estimates of the size limits show that particles can coagulate to maximum sizes of $\sim 1\,\mathrm{m}$.

Equilibrium Size Distributions

The outcome of a destructive collisional cascade was first studies by Dohnanyi (1969) for collisions between asteroids. If collisions exceed the critical break-up velocity, a number of smaller fragments is created that again collide and fragment. The result is a size distribution which can be approximated by a power law $n(m) \propto m^{-\xi} = m^{-11/6} \Leftrightarrow n(a) \propto a^{-3.5}$. The same size distribution is also encountered for interstellar dust grains (Mathis et al., 1977). We have, however, seen that the conditions in protoplanetary disks are much different from the dilute interstellar medium. The high gas densities mean that dust and gas are aerodynamically coupled and collisions for small particles are slow enough to allow for sticking. Only once the particles coagulate towards the growth barriers, relative velocities can become high enough to cause fragmentation or erosion (Windmark et al., 2012). The smaller grains which are produced in catastrophic collisions are again better coupled to the gas and will not undergo a continuous collision cascade. Instead, small fragments can coagulate again, which leads to a steady state in which coagulation and fragmentation are balanced. Such a distribution will thus be cut off at the fragmentation barrier, as can be seen in the examples in Figure 2.9. These size distributions are based on the model by Birnstiel et al. (2011). They analytically derived the typical size distributions in coagulation-fragmentation equilibrium in different regimes under the assumption of mass conservation, i.e., ignoring any loss due to dust transport. They used these analytic prescriptions to interpret the results of numerical dust coagulation simulations and derived the model shown in Figure 2.9, which depends on the local environmental conditions.

From the various regimes investigated by Birnstiel et al. (2011), I will only introduce the case in which the fragmenting particles are more or less equally distributed across all sizes. The distribution of fragments is then usually assumed to be the collisional cascade

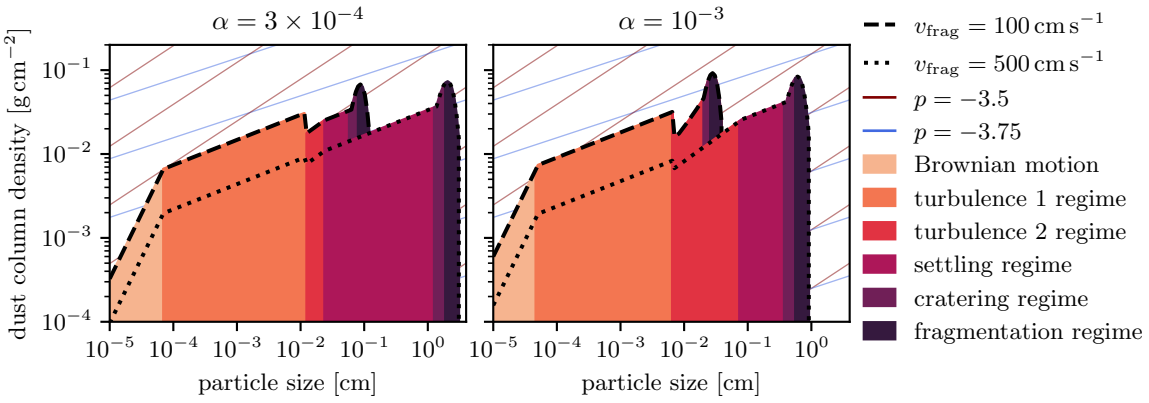

Figure 2.9
Size distribution fits in fragmentation-coagulation equilibrium, calculated with the model by Birnstiel et al. (2011). The only parameters varied between the different curved are the strength of the turbulence ($\alpha = 3\times10^{-4}$, 10^{-3}, left and right panel) and the fragmentation velocity ($v_{\mathrm{fr}} = 100\,\mathrm{cm\,s^{-1}}$ and $500\,\mathrm{cm\,s^{-1}}$, within each panel). Smaller v_{fr} and α lead to larger maximum particle sizes. The slopes of the distributions depend on the physical mechanism that dominates the collision velocities (colors).

$\xi = {}^{11}/_{6}$. Fragmentation is generally only occurring in collisions between particles of similar size, while collisions between a large and a small particles lead to erosion of the large grain but not to a complete break-up. As eroding collisions slow down growth, this effect causes the formation of a bump at the upper end of the size distribution, as can be seen in the examples in Figure 2.9. Since the flux of particles along the size spectrum must be constant in an equilibrium distribution, slower growth results in an increased density. It turns out that the dominating physical mechanism behind the grain collision velocities is the most important factor for the shape of the resulting size distribution. In general we can distinguish between three characteristic outcomes:

$\Delta v \propto a^{-3/2}$, which is the case for Brownian motion (Equation 2.52). The size distribution is much steeper than the MRN distribution, with $n(a) \propto a^{-2.5}$.

$\Delta v \propto a$, as in the case of the first regime of turbulence (Equation 2.55), or drift at small Stokes numbers (Equation 2.49). In this case, the equilibrium size distribution scales as $n(a) \propto a^{-3.75}$.

$\Delta v \propto a^{1/2}$, which is the case in the intermediate, second regime of turbulence (Equation 2.56). The MRN size distribution $n(a) \propto a^{-3.5}$ is recovered if this is the dominant source of grain collision velocities.

If settling plays a role, the number densities change according to the settling-mixing equilibrium and the slope is slightly altered. The resulting size distribution depends on the local physical conditions in the protoplanetary disk. If turbulence is weak, as in the left panel of Figure 2.9, other effects, like settling, will become more dominant and cause the distribution to deviate from the MRN distribution. Different fragmentation velocities result in different size limits and thus also determine what effects are dominant under the given conditions. Note that these models do not consider the relative drift velocities, which, if dominant, further push the size distribution towards $n(a) \propto a^{-3.75}$. In general, the more

collisions are dominated by the second regime of turbulence, the closer is the distribution to $n(a) \propto a^{-3.5}$. If drift or the first regime dominate, most of the mass will follow a shallower size distribution with $n(a) \propto a^{-3.75}$. These considerations only hold if the local dust density is constant and not if material is removed by drift. Size distributions in the outer disk are drift-limited and thus not in fragmentation-coagulation equilibrium. The exact size distribution is then dependent on the radial dust fluxes.

2.3 Large-Scale Structure and Planet Formation

The growth barriers for dust particles pose significant obstacles for the formation of planetesimals and planets (Morbidelli & Raymond, 2016). Large aggregates are either destroyed in collisions (Brauer et al., 2008) or lost due to radial drift in just a few hundred years (Weidenschilling, 1977). Other mechanisms have to be in place to enable the formation of larger bodies. Early theories on the formation of planetesimals mostly focused on processes to enhance the dust-to-gas ratio in smooth protoplanetary disks, i.e., without any substructure. Goldreich & Ward (1973) proposed that settling of dust particles could form a midplane layer dense enough to trigger gravitational collapse. We have however seen before that turbulent diffusion prevents dust particles from settling completely (Dubrulle et al., 1995). Furthermore, a dense dust layer causes feedback on the gas and thus induces a vertical shear that can trigger Kelvin-Helmholtz instability around the disk's midplane. The settling process is thus self-regulatory and the Goldreich-Ward mechanism likely not feasible. In the outer regions of protoplanetary disks, gravitational instability could trigger clumping and turbulence (Boss, 1997). This is however only feasible in massive disks or in the very early stages and generally produces massive planets (Forgan et al., 2018; Wagner et al., 2019). Other sources of turbulence are also able to clump dust particles, as shown by Johansen et al. (2007), where dust accumulated in filamentary structures due to MRI-induced turbulence.

Observational advances in the last 10 years (e.g., ALMA-Partnership et al., 2015) have revealed that protoplanetary disks are generally not smooth, but highly structured (see Bae et al., 2023). The DSHARP program (Figure 2.10, Andrews et al., 2018) in particular showed that rings, spirals, and vortices are almost ubiquitous substructures in disks around young stars, which has been confirmed by other programs (e.g., Öberg et al., 2021).

Substructures offer a path towards planetesimal formation, as they are often associated with pressure perturbation that can accumulate dust particles (Whipple, 1972). If sufficiently high amounts of dust collect in a substructure, secondary mechanisms like the streaming instability (Zagaria et al., 2023) and gravitational collapse (Gerbig et al., 2020) can kick in and cause planetesimal formation. We are however confronted with a "chicken and egg" problem. Are the observed substructures a consequence of planet formation, i.e., the tidal effects of the emerging planets, or is planet formation a consequence of the presence of substructures? This question cannot be answered yet. Arguments for both possibilities exist. The detection of planets inside of gaps (Keppler et al., 2018) seems to hint towards a connection between substructures and planets. Bae et al. (2023) compiled the recent observational and theoretical concepts regarding substructures. Several known mechanisms could account for their formation, as shown in Figure 2.11.

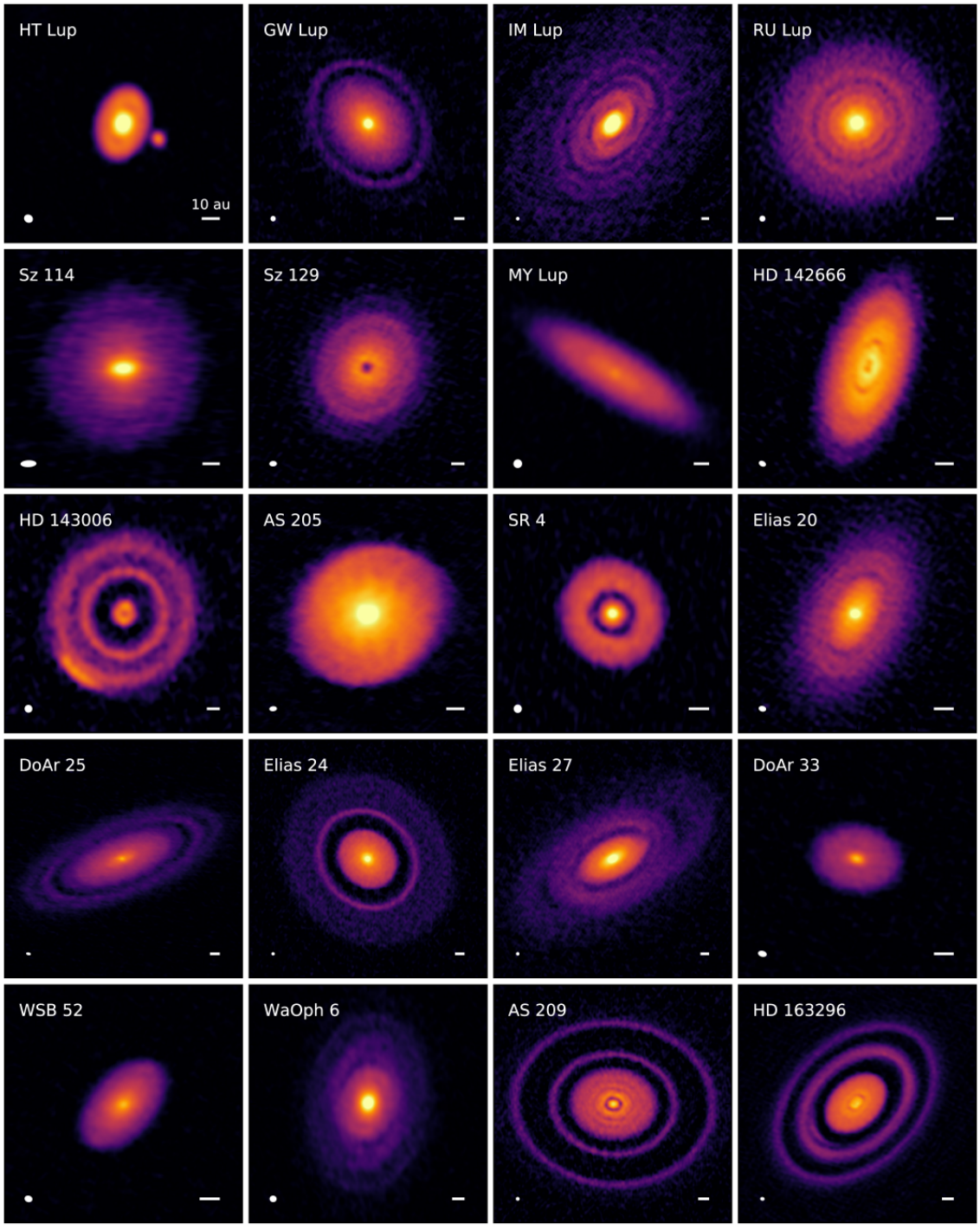

Figure 2.10
Protoplanetary disks observed during the *Disk Substructures at High Angular Resolution Project* (DSHARP) with ALMA in various star-forming regions show a variety of substructures (figure by Andrews et al. (2018), licensed under CC BY 4.0).

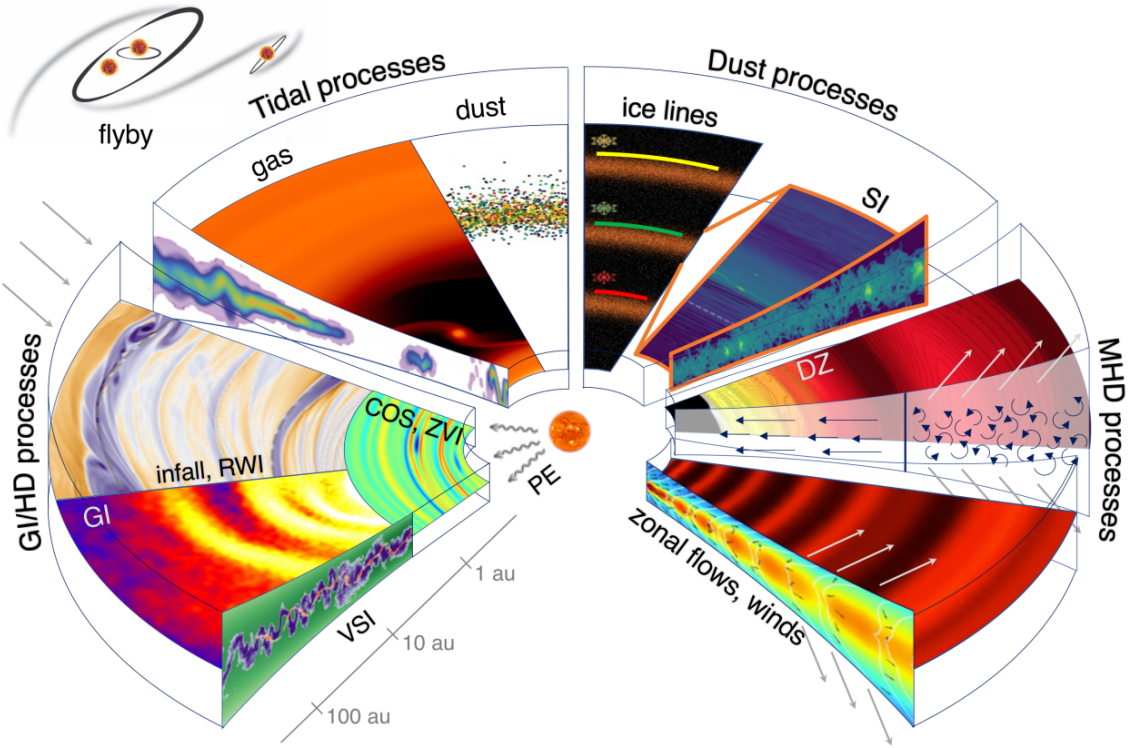

Figure 2.11
Overview of several substructure-forming processes in protoplanetary disks. Hydrodynamic and gravitational instabilities can cause turbulence in protoplanetary disks that can lead to the formation of vortices and rings. Forming planets and stellar flybys induce gaps and spirals via gravitational interaction and angular momentum exchange. The solids themselves can also contribute to structure formation. Sublimation of volatiles at the so-called icelines causes "traffic jams" of inwards drifting particles. At high concentrations, dust particles can also trigger feedback instabilities like the streaming instability (SI). (figure by Bae et al. (2023), licensed under CC BY 4.0)

Purely Hydrodynamic Processes like flow instabilities, photoevaporation and infall can modify the velocities and densities in the disk. VSI was shown by various authors to induce the formation of large-scale anticyclonic vortices (Richard et al., 2016; Manger & Klahr, 2018; Pfeil & Klahr, 2021). The resulting structures are long-lived and associated with pressure perturbation that can potentially cause dust trapping (Barge & Sommeria, 1995). What mechanism causes the vortex to form out of the VSI-active state of the disk is not finally clarified yet. Richard et al. (2016) and Manger & Klahr (2018) suggest the Rossby wave instability (RWI, see Lovelace et al., 1999) could be triggered by the VSI-induced perturbation of the potential vorticity; but also parasitic Kelvin-Helmholtz instability could be responsible (Latter & Papaloizou, 2018). Also COS can lead to vortex formation in its saturated state, as shown by Lyra (2014) and Raettig et al. (2021). These vortices are, however, often much smaller than their planet-induced counterparts and it is questionable if they are associated with the observed vortices. They could nonetheless facilitate planetesimal formation and thus trigger further substructure formation. Photoevaporation under the influence of high-energy stellar photons (Bally, 1982) can form inner

cavities that could potentially trap dust particles (Gárate et al., 2021). The respective pressure bump can also trigger RWI. Gravitational instability (Toomre, 1964) can cause the formation of spiral density waves and clumps at large distances to the central star (Vorobyov & Basu, 2005).

Magneto-hydrodynamic Processes like the MRI (Balbus & Hawley, 1991) were shown to contribute to structure formation. In ideal MHD, ring structures in the form of zonal flows can form out of MRI turbulence (Hawley et al., 2001). MRI-dead zones exist in the dense regions when Ohmic resistivity is considered and create radial gradients in turbulent viscosity (Lyra & Mac Low, 2012). The resulting pressure bumps can trigger RWI and trap dust particles in substructures that could be observable (Flock et al., 2015). If a vertical magnetic field is present in the disk, a magneto-centrifugal wind can be launched (Blandford & Payne, 1982). The associated angular momentum transport and accretion can lead to the formation of gaps and rings as shown by Moll (2012).

Dust processes like the streaming instability (Youdin & Goodman, 2005) as a dust-feedback-induced mechanism can drive structure formation. If a sufficiently high dust-to-gas ratio exists, SI can form small filamentary structures that facilitate gravitational collapse and planetesimal formation. These structures have typical sizes of $\sim 0.1\,H_\mathrm{d}$ (Yang & Johansen, 2014). Nesvorný et al. (2019) have shown that the binary fraction of the planetesimals formed via gravitational collapse in streaming instability filaments matches the binary fraction in the Solar system's Kuiper belt. SI is therefore believed to be an important mechanism in the formation of planetesimals. Unfortunately, it requires already enhanced dust-to-gas ratios which have to be created by some other mechanism.

The evaporation of ices contained in dust aggregates or on their surfaces occurs when dust drifts towards the central star and thus reaches warmer regions. The respective locations at which the evaporation occurs are called icelines. Particles entering these region can completely break up when their ice content is removed. The smaller fragments drift slower and thus pile up (Saito & Sirono, 2011). The resulting vapors can be diffused outwards and recondense on the incoming dust particles, thus increasing the local solid content. This is called the *cold finger effect* (Ros & Johansen, 2013; Drążkowska et al., 2021). It is not yet clear whether the ice content of the dust grains also has a positive effect on the sticking probability, as indicated by some studies (Dominik & Tielens, 1997). This would mean that the particle size varies across the ice lines, which would cause a pile up. However more recent studies seem to find no significant effect of the ice content on the stickiness (Kimura et al., 2015).

Tidal processes are the last class of possible causes for substructure formation. The presence of a planet in the disk perturbs the gravitational field and thus launches spiral density waves through resonance with the local epicyclic frequency, called Lindblad resonances (Goldreich & Tremaine, 1978). The waves can constructively interfere and create coherent spiral structures (Ogilvie & Lubow, 2002; Bae & Zhu, 2018). Only small dust particles can effectively be trapped in these structures as they orbit the star at the Keplerian frequency of the planet (Bae et al., 2023).

The spiral density waves launched by a planet with mass smaller than the thermal mass $M_{\mathrm{th}} = (H_g/R)^3_{\mathrm{Planet}} M_\star$ steepen into shocks and thus transfer angular momentum to the gas in the disk. Gas at some distance to the planet is therefore moving away from the planet's co-orbital region, thus opening a gap. For planets more massive than the thermal mass, spiral density waves are already steepened at launch and thus remove the gas at the co-orbital region of the planet itself (Rafikov, 2002; Dong & Fung, 2017). The mass of the planet in combination with the viscosity of the gas therefore determine the width and depth of the resulting gap. A pressure maximum forms outside of the gap which collects inwards drifting dust particles. RWI can also be triggered due to the pressure perturbation and cause the formation of large-scale vortices (Zhu et al., 2014).

Studying these large-scale structure forming processes, which are needed to explain the formation of planetesimals and planets requires numerical simulations of gas and dust in protoplanetary disks. The dust dynamic's sensitivity to the grain sizes and the dust size distribution makes numerical models of dust coagulation and fragmentation necessary.

2.4 Radiative Transfer

In Section 2.1.4, it was already highlighted that for hydrodynamic turbulence to emerge in protoplanetary disks, thermal relaxation is required, i.e., the decay of temperature perturbations with respect to some equilibrium state. Since thermal conductivity is extremely low in the dilute gas of the circumstellar environment, thermal relaxation is only achievable via the emission or absorption of electromagnetic radiation. The consideration of radiative transfer is thus necessary to describe how the gas and dust in protoplanetary disks can be heated or cooled.

Irradiation from the central star furthermore determines most of the disk's temperature structure (Armitage, 2020). Heating of the upper layers of protoplanetary disks can cause photoevaporation, where heated material achieves thermal velocities higher than the escape velocity from the star's gravitational field (Bally, 1982).

Another important field of applications is the radiative transfer modeling of theoretical models. By calculating how radiation traverses a model of a protoplanetary disk, we can obtain artificial observables. This allows us to directly compare the results of numerical simulations or analytic models with real astronomical data. In the following, I will give a brief overview of radiative transfer, where I follow the book by Rybicki & Lightman (1985).

The basic quantity in radiative transfer is the intensity I_ν—that is the energy passing through a defined area with normal vector $\boldsymbol{n}$, per time interval, per frequency interval, coming from a defined solid angle along a beam $\boldsymbol{s}$. For a steady radiation field it can be described by the radiative transfer equation

$$\boldsymbol{n} \cdot \boldsymbol{\nabla} I_\nu = j_\nu - \alpha_\nu I_\nu \quad \Leftrightarrow \quad \frac{\mathrm{d}I_\nu}{\mathrm{d}s} = j_\nu - \alpha_\nu I_\nu \,, \tag{2.66}$$

where s is the distance along the ray of radiation. The quantity α_ν is known as the absorption coefficient. It describes how much intensity is lost along the path of the ray due to interactions with matter. In astrophysics, it is often described through the density

weighted absorption opacity $\kappa_\nu^{\mathrm{abs}} = \alpha_\nu/\rho$. Emission of radiation into the ray is characterized by the emissivity j_ν. The radiative transfer equation is often written in terms of the optical depth τ_ν as

$$\mathrm{d}\tau_\nu = \rho\kappa_\nu^{\mathrm{abs}}\,\mathrm{d}s \tag{2.67}$$

$$\frac{\mathrm{d}I_\nu}{\mathrm{d}\tau_\nu} = S_\nu - I_\nu\,, \tag{2.68}$$

where we have introduced the definition of the source function $S_\nu = j_\nu/\alpha_\nu$. With these definitions, the transfer equation has the formal solution

$$I_\nu(\tau_\nu) = I_\nu(0)e^{-\tau_\nu} + \int_0^{\tau_\nu} e^{-(\tau_\nu-\tau'_\nu)}S_\nu(\tau'_\nu)\,\mathrm{d}\tau'_\nu\,. \tag{2.69}$$

A medium with integrated optical depth $\tau_\nu \gg 1$ is called optically thick. It absorbs most of the incident photons. If $\tau \ll 1$, the medium is referred to as optically thin. If the medium is homogenious, isothermal, and isotropic, it can be assumed to be in local thermodynamic equilibrium. In this case, the intensity should be equal to the Planck function and constant in space. From the transfer equation we thus get *Kirchhoff's law*

$$j_\nu^{\mathrm{LTE}} = \alpha_\nu^{\mathrm{LTE}}B_\nu(T)\,. \tag{2.70}$$

Oftentimes we are interested in the amount of energy arriving per unit area, time, and frequency interval. For that we have to integrate the intensity over all solid angles ω, taking the incident angle of the rays ϑ with respect to the normal direction of the surface into account. This gives us

$$F_\nu = \oint I_\nu\cos(\vartheta)\mathrm{d}\omega\,. \tag{2.71}$$

If the intensity is isotropic, the net flux is zero. An example of flux in a non-isotropic radiation field is the observed flux coming from a star. We assume the star to radiate as a sphere with radius $R_\star$ and constant intensity $I_\nu^\star$, called the brightness. The amount of energy received per unit area at distance R is then the intensity integrated over the solid angle ($\mathrm{d}\omega = \sin(\vartheta)\,\mathrm{d}\vartheta\,\mathrm{d}\varphi$)

$$F_\nu^\star = \int_0^{2\pi}\int_0^{\pi} I_\nu^\star\Theta(\vartheta-\vartheta_\star)\sin(\vartheta)\cos(\vartheta)\,\mathrm{d}\vartheta\mathrm{d}\varphi = \int_0^{2\pi}\int_0^{\vartheta_\star} I_\nu^\star\sin(\vartheta)\cos(\vartheta)\,\mathrm{d}\vartheta\mathrm{d}\varphi\,, \tag{2.72}$$

where we have inserted $I_\nu = I_\nu^\star\Theta(\vartheta_\star-\vartheta)$ with the Heaviside step function $\Theta(\vartheta-\vartheta_\star)$ that limits the constant intensity $I_\nu^\star$ to the observed surface area of the star. Integration yields the inverse square law

$$F_\nu^\star = I_\nu^\star\pi\left(\frac{R_\star}{R}\right)^2\,. \tag{2.73}$$

If we assume the star to be a black body, we can substitute $I_\nu^\star = B_\nu(T_\star)$. This result makes it possible to calculate the temperature of a dust particle orbiting the star. Given the

absorption opacity of the dust, the total amount of energy received is then

$$Q_+ = \int_0^\infty \kappa_\nu^{\mathrm{abs}} F_\nu^\star \,\mathrm{d}\nu = \pi \left(\frac{R_\star}{R}\right)^2 \int_0^\infty \kappa_\nu^{\mathrm{abs}} B_\nu(T_\star)\,\mathrm{d}\nu\,.$$

Assuming the grain to be spherical and in thermodynamic equilibrium, we can calculate the outgoing flux—which has no angular dependency—and get

$$Q_- = 4\pi \int_0^\infty \kappa_\nu^{\mathrm{abs}} B_\nu(T_\mathrm{d})\,\mathrm{d}\nu\,,$$

where we have introduced the particle's temperature T_d. Equating these expressions gives us a way to determine the temperature through $B_\nu(T_\mathrm{d})$. We use $\int_0^\infty B_\nu(T)\,\mathrm{d}\nu = \sigma_{\mathrm{SB}} T^4/\pi$ with the Stefan-Boltzmann constant σ_{SB}, and define the *Planck-mean opacity*

$$\kappa_\mathrm{P}(T) = \frac{\int_0^\infty \kappa_\nu^{\mathrm{abs}} B_\nu(T)\,\mathrm{d}\nu}{\int_0^\infty B_\nu(T)\,\mathrm{d}\nu} = \frac{\pi}{\sigma_{\mathrm{SB}} T^4} \int_0^\infty \kappa_\nu^{\mathrm{abs}} B_\nu(T)\,\mathrm{d}\nu \tag{2.74}$$

to arrive at

$$T_\mathrm{d} = \left(\frac{R_\star}{2R}\right)^{1/2} \left(\frac{\kappa_\mathrm{P}(T_\star)}{\kappa_\mathrm{P}(T_\mathrm{d})}\right)^{1/4} T_\star\,, \tag{2.75}$$

(see Armitage, 2020). The temperature of the dust particle (or any other passively irradiated, spherical astronomical body) is thus dependent on the ratio of its Planck opacity at the temperature of the stellar radiation, and the efficiency of emission given by its opacity at its own temperature. Note that these calculation ignored scattering and assume either perfect vacuum, or an optically thin medium between the body and the star.

2.4.1 Scattering

Solving the transfer equation in three dimensions and for spatially varying opacities is usually not analytically possible—especially if the effects of scattering are considered. Scattering is described via the scattering coefficient or the scattering opacity, related via $\kappa_\nu^{\mathrm{sca}} = \alpha_\nu^{\mathrm{sca}}/\rho$. The total absorption coefficient is then given as the sum $\alpha_\nu = \alpha_\nu^{\mathrm{sca}} + \alpha_\nu^{\mathrm{abs}}$. Similarly, the emissivity has two contributions, one from direct emission into the ray and one from scattering of photons into the ray $j_\nu = j_\nu^{\mathrm{emis}} + j_\nu^{\mathrm{sca}}$. The source function is thus defined as

$$S_\nu = \frac{j_\nu^{\mathrm{emis}} + j_\nu^{\mathrm{sca}}}{\alpha_\nu^{\mathrm{sca}} + \alpha_\nu^{\mathrm{abs}}} \coloneqq \epsilon_\nu S_\nu^{\mathrm{abs}} + \eta_\nu S_\nu^{\mathrm{sca}}\,, \tag{2.76}$$

where we have used the definition of the albedo $\eta_\nu = {}^{\alpha_\nu^{\mathrm{sca}}}/_{\alpha_\nu^{\mathrm{sca}}+\alpha_\nu^{\mathrm{abs}}}$ and the absorption probability $\epsilon_\nu = 1 - \eta_\nu$. If the scattering is isotropic, the total scattering emissivity can be written as

$$j_\nu^{\mathrm{sca}} = \alpha_\nu^{\mathrm{sca}} \oint I_\nu \,\mathrm{d}\omega \coloneqq \alpha_\nu^{\mathrm{sca}} J_\nu\,. \tag{2.77}$$

J_ν is called the mean intensity. For thermal emission, we find the complete source function to be

$$S_\nu = (1 - \epsilon_\nu) J_\nu + \epsilon_\nu B_\nu(T)\,. \tag{2.78}$$

If the absorption probability is unity, we retrieve the usual transfer equation with Kirchhoff's law. If on the other hand ϵ_ν is close to zero, scattering will commence many times for a photon. The intensity of a ray is thus dependent on the intensity in any other direction, which makes the equation of radiative transfer impossible to solve analytically without further assumptions.

The problem becomes much more complicated if scattering is anisotropic, i.e., if radiation is preferentially scattered in specific directions. In such a case, we have to consider the scattering phase function ϕ, which describes the angular dependency of the scattering problem. For the direction of the incoming ray $\boldsymbol{n}$ and the outgoing direction $\boldsymbol{n}'$, Equation 2.77 takes the form

$$j_\nu^{\mathrm{sca}}(\boldsymbol{n}') = \alpha_\nu^{\mathrm{sca}} \frac{1}{4\pi} \oint I_\nu(\boldsymbol{n}) \phi(\boldsymbol{n}, \boldsymbol{n}') \, \mathrm{d}\omega \,. \tag{2.79}$$

The phase function describes the probability at which a ray is scattered into a specific direction and is thus normalized to one. If the photons are scattered off particles with complex shape and composition, ϕ can become extremely difficult to compute. Simplified models are thus often used.

2.4.2 Optically Thick Radiative Transfer

In the optically thick regime ($\tau_\nu \gg 1$) it is reasonable to assume that the radiation field is mostly isotropic due to continuous scattering and absorption and re-emission events. Eddington (1926) used this assumption to first order accuracy (allowing for linear deviations from isotropy) and derived expressions for the radiative quantities in the optically thick regime. For this, he expressed the radiative transfer equation in terms of its angular moments in a power-law series. I will only show the main result, which is that photons in the optically thick limit diffusive through the medium following

$$\frac{1}{3} \frac{\partial^2 J_\nu}{\partial \tau_\nu^2} = J_\nu - S_\nu \,. \tag{2.80}$$

If the material only emits thermal radiation, we can further substitute Equation 2.78 and we get

$$\frac{1}{3} \frac{\partial^2 J_\nu}{\partial \tau_\nu^2} = \epsilon_\nu \left(J_\nu - B_\nu(T) \right) \,, \tag{2.81}$$

known as the *radiative diffusion equation*. Given the temperature of the medium, we can thus solve for J_ν and determine S_ν through Equation 2.78. Knowing the source function then allows us to use the formal solution to the transfer equation and calculate the entire radiation field. An even more severe assumption than the Eddington approximation is to demand that the radiation field is not only isotropic to first order, but also that it only deviates from the local Planck function to first order. This leads to the Rosseland approximation. Because the intensity of thermal radiation only depends on the local temperature, only temperature variations in the medium can cause radiative flux. Locally, the flux is then given by

$$F_\nu = -\frac{4\pi}{3\rho(\kappa_\nu^{\mathrm{sca}} + \kappa_\nu^{\mathrm{abs}})} \frac{\partial B_\nu(T)}{\partial T} \frac{\partial T}{\partial s} \,. \tag{2.82}$$

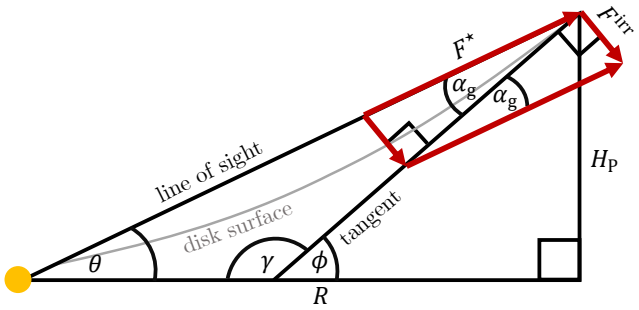

Figure 2.12
Geometry of the irradiation flux calculation for a flaring protoplanetary disk. The grazing angle α_{g}, which gives the normal component of the flux $F^{\mathrm{irr}} = \sin(\alpha_{\mathrm{g}})F^{\star}$, can be calculated through $\theta + \alpha_{\mathrm{g}} + \gamma = 180°$, and $\gamma + \phi = 180°$. With $\theta \approx H_{\mathrm{P}}/R$ and $\phi \approx \partial H_{\mathrm{P}}/\partial R$, we have $\alpha_{\mathrm{g}} \approx \partial H_{\mathrm{P}}/\partial R - H_{\mathrm{P}}/R$.

The total energy flux related with this diffusive process can be calculated by integrating over all frequencies. Using the frequency integrated Planck function, the total diffusion flux follows as

$$F = -\frac{16}{3}\frac{\sigma_{\mathrm{SB}}T^3}{\rho\kappa_{\mathrm{R}}}\frac{\partial T}{\partial s}\,, \tag{2.83}$$

where the Rosseland mean opacity κ_{R} was introduced, which is given by

$$\frac{1}{\kappa_{\mathrm{R}}} = \frac{\displaystyle\int_0^{\infty} \frac{1}{\kappa_\nu^{\mathrm{abs}} + \kappa_\nu^{\mathrm{sca}}}\frac{\partial B_\nu(T)}{\partial T}\,\mathrm{d}\nu}{\displaystyle\int_0^{\infty}\frac{\partial B_\nu(T)}{\partial T}\,\mathrm{d}\nu}\,. \tag{2.84}$$

This process is therefore mathematically identical to heat conduction with a conductivity $D_{\mathrm{rad}} = {}^{16\sigma_{\mathrm{SB}}T^3}/_{3\rho\kappa_{\mathrm{R}}}$. Radiative diffusion is applicable in dense astrophysical environments like stellar interiors or the midplane of the inner regions of protoplanetary disks.

Given the inverse square law, we can also calculate the equilibrium temperature of an irradiated, flaring disk, i.e., a disk in which the scale height varies with radius. The distance from the midplane at which the stellar photons are absorbed is referred to as the photospheric scale height H_{P}. The disk is thus assumed to be optically thick to stellar photons below the photosphere. In contrast to the single dust grain considered before, we now have to take the grazing angle of the radiation at the photospheric surface into account, denoted by α_{g}. It can be calculated from the line-of-sight angle $\theta \approx {}^{H_{\mathrm{P}}}/_{R}$ and the surface tangent $\phi \approx {}^{\partial H_{\mathrm{P}}}/_{\partial R}$ (see Figure 2.12 and Armitage, 2020). For the energy budget of the disk, we are interested in the normal flux component, which is then given by

$$F^{\mathrm{irr}} = \sin(\alpha_{\mathrm{g}})F^{\star}\,.$$

We assume the disk to be a black body which gives

$$T_{\mathrm{disk}} = \left(\frac{R_\star}{R}\right)^{1/2}\sin(\alpha_{\mathrm{g}})T_\star\,. \tag{2.85}$$

If we assume the flaring angle to be constant, we can thus directly calculate the disk temperature and see that $T_{\mathrm{disk}} \propto R^{-1/2}$.

2.4.3 Dust Opacities

Dust particles in protoplanetary disks are predominantly composed of amorphous silicates and carbon, which make it possible for the grains to absorb a broad range of wavelengths. Radiation in protoplanetary disks is thus mostly scattered and absorbed by dust grains instead of gas molecules which emit and absorbs radiation at specific frequencies.

Dust opacities are however highly dependent on the composition, size, and shape of the grains. In general, Maxwell's equations have to be solved to derive the details of the scattering and absorption processes (Min, 2015).

If the particles are much larger than the wavelength of the radiation, i.e. $\lambda \ll 2\pi a$, we can ignore the wavelike character of the radiation in the near-field and treat the grains in the limit of geometric optics. In this case, we can define the opacity per gram of dust as

$$\kappa_\nu = \frac{\sigma_{\mathrm{geo}}}{m_{\mathrm{d}}} = \frac{\pi a^2}{m_{\mathrm{d}}} \,. \tag{2.86}$$

Absorption and scattering opacity then follow through the albedo of the material as $\kappa_\nu^{\mathrm{sca}} = \eta_\nu \kappa_\nu$ and $\kappa_\nu^{\mathrm{abs}} = (1 - \eta_\nu)\kappa_\nu$.

At longer wavelengths, this assumption is no longer valid. Particles fulfilling $\lambda \gg 2\pi a$, instead behave like a single oscillating dipole under the influence of an external electromagnetic field. Thus, radiation is Rayleigh scattered and the respective opacities are

$$\kappa_\nu^{\mathrm{sca}} \propto \frac{a^3}{\lambda^4} \qquad \kappa_\nu^{\mathrm{abs}} \propto \frac{1}{\lambda} \,. \tag{2.87}$$

In the intermediate wavelength regime, where $\lambda \sim 2\pi a$, Mie theory (Mie, 1908) is often applied to avoid the full treatment of Maxwell's equations (Bohren & Huffman, 1998). Incoming and outgoing electromagnetic waves are decomposed into vector spherical harmonics. The dust particles are assumed to be spheres with a complex refractive index that depends on the composition. Various numerical codes exist that can compute scattering and absorption opacities via Mie theory. The determination of the complex refractive indices of the material however remains challenging. Seminal works like Pollack et al. (1994) and Jaeger et al. (1994) assume mixtures of water ice, troilite (FeS),astronomical silicates, and refractory organics. Astronomical silicates refer to Si-O groups in combination with positively charged metal ions. The most common silicates in astronomical environments are Olivine ($(\mathrm{Mg,Fe})_2\mathrm{SiO}_4$) and Pyroxene ($(\mathrm{Mg,Fe})\mathrm{SiO}_3$). Their presence in protoplanetary disks is indicated by spectral features specific to the Si-O bonds vibrational harmonics at ~10 µm and ~20 µm (Aitken et al., 1988). Birnstiel et al. (2018) compiled much of the frequently used optical data and combined them with standard assumptions of composition in Mie opacity calculations. Their opacity model also allows for the treatment of arbitrary particle size distributions. Figure 2.13 shows their model of the absorption opacities computed for a realistic grain size distribution in comparison with other commonly used opacity prescriptions, which often only assume micrometer-sized grains. We see the 10 µm silicate feature in all models. Beckwith et al. (1990) assumed the simple scaling relation for Rayleigh scattering with $\kappa_\nu^{\mathrm{abs}} \propto \lambda^{-1}$. In the model by D'Alessio et al. (2001) and in the Birnstiel et al. (2018) opacities we also find the water feature at 3 µm. However, as particle

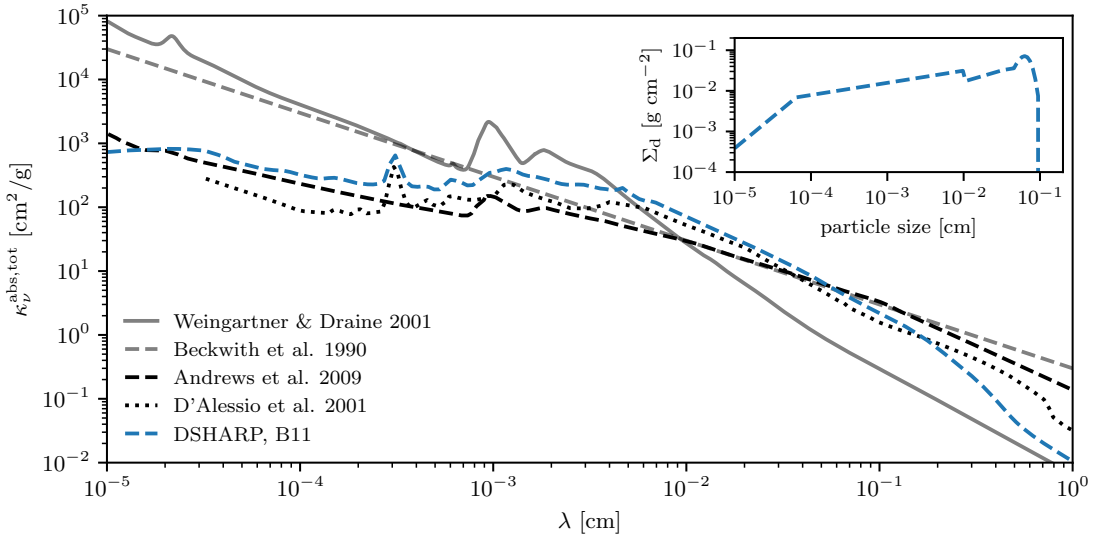

Figure 2.13
Comparison of different dust opacity models by Weingartner & Draine (2001), Beckwith et al. (1990), Andrews et al. (2009), D'Alessio et al. (2001), and the DSHARP opacity model (Birnstiel et al., 2018). The DSHARP model takes an evolved dust size distribution in fragmentation-coagulation equilibrium into account (Birnstiel et al., 2011), which is shown in the inlay plot. (figure adapted from (Birnstiel et al., 2018), originally licensed under CC BY 4.0)

growth is considered, the opacity slope in the millimeter-range changes—it is sensitive to the maximum particle size of the distribution (Miyake & Nakagawa, 1993).

CHAPTER 3

ESTABLISHED METHODS

3.1 Grid-Based Hydrodynamics

Godunov's Methods and the Riemann Problem

In order to solve the Navier-Stokes equations with the initial and boundary conditions appropriate for protoplanetary disks, we have to make use of numerical methods. One family of methods is grid-based hydrodynamics. Space and time are divided into discrete steps giving each cell initial and boundary conditions defined by the neighboring cells. The goal is to evolve the conserved fluid quantities on this grid in time. In general, a hyperbolic conservation law can be written

$$\frac{\partial \boldsymbol{U}}{\partial t} + \boldsymbol{\nabla} \cdot \boldsymbol{F} = 0\,. \tag{3.1}$$

For this short overview I follow Toro (1999). We will have a look at the inviscid Navier-Stokes equations, i.e., the Euler equations, for which the vector of conserved variables $\boldsymbol{U}$ and flux $\boldsymbol{F}$ are

$$\boldsymbol{U} = \begin{bmatrix} \rho \\ \rho \boldsymbol{v} \\ E \end{bmatrix} \qquad \boldsymbol{F} = \begin{bmatrix} \rho \boldsymbol{v} \\ \rho \boldsymbol{v} \otimes \boldsymbol{v} + P \mathbb{I}_3 \\ \boldsymbol{v}(E + P) \end{bmatrix}, \tag{3.2}$$

where $\mathbb{I}_3$ is the 3×3 identity matrix. Writing the conservation laws in their integral form gives us a helpful interpretation for the hydrodynamics on our grid. Using Gauss' theorem and integrating over a volume V, we can write the integral form of the conservation law as

$$\frac{\partial}{\partial t} \iiint_V \boldsymbol{U} \, \mathrm{d}V = - \oiint_S \boldsymbol{F} \cdot \boldsymbol{n} \, \mathrm{d}S\,, \tag{3.3}$$

This means the time evolution of our conserved quantities (mass, momentum, energy) in the cell depends on the net flux through the surface of our grid cells. Given the discrete grid where $\boldsymbol{x}_i$ denotes center of the grid cell number i, Godunov (1959) introduced the cell averaged quantity at time t

$$\bar{\boldsymbol{U}}_i = \frac{1}{\Delta V_i} \iiint_{\Delta V_i} \boldsymbol{U}(\boldsymbol{x}, t) \, \mathrm{d}V\,, \tag{3.4}$$

where ΔV_i is the cell's volume. We want to advance Equation 3.3 over a time step $\Delta t = t^{(n+1)} - t^{(n)}$ (where n denotes the current time in terms of our discrete time grid). For this,

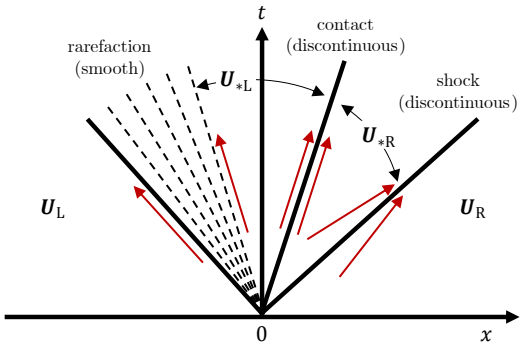

Figure 3.1
Wave pattern for an exact solution of the Riemann problem. The initial discontinuity at 0 evolves into a shock wave (traveling to the right), a contact discontinuity (traveling to the right), and a rarefaction fan with a smooth transition from $\boldsymbol{U}_\mathrm{L}$ to $\boldsymbol{U}_{*\mathrm{L}}$. Depending on the initial conditions, ten different of such wave patterns have to be distinguished to derive the exact solution (see Fig. 3.2 and 6.5 in Toro, 1999).

a time-averaged flux can be defined as

$$\bar{\boldsymbol{F}} = \frac{1}{\Delta t} \int_{t^{(n)}}^{t^{(n+1)}} \boldsymbol{F}(\boldsymbol{U}(\boldsymbol{x}), t)\ \mathrm{d}t\,. \tag{3.5}$$

With these definitions, we can apply a time integration from $t^{(n)}$ to $t^{(n+1)}$ to Equation 3.3, which gives us the exact formal solution for the cell-averaged quantities

$$\bar{\boldsymbol{U}}_i^{(n+1)} = \bar{\boldsymbol{U}}_i^{(n)} - \frac{\Delta t}{\Delta V_i} \oiint_S \bar{\boldsymbol{F}} \cdot \boldsymbol{n}\, \mathrm{d}S\,. \tag{3.6}$$

If we define a Cartesian grid in one dimension, with cell interfaces at $i - 1/2$ and $i + 1/2$, we can write the solution as

$$\bar{\boldsymbol{U}}_i^{(n+1)} = \bar{\boldsymbol{U}}_i^{(n)} - \frac{\Delta t}{\Delta x_i}(\bar{\boldsymbol{F}}_{i+1/2} - \bar{\boldsymbol{F}}_{i-1/2})\,. \tag{3.7}$$

As we want the solution to only depend on the fluxes at the boundaries to the directly adjacent cells, we have to demand that the time step is short enough to prevent overshooting, i.e.,

$$\Delta t \leq \frac{\Delta x}{v_\mathrm{max}}\,, \tag{3.8}$$

where v_max is the maximum wave speed of the fluxes. This is known as the Courant, Friedrichs, & Lewy (1928) (CFL) condition. At the cell boundaries we are now confronted with the task to determine the fluxes $\bar{\boldsymbol{F}}_{i+1/2}$ and $\bar{\boldsymbol{F}}_{i-1/2}$. If we assume the conserved quantities to be constant in each cell, we introduce flow discontinuities at the two interfaces. The resulting initial conditions define a so-called *Riemann problem* at the inner and outer cell boundary (here set to $x = 0$),

$$\boldsymbol{U}(\boldsymbol{x}, 0) = \begin{cases} \boldsymbol{U}_\mathrm{L} & \text{if } x < 0 \\ \boldsymbol{U}_\mathrm{R} & \text{if } x > 0\,. \end{cases} \tag{3.9}$$

The Riemann problem for the Euler equations has an exact solution that determines the flux, based on the Rankine-Hugoniot shock conditions. Its calculation is however lengthy and computationally expensive. It consists of a number of waves whose characteristic speeds depend on the initial conditions of the flow. One schematic example for a subsonic flow is

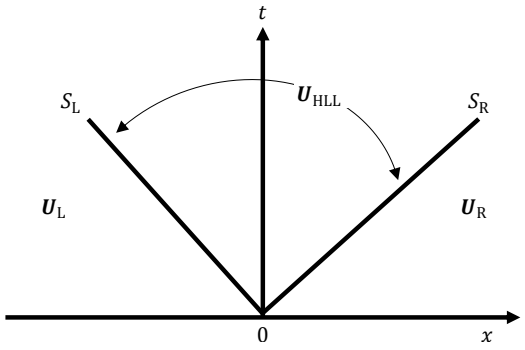

Figure 3.2
Wave pattern for the HLL approximate Riemann solver. The initial discontinuity at 0 evolves into a shock wave and a rarefaction wave, traveling at wave speeds S_R and S_L, depending on the initial conditions. Outside of the area crossed by the waves, the original states $\boldsymbol{U}_L$ and $\boldsymbol{U}_R$ remain. In between the two waves, the state is changes into $\boldsymbol{U}_{HLL}$ (based on Fig. 10.3 from Toro, 1999).

shown in Figure 3.1. A rarefaction wave, associated with smoothly changing flow quantities from $\boldsymbol{U}_L$ to $\boldsymbol{U}_{*L}$, indicated by the dashed lines, is propagating to the left. A contact discontinuity, separating the states $\boldsymbol{U}_{*L}$ and $\boldsymbol{U}_{*R}$ originating from the initial discontinuity in density, and a discontinuous shock wave propagates to the right. However, this is only one realization of the three waves that depends on the initial condition of the problem. Ten possible wave patterns have to be distinguished, depending on the initial conditions (see Toro, 1999, for the comprehensive calculations). The iterative procedure to exactly solve the Riemann problem is numerically costly. In practice, approximate Riemann solvers are thus oftentimes applied. Harten, Lax, & van Leer (1983) (HLL) introduced an approximate Riemann solver that assumes the propagation of only two waves from the discontinuity, as shown in Figure 3.2. Given the left and right maximum wave speeds S_L and S_R, the corresponding flux at the interface is then given by

$$\boldsymbol{F}^{HLL} = \begin{cases} \boldsymbol{F}_L & \text{if } 0 \leq S_L \\ \dfrac{S_R \boldsymbol{F}_L - S_L \boldsymbol{F}_R + S_L S_R (\bar{\boldsymbol{U}}_R - \bar{\boldsymbol{U}}_L)}{S_R - S_L} & \text{if } S_L \leq 0 \leq S_R \\ \boldsymbol{F}_R & \text{if } 0 \geq S_R \,. \end{cases}$$

The wave speeds can be estimated in different ways. The simplest possibility is to assume they propagate with the speed of sound relative to the gas velocities

$$S_L = v_L - c_{s,L} \qquad S_R = v_R + c_{s,R} \,.$$

With the given flux, the Godunov scheme can be readily solved. The HLL solver however has some vital flaws. The biggest one is the disregard of the contact discontinuity that originates at the cell boundary in the exact solution to the Riemann problem. This leads to strong numerical diffusivity and means that sharp flow features can not be sustained.

Toro et al. (1994) therefore introduced a modification to the HLL Riemann solver, called the HLLC Riemann solver (C for contact discontinuity). In this scheme (shown in Figure 3.3), the contact discontinuity from the exact solution is reintroduced. This means, new estimates for the wave speed of the contact discontinuity S_* and the in-between states $\boldsymbol{U}_{*L}$ and $\boldsymbol{U}_{*R}$ are necessary to calculate the flux across the boundary. The result of these

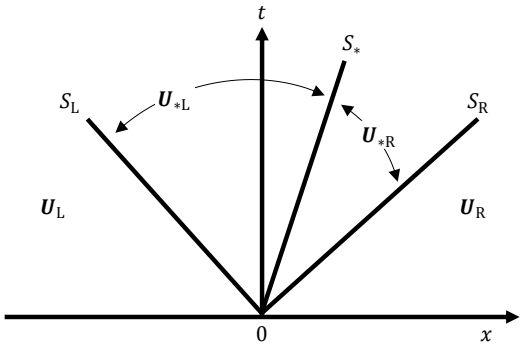

Figure 3.3
Wave pattern for the HLLC approximate Riemann solver. The initial discontinuity at 0 evolves into a shock wave, a contact discontinuity, and a rarefaction wave, traveling at wave speeds S_R, S_*, and S_L, depending on the initial conditions. Outside of the area crossed by the waves, the original states $\boldsymbol{U}_L$ and $\boldsymbol{U}_R$ remain. In between the waves, the state is changes into $\boldsymbol{U}_{*R}$ and $\boldsymbol{U}_{*L}$ (based on Fig. 10.4 from Toro, 1999).

considerations is

$$\boldsymbol{F}^{\mathrm{HLLC}} = \begin{cases} \boldsymbol{F}_L & \text{if } 0 \le S_L \\ \boldsymbol{F}_L + S_L(\boldsymbol{U}_{*L} - \boldsymbol{U}_L) & \text{if } S_L \le 0 \le S_* \\ \boldsymbol{F}_R + S_R(\boldsymbol{U}_{*R} - \boldsymbol{U}_R) & \text{if } S_* \le 0 \le S_R \\ \boldsymbol{F}_R & \text{if } 0 \ge S_R\,. \end{cases}$$

To calculate the flux, we require the new wave speed S_*. Batten et al. (1997) derived an equation for S_* that only depends on the wave speeds S_L and S_R

$$S_* = \frac{P_R - P_L + \rho_L v_L(S_L - v_L) - \rho_R v_R(S_R - v_R)}{\rho_L(S_L - v_L) - \rho_R(S_R - v_R)}\,.$$

The HLLC Riemann solver generally yields much better results than the HLL solver in terms of numerical diffusivity, especially of course for the contact discontinuity. However, all Godunov type methods that assume constant fluid states in each grid cell are only accurate to first order and thus generally diffusive.

The PLUTO Code

Modern hydrodynamics codes employ high-order, total-variation-diminishing (TVD) schemes to solve the Euler (Equations 3.1 and 3.2) or the Navier-Stokes equations. Here, I give a brief introduction to the publicly available astrophysical hydrodynamics code PLUTO[1] (Mignone et al., 2007) which is used throughout the next chapters of this thesis. Instead of solving the first order accurate Godunov scheme with piecewise-constant fluid quantities, PLUTO utilizes a *reconstruct-solve-average* strategy. At first, the code produces a piecewise-polynomial reconstruction of the primitive flow variables (e.g., ρ, $\boldsymbol{v}$, P) in each grid-cell. These interpolation routines provide boundary values for the primitive variables at each side of the cell interfaces (second step in Figure 3.4). For this, monotonicity conditions are imposed to avoid the occurence of too steep gradients or spurious oscillations in the solutions. The code provides various methods to construct these interface values, from piecewise-linear (second order accurate) to more sophisticated methods like piecewise-parabolic reconstruction (Mignone et al., 2005), or the WENO scheme (fifth order accurate

[1] http://plutocode.ph.unito.it/

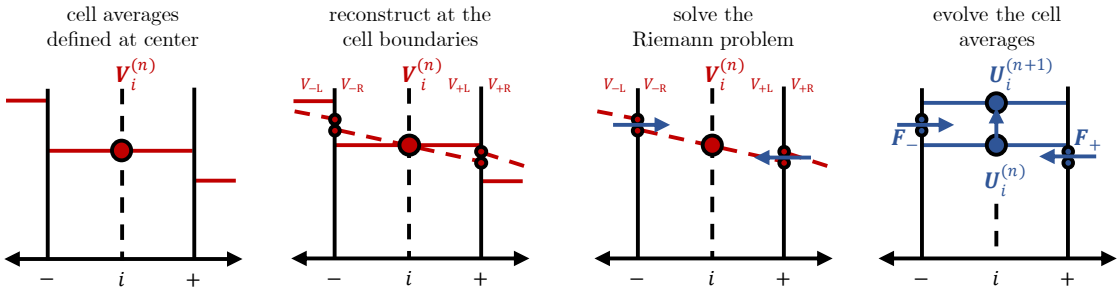

Figure 3.4
Reconstruct-solve average scheme as utilized by the PLUTO code (Mignone et al., 2007). Primitive variables $\boldsymbol{V}$ are interpolated to the cell boundaries (denoted as ±) and used to construct a Riemann problem. The Riemann problem is solved and the cell-averaged conserved quantities $\boldsymbol{U}$ are evolved in time using Godunov's method and a timestep determined by the CFL condition.

Liu, 1994). As these reconstructions are carried our for each cell individually, discontinuities remain at the cell interfaces. The next step is to apply Riemann solvers to calculate the inter-cell flux for the Gudunov scheme from the interpolated primitive variables (third step in Figure 3.4). PLUTO provides several approximate Riemann solvers like HLL (applicable to isothermal setups), HLLC, or the Roe solver (Roe, 1981).

Given these fluxes, the conserved quantities (e.g., ρ, $\rho\boldsymbol{v}$, E) can be updated via Godunov's scheme and various different time-stepping methods (fourth step in Figure 3.4). Commonly used are Runge-Kutta time integration schemes to second or third order. These multi-step algorithms require multiple applications of the Riemann solver for a single complete time-step. To ensure numerical stability, the time step has to fulfill the CFL condition

$$\Delta t = C_{\mathrm{d}} \min_{\mathrm{d}} \left(\frac{\Delta l^{\mathrm{d}}_{\mathrm{min}}}{|\lambda^{\mathrm{d}}_{\mathrm{max}}|} \right) , \tag{3.10}$$

where $l^{\mathrm{d}}_{\mathrm{min}}$ is the smallest grid cell length in dimension d, and $|\lambda^{\mathrm{d}}_{\mathrm{max}}|$ is the fastest signal speed. The value of the CFL number $C_{\mathrm{d}} \leq 1$ depends on the chosen configuration of solver and reconstruction method. Once the time integration is completed, the cycle begins again until the desired simulation time is reached.

PLUTO also allows for the treatment of parabolic terms in the conservation equation, which I have not discussed here. The treatment of thermal conduction or viscosity imposes stricter constraints on the timestep, which can become an issue when solving the equations explicitly. Algorithms like super-time-stepping (Alexiades et al., 1996) are available in PLUTO, which are much faster than then the standard explicit integration schemes.

It is also possible to add k passive scalars Q to a simulation that are advected with the gas flow velocities $\boldsymbol{v}$ according to the standard conservation law

$$\frac{\partial(\rho Q_k)}{\partial t} + \boldsymbol{\nabla} \cdot (\rho \boldsymbol{v} Q_k) = 0 \, . \tag{3.11}$$

We will use this feature to construct a simple dust advection method in the PLUTO code in the next chapters.

3.2 Numerical Methods for Dust Coagulation

The shear number of particles and collision outcomes in protoplanetary disks prohibits us from calculating the evolution of every individual grain. Two established methods exist to circumvent this problem. Firstly, dust grains can be clustered together and treated as representative particles whose properties are evolved via Monte Carlo methods. This allows for the uncomplicated incorporation of additional particle properties (see, e.g., Zsom et al., 2011; Drazkowska et al., 2013). However, being a particle based method, it might suffer from mass resolution issues and it is computationally expensive. Secondly, the entire dust size distribution can be evolved in time and particles can be treated in terms of size-dependent mass densities (e.g., Weidenschilling, 1980; Brauer et al., 2008; Birnstiel et al., 2010). In this thesis we make use of the latter method, and develop approximate methods based on it. I give a short introduction to the state-of-the art dust coagulation software `DustPy` (Stammler & Birnstiel, 2022). `DustPy` also simulates the dust advection and diffusion in the radial direction of protoplanetary disk, which I will omit in the following. The continuous size distribution, whose evolution is given by Smoluchowski's equation, is represented by a discrete grid of N_m particle masses. The equation can then be written

$$\frac{\partial n_k}{\partial t} = \sum_{i=1}^{N_m} \sum_{j=1}^{i} \mathcal{K}_{ijk} \mathcal{R}_{ij} n_i n_j - n_k \sum_{j=1}^{N_m} n_j \mathcal{R}_{jk} (1 + \delta_{jk}) \,, \tag{3.12}$$

where the second sum in the first term only goes up to i to avoid double counting identical collisions $m_i \leftrightarrow m_j$ and $m_j \leftrightarrow m_i$. The collision rate $\mathcal{R}_{jk}$ and the coagulation and fragmentation kernel $\mathcal{K}_{ijk}$ are now matrices that describe the outcomes of every possible collision. Whether a collision leads to fragmentation or coagulation is determined via the fragmentation probability. For this, `DustPy` assumes particle collision velocities follow a Maxwell-Boltzmann distribution

$$\mathcal{P}_{ij}(\Delta v_{ij}, \Delta v_{ij}^{\mathrm{rms}}) = \sqrt{\frac{54}{\pi}} \frac{\Delta v_{ij}^2}{\left(\Delta v_{ij}^{\mathrm{rms}}\right)^3} \exp\left[-\frac{3}{2} \left(\frac{\Delta v_{ij}}{\Delta v_{ij}^{\mathrm{rms}}} \right)^2 \right] , \tag{3.13}$$

where Δv_{ij} is the actual collision velocity and the rms velocity of the distribution is given by $\Delta v_{ij}^{\mathrm{rms}}$, which is the total collision velocity from Equation 2.58. With this definition, the rate at which particles fragment is depending on the frequency of particle collisions with relative particle velocities larger than v_{frag}, i.e.,

$$\mathcal{R}_{ij}^{\mathrm{frag}} = \sigma \int_{v_{\mathrm{frag}}}^{\infty} \Delta v_{ij}\, \mathcal{P}(\Delta v_{ij}, \Delta v_{ij}^{\mathrm{rms}})\, \mathrm{d}\Delta v_{ij} = \sigma \langle \Delta v_{ij} \rangle \Pi_{ij}^{\mathrm{frag}} \,, \tag{3.14}$$

where $\langle \Delta v_{ij} \rangle = \int_{v_{\mathrm{frag}}}^{\infty} \Delta v_{ij}\, \mathcal{P}(\Delta v_{ij}, \Delta v_{ij}^{\mathrm{rms}})\, \mathrm{d}\Delta v_{ij} = \sqrt{8\pi/3}\, \Delta v_{ij}^{\mathrm{rms}}$ is the mean velocity of the Maxwell-Boltzmann distribution. The integral has an analytic solution from which the

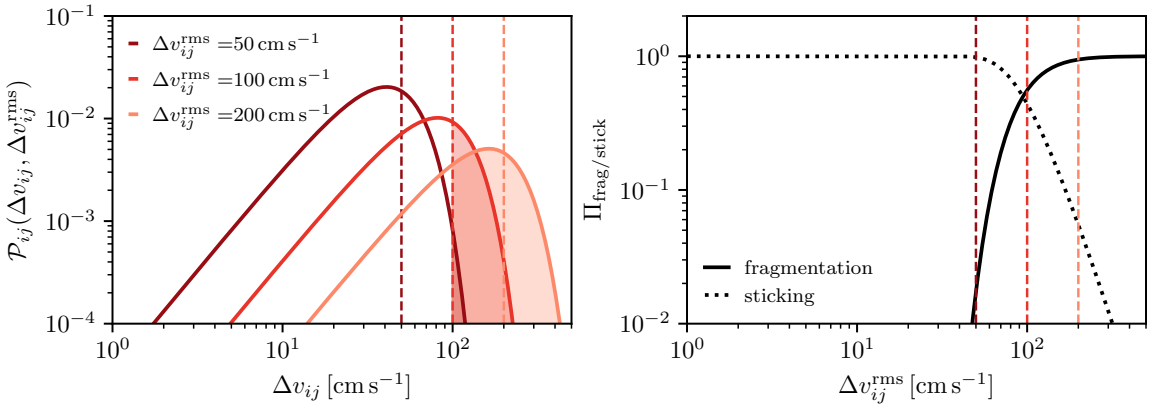

Figure 3.5
Fragmentation and sticking probabilities (right panel), and Maxwell-Boltzmann distributions as implemented in the `DustPy` code (Stammler & Birnstiel, 2022) for three different rms collision velocities. Colored areas in the left panel indicate the fragmentation regime for a fragmentation velocity of 100 cm s^{-1}.

fragmentation and sticking probabilities follows as

$$\Pi_{ij}^{\mathrm{frag}} = \left[\frac{3}{2}\left(\frac{v_{\mathrm{frag}}}{\Delta v_{ij}^{\mathrm{rms}}}\right)^2 + 1\right] \exp\left[-\frac{3}{2}\left(\frac{v_{\mathrm{frag}}}{\Delta v_{ij}^{\mathrm{rms}}}\right)^2\right] \tag{3.15}$$

$$\Pi_{ij}^{\mathrm{stick}} = 1 - \Pi_{ij}^{\mathrm{frag}}\,, \tag{3.16}$$

which are shown in Figure 3.5. If fragmentation occurs, `DustPy` distinguishes between collisions with full fragmentation and erosive collisions, depending on the particles' mass ratio. For similarly sized particles, complete fragmentation occurs and the mass of the colliders is distributed over the size distribution following the fragmentation power law by Dohnanyi (1969). If one of the particles (the projectile) is much smaller than the other (the target), erosion occurs. The projectile fully fragments, while the target loses only a small amount of mass.

The contributions of coagulation and fragmentation are added up and the equation can be brought into the general form

$$\frac{\partial \boldsymbol{n}}{\partial t} = \dot{\boldsymbol{n}}^{\mathrm{frag}} + \dot{\boldsymbol{n}}^{\mathrm{coag}} = (\mathbb{J}_{\mathrm{frag}} + \mathbb{J}_{\mathrm{coag}})\boldsymbol{n}\,, \tag{3.17}$$

where $\mathbb{J}_{\mathrm{frag}}$ and $\mathbb{J}_{\mathrm{coag}}$ are the fragmentation and coagulation Jacobians. The discretized version of the coagulation equation can then be implicitly written in terms of the dust column density vector $\boldsymbol{\Sigma}_{\mathrm{d}}$ as

$$\frac{\boldsymbol{\Sigma}_{\mathrm{d}}^{(n+1)} - \boldsymbol{\Sigma}_{\mathrm{d}}^{(n)}}{\Delta t} = (\mathbb{J}_{\mathrm{frag}} + \mathbb{J}_{\mathrm{coag}})\boldsymbol{\Sigma}_{\mathrm{d}}^{(n+1)}\,, \tag{3.18}$$

which has the solution

$$\boldsymbol{\Sigma}_{\mathrm{d}}^{(n+1)} = \left[\mathbb{I} - \Delta t(\mathbb{J}_{\mathrm{frag}} + \mathbb{J}_{\mathrm{coag}})\right]^{-1} \boldsymbol{\Sigma}_{\mathrm{d}}^{(n)}\,. \tag{3.19}$$

Calculating the Jacobians to construct a reliable numerical scheme is a highly non-trivial task and I refer to Brauer et al. (2008) and Stammler & Birnstiel (2022) for the details and explanations of the involved numerical difficulties. One of the general problems of this family of methods is the required resolution. A logarithmic size grid must be employed to resolve the ∼ 21 orders of magnitude in particle mass that have to be bridged during the dust coagulation process. Thus, the outcomes of sticking collisions will generally not directly produce results that correspond to the centers of another mass grid cell. The associated density shift is therefore distributed across the neighboring cells depending on the relative position of the produced particles on the mass grid. This means that some mass will inevitably be shifted into a mass bin that is larger than the combined mass of the colliders, giving rise to artificial growth. The numerical method is furthermore diffusive, which means that a mass grid with high enough resolution is required. In general, at least 7 mass bins per decade are require to keep the result reasonably accurate, i.e., a minimum of ∼ 147 bins to resolve the evolution from 0.1 µm-sized monomers to 1 m-sized boulders (Ohtsuki et al., 1990; Stammler & Birnstiel, 2022). Furthermore, the commonly used algorithms have time complexity scaling as $O(N_m^2)$, which means an increase in grid size or resolution comes with large additional computation time.

Nonetheless, `DustPy` allows for accurate studies of dust evolution in axisymmetric, vertically-integrated disk models. The code is easily modifiable and allows for the inclusion of new source terms and protoplanetary disk processes. Two-dimensional or three-dimensional phenomena, like turbulence, can however not be investigated with this method.

In recent years, effords have been made to develop faster alternative methods to allow for the inclusion of dust coagulation in large-scale hydrodynamic simulations.

3.3 Monte-Carlo Radiative Transfer with RADMC-3D

Radiative transfer is an essential part of astrophysics. Many properties and processes of protoplanetary disks are driven or influenced by the interactions of matter and radiation, such as photoevaporation, the degree of ionization, the thermal relaxation times, and many more. However, solving the radiative transfer equation is not directly possible in most cases, which makes numerical methods indispensable for modeling the interaction of radiation and matter in protoplanetary disks. Even more importantly, astronomy and astrophysics, in general, rely on the observation of radiation coming from distant objects. The interactions of radiation with dust particles and gas molecules determine the properties of the radiation emitted or scattered off, e.g., protoplanetary disks. Especially the advances in radio interferometry have made highly-resolved observations of protoplanetary disks possible. These images offer new benchmarks for numerical models that can now be compared to real data in unprecedented detail.

Multiple scattering and the related angular dependency of the radiation field are the main issue when solving the radiative transfer equation. Monte Carlo methods offer an alternative to the solution of the discretized radiative transfer equation (see Noebauer & Sim, 2019, for a comprehensive overview). The interactions of a photon with matter are treated stochastically. Each interaction is randomly sampled from a corresponding probability distribution that reflects the underlying physics. Random numbers have to

be drawn to determine whether scattering, absorption or emission occur. Similar to the dust coagulation problem, we are confronted with a huge number of particles, in this case photons, to simulate. Large numbers of photons are thus assembled into representative *photon packages*. A large enough ensemble of photon packages is then necessary to reach a good statistical sample for the path of the radiation. The simplicity of the Monte Carlo procedure thus comes at high computational cost. These computations however scale extremely well because the photon packages are independent of each other.

In the coming chapter, we will use the publicly available Monte Carlo radiative transfer code `RADMC-3D` (Dullemond et al., 2012)[2] to derive radiation intensities from protoplanetary disk models. The code is based on the method by Bjorkman & Wood (2001). It allows for the input of custom opacity models and simulation data defined on cartesian, cylindrical, or spherical grids. Given a spatial distribution of dust and/or gas, `RADMC-3D` can be used to calculate the local temperatures based on stellar irradiation and other customizable heat sources. Once the temperature structure of the models is calculated (or pre-defined by the user), `RADMC-3D` can calculate the radiation intensities seen by an observer at arbitrary orientation relative to the data. These calculations can produce multi-wavelength, two-dimensional images of the simulation or entire spectra. The images or spectra can be further processed by the user and compared to actual observations to test the validity of theoretical models.

[2] `https://www.ita.uni-heidelberg.de/~dullemond/software/radmc-3d/index.php`

ABOUT THE STRUCTURE OF THIS THESIS

The question of how the evolution of the dust influences the evolution of hydrodynamic turbulence is the main topic of the first half of this thesis. Through collisional cooling, dust particles greatly contribute to the thermal balance of the gas and thus enable flow instabilities in protoplanetary disks that are not unlike atmospheric phenomena on Earth. The first study presented in this thesis, Chapter 4, deals with the implications of the dust evolution process on the VSI. We present a model that uses results of dust coagulation simulations of protoplanetary disks to predict the cooling rates and thus the initial conditions for hydrodynamic simulations that result in disks with varying VSI activity depending on the parameters of the dust coagulation model. Although these models give insights into the impact of dust coagulation on the VSI, they can not account for the underlying cooling times as a result of the moving dust fluids. The advection of gas and dust and the growth of the particles would continuously alter the cooling times. In Chapter 5, we present a new approach to the cooling time calculation that makes it possible to dynamically evolve them throughout a hydrodynamic simulation, taking into account the evolving dust densities.

One of the biggest computational hurdles, however, remains in these studies: modeling the dust coagulation process itself. Starting from microscopic scales, dust particles grow up to centimeter sizes, where they reach an equilibrium of coagulation and fragmentation. Classical numerical approaches to solve the underlying evolution equations are computationally costly and are thus infeasible for large-scale studies of protoplanetary disks. As a possible solution to this problem, we have developed two new, simplified approaches to model dust evolution in hydrodynamic simulations of protoplanetary disks, which are presented in the second half of this thesis. In Chapter 6, we present a semi-analytic approach to dust coagulation, called `TriPoD`. With this method, we are now able to co-evolve the gas and dust size distribution in a vertically integrated disk model, taking into account the coagulation and fragmentation process. An alternative methodology is laid out in Chapter 7. Modern machine learning techniques are used to solve a simplified version of dust coagulation accurately and efficiently in the `TriPoD-ML` model. I give a summary and an outlook to future projects in Chapter 8.

CHAPTER 4

DUST COAGULATION RECONCILES PROTOPLANETARY DISK OBSERVATIONS WITH THE VERTICAL SHEAR INSTABILITY

DUST COAGULATION AND THE VSI DEAD ZONE

Thomas Pfeil, Til Birnstiel, and Hubert Klahr

the following chapter was published in
The Astrophysical Journal, 959, 121, 2023

Abstract: Protoplanetary disks exhibit a vertical gradient in angular momentum, rendering them susceptible to the Vertical Shear Instability (VSI). The most important condition for the onset of this mechanism is a short timescale of thermal relaxation ($\lesssim 0.1$ orbital timescales). Simulations of fully VSI-active disks are characterized by turbulent, vertically extended dust layers. This is in contradiction with recent observations of the outer regions of some protoplanetary disks, which appear highly settled. In this work, we demonstrate that the process of dust coagulation can diminish the cooling rate of the gas in the outer disk and extinct the VSI activity. Our findings indicate that the turbulence strength is especially susceptible to variations in the fragmentation velocity of the grains. A small fragmentation velocity of $\approx 100\,\mathrm{cm\,s^{-1}}$ results in a fully turbulent simulation, whereas a value of $\approx 400\,\mathrm{cm\,s^{-1}}$ results in a laminar outer disk, being consistent with observations. We show that VSI turbulence remains relatively unaffected by variations in the maximum particle size in the inner disk regions. However, we find that dust coagulation can significantly suppress the occurrence of VSI turbulence at larger distances from the central star.

Author Contributions:

Thomas Pfeil:	numerical simulations, data analysis, figure plotting, manuscript writing
Prof. Til Birnstiel:	scientific discussion, proof reading, project supervision
Prof. Hubert Klahr:	scientific discussion, proof reading, project supervision

4.1 Introduction

Around 1 % of the mass of protoplanetary disks is initially composed of solids (Lodders, 2003; Magg et al., 2022). Despite its small contribution to the overall mass budget, this dust is the building material for planetesimals and planets and an essential observable for infrared and radio observations. It can have a considerable influence on the gas dynamics within the disk via drag forces (Weidenschilling, 1980; Youdin & Goodman, 2005) and is the main source of opacity. Therefore, cooling and heating are mostly determined by the solids for the bulk of the disk (Semenov et al., 2003; Woitke, 2015; Malygin et al., 2017). Many linear instabilities of the gas flow depend on the local rate of thermal relaxation (Klahr & Bodenheimer, 2003; Petersen et al., 2007a,b; Klahr & Hubbard, 2014; Lin & Youdin, 2015; Marcus et al., 2015; Lyra & Umurhan, 2019) or the ionization state of the gas (Balbus & Hawley, 1991; Blaes & Balbus, 1994), and are therefore sensitive to the assumed dust size distribution (Barranco et al., 2018; Fukuhara et al., 2021; Kawasaki & Machida, 2023).

In this work, we are specifically interested in the evolution of the vertical shear instability (VSI, Urpin & Brandenburg, 1998), which requires a short thermal relaxation time of the gas (Lin & Youdin, 2015; Manger et al., 2021; Fukuhara et al., 2021). VSI was studied in much detail in isothermal and adiabatic disk models at various rates of β cooling (e.g., Nelson et al., 2013) and in models with radiative transfer (e.g., Stoll & Kley, 2016; Stoll et al., 2017; Flores-Rivera et al., 2020). Due to the numerical obstacles of incorporating dust evolution models in hydrodynamic simulations (Drążkowska et al., 2014; Gonzalez et al., 2017; Drążkowska et al., 2019; Lombart et al., 2022), most previous studies consider a static dust population, perfectly coupled to the gas. These studies often aim for a detailed analysis of the instability mechanism itself (e.g., Nelson et al., 2013; Manger et al., 2021; Svanberg et al., 2022). They showed the VSI's ability to cause large-scale vortex formation (Richard et al., 2016; Manger & Klahr, 2018; Pfeil & Klahr, 2021) and strong corrugations in the dust layer (Stoll & Kley, 2016; Flores-Rivera et al., 2020). Simulations assuming perfectly coupled dust or isothermal conditions cannot, however, model the conditions in real protoplanetary disks, for which observations show an evolved dust population (Pérez et al., 2012; Tazzari et al., 2016; Huang et al., 2018; Ohashi & Kataoka, 2019; Sierra et al., 2021), substructures (ALMA-Partnership et al., 2015; Andrews et al., 2018; Dong et al., 2018), and planets (Keppler et al., 2018). In this work, we intend to go one step further by considering an evolved—yet static—dust population in two-dimensional simulations of smooth protoplanetary disks.

Our work is motivated by the results of Dullemond et al. (2022), which show that VSI turbulence in an isothermal disk model is not consistent with observations of thin dust layers in protoplanetary disks. In Pfeil & Klahr (2021), we have explored the impact of a more realistic cooling time prescription on the strength of VSI turbulence. For this, we assumed the presence of a static, µm-sized dust population in the inner parts of a protoplanetary disk (at $\sim 5\,\mathrm{au}$). For these setups, we found that the collisional decoupling of the gas and dust particles inhibits thermal relaxation in the disk atmosphere and thus reduces VSI turbulence. The respective collisional coupling time scale depends on the size distribution and is, thus, sensitive to the fragmentation velocity and other dust properties. Fukuhara et al. (2021) further studied this effect in models with a more detailed prescription of the dust size distribution. They found that coagulation can indeed inhibit the VSI by

depleting the number of small grains that provide radiative cooling. In their most recent study, Fukuhara et al. (2023) attempted to simulate this in a more self-consistent way, by taking into account the effect of the VSI on the diffusivity and the cooling times. Since they could not afford to dynamically evolve the dust population within their hydrodynamic simulations, they relied on analytic prescriptions for the cooling time for a static dust size distribution.

In this work, we study the effect of a more realistic steady-state dust distribution for varying coagulation parameters using `DustPy` (Stammler & Birnstiel, 2022) and `PLUTO` (Mignone et al., 2007). We deduce thermal relaxation times from dust coagulation models in Section 4.3 which are then implemented in hydrodynamic simulations, from which we study the VSI activity in Section 4.4. This makes it possible to study the influence of dust coagulation and the coagulation parameters on VSI turbulence. These steps are schematically displayed in Figure 4.1. In the next step, we introduce passive dust fluids to our simulations in Section 4.4 to study the effect of the emerging VSI turbulence on the thickness of the dust layer. To make our results comparable to observations, we create synthetic intensity maps with `RADMC-3D` (Dullemond et al., 2012) in Section 4.5.

4.2 Theory

Cooling Requirements for the Vertical Shear Instability

Vertical shear, in the geophysical context also known as thermal wind (Holton & Hakim, 2012), is a consequence of the radial temperature gradient in the vertically stratified protoplanetary disks. The temperature gradient itself is maintained by stellar irradiation. Consequently, fluid parcels can be displaced upward into a region of lower specific kinetic energy and thus experience an outward acceleration. A perturbation along such a trajectory violates Rayleigh's stability criterion and leads to a continued acceleration of the fluid parcel. This mechanism is called the Vertical Shear Instability (Urpin & Brandenburg, 1998) and results in vertically elongated and radially narrow flow patterns. However, as the gas parcels enter the lower-density regions of the disk atmosphere, they are subjected to buoyancy forces, which, in a stably stratified atmosphere, would lead to an oscillation around their equilibrium position. The characteristic frequency of this oscillation is the Brunt-Väisälä frequency

$$N_z^2 = -\frac{1}{\rho_\mathrm{g} C_P} \frac{\partial P}{\partial z} \frac{\partial S}{\partial z} \,, \tag{4.1}$$

where z is the distance from the disk midplane, ρ_g is the gas density, P is the pressure S is the gas entropy, and C_P is the gas' specific heat capacity at constant pressure. Thermal relaxation counteracts the restoring force of this oscillation by adjusting a gas parcel's specific entropy to the background. In order for the vertical shear to overcome buoyancy and trigger the VSI, thermal relaxation must be fast. Lin & Youdin (2015) have shown that vertically global VSI grows the fastest if the cooling timescale fulfills

$$t_\mathrm{c} < \frac{H_\mathrm{g}}{R} \frac{|\beta_T|}{\gamma - 1} \Omega_\mathrm{K}^{-1} \,, \tag{4.2}$$

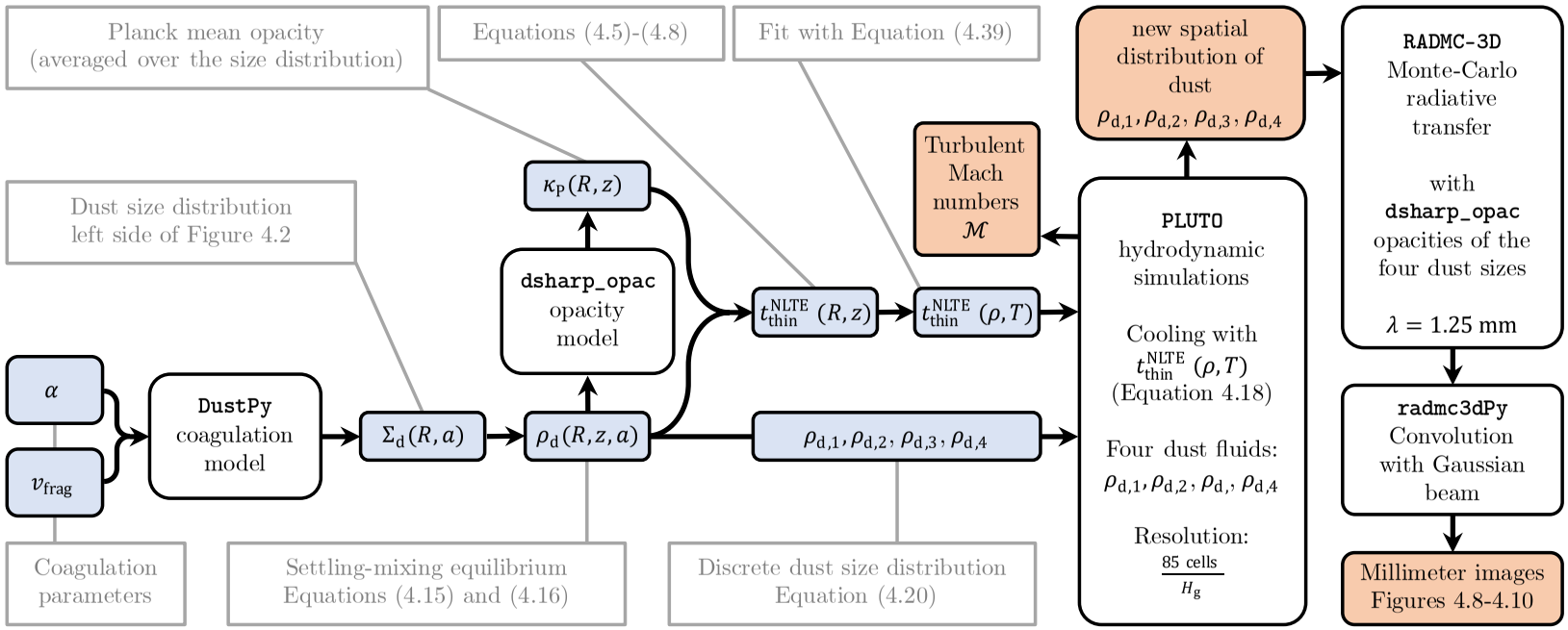

Figure 4.1
Workflow from our dust coagulation models with `DustPy` to the hydrodynamic simulations with `PLUTO` to the radiative transfer modeling with `RADMC-3D`. Used methods and tools are shown as white boxes. Input parameters and intermediate results are shown in light blue. The results of our work are schematically displayed as orange boxes. The details of our methodology are laid out in Section 4.3 (`DustPy` and cooling times), Section 4.4 (`PLUTO` simulations and results), and Section 4.5 (radiative transfer and synthetic observations with `RADMC-3D`).

where R is the distance to the central star, β_T is the power-law exponent of the temperature profile, H_g is the pressure scale height, Ω_K is the local Keplerian frequency, and $\gamma = c_P/c_V$ is the gas' heat capacity ratio. Equation 4.2 was derived under the assumption of a vertically constant thermal relaxation time. As we specifically consider the height dependence of thermal relaxation, we will use the local definition of a critical cooling time (Urpin, 2003; Klahr et al., 2023) for local VSI modes

$$t_c \lesssim \frac{|r\partial_z\Omega|}{N_z^2} \approx \frac{H_g}{R}\frac{|\beta_T|\gamma}{2(\gamma-1)}\left(\frac{z}{H_g}\right)^{-1}\Omega_K^{-1}\,. \tag{4.3}$$

In fact, numerical studies like Manger et al. (2021) investigated the dependency of the VSI turbulence on a vertically constant thermal relaxation time and found VSI not to develop for cooling times beyond the critical value for global modes. This may be due to numerical resolution, as Lin & Youdin (2015) show that VSI exists for all cooling times, yet at reduced efficiency. Urpin (2003) derived growth rates in this regime, which show a decay proportional to t_c^{-1}. This behavior was recently confirmed in high-resolution[1] studies of the VSI and other thermal instabilities in disks by Klahr et al. (2023). It is still subject to investigation how longer growth times will translate into turbulence levels for the non-linear regime, especially in terms of angular momentum transport, diffusion, and gas rms velocities. The saturation behavior of VSI and other thermal baroclinic instabilities especially for longer cooling times at sufficient resolution is still being investigated (Latter & Papaloizou, 2018; Cui & Latter, 2022; Klahr et al., 2023).

Optically Thin Thermal Relaxation

Thermal relaxation of the gas in a protoplanetary disk is mostly achieved via thermal coupling with the dust in a two-stage process. At low temperatures, the emission timescale of the gas molecules is long, which means that cooling is only possible via thermal accommodation with the strongly emitting dust particles through collisions. Barranco et al. (2018), derived the thermal relaxation times for the non-LTE case between dust grains and the gas based on the calculation of cooling rates (see Section 4.A for a recap of the derivations). For a given dust size distribution $n(a)$, the Sauter mean radius is an instructive parameter in this context, defined as (Sauter, 1926)

$$a_S = \frac{\int n(a)a^3\,\mathrm{d}a}{\int n(a)a^2\,\mathrm{d}a}\,, \tag{4.4}$$

where the size integral is executed over the entire size distribution. Corresponding to the Sauter mean, we define a respective number density $n_S = \rho_d/\left(\frac{4}{3}\pi\rho_m a_S^3\right)$ and a collisional cross-section $\sigma_S = \pi a_S^2$, where $\rho_m = 1.67\,\mathrm{g\,cm^{-3}}$ is the interior density of the dust grains. With these definitions, we write the thermal accommodation timescale for the gas molecules

[1] `PLUTO-4.2` simulation with 256 cells per gas scale height, WENO reconstruction, and RK3 time integration (Klahr et al., 2023).

and the dust grains (Probstein, 1969; Burke & Hollenbach, 1983) as

$$t_{\mathrm{g}}^{\mathrm{coll}} = \frac{\gamma}{\gamma - 1} \frac{1}{n_{\mathrm{S}} \sigma_{\mathrm{S}} \bar{v}_{\mathrm{g}}} , \tag{4.5}$$

where $\bar{v}_{\mathrm{g}} = c_{\mathrm{s}} \sqrt{8/\pi}$ is the average gas molecule velocity of a Maxwell-Boltzmann distribution with the isothermal speed of sound c_{s}. Similarly, a timescale for the thermal relaxation of the dust component can be derived, which reads

$$t_{\mathrm{d}}^{\mathrm{coll}} = \left(\frac{\rho_{\mathrm{d}}}{\rho_{\mathrm{g}}} \right) \left(\frac{C_{\mathrm{d}}}{\mathrm{C_P}} \right) t_{\mathrm{g}}^{\mathrm{coll}} , \tag{4.6}$$

with the dust-to-gas density ratio $\rho_{\mathrm{d}}/\rho_{\mathrm{g}} = \varepsilon$ and the specific heat capacity of the dust particles C_{d}. As a typical value we pick $C_{\mathrm{d}} = 800\,\mathrm{J\,kg^{-1}\,K^{-1}}$, as used by Barranco et al. (2018) (see Wasson, 1974; Piqueux et al., 2021; Biele et al., 2022). If the collisional coupling is efficient, i.e., temperature perturbations in the gas are transferred to the dust, the thermal equilibrium of the grains will be restored by the emission of radiation. This happens on the black body timescale, depending on the dust density distribution $\rho_{\mathrm{d}}(a)$ in units of $[\mathrm{g/cm^4}]$ and the respective Planck mean opacity distribution $\kappa_{\mathrm{P}}(a, T)$, in units of $[\mathrm{cm^2/g}]$

$$t_{\mathrm{d}}^{\mathrm{rad}} = \frac{\rho_{\mathrm{d}} C_{\mathrm{d}}}{16\,\sigma_{\mathrm{SB}}\,T_{\mathrm{eq}}^3} \left(\int \rho_{\mathrm{d}}(a) \kappa_{\mathrm{P}}(a, T_{\mathrm{eq}})\,\mathrm{d}a \right)^{-1} , \tag{4.7}$$

with the Stefan-Boltzmann constant σ_{SB}. The total thermal relaxation time of the dust gas mixture can then be calculated following Equation (19) from Barranco et al. (2018)

$$t_{\mathrm{thin}}^{\mathrm{NLTE}} = 2 t_{||} \left[1 - \sqrt{1 - \frac{4 t_{||}^2}{t_{\mathrm{g}}^{\mathrm{coll}} t_{\mathrm{d}}^{\mathrm{rad}}}} \right]^{-1} \tag{4.8}$$

with $1/t_{||} = 1/t_{\mathrm{d}}^{\mathrm{rad}} + 1/t_{\mathrm{d}}^{\mathrm{coll}} + 1/t_{\mathrm{g}}^{\mathrm{coll}}$. In practice, this means the slowest channel of energy transfer acts as a bottleneck and the longest timescale of thermal relaxation determines the cooling time scale of the gas. If the dust's emissivity is low, energy cannot be emitted effectively by the grains, and temperature perturbations cannot decay, no matter how well the grains and molecules are coupled ($t_{\mathrm{thin}}^{\mathrm{NLTE}} \approx t_{\mathrm{d}}^{\mathrm{rad}}$). This situation is unlikely to occur in protoplanetary disks because of the large dust opacities. Another case is the collisional decoupling of dust grains and gas molecules. At low densities and in regions where small grains are depleted, heat cannot be transferred between the main carriers of thermal energy (the gas molecules) and the emitters (the dust grains). The high emissivity of the grains does not matter in such a case, since temperature perturbations stay locked in the poorly emitting gas ($t_{\mathrm{thin}}^{\mathrm{NLTE}} \approx t_{\mathrm{g}}^{\mathrm{coll}}$).

Muley et al. (2023) introduced a three-temperature radiation transport scheme, which treats dust and gas temperatures separately, yet coupled via collisions. They also find that in most cases the collisional time scale is the most relevant to determine thermal relaxation.

In this case, the cooling time is proportional to the square root of the maximum particle size. This can be shown by assuming the size distribution to be a truncated power law

with maximum particle size $a_{\max}$, minimum size $a_{\min}$, and power-law exponent $p = -3.5$. Then $a_s = \sqrt{a_{\max} a_{\min}}$ and thus $t_g^{\text{coll}} \propto (n_S \sigma_S)^{-1} \propto \sqrt{a_{\max}}$. Sticking collisions between grains typically increase the maximum particle size until a fragmentation-coagulation equilibrium is reached. In this case, $a_{\max} \approx a_{\text{frac}} \propto v_{\text{frag}}^2$ holds (Birnstiel et al., 2012), and we deduce that the collisional timescale is directly proportional to the fragmentation velocity in this case. Laboratory experiments aim to determine the actual value of v_{frag} which is dependent on the composition and porosity of grains (Blum, 2000; Wurm et al., 2001; Blum et al., 2006; Musiolik & Wurm, 2019). Typical values lie within a range of 100–1000 $\text{cm}\,\text{s}^{-1}$.

An additional uncertainty arises from the unknown relative grain velocities, which depend on the strength of turbulence, differential drift, and settling. Especially the strength of turbulence in protoplanetary disks is highly uncertain and also a subject of this article. The simplest assumption for the turbulent transfer of energy across length scales is the Kolmogorov cascade. For the resulting energy spectrum, relative grain velocities can be approximated as $\Delta v \approx \sqrt{3\alpha \text{St}} c_s$ (Ormel & Cuzzi, 2007), with the Stokes number St (see Equation 4.14). This is the underlying assumption for the derivation of a_{frag}. In this turbulence prescription, which is Based on the assumption of a mixing length model (Prandtl, 1925), turbulent stresses result in an effective viscosity

$$\nu_T = \alpha c_s H_g \,, \tag{4.9}$$

where c_s is the local sound speed (Shakura & Sunyaev, 1973). From this, turbulent rms velocities can be related to α by assuming a turbulent correlation time of Ω_K^{-1} via

$$\alpha = \frac{\langle v_{\text{turb}}^2 \rangle}{c_s^2} \,. \tag{4.10}$$

With this, $a_{\text{frag}} \propto \alpha^{-1}$, implying $t_g^{\text{coll}} \propto \alpha^{-1/2}$. Low α therefore corresponds to longer cooling times, as a consequence of the presence of larger particles. Additionally, lower levels of turbulence correspond to smaller dust scale heights, leading to a depletion of the upper layers and an additional dampening of the VSI in these regions.

Fukuhara et al. (2021) investigated the effect of varying maximum particle sizes throughout a protoplanetary disk and found that the presence of VSI depends on particle sizes via the cooling time dependency.

In the following sections, we investigate this effect through the use of more realistic dust coagulation models and subsequent hydrodynamic simulations. We aim to determine the implications for the interpretation of observational data and the respective feedback onto the dust layer by turbulent mixing through the VSI.

4.3 `DustPy` Coagulation Models

In the previous sections, we discussed the importance of thermal relaxation for the VSI. We have also highlighted that the cooling times are highly sensitive to the present dust population, most importantly, the maximum particle size.

In this section, we present a series of dust coagulation simulations, conducted with `DustPy`, that further illustrate the impact of dust coagulation on the cooling times. We

use the output of these simulations to calculate cooling time distributions for our subsequent hydrodynamic simulations with the PLUTO code.

For our disk model we employ the standard Lynden-Bell & Pringle (1974) profile for a solar-mass star and a $0.05\,M_\odot$ disk with dust-to-gas ratio (metallicity) $\mathcal{Z} = 0.01$ (see Table 4.1)

$$\Sigma_g = \frac{M_d(1+\beta_\Sigma)}{2\pi R_c^2}\left(\frac{R}{R_c}\right)^{\beta_\Sigma}\exp\left[-\left(\frac{R}{R_c}\right)^{2+\beta_\Sigma}\right]. \tag{4.11}$$

We set the radial column density gradient to $\beta_\Sigma = -0.85$, and the characteristic radius to $R_c = 100\,\mathrm{au}$. Our radial temperature profile is determined by passive stellar irradiation and assumed to be constant in the vertical direction (see Chiang & Goldreich, 1997; D'Alessio et al., 1998; Dullemond et al., 2018)

$$T = \left(\frac{\varphi L_*}{4\pi R^2 \sigma_{SB}}\right)^{1/4}, \tag{4.12}$$

where L_* is stellar luminosity, and $\varphi = 0.02$ is the flaring angle. Gas evolution and dust drift alter the dust size distribution in protoplanetary disks. The overall effect of these transport phenomena on the shape of the distribution is, however, most relevant in the final stages of disk evolution, when the growth front has reached the outer disk edge and the mass budget is quickly decreasing (i.e., when the dust accretion rate is no longer radially constant, Birnstiel & Andrews, 2014). At what point in time after disk formation this becomes relevant is dependent on the disk's size, its radial structure, the dust-to-gas ratio, the strength of turbulence, the fragmentation velocity, etc. In this study, we are interested in the effect of dust coagulation on the cooling times and, through the cooling times, on the VSI. In the inner parts of the disk, a steady-state distribution, determined by fragmentation and coagulation, will be reached and approximately maintained as long as the outer disk edge is not yet moving inward. We have therefore decided to completely disregard any transport effects (except the vertical settling-mixing equilibrium). We are thus calculating a steady-state dust distribution for each parameter set that is only determined by fragmentation and coagulation. The output of our models is, therefore, time-independent once the equilibrium size distribution is reached at each radius. In that way, we avoid selecting an arbitrary simulation snapshot.

Note that this is still an idealized assumption. In reality, radial drift and gas evolution could slightly alter the radial structure and the size distributions at similar timescales. Typically, drift-limited size distributions are slightly steeper than in the fragmentation limit (Birnstiel et al., 2011). In recent studies, the VSI itself was also shown to alter the radial disk structure (Manger et al., 2021). Our DustPy models are run for $10^5\,\mathrm{yr}$, after which coagulation-fragmentation equilibrium is reached at every radial grid cell.

We conduct simulations for three different fragmentation velocities $v_{frag} = 100$, 200, and $400\,\mathrm{cm\,s^{-1}}$ and for a turbulence parameter $\alpha = 10^{-3}$. Additionally we probe two different turbulent diffusivities with $\alpha = 10^{-4}$ and 10^{-2}, at $v_{frag} = 100\,\mathrm{cm\,s^{-1}}$. At this point we do not further specify the origin of the diffusivity α, making it a free parameter for the coagulation models. We show the resulting dust size distribution at 50 au and 100 au on the left-hand side of Figure 4.2 and some key particle properties are shown in Table 4.1.

We can see that the particles grow to larger sizes at smaller distances to the central star, in accordance with analytic estimates of the fragmentation-limited particle size (Birnstiel et al., 2012). The respective size distributions can be approximated with power laws with exponents $-p \approx 3.6$–3.7. These values lie within the typical range for fragmentation-limited size distributions derived by Birnstiel et al. (2011).

Thermal Relaxation Times Derived from Dust Coagulation Simulations

We derive the vertical structure from these, vertically integrated, `DustPy` models by assuming vertical hydrostatic equilibrium for the gas and vertical settling-mixing equilibrium for the dust. Gas densities thus follow as

$$\rho_\mathrm{g} = \rho_\mathrm{g,mid} \exp\left[\left(\frac{H_\mathrm{g}}{R}\right)^{-2}\left(\frac{R}{\sqrt{R^2+z^2}}-1\right)\right], \tag{4.13}$$

with the midplane gas density $\rho_\mathrm{g,mid} = \Sigma_\mathrm{g}(R)/\sqrt{2\pi H_\mathrm{g}^2}$. We assume an ideal equation of state $P = \rho_\mathrm{g} c_\mathrm{s}^2$. The vertical dust distribution is determined by the diffusion parameter δ and the Stokes number of the individual size bins on the size distribution, which is defined as

$$\mathrm{St} = \frac{\pi}{2}\frac{a\rho_\mathrm{m}}{\Sigma_\mathrm{g}}\,. \tag{4.14}$$

Volume dust densities for each size are then derived by calculating the dust scale height

$$H_\mathrm{d} = H_\mathrm{g}\sqrt{\frac{\delta}{\delta+\mathrm{St}}} \tag{4.15}$$

$$\rho_\mathrm{d} = \rho_\mathrm{d,mid} \exp\left[\left(\frac{H_\mathrm{d}}{R}\right)^{-2}\left(\frac{R}{\sqrt{R^2+z^2}}-1\right)\right], \tag{4.16}$$

with $\rho_\mathrm{d,mid} = \Sigma_\mathrm{d}(R)/\sqrt{2\pi H_\mathrm{d}^2}$.

The resulting temperature and density structure is used to calculate the Planck mean opacities of the dust. We use the DSHARP opacity model by Birnstiel et al. (2018) as implemented in the `dsharp_opac` python package with the standard DSHARP particle properties. Thermal relaxation times of the gas can then be calculated from the disk structure and opacities via Equations 4.5 to 4.8. For the given parameters in our simulations, we find that the thermal relaxation time is limited by the collision timescale outside of $\sim 10\,\mathrm{au}$. At smaller radii, the disk might become optically thick, meaning the relaxation time of temperature perturbations depends on the respective length scale. We are therefore only modeling the parts of the disk around 50 au, where thermal relaxation operates in the optically thin regime. Figure 4.2 shows the size distributions and the vertical profile of the thermal relaxation times for the respective coagulation and turbulence parameters at 50 au and 100 au. We find that the cooling times increase with height above the midplane. The reason for this is that cooling is achieved via collisions between dust particles and gas molecules, which become rarer at lower densities. This also means that models with larger particles have longer thermal relaxation times because of the reduced number densities of dust particles and the stronger settling. Higher fragmentation velocities are counteracting

Table 4.1: Dust coagulation parameters of our five DustPy simulations and the respective maximum particle size measured at 50 au in the DustPy simulation.

M_*	R_*	T_*	$M_{\mathrm{disk,g}}$	$\mathcal{Z}$	v_{fr}	α_{turb}	ρ_{m}	a_{min}	a_{max} (50 au)	$\mathrm{St}_{\mathrm{max}}$ (50 au)	a_{s} (50 au)	St_{s} (50 au)
$[M_\odot]$	$[R_\odot]$	[K]	$[M_*]$		$[\mathrm{cm\,s^{-1}}]$		$[\mathrm{g\,cm^{-3}}]$	[cm]	[cm]		[cm]	
1	2	5772	0.05	0.01	100	10^{-3}	1.67	10^{-5}	1.1×10^{-2}	2.5×10^{-3}	2.0×10^{-4}	4.6×10^{-5}
"	"	"	"	"	200	10^{-3}	"	"	4.0×10^{-2}	9.3×10^{-3}	4.3×10^{-4}	1.0×10^{-4}
"	"	"	"	"	400	10^{-3}	"	"	1.5×10^{-1}	3.4×10^{-2}	1.3×10^{-3}	2.9×10^{-4}
"	"	"	"	"	100	10^{-4}	"	"	6.3×10^{-2}	1.5×10^{-2}	9.7×10^{-4}	2.3×10^{-4}
"	"	"	"	"	100	10^{-2}	"	"	1.6×10^{-3}	3.7×10^{-4}	8.5×10^{-5}	2.0×10^{-5}

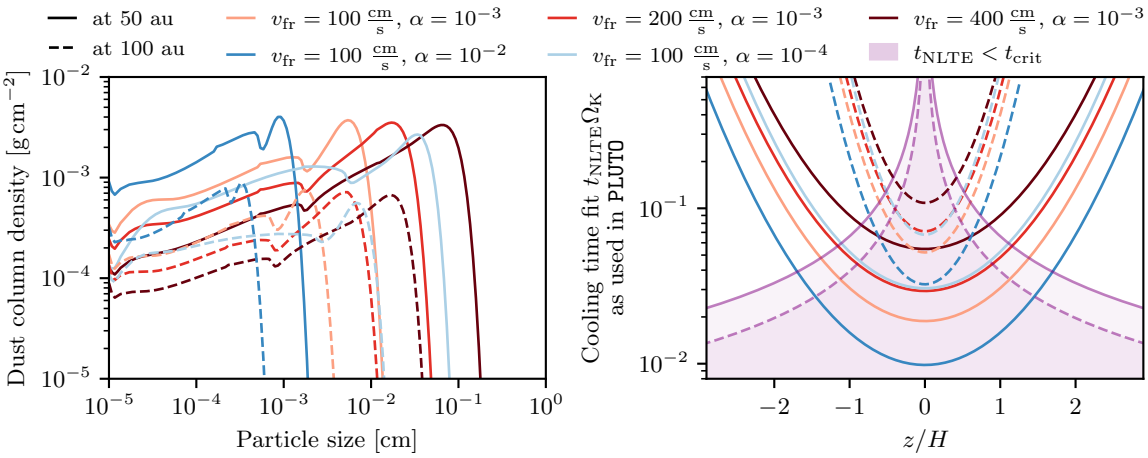

Figure 4.2
Dust size distributions at 50 au (solid lines) and 100 au (dashed lines) of our DustPy models (left side). On the right-hand side, we show the respective vertical cooling time profiles, assuming vertical settling-mixing equilibrium for the given α and the critical VSI cooling time. Models with larger particles also exhibit longer cooling times due to collisional decoupling between dust and gas. We also show the height-dependent cooling time for local VSI modes as purple lines (see Equation 4.3).

the VSI. Likewise, models with weaker turbulence parameter α can also be expected to have less VSI activity, as demonstrated by our numerical simulations.

4.4 PLUTO Simulations based on Coagulation Models

We set up axisymmetric PLUTO simulations with the same radial structure as our DustPy models to study the evolution of VSI with the respective model's cooling times. Pressure forces act in the outward direction of the disk and therefore decrease the equilibrium rotation frequency of the gas, especially at the steep outer edge of the disk. We define our hydrostatic initial rotation profile accordingly as

$$\frac{\Omega^2(R,z)}{\Omega_{\mathrm{K}}^2} = \left(\frac{H_{\mathrm{g}}}{R}\right)^2 \left(\beta_T + \beta_\rho - (\beta_\Sigma + 2)\left(\frac{R}{R_{\mathrm{c}}}\right)^{\beta_\Sigma+2}\right) - \frac{\beta_T R}{\sqrt{R^2+z^2}} + \beta_T + 1\,, \tag{4.17}$$

where β_ρ is the power-law exponent of the midplane gas density $\rho_{\mathrm{mid}} \propto R^{\beta_\rho}$ and β_T is the power-law exponent of the radial temperature profile $T \propto R^{\beta_T}$. Thermal relaxation is realized as in Pfeil & Klahr (2021), by analytically relaxing the gas pressure toward the equilibrium profile (determined by stellar irradiation). Density is kept constant in this cooling step, which makes a relaxation in pressure equal to a relaxation in temperature for an ideal equation of state.

$$\begin{aligned} P^{(n+1)} &= P_{\mathrm{eq}} + (P^{(n)} - P_{\mathrm{eq}}) \exp\left(-\frac{\Delta t}{t_{\mathrm{thin}}^{\mathrm{NLTE}}}\right) \\ \overset{\rho}{\overset{\text{const.}}{\Longleftrightarrow}} T^{(n+1)} &= T_{\mathrm{eq}} + (T^{(n)} - T_{\mathrm{eq}}) \exp\left(-\frac{\Delta t}{t_{\mathrm{thin}}^{\mathrm{NLTE}}}\right), \end{aligned} \tag{4.18}$$

where (n) denotes the number of the current simulation timestep of length Δt. The equilibrium temperature T_{eq} is defined by stellar irradiation (Equation 4.12). Cooling times, presented in the previous section, are derived from `DustPy` simulations (see Figure 4.2) and subsequently fitted as a function of local gas density and temperature for each simulation (for a detailed description of the fits, see Section 4.B).

Fitting the spatial distributions of the thermal relaxation times as functions of density and temperature also introduces uncertainties in the cooling times for PLUTO. For all models except one, these errors lie within 25 % with respect to the real distribution of cooling times. For the case of the most settled particles ($v_{\mathrm{frag}} = 100\,\mathrm{cm\,s^{-1}}$, $\alpha = 10^{-4}$), however, the fitting function seems to diverge further from the real distribution and the fit deviates up to 58 % from the cooling times close to the midplane. This is likely due to the difference between this particular highly settled model and the other less settled cases. Since the cooling times vary over several orders of magnitude throughout the simulation domain and between the models, we deem this uncertainty acceptable—also because the overall distribution of cooling times is still well reproduced (this can be seen in the matching contours in Figure 4.12). It is worth noting, however, that in this work, we only study the overall trends of VSI turbulence with the coagulation parameters and do not aim to exactly reproduce specific systems or observations.

The resulting analytic cooling time prescriptions are used within our `PLUTO` simulations to calculate $t_{\mathrm{thin}}^{\mathrm{NLTE}}$ from the local disk structure. Since cooling is dominated by the small grains, which predominantly move along with the gas, minor disturbances in the gas densities, as caused by the VSI, can also influence the cooling times in this model. We emphasize that this is a minor effect in our simulation, and does not have an impact on the resulting turbulence. It should be noted, that our cooling time prescription, which is derived from dust coagulation models, is static throughout the simulation.

Although our coagulation models assumed a certain turbulent diffusivity δ to calculate relative particle velocities, we set up our hydrodynamic simulations to be inviscid. This is because we want to study the onset of the VSI and the resulting turbulence strength. Applying the same diffusivities as for the coagulation models ($\delta = 10^{-4}$–10^{-2}) as viscosity in `PLUTO` would likely stop the VSI from emerging in the first place (Barker & Latter, 2015). Note that setting up viscous simulations would also not be fully self-consistent since relative particle velocities in `DustPy` are inferred from perfectly isotropic turbulence and

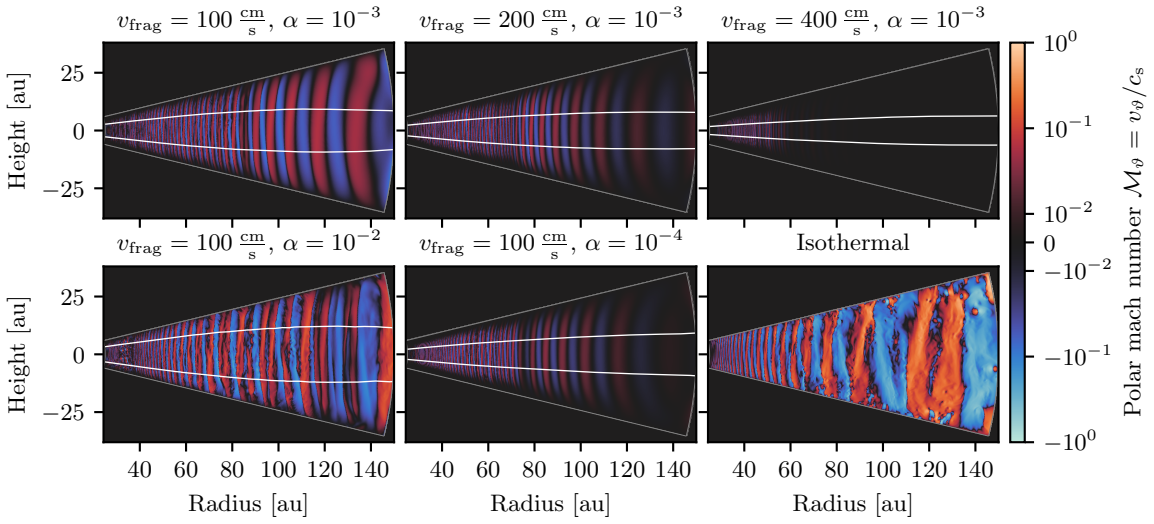

Figure 4.3
Vertical velocities in units of the local speed of sound in our six PLUTO runs after 500 orbital time scales at 50 au. The isothermal run shows a snapshot after only 200 orbits. White contours mark the position at which the critical cooling time for the VSI is reached (Equation 4.3), i.e., VSI is theoretically possible within the white lobes.

the resulting Kolmogorov cascade, which would not be the case for the developing VSI turbulence in our simulations.

We carry out the calculations for 500 orbital periods at 50 au (= 176 777 yr). Simulation domains are set up in spherical coordinates and extend from 25–150 au in the radial direction, and over ±3 pressure scale heights from the midplane of the disk in the polar direction. We resolve one scale height at 50 au with 85 cells and employ logarithmic griding in the radial direction to preserve the cells' aspect ratios, resulting in a $2011_r \times 513_\vartheta$ grid. Periodic boundary conditions are set up in the azimuthal direction with only one grid cell, making our simulations axisymmetric. Radial and polar boundaries are set up as reflective for the orthogonal velocity components and as zero-gradient for the respective tangential velocity components. Pressure and density in the boundary cells are kept at the initial condition.

In Figure 4.3, we show the vertical velocities in our simulations at the end of the simulation time. It is evident, that the spatially varying cooling times set constraints on where the VSI can be active and where vertical motions are suppressed by buoyancy. As a comparison, we also show an isothermal simulation (i.e., ideal VSI), in which the resulting turbulence is present in the entire simulation domain and at higher turbulent Mach numbers. For the case of $v_{\mathrm{fr}} = 400\,\mathrm{cm\,s^{-1}}$ and $\alpha = 10^{-3}$, we find the disk to be completely quiescent outside of ∼ 80 au, due to the long cooling times. In this case, dust would settle into a very thin layer in the outer disk, which we will further investigate in the next sections. Similarly, the disk regions outside of ∼ 100 au show only very little VSI activity for the coagulation model with $v_{\mathrm{fr}} = 100\,\mathrm{cm\,s^{-1}}$ and $\alpha = 10^{-4}$.

To characterize the development and strength of the VSI turbulence, we measure the Favre-averaged (i.e. density-weighted) turbulent Mach numbers over the whole simulation

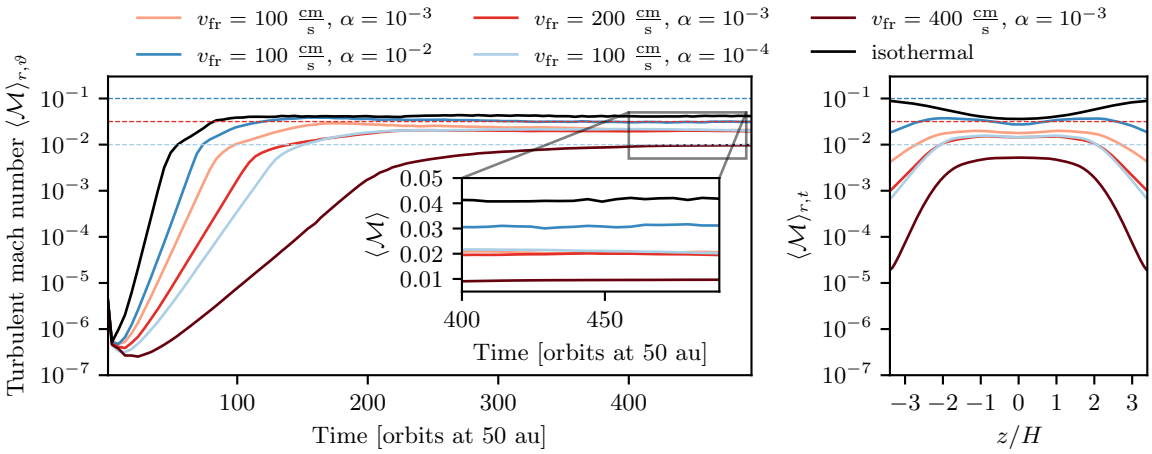

Figure 4.4
Time evolution of vertical shear instability simulations based on the different dust models. Turbulent Mach numbers are shown as a function of time (radially and vertically Favre-averaged) and as a function of height above the midplane (time-averaged and radially Favre-averaged). In models with larger particles, cooling times are generally longer, which results in lower growth rates and lower Mach number turbulence. The vertical profiles on the right-hand side change accordingly. Cooling times in models with larger maximum particle size increase more rapidly with height above the midplane, which also cuts off the VSI turbulence. Isothermal models typically have vertically increasing turbulent velocities. The three dashed horizontal lines show the Mach numbers corresponding to the three α values that we assumed for our coagulation models (see Equation 4.10). Note that the conversion between turbulent Mach numbers and diffusivities assumes a perfect Kolmogorov turbulence spectrum (see discussion in Section 4.6), which is likely not given for the anisotropic VSI turbulence.

domains, where the average in a direction x (polar, radial, or both) is defined as

$$\langle \mathcal{M} \rangle_x = \frac{\int \frac{\sqrt{v_r^2 + v_\vartheta^2}}{c_s} \rho \, \mathrm{d}x}{\int \rho \, \mathrm{d}x}, \tag{4.19}$$

where v_r and v_ϑ represent the radial and polar velocity components. Since our simulations are set up hydrostatically, these components measure turbulent fluctuations caused by the VSI. While velocities in our isothermal simulation saturate after $\sim$ 100 orbits at $\langle \mathcal{M} \rangle \approx 4 \times 10^{-2}$, all other, non-ideal simulations, reach lower Mach numbers and have longer growth time scales (see Figure 4.4). The vertical profile of the Mach numbers shows the typical vertical increase and a sharp upper cutoff, similar to the results in Pfeil & Klahr (2021). The collisional decoupling of dust particles and gas molecules is the reason for this behavior. Figure 4.4 also shows the three Mach numbers corresponding to the diffusivities chosen to calculate turbulent relative velocities between particles in our coagulation model (α= 10^{-4}, 10^{-3} and 10^{-2}). As can be seen, the three lines do not exactly correspond to the measured Mach numbers of our simulations. This is, however, also not to be expected, since the direct conversion between Mach numbers and particle collision speed (see Equation 4.10) assumes a perfect Kolmogorov spectrum and, thus, isotropic turbulence which is not given for the VSI. The calculation of collision speeds would furthermore depend on the correlation time spectrum which was not taken into account here.

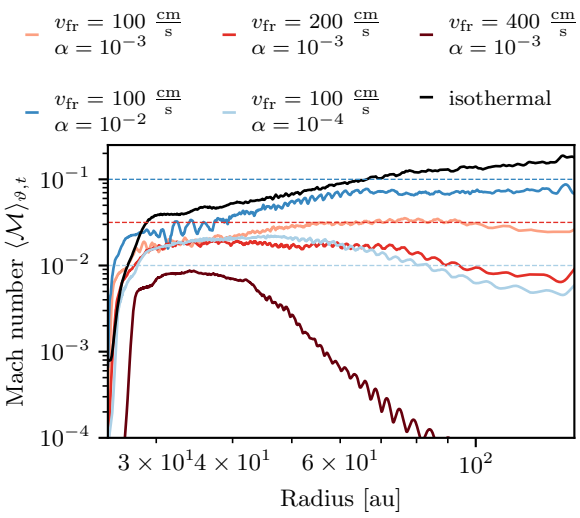

Figure 4.5
Radial dependency of the turbulent Mach numbers in a polar and time Favre average over 200 orbits in our VSI simulations. VSI simulations based on `DustPy` models with larger particles have lower levels of turbulence. For our model with the largest particles $v_{fr} = 400\,\mathrm{cm\,s^{-1}}$ and $\alpha = 10^{-3}$, the outer disk, beyond 80 au is completely quiescent. The three dashed horizontal lines show the Mach numbers corresponding to the three α values that we assumed for our coagulation models (see Equation 4.10). Note that such a conversion assumes a perfect Kolmogorov turbulence spectrum (see discussion in Section 4.6).

Figure 4.5 depicts the radial dependence of the Mach numbers in our simulations. The lowest turbulence levels of $\langle \mathcal{M} \rangle \approx 8 \times 10^{-3}$ are reached in our simulations based on the `DustPy` model with $\alpha = 10^{-3}$ and $v_{fr} = 400\,\mathrm{cm\,s^{-1}}$, i.e., in the model with the largest particles ($a_{max}(50\,\mathrm{au}) \approx 0.14\,\mathrm{cm}$). For this simulation, we observe a decrease in turbulence outside of 40 au. At 60 au, turbulent Mach numbers have already decreased by a factor 10 compared to the inner regions. Also our models with $v_{fr} = 200\,\mathrm{cm\,s^{-1}}$ and $\alpha = 10^{-3}$ and the model with $v_{fr} = 100\,\mathrm{cm\,s^{-1}}$ and $\alpha = 10^{-4}$ show a radially decreasing level of turbulence in the outer disk.

We conclude that the level of VSI turbulence is highly dependent on the physical details of the dust coagulation process. If dust grains can grow up to the fragmentation limit—which is to be expected in most parts of protoplanetary disks in the early evolutionary stages—we can expect weak collisional coupling between dust grains and gas molecules in the optically thin, outer regions, leading to inefficient cooling and only weak VSI turbulence. The magnitude of the impact of dust coagulation on the hydrodynamic turbulence depends mostly on the maximum size of the grains, where larger grains correspond to less cooling and, thus, stronger damping of VSI.

Dust Dynamics in the PLUTO Simulations

In the previous section, we have shown that the VSI activity in protoplanetary disks is highly sensitive to the properties of the present dust grain population, especially the largest grain size. However, we cannot directly infer the VSI's feedback on the dust population. Dullemond et al. (2022) have clearly shown that the ideal VSI is inconsistent with the observed thickness of protoplanetary disks in millimeter-wave observations with ALMA (Villenave et al., 2020, 2022). Our simulations show that the level of turbulent vertical velocities can vary by orders of magnitude across the disk, depending on the details of the dust size distribution.

In this section, we explore how these different levels of turbulence impact the thickness of the dust layer. For this, we restart the simulations after the VSI has reached a saturated

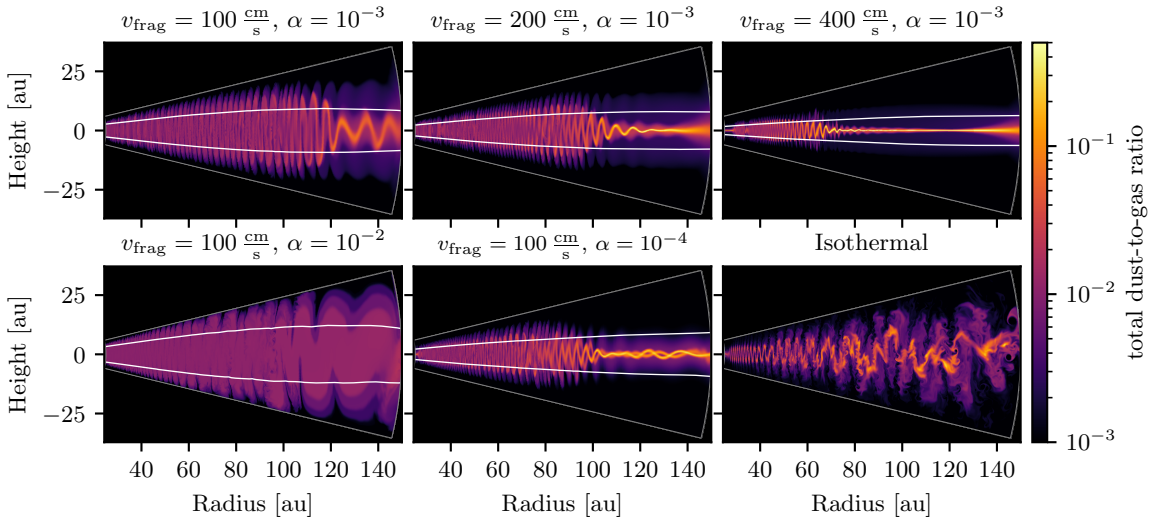

Figure 4.6
Total dust to gas ratios in VSI simulations restarted after 425 orbits with four passive dust fluids. Each simulation is started with a dust distribution similar to the one derived from the respective `DustPy` simulations. Snapshots are taken after 150 orbits of evolution. White contours mark the position at which the critical cooling time for the VSI is reached (Equation 4.3), i.e., VSI is theoretically possible within the white lobes.

level of turbulence. We add four dust fluids, resembling a power-law size distribution $n(a) \propto a^p$, and thus $\Sigma_{\mathrm{d}}(a) \propto n(a)m(a) \propto a^{p+3}$. Normalizing to the total dust column density (column dust-to-gas ratio $\mathcal{Z} = 0.01$) and integrating the distribution over the size bin i with boundaries a_i and a_{i+1}, we get

$$\Sigma_{\mathrm{d},i} = \begin{cases} \Sigma_{\mathrm{d,tot}} \frac{a_{i+1}^{p+4} - a_i^{p+4}}{a_{\mathrm{max}}^{p+4} - a_{\mathrm{min}}^{p+4}} & \text{for } p \neq -4 \\ \Sigma_{\mathrm{d,tot}} \frac{\log(a_{i+1}) - \log(a_i)}{\log(a_{\mathrm{max}}) - \log(a_{\mathrm{min}})} & \text{for } p = -4\,. \end{cases} \tag{4.20}$$

The maximum grain sizes a_{max} and exponents p are derived from the underlying `DustPy` models (measured at a distance of 50 au as the size including 99.9 % of the dust mass, see Table 4.1). Similar to the `DustPy` simulations, the minimum grain size is set to 0.1 µm, which is a typical size assumed for monomers in protoplanetary disks (Tazaki & Dominik, 2022) and which is constant throughout the simulations. We divide the power-law size distribution into four sections, equally spaced in logarithmic size space between a_{min} and a_{max}. The initial vertical dust distribution is determined by the midplane Stokes numbers and the level of turbulence assumed in the respective `DustPy` runs, follwing Equation 4.16. Dust is allowed to flow in from the outer boundary of the simulation domain with the initial vertical distribution. As to the time of this work, the `PLUTO` code has no built-in dust fluids. Therefore, we make use of the available gas tracer fluids. To model radial dust drift and vertical settling we modify the tracer fluxes according to the respective grain sizes' relative velocity to the gas, which is given by the prescriptions of Nakagawa et al. (1986) (terminal velocity approximation). Each dust fluid is advected with the gas velocity plus the drift correction of the mass-averaged size of the respective size bin. In Section 4.C we

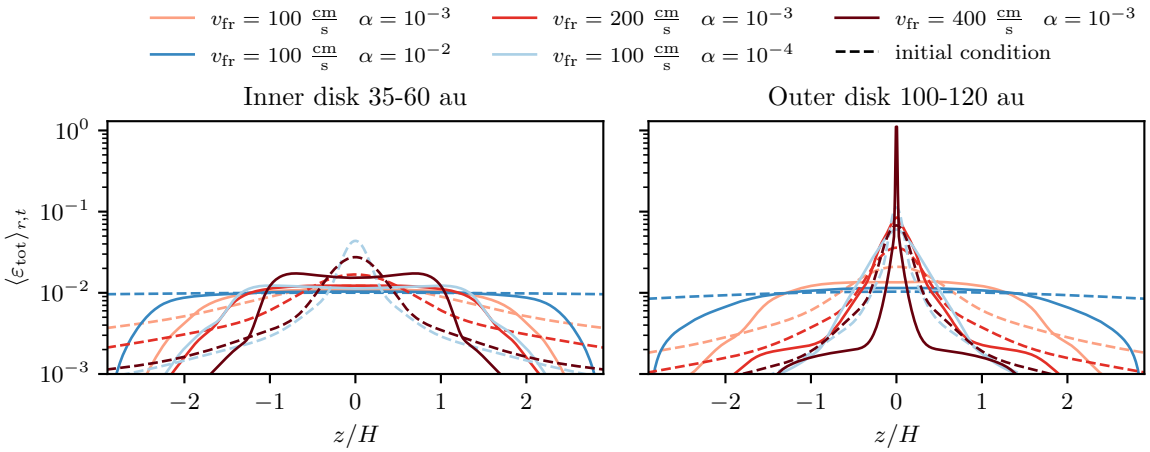

Figure 4.7
Radially and time-averaged dust-to-gas ratios in the inner and outer parts of our simulations. The inner regions are VSI-active, forming plateau-like dust distributions in all simulations with a cutoff at the edges of the VSI-active zones. The outer disk regions appear much more settled in that cases of $v_{fr} = 200\,\mathrm{cm\,s^{-1}}$ and $v_{fr} = 400\,\mathrm{cm\,s^{-1}}$, in which the outer regions are quiescent.

present tests of this method that verify its accuracy.

We continue the previous, gas-only, VSI simulations with dust for another 150 orbits (measured at 50 au). Figure 4.6 depicts the distribution of dust-to-gas ratios in our simulations after 150 orbits. In our model with $\alpha = 10^{-3}$ and $v_{fr} = 400\,\mathrm{cm\,s^{-1}}$, we have the largest particles of $\approx 0.14\,\mathrm{cm}$ radius, while the smallest particles are present in the model with $\alpha = 10^{-2}$ and $v_{fr} = 100\,\mathrm{cm\,s^{-1}}$, with a maximum size of $\approx 15\,\mu\mathrm{m}$ (see Table 4.1). As a comparison, we initialize the isothermal simulation with the largest grains, to get an estimate of the effect of ideal VSI on a grown dust population (as in Dullemond et al., 2022). The effect of the different levels of VSI turbulence, depending on the coagulation parameters and the respective thermal relaxation times becomes visible in the dust-to-gas ratios, where the simulations with larger particles, longer cooling times, and less VSI turbulence have more settled dust layers. Especially the outer disk regions are affected by this, as can be seen in the cases with $v_{fr} > 100\,\mathrm{cm\,s^{-1}}$ and $\alpha < 10^{-2}$.

We can furthermore see, that the isothermal simulation provides a good approximation for the models with the smallest particles. This is to be expected because the models with the smallest particles also have the shortest cooling times, making the VSI modes almost isothermal. To visualize the clear distinction between the inner VSI-active region and the outer VSI inactive regions, we plot the time and radially averaged total dust-to-gas ratios in Figure 4.7. For the models with fully VSI-active disks, we find flat top, or double-peaked dust distributions throughout the entire disks. In contrast, models with larger grains and inactive outer disks, show flat-topped, or double-peaked profiles in the inner disk regions and highly settled outer regions.

A perfect flat-top distribution would indicate spatially homogeneous diffusion and could easily be fitted by an analytic expression (see Equation 4.21, Fromang & Nelson, 2009). The double hump, on the other hand, cannot be a feature of isotropic turbulence and reflects the action of the quasi-periodic VSI motions.

At this point, we can only speculate what the feedback of these dust distributions onto the VSI would be. Lin & Youdin (2017) and Lin (2019) studied the influence that dust back-reaction could have on the VSI and found that this process generally damps the VSI turbulence. For the highly settled cases, with midplane dust-to-gas ratios near unity, one would have to include hydrodynamic back-reaction, as in the work by Schäfer et al. (2020); Schäfer & Johansen (2022). In these scenarios, the presence of VSI would probably be further inhibited by the hydrodynamic feedback of the dust onto the gas. Cooling times would also increase significantly in these regions. The areas above the midplane would be in the collision-limited regime, whereas the midplane could become optically thick (see Section 4.5).

4.5 Radiative Transfer Post Processing

We have shown the impact of the dust grain sizes on the strength of the VSI and the morphology of the dust layer in the previous section. Now, we want to determine the visual appearance of the simulated disks in synthetic millimeter-wavelength observations. Our goal is a qualitative comparison of our results with ALMA observations of edge-on or almost edge-on protoplanetary disks. Specifically, the works of Villenave et al. (2020, 2022, 2023) have shown that many protoplanetary disks appear settled in $\lambda = 1.25\,\mathrm{mm}$ images obtained with ALMA. Oph 163131 is the most prominent example with a very thin dust disk of height $H_{\mathrm{d},100\,\mathrm{au}} \approx 0.5\,\mathrm{au}$. Villenave et al. (2022) obtained this result by modeling the appearance of one of the disk's gaps.

For our approach, we create radiation intensity maps of edge-on disks ($i = 90°$) from the dust distributions of the last snapshot of our hydrodynamic simulations with `RADMC-3D`. For comparison, we also simulate the intensities arising from steady-state dust distributions under the assumption of a fixed diffusivity. In this settling-mixing equilibrium, the vertical dust distribution can be written

$$\varepsilon = \varepsilon_{\mathrm{mid}} \exp\left[-\frac{\mathrm{St}_{\mathrm{mid}}}{\delta}\left(\exp\left(\frac{z^2}{2H_{\mathrm{g}}^2}\right) - 1\right)\right], \tag{4.21}$$

(Fromang & Nelson, 2009). Opacities are calculated for each of the four populations using the standard DSHARP particle properties with the `dsharp_opac` python package (Birnstiel et al., 2018). We consider a photon package to be fully extinct after being scattered over a length of five optical depths. Our models are axisymmetric and we treat the anisotropic scattering angle for 60 angular sample points. Before running the ray tracing algorithm, we use the `mctherm` task to calculate the dust temperatures from a thermal Monte Carlo simulation. For this, we use 10^7 photon packages.

To mimic the effect of a finite beam size in ALMA observations, we convolve our images with a circular Gaussian beam, which for DSHARP observations had a typical FWHM of 35 mas. We place our disk at a distance of 100 pc to the observer.

We show the resulting images for the VSI simulation with $v_{\mathrm{fr}} = 100\,\mathrm{cm\,s^{-1}}$ in Figure 4.8, $v_{\mathrm{fr}} = 200\,\mathrm{cm\,s^{-1}}$ in Figure 4.9, and for $v_{\mathrm{fr}} = 400\,\mathrm{cm\,s^{-1}}$ in Figure 4.10. The right-hand side of each figure depicts three minor axis cuts through the intensity map at the locations of the

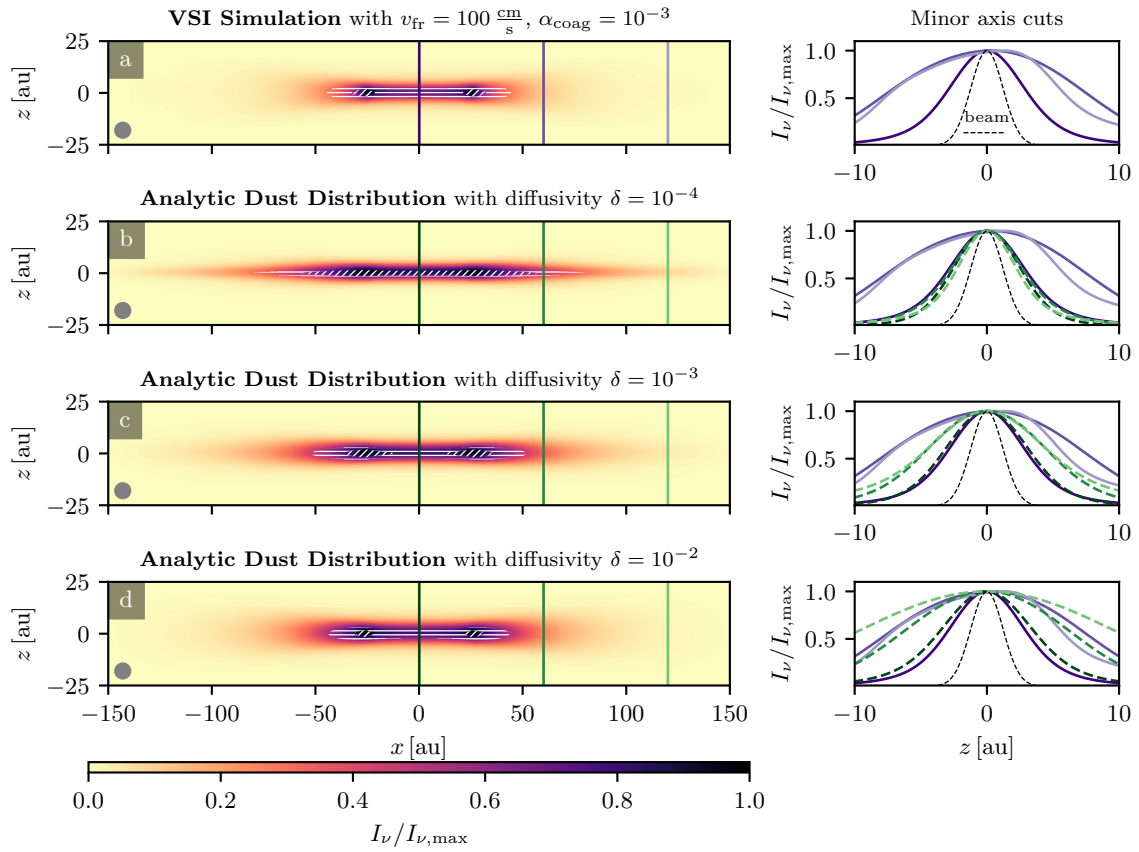

Figure 4.8
Upper row a: RADMC-3D intensity maps of our VSI simulation with $v_{\rm fr} = 100\,{\rm cm\,s^{-1}}$ and $\alpha = 10^{-3}$, seen edge-on. Rows b, c, and d show intensity maps calculated from analytic dust distribution that assume different diffusivities δ. The grain sizes are identical in all simulations. We convolve the images with a typical ALMA beam with FWHM of 35 mas for a distance of 100 pc shown as a grey circle. Hatched areas mark regions that have optical depth $\tau \geq 1$. Horizontal hatches correspond to areas for which the $\tau = 1$ surface lies on the far side of the disk. Diagonally hatched regions mark $\tau = 1$ surfaces that lie on the observer's side of the disk. The panels on the right-hand side show minor axis cuts through the images along the vertical lines in the intensity maps. Purple lines in all plots are the minor axis cuts from the VSI simulation (panel a).

vertical lines in the images. The images within each figure are created from disk models with identical particle sizes. As a result of optical depth effects, we find that the models with $v_{\rm fr} = 200\,{\rm cm\,s^{-1}}$ (Figure 4.9) $v_{\rm fr} = 400\,{\rm cm\,s^{-1}}$ (Figure 4.10), have a double-peaked intensity profile in the optically thick regions, marked by the hatched areas in each image. Above the midplane, these models have optical surfaces closer to the central star. Therefore, we observe the hotter inner regions above the midplane and the cooler outer regions in the disk midplane, as illustrated in Figure 4.11. Double-peaked profiles have already been observed in synthetic images of a VSI-active disk in Blanco et al. (2021). Their work is based on the simulation presented in Flock et al. (2020) and also treats radiative transfer through radiative diffusion in combination with ray-tracing from the central star for up to 10 µm dust particles.

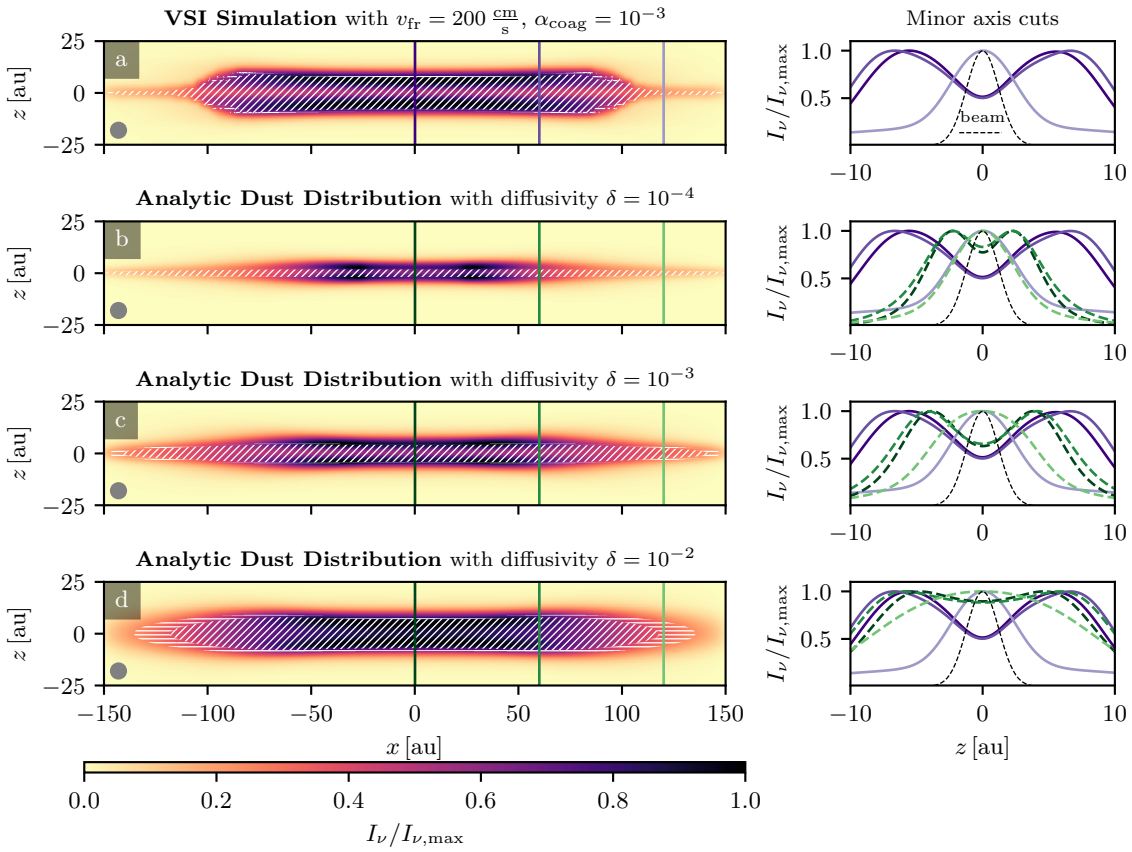

Figure 4.9
Upper row a: RADMC-3D intensity maps of our VSI simulation with $v_{fr} = 200\,\mathrm{cm\,s^{-1}}$ and $\alpha = 10^{-3}$, seen edge-on. Rows b, c, and d show intensity maps calculated from analytic dust distribution that assume different diffusivities δ. The grain sizes are identical in all simulations. We convolve the images with a typical ALMA beam with FWHM of 35 mas for a distance of 100 pc shown as a grey circle. Hatched areas mark regions that have optical depth $\tau \geq 1$. Horizontal hatches correspond to areas for which the $\tau = 1$ surface lies on the far side of the disk. Diagonally hatched regions mark $\tau = 1$ surfaces that lie on the observer's side of the disk. The panels on the right-hand side show minor axis cuts through the images along the vertical lines in the intensity maps. Purple lines in all plots are the minor axis cuts from the VSI simulation (panel a).

The disk model with the smaller particles ($v_{fr} = 100\,\mathrm{cm\,s^{-1}}$), is subject to the strongest VSI and the strongest vertical mixing (row a of Figure 4.8). Therefore, the disk midplane is not as strongly enriched and remains optically thin outside of ~ 45 au. We are therefore not observing any double-peaked minor axis intensity profiles in these cases. The minor cut intensity profiles in the inner disk match best with the analytic profile with $\delta = 10^{-4}$ or $\delta = 10^{-3}$ (rows b and c in Figure 4.8). In the outer disk, they show almost no settling, since the VSI is still active under the given conditions (more comparable with large diffusivities as in row c in Figure 4.8). Similar to the conclusions of Dullemond et al. (2022), we confirm that such a disk structure is not consistent with observations of highly settled edge-on disks like Oph 163131.

In our disk model with $v_{fr} = 200\,\mathrm{cm\,s^{-1}}$, we find a vertically extended and optically thick

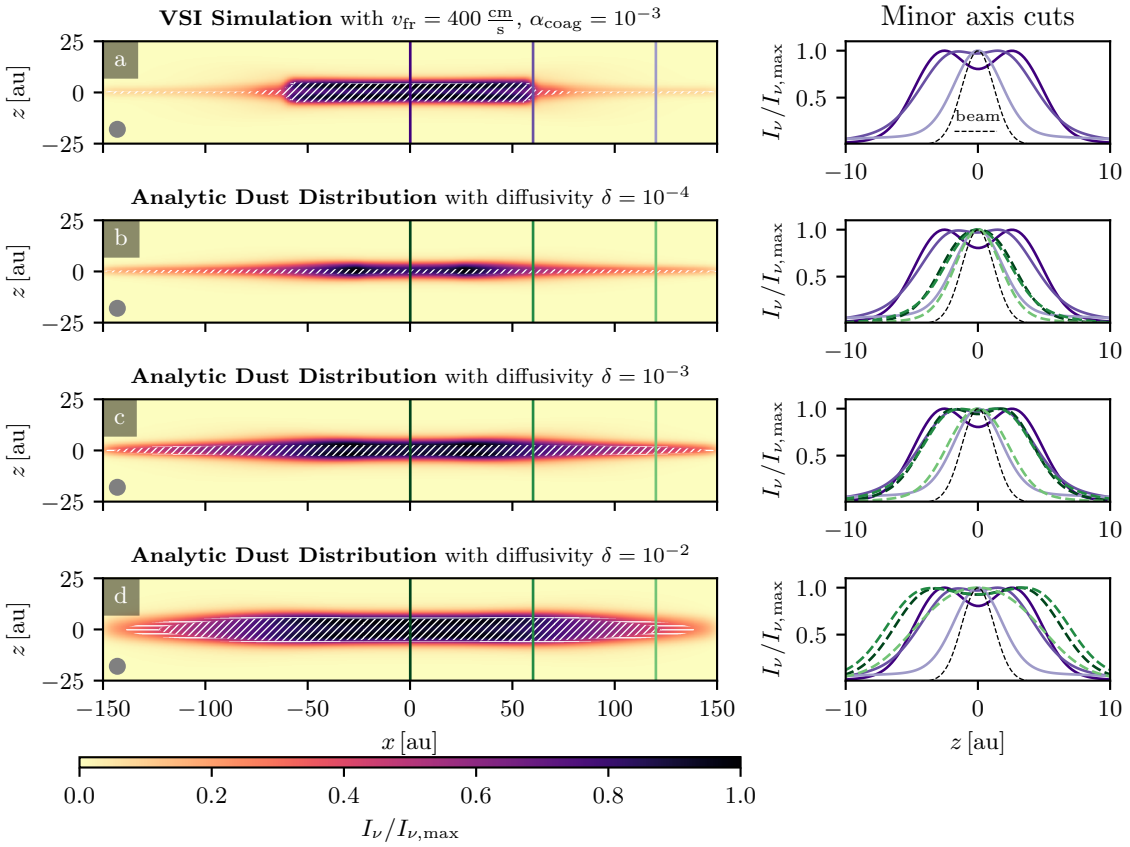

Figure 4.10
Upper row a: `RADMC-3D` intensity maps of our VSI simulation with $v_{fr} = 400\,\mathrm{cm\,s^{-1}}$ and $\alpha = 10^{-3}$, seen edge-on. Rows b, c, and d show intensity maps calculated from analytic dust distribution that assume different diffusivities δ. The grain sizes are identical in all simulations. We convolve the images with a typical ALMA beam with FWHM of 35 mas for a distance of 100 pc shown as a grey circle. Hatched areas mark regions that have optical depth $\tau \geq 1$. Horizontal hatches correspond to areas for which the $\tau = 1$ surface lies on the far side of the disk. Diagonally hatched regions mark $\tau = 1$ surfaces that lie on the observer's side of the disk. The panels on the right-hand side show minor axis cuts through the images along the vertical lines in the intensity maps. Purple lines in all plots are the minor axis cuts from the VSI simulation (panel a).

inner disk with the typical two intensity peaks. However, we can already see the effect of the radially increasing cooling times in the regions beyond 100 au. While the inner, VSI-active regions appear the be more consistent with the analytic models of high diffusivity (row d in Figure 4.9), we can see that the outer regions are most consistent with a low diffusivity of $\sim 10^{-4}$ (row b in Figure 4.9). This would still not be in agreement with observations of Oph 163131, which find the disk to be highly settled at $r \approx 80$ au.

Ramping up the fragmentation threshold further, as in our model with $v_{fr} = 400\,\mathrm{cm\,s^{-1}}$, results in a highly settled outer dust layer outside of ~ 60 au, as can be seen in Figure 4.10. The minor axis cuts illustrate the transition from an optically thick vertical structure in the inner regions to a mostly optically thin profile in the outer regions, which occurs at the outer edge of the VSI-active region. For the inner regions, we find a good agreement

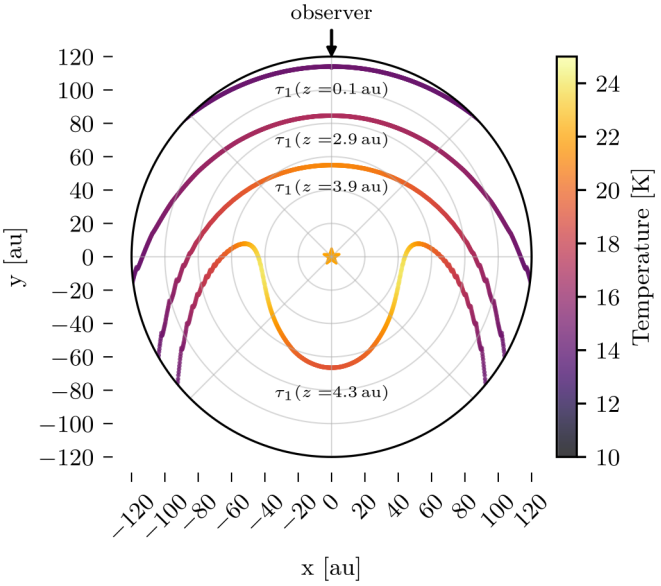

Figure 4.11
Origin of the double-peaked intensity profiles in Figure 4.9 and Figure 4.10. The $\tau = 1$ surfaces for the layers above the midplane lie closer to the central star due to the lower densities. The respectively higher temperatures lead to higher intensities above the midplane. Here shown are the $\tau = 1$ surfaces for row c in Figure 4.9.

between the VSI simulation and the analytic model with $\delta = 10^{-3}$ (row c in Figure 4.10). Similar to Dullemond et al. (2022), we find that the VSI can still lift up large particles in these inner regions. In contrast, the outer regions are strongly settled, and more consistent with the analytic profile with $\delta = 10^{-4}$ (row b in Figure 4.10). At this level of settling, it is unlikely that the outer regions of the VSI simulation could still be distinguished from a fully-settled disk ($\delta = 0$), due to the applied beam smearing. Note that in this simulation, we allow dust to flow into the simulation domain with a vertical distribution equal to the initial condition (which assumes $\delta = 10^{-3}$). Any remaining vertical extent of the dust layer in the outer disk therefore likely exists as a result of the boundary condition.

4.6 Discussion

Other Modes of Thermal Relaxation

We assumed the dust to be the only source of cooling in the outer regions of protoplanetary disks. However, molecules like CO, H_2O, CO_2, etc, with electromagnetic dipole moments, might also contribute to the cooling of the gas through line emission when gas and dust are thermally decoupled (Woitke et al., 2009; Malygin et al., 2014). In this case, thermal energy must also be transferred from the bulk constituent of the disk, H_2, to the emitting species via collisions. Cooling the VSI modes could, thus, again become a matter of collision timescales at the very low densities of the outer disk. At low temperatures, emission lines may also become extremely inefficient at cooling the gas at the required rate. Freeze-out of emitting molecules might also reduce the rate of thermal relaxation that can be achieved by emission line cooling. How much material can freeze out and thus be stopped from cooling the H_2, depends also on the availability of small grains. Cooling of the disk via gas emission lines is, thus, also dependent on the details of the dust population. Future studies

should aim to incorporate some treatment of gas cooling via emission lines. Models for this exist (Woitke, 2015), but are very complex and currently not feasible for implementation in a hydrodynamic simulation.

Furthermore, we have omitted the optically thick regions of protoplanetary disks ($R < 10\,\mathrm{au}$) in our simulations. Optically thick in this context does not refer to the bulk optical depth of the disk ($\tau \sim \Sigma\kappa$), as discussed in the previous section, but to the optical depth of individual VSI flow structures, which in the inner disk measure only a fraction of the disk scale height in the radial direction (denoted as l in the following). We attempted to simulate these regions in Pfeil & Klahr (2021) by assuming a characteristic diffusion length scale. However, self-consistent modeling requires some treatment of radiative transfer, as in Stoll & Kley (2016) or Flores-Rivera et al. (2020). Our findings nonetheless allow us to make predictions about the effect of dust coagulation on the cooling times in these regions, based on the results obtained here. If radiative diffusion becomes the dominant channel for thermal relaxation, we can write the respective cooling time as

$$t_{\mathrm{LTE}}^{\mathrm{diff}} = \frac{3}{16}\frac{C_V \rho_{\mathrm{small}} \rho_{\mathrm{g}} \kappa_{\mathrm{R}} l^2}{\sigma_{\mathrm{SB}} T^3}\,, \tag{4.22}$$

where κ_{R} is the Rosseland mean opacity, which is mostly determined by the small grains of density ρ_{small} (Lin & Youdin, 2015; Dullemond et al., 2022). If coagulation is increasing the maximum particle size, the density of small particles will be reduced, therefore reducing the diffusion timescale. At the same time, the size-distribution-averaged opacity will also be reduced. Therefore, dust coagulation would effectively reduce the diffusion time scale and thus be beneficial for the VSI in the inner disk regions.

Implication for the Vertical Shear Instability

We have shown that the vertical shear instability is highly sensitive to the underlying dust size distribution, which determines the timescale of thermal relaxation. Manger et al. (2021) and Klahr et al. (2023) have shown that the VSI growth rate almost instantaneously drops to almost zero once the critical cooling time threshold is reached. This is also what we observe as a sudden cutoff in the VSI activity at large disk radii. Therefore, the VSI-active zones in protoplanetary disks are not extending throughout the entire outer disk. Our simulations predict a VSI dead zone at large radii, which is caused by the reduced efficiency of cooling.

Our simulations omit a treatment of dust back-reaction onto the gas. Schäfer et al. (2020) have shown, that if the dust can settle into a thin layer in the disk midplane before the VSI starts to grow, dust feedback can counteract the VSI. Since dust coagulation, settling, and the onset of the VSI, occur on comparable timescales, it is not trivial to predict the outcome of such a situation without a realistic disk simulation that treats all of the aforementioned effects simultaneously. Our results show that if some dust settling and coagulation can occur before the onset of the VSI, the effect of the reduced cooling time would reduce the VSI activity and therefore probably enhance the dampening effect of the dust's dynamic back-reaction onto the gas.

The Need for a Self-consistent Three-dimensional Model and the Limitations of Our Approach

Simulations that aim to study the VSI under realistic conditions cannot ignore the implications of an evolved dust population, as presented in our and previous studies (see Fukuhara et al., 2021, 2023). Measurements of the spectral index in protoplanetary disks (Tazzari et al., 2016; Pérez et al., 2012; Huang et al., 2018; Sierra et al., 2021) and polarization observations (Ohashi & Kataoka, 2019) imply that dust coagulation is occurring and that grains in the outer disk can reach sizes of 0.1–1 mm, similar to the outcome of the `DustPy` models that our VSI simulations are based on. Note, however, that our studies are no self-consistent representations of protoplanetary disks. The dust size distributions used to calculate the cooling time in our setups are static. In a real disk, they would evolve together with the VSI. Settling and stirring of the dust layer would impact the cooling times. It is unclear if this would lead to some sort of equilibrium situation in which the dust stirring by the VSI can maintain a thick enough dust layer to support the necessary cooling times. Continuous coagulation of grains would counteract the turbulent mixing further.

Fukuhara et al. (2023) presented an approach to study this equilibrium by using analytic, yet physically motivated, cooling time profiles. They iterated between VSI simulations and calculations of the resulting steady-state dust distribution from the measured turbulent diffusivity. In that way, they were able to reach a convergent state in which the VSI turbulence creates the necessary diffusivity to maintain the underlying cooling times. Their studies did, however, not consider the effect of the changing diffusivity on the grain size itself through coagulation and fragmentation. This poses an additional uncertainty in their and our studies. We can already see that the measured Mach numbers in our simulations do not always correspond to the α values used in the underlying coagulation models (see Figure 4.4). Note that $\mathcal{M}$ is only part of the generation of turbulent collision speeds (Ormel & Cuzzi, 2007). The turbulent spectrum in correlation time space is also required to calculate the acceleration that can be imposed on various particle sizes. Collision speeds can only be obtained from the large scale rms velocity $U(L)$ and the associated length scale $L = \sqrt{\alpha}H$, for an ideal Kolmogorov turbulence cascade which causes isotropic turbulent diffusivities (Youdin & Lithwick, 2007; Binkert, 2023).

If any source of additional turbulence would be present that causes the turbulent diffusivities used in our coagulation models, this would also have an effect on the developing VSI. Even small viscosities of $\alpha = 10^{-4}$–10^{-3} are enough to hinder the evolution of the VSI (Barker & Latter, 2015). Future studies should try to apply a more realistic, self-consistent prescription of diffusivities in the coagulation model.

In our cooling time calculations, we have also neglected the effects of radial drift. Drift-limited size distributions are characterized by smaller maximum particle sizes and are more top-heavy than fragmentation-limited distributions. This results in longer thermal accommodation timescales and would further inhibit the VSI turbulence.

The effect of the drag force onto the gas was also not considered in our simulations. Schäfer et al. (2020) and Schäfer & Johansen (2022) have shown that back-reaction can indeed inhibit the VSI turbulence close to the disk midplane if the dust has time to sediment before the VSI is saturated. Future studies should therefore aim to incorporate more realistic dust dynamics.

In our two-dimensional simulations with dust, we have observed flat top or double-peaked dust-to-gas ratio distributions. This reflects the periodic and non-isotropic nature of the VSI-driven turbulence, which is not accounted for in the coagulation simulations. However, as our simulations are two-dimensional, the prominence of these features might be artificially enhanced, as the $\varphi-$dimension is missing as a degree of freedom. Three-dimensional simulations (Manger & Klahr, 2018; Flock et al., 2020; Manger et al., 2021; Pfeil & Klahr, 2021) are needed for the study of the non-linear saturation and fully developed turbulent state of VSI-driven turbulence, before deriving the turbulence properties as diffusivity, correlation times, and energy spectra.

The main conclusions of our study and Fukuhara et al. (2021), however, remain unchanged by all these considerations. Dust coagulation and dynamics are essential components in studies of cooling-time-sensitive instabilities like the VSI.

This highlights the need for a more-self consistent numerical approach. Cooling times have to be constantly recalculated throughout a simulation from the present dust size distributions in order to study such systems. In the inner, optically thick parts of the disk, radiative transfer models have to be employed to study the effect of coagulation on diffusive radiative cooling.

4.7 Summary and Conclusions

In this work, we studied the effect of evolved dust size distributions on the VSI activity in protoplanetary disks. We conducted hydrodynamic simulations based on five different dust coagulation models for different fragmentation velocities and assumed turbulence strengths, which resulted in maximum particle sizes between $\sim 10\,\mu\mathrm{m}$ and $\sim 0.1\,\mathrm{cm}$. Based on these dust size distributions, we calculated the cooling times for our subsequent hydrodynamic simulations. Our results show a strong dampening effect of dust coagulation on the VSI, as predicted by previous studies (Lin & Youdin, 2015; Fukuhara et al., 2021; Pfeil & Klahr, 2021; Dullemond et al., 2022; Fukuhara et al., 2023). The reason for this is the collisional decoupling between dust particles and gas molecules that is enhanced if dust coagulation is increasing the maximum particle size. Reduced collision rates inhibit the thermal accommodation of dust and gas and therefore reduce the cooling rate of the gas.

The effect can be strong enough to hinder the development of the VSI, leading to a highly settled dust layer even for moderate fragmentation velocities of $v_{\mathrm{fr}} \gtrsim 200\,\mathrm{cm\,s^{-1}}$. At the same time, the inner regions—in which the gas and dust components remain well coupled—can maintain some level of VSI turbulence. This finding is consistent with recent observations of highly settled dust layers in protoplanetary disks (Villenave et al., 2020, 2022). Our simulations also show that even a low level of VSI can still significantly alter the vertical distribution of dust, which we can observe in the inner disk regions of our simulations with the largest particles. Synthetic images of these VSI-active regions at millimeter-wavelength are mostly consistent with analytic models that assume large diffusivities of $\delta \sim 10^{-3}$–10^{-2}. At the same time, outer disk regions can appear completely settled in our simulations. We thus report the existence of a VSI dead zone in the outer regions of protoplanetary disks. The existence of the VSI dead zone in the outer regions of protoplanetary disks reconciles recent millimeter-wavelength observations with models of

hydrodynamic turbulence.

Future studies of VSI-active disks should aim to incorporate a more self-consistent treatment of dust coagulation and dynamics. Additionally, cooling via gas emission lines has to be considered to gain a better understanding of the impact of thermal relaxation on the VSI in protoplanetary disks. For this, thermochemical modeling is required to track the amounts and the evolution of relevant species, which in fact also depends on the dust coagulation process. Modeling the optically thick parts of protoplanetary disks and the impact of stellar irradiation furthermore requires radiative transfer modeling.

After applying our methodology to smooth disks in this article, we will extend our studies to disks with substructure in Part II. Specifically, Oph 163131 (Villenave et al., 2020; Wolff et al., 2021; Villenave et al., 2022) and HD 163296 (Dullemond et al., 2018; Rosotti et al., 2020; Doi & Kataoka, 2021) have been extensively surveyed with a focus on the dust diffusivities and provide good conditions for comparison with simulations.

Acknowledgments

T.P., H.K., and T.B. acknowledge the support of the German Science Foundation (DFG) priority program SPP 1992 “Exploring the Diversity of Extrasolar Planets” under grant Nos. BI 1816/7-2 and KL 1469/16-1/2. T.B. acknowledges funding from the European Research Council (ERC) under the European Union’s Horizon 2020 research and innovation programme under grant agreement No 714769 and funding by the Deutsche Forschungsgemeinschaft (DFG, German Research Foundation) under grants 361140270, 325594231, and Germany’s Excellence Strategy - EXC-2094 - 390783311. Computations were conducted on the computational facilities of the University of Munich (LMU).

We thank the anonymous referee for their constructive comments, which helped us to improve the quality of this article.

Software

- `PLUTO-4.4` (Mignone et al., 2007)
- `RADMC-3D` (Dullemond et al., 2012)
- `Python` with the packages:
  - `NumPy` (Harris et al., 2020)
  - `SciPy` (Virtanen et al., 2020)
  - `matplotlib` (Hunter, 2007)
  - `DustPy` (Stammler & Birnstiel, 2022)
  - `DustPyLib`
  - `dsharp_opac` (Birnstiel, 2018)
  - `RADMC-3DPy`

4.A Cooling Time Derivations by Barranco et al. (2018)

To calculate the cooling times, we follow the derivations by Barranco et al. (2018). We assume that the emission of dust grains determines the thermal relaxation of the gas in a two-stage process. Thermal energy is transferred between gas and dust molecules through collisions. The dust, which at low temperatures typically has much higher emissivity, can radiate an excess of thermal energy and thus effectively cool the gas.

Dust Emission Timescale This is the timescale on which the dust grains of temperature T_d reach thermal equilibrium with their surroundings (of temperature T_eq, set by stellar irradiation in our model) via emission or absorption of electromagnetic radiation. We assume the dust grains to radiate as black bodies, meaning the cooling rate per unit volume of material can be derived by integrating the cooling rate per gram of dust of size a, over the size distribution

$$\Lambda^\mathrm{d}_\mathrm{rad} = \int_{a_\mathrm{min}}^{a_\mathrm{max}} \rho(a)\Lambda_\mathrm{rad}(a)\,\mathrm{d}a \tag{4.23}$$

$$= 4\sigma_\mathrm{SB}(T_\mathrm{d}^4 - T_\mathrm{eq}^4)\int_{a_\mathrm{min}}^{a_\mathrm{max}} \rho(a)\kappa_\mathrm{P}(a, T_\mathrm{eq})\,\mathrm{d}a\,. \tag{4.24}$$

The respective cooling timescale follows from

$$t^\mathrm{rad}_\mathrm{d} = \frac{\rho_\mathrm{d} C_\mathrm{d}}{\Lambda^\mathrm{d}_\mathrm{rad}}|T_\mathrm{d} - T_\mathrm{eq}| \tag{4.25}$$

$$= \frac{\rho_\mathrm{d} C_\mathrm{d}}{4\sigma_\mathrm{SB}}\left(\frac{T_\mathrm{d} - T_\mathrm{eq}}{T_\mathrm{d}^4 - T_\mathrm{eq}^4}\right)\left(\int_{a_\mathrm{min}}^{a_\mathrm{max}} \rho_\mathrm{d}(a)\kappa_\mathrm{P}(a, T_\mathrm{eq})\,\mathrm{d}a\right)^{-1}. \tag{4.26}$$

Expanding this expression in a Taylor series for small $\delta T = T_\mathrm{d} - T_\mathrm{eq}$, results in

$$t^\mathrm{rad}_\mathrm{d} \approx \frac{\rho_\mathrm{d} C_\mathrm{d}}{16\,\sigma_\mathrm{SB}\,T_\mathrm{eq}^3}\left(\int_{a_\mathrm{min}}^{a_\mathrm{max}} \rho_\mathrm{d}(a)\kappa_\mathrm{P}(a, T_\mathrm{eq})\,\mathrm{d}a\right)^{-1}, \tag{4.27}$$

Thermal Accommodation of the Gas via Collisions with the Dust The emission or absorption of radiation by the dust grains can relax temperature perturbations in the gas only if dust and gas are thermally coupled via collisions. We calculate this collisional accommodation timescale by integrating the collision rate per unit volume over the entire size distribution, assuming a thermal accommodation coefficient $\mathcal{A} = 0.5$, as in Barranco et al. (2018). In this case, the thermal energy transferred between gas and dust can be written as

$$\Lambda_\mathrm{coll} = \int_{a_\mathrm{min}}^{a_\mathrm{max}} n_\mathrm{d}(a)\sigma_\mathrm{coll}\bar{v}_\mathrm{g} n_\mathrm{g}\, 2\mathcal{A}k_\mathrm{B}(T_\mathrm{g} - T_\mathrm{d})\,\mathrm{d}a \tag{4.28}$$

$$= \pi\bar{v}_\mathrm{g} n_\mathrm{g}\, k_\mathrm{B}(T_\mathrm{g} - T_\mathrm{d})\int_{a_\mathrm{min}}^{a_\mathrm{max}} n(a)a^2\,\mathrm{d}a\,, \tag{4.29}$$

where n_g is the number density of gas molecules and T_g is the gas temperature (Probstein, 1969; Burke & Hollenbach, 1983). Now we multiply by ρ_d/ρ_d where the total dust density can be written $\rho_d = \int n(a)m(a)\,da$, with the particle mass $m(a) = 4/3\,\pi a^3 \rho_m$. Thus, we obtain

$$\Lambda_{coll} = \bar{v}_g n_g\, k_B (T_g - T_d) \frac{3\rho_d}{4\rho_s} \frac{\int_{a_{min}}^{a_{max}} n(a) a^2\,da}{\int_{a_{min}}^{a_{max}} n(a) a^3\,da}\,. \tag{4.30}$$

Here, we can insert the definition of the Sauter mean radius $a_s = \langle a^3\rangle/\langle a^2\rangle$, where $n_d\langle a^2\rangle := \int_{a_{min}}^{a_{max}} n(a)a^2\,da$ is the second moment of the size distribution and $n_d\langle a^3\rangle := \int_{a_{min}}^{a_{max}} n(a)a^3 da$ is the third moment of the size distribution. With this, we arrive at Equation 12 from Barranco et al. (2018)

$$\Lambda_{coll} = \left(\frac{3}{4\rho_m}\right)\left(\frac{1}{a_s}\right)\left(\frac{\rho_d}{\rho_g}\right)\left(\frac{\rho_g^2 \bar{v}_g}{\bar{m}_g}\right) k_B (T_g - T_d)\,. \tag{4.31}$$

The collisional cooling time of the gas via collisions with the dust follows from

$$t_g^{coll} = \frac{\rho_g C_P}{\Lambda_{coll}} |T_g - T_d|\,. \tag{4.32}$$

We insert Equation 4.31 and multiply by $\pi a_S^3/\pi a_S^3$. For particles of size a_S, we define a hypothetical number density of $n_S = \rho_d/m_S$ and a collisional cross-section $\sigma_S = \pi a_S^2$. We apply Meyer's relation $k_B/\bar{m} = C_P - C_V$ and the definition of the heat capacity ratio $\gamma = C_P/C_V$ and arrive at Equation 4.5

$$t_g^{coll} = \frac{\gamma}{\gamma - 1}\frac{1}{n_S \sigma_S \bar{v}_g}\,.$$

Likewise, the dust grains adjust their temperature on a timescale

$$t_d^{coll} = \frac{\rho_d C_d}{\Lambda_{coll}}(T_g - T_d). \tag{4.33}$$

$$= \left(\frac{\rho_d}{\rho_g}\right)\left(\frac{C_d}{C_P}\right) t_g^{coll}\,, \tag{4.34}$$

where C_d is the specific heat capacity of the dust grains, which we take to be $800\,J\,K^{-1}\,kg^{-1}$ (see Barranco et al., 2018). We note that for a truncated power-law size distribution $n(a) \propto a^p$, the Sauter mean radius can be written

$$a_S = \begin{cases} \frac{a_{max} - a_{min}}{\log(a_{max}) - \log(a_{min})} & \text{for } p = -3 \\ \frac{a_{max} a_{min}}{a_{max} - a_{min}} \log\left(\frac{a_{max}}{a_{min}}\right) & \text{for } p = -4 \\ \left(\frac{p+3}{p+4}\right)\frac{a_{max}^{p+4} - a_{min}^{p+4}}{a_{max}^{p+3} - a_{min}^{p+3}} & \text{for } p \neq -4, -3\,, \end{cases} \tag{4.35}$$

which, for a typical size distribution with $p = -3.5$, leads to to $a_S = \sqrt{a_{max} a_{min}}$. The collisional cooling time of the gas (Equation 4.5), therefore scales as $t_g^{coll} \propto \sqrt{a_{max}}$. If the

size distribution is fragmentation limited, which is to expected for most parts of the disk, this translates to

$$t_{\mathrm{g}}^{\mathrm{coll}} \propto \frac{v_{\mathrm{fr}}}{\sqrt{\alpha}} \,. \tag{4.36}$$

Total Thermal Relaxation Time of the Gas In order to derive the total thermal relaxation time of the gas, Barranco et al. (2018) write the equations of thermal relaxation as

$$\frac{\mathrm{d}(\delta T_{\mathrm{g}})}{\mathrm{d}t} = -\frac{\delta T_{\mathrm{g}} - \delta T_{\mathrm{d}}}{t_{\mathrm{g}}^{\mathrm{coll}}} \tag{4.37}$$

$$\frac{\mathrm{d}(\delta T_{\mathrm{d}})}{\mathrm{d}t} = \frac{\delta T_{\mathrm{g}} - \delta T_{\mathrm{d}}}{t_{\mathrm{d}}^{\mathrm{coll}}} - \frac{\delta T_{\mathrm{d}}}{t_{\mathrm{d}}^{\mathrm{rad}}} \,. \tag{4.38}$$

For this coupled system, one can look for solution of the form $\delta T_{\mathrm{g}} = \hat{T}_{\mathrm{g}} \exp\left(-t/t_{\mathrm{thin}}^{\mathrm{NLTE}}\right)$, $\delta T_{\mathrm{d}} = \hat{T}_{\mathrm{d}} \exp\left(-t/t_{\mathrm{thin}}^{\mathrm{NLTE}}\right)$. The resulting equation system can be solved for $t_{\mathrm{thin}}^{\mathrm{NLTE}}$, which results in Equation 4.8.

4.B Cooling Time Maps

To make our cooling time maps, derived from `DustPy` models, usable for our `PLUTO` simulation, we fitted the data as a function of gas density and temperature. In this way, we can easily calculate the cooling time for each grid cell in `PLUTO` from the local disk structure.

We found that for a given temperature, the cooling time can be fitted by a power law in density,

$$t_{\mathrm{NLTE,Fit}} = t_{10^{-15}}(T) \left(\frac{\rho_{\mathrm{g}}}{10^{-15}\,\mathrm{g\,cm^{-3}}} \right)^{p(T)} \,. \tag{4.39}$$

The power law's parameters themselves can be fitted as broken broken power laws of temperature:

$$t_{10^{-15}}(T) = \left(\frac{T}{T_{t,\mathrm{c}}} \right)^{q_t + s_t} \frac{T_{t,\mathrm{c}}^{s_t}}{(T_{t,\mathrm{c}}^{s_t} + T^{s_t})} + p_t \tag{4.40}$$

$$p(T) = \left(\frac{T}{T_{p,\mathrm{c}}} \right)^{q_p + s_p} \frac{T_{p,\mathrm{c}}^{s_p}}{(T_{p,\mathrm{c}}^{s_p} + T^{s_p})} + p_p \,. \tag{4.41}$$

This means that our two-dimensional cooling time distribution can be described as a function of ρ_{g} and T with a total of eight parameters. For the actual fitting procedure, we use the `scipy` routine `curve_fit`. Residuals between the actual cooling time maps and our fitting functions are displayed in Figure 4.12. With the exception of our model with $v_{\mathrm{fr}} = 100\,\mathrm{cm\,s^{-1}}$ and $\alpha = 10^{-4}$, all fits have maximum deviations from the data of $< 30\,\%$ in the entirety of the simulation domain. The respective model with higher deviations corresponds to a highly settled particle layer with $\alpha = 10^{-4}$, making it distinct from the other models with $\alpha = 10^{-3}$. Thus, some deviation had to be expected for this case. Note

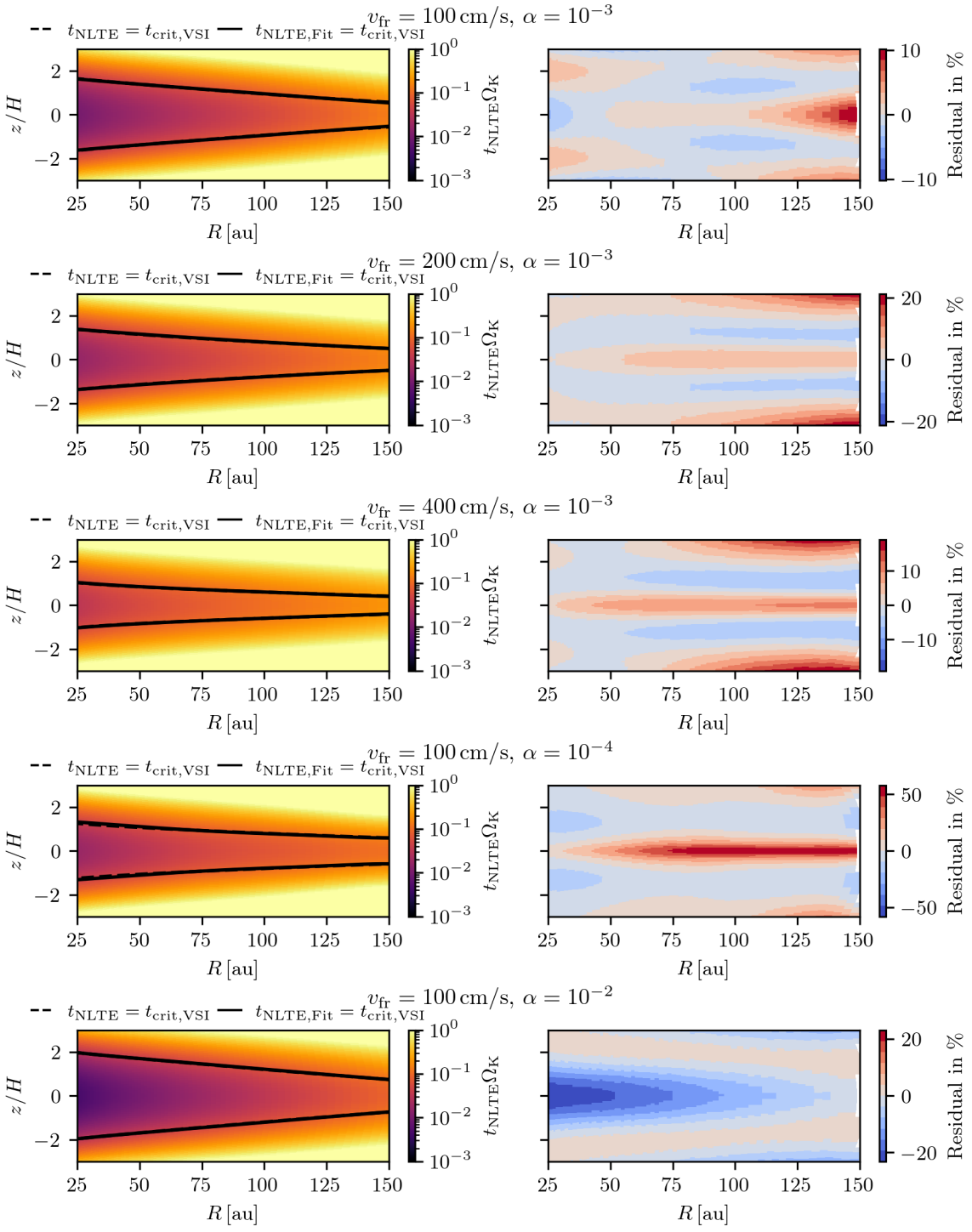

Figure 4.12
Cooling time maps in our 5 VSI PLUTO simulations on the left-hand side, and the residuals between the fit used in our simulations, and the actual cooling time distributions derived from DustPy simulations.

that we are generally interested in trends of the VSI activity with the given coagulation parameters, which are well captured by our fits. Uncertainties of 10–60 % in the cooling times thus do not influence the conclusions of our work.

4.C Dust Advection and Diffusion in PLUTO

As a consequence of the sub-Keplerian azimuthal gas velocity, particles in aerodynamic force equilibrium with the gas also have sub-Keplerian terminal velocities. Radial pressure forces, which contribute the to gas' radial force balance, do not significantly act on the dust grains. Therefore, the grains embedded in the gas cannot stay on circular orbital trajectories and spiral inward at a given terminal drift speed. Nakagawa et al. (1986) derived this radial drift velocity as

$$v_{\mathrm{d-g,r}} = v_{\mathrm{d},r} - v_{\mathrm{g},r} = \frac{\mathrm{St}(1+\varepsilon)}{\mathrm{St}^2 + (1+\varepsilon)^2} \frac{1}{\rho_{\mathrm{g}}\Omega_{\mathrm{K}}} \frac{\partial P}{\partial R} \approx \frac{\mathrm{St}}{\mathrm{St}^2 + 1} \frac{1}{\rho_{\mathrm{g}}\Omega_{\mathrm{K}}} \frac{\partial P}{\partial R}\,, \tag{4.42}$$

where in our simulations P is the gas pressure, and therefore subject to fluctuations arising from the VSI. We use the zeroth order approximation for small dust-to-gas ratios on the right-hand side. This approximation is robust in the VSI-active regions, where the dust-to-gas ratios are generally smaller than 0.05 in our simulations. A similar derivation can be made for the vertical velocity component. Pressure forces keep the gas on elevated trajectories around the central star (acting against the vertical component of the gravitational force). Again, these forces have a negligible effect on the grains. An expression, equal to Equation 4.42, can be found for the settling velocity of the grains

$$v_{\mathrm{d-g,z}} = v_{\mathrm{d},z} - v_{\mathrm{g},z} = \frac{\mathrm{St}}{\mathrm{St}^2 + 1} \frac{1}{\rho_{\mathrm{g}}\Omega_{\mathrm{K}}} \frac{\partial P}{\partial z}\,. \tag{4.43}$$

The PLUTO code already allows for the treatment of passive tracer fluids, which are simply advected with the gas following

$$\frac{\partial(\rho_{\mathrm{g}}\varepsilon)}{\partial t} + \boldsymbol{\nabla}\cdot(\varepsilon\,\rho_{\mathrm{g}}\,\boldsymbol{v}_{\mathrm{g}}) = 0\,. \tag{4.44}$$

In our case, the advected quantity ε represents a local dust-to-gas ratio $\varepsilon = \rho_{\mathrm{d}}/\rho_{\mathrm{g}}$. In the short friction time, terminal velocity approximation, the respective dust flow is modified to simulate a dust fluid that is aerodynamically coupled to the gas, i.e., undergoes radial and azimuthal drift, and vertical sedimentation, with terminal velocities given by Equation 4.42 and Equation 4.43. to the tracer flux, which is valid for small dust-to-gas ratios (Youdin & Goodman, 2005). The tracer flux is then calculated with the upstream dust density based on the above velocity at the respective cell interface

$$\boldsymbol{F}_{\mathrm{drift,interface}} = \rho_{\mathrm{d,upstream}}\boldsymbol{v}_{\mathrm{d-g,interface}}\,. \tag{4.45}$$

Test Case for Dust Drift

Youdin & Shu (2002), presented an analytic description for the time evolution of a dust

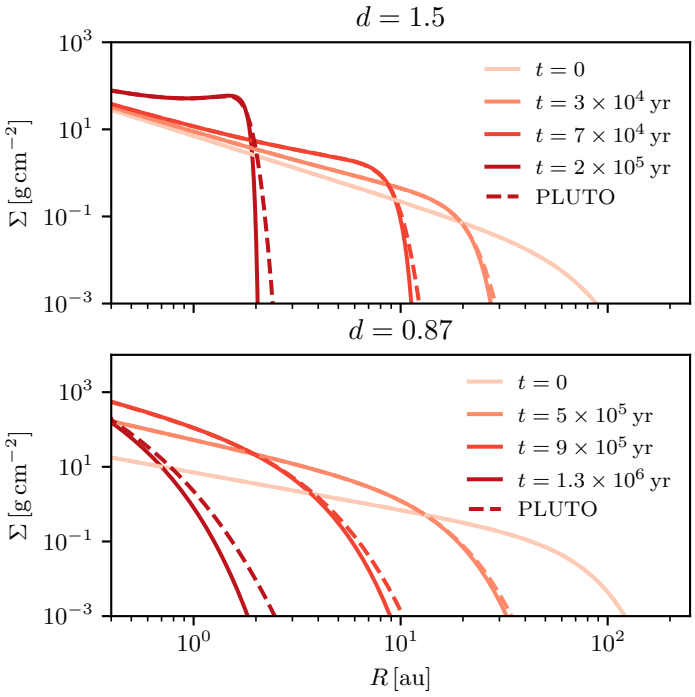

Figure 4.13
Radial dust advection tests based on Youdin & Shu (2002).

fluid with a fixed grain size in a protoplanetary disk due to radial drift. Their prescription was further developed in Birnstiel & Andrews (2014), and their general solution to the advection equation is given by

$$\Sigma(r,t) = \Sigma(r_0,t)\frac{v(r_0)r_0}{v(r)r}\,, \tag{4.46}$$

with the velocity $v(r)$ and the original location of the characteristic r_0, defined via

$$\frac{t}{r_c} = \int_{r_0}^{r} \frac{1}{u(r')}\,\mathrm{d}r'\,. \tag{4.47}$$

Based on the assumption that the transport velocity scales as a radial power law $v_{dr} \propto R^d$, one can solve the above integral and, thus, write a complete solution for the transport equation as

$$\Sigma(r,t) = \Sigma_0 r^{-d-1} r_0^{d+1-\beta_\Sigma}\,, \tag{4.48}$$

with the time dependence entering through the initial radius of the characteristic

$$r_0 = r\left[1-(d-1)\frac{v_{dr}t}{r}\right]^{-\frac{1}{d-1}}\,. \tag{4.49}$$

We are using this analytic solution of the advection equation to verify our transport scheme for the PLUTO code with a passive dust fluid. We present two cases for different drift parameters d in Figure 4.13 for a particle size of 0.1 cm. As can be seen, our transport scheme provides good agreement with the analytic transport solutions even for long integration

times. However, we can also see that our simple donor-cell flux prescription is associated with a certain numerical diffusivity which is especially evident over very long integration times, as in the lower panel of Figure 4.13.

Tests for Dust Diffusion (not used in VSI simulations)

For completeness, we also introduce a diffusion velocity to our dust advection model, determined by the gradient in dust-to-gas ratio ε and the diffusion coefficient D

$$\boldsymbol{v}_{\text{diff}} = -D\boldsymbol{\nabla} \ln(\varepsilon)\,, \tag{4.50}$$

which we add to the advection velocity before the calculation of the complete upstream transport flux. We do not employ any additional diffusivity in our VSI simulations, meaning $\boldsymbol{v}_{\text{diff}} = 0$ in all presented simulation. To test this very simple approach to dust diffusion in the PLUTO code, we run two simulations with dust species of fixed Stokes numbers that reach a steady state that can be compared to steady-state solutions of the diffusion equation. Our first test case considers dust trapping in a radial pressure bump and a fixed diffusivity parameter δ. Dullemond et al. (2018), considered this scenario and derived an

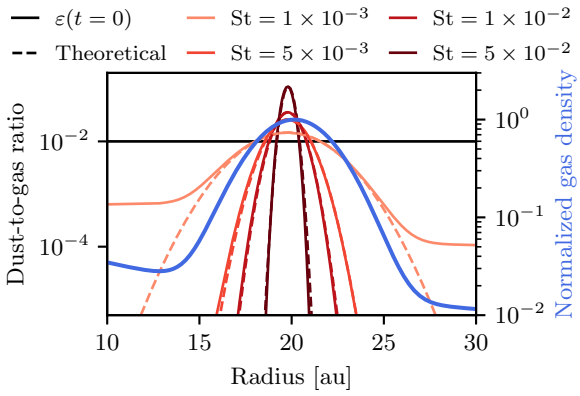

Figure 4.14
Dust concentration in a steady-state radial pressure bump, embedded in a power-law density profile. Within the pressure bump, we find excellent agreement between our numerical simulation and the predicted profiles.

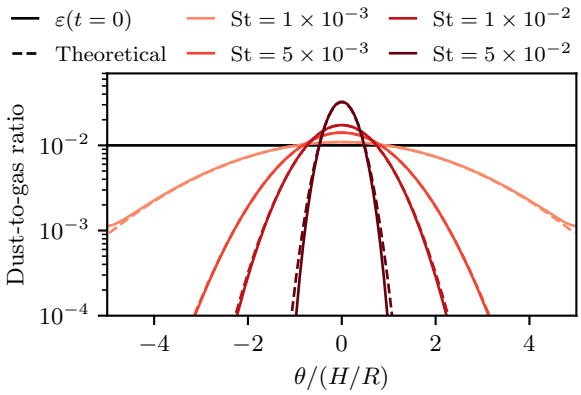

Figure 4.15
Vertical diffusion test for our passive dust fluid in PLUTO. We assume a vertically isothermal disk in hydrostatic equilibrium. The resulting dust density distribution agrees well with the analytic prediction.

approximate analytic solution for a Gaussian pressure bump of amplitude P_0 and width w,

$$P(r) = P_0 \exp\left(-\frac{(r-r_0)^2}{2w^2}\right) . \tag{4.51}$$

This results in a steady-state dust distribution, given by

$$\Sigma_\mathrm{d} = \Sigma_{\mathrm{d},0} \exp\left(-\frac{(r-r_0)^2}{2w_\mathrm{d}^2}\right) , \tag{4.52}$$

where the width of the dust density distribution is related to the pressure bump's width via

$$w_\mathrm{d} = w\sqrt{\frac{\delta}{\delta+\mathrm{St}}} . \tag{4.53}$$

We conducted a simulation of this setup embedded in a protoplanetary disk with a power-law background gas density and four dust fluids with Stokes numbers 10^{-3}, 5×10^{-3}, 10^{-2} and 5×10^{-2}. The test domain spans from 10 au to 30 au with 200 grid cells, and contains a pressure bump of 2 au width at 20 au distance to a solar mass star. Within the pressure bump, where the analytical solution applies, the resulting dust profiles are in excellent agreement with the analytic solutions. As a second test, we set up a two-dimensional, axisymmetric simulation in spherical coordinates. We set up a vertically isothermal disk in hydrostatic equilibrium. Similar to the radial pressure bump, an analytic solution for the settling-mixing equilibrium can be derived which reads

$$\varepsilon(z) = \varepsilon_0 \exp\left(-\frac{z^2}{2H_\mathrm{g}^2}\frac{\mathrm{St}}{\delta}\right) \overset{z\ll R}{\approx} \varepsilon_0 \exp\left(-\frac{\vartheta^2}{2(H_\mathrm{g}/R)^2}\frac{\mathrm{St}}{\delta}\right) , \tag{4.54}$$

where $\vartheta = \tan(z/R)$. We find a good agreement between the steady-state profiles and the theoretically predicted steady state, as can be seen in Figure 4.15.

CHAPTER 5

VERTICAL SHEAR INSTABILITY WITH DUST EVOLUTION AND CONSISTENT COOLING TIMES

SETTLING AND MIXING OF DUST DO NOT ERASE THE INITIAL CONDITION

Thomas Pfeil, Tilman Birnstiel, and Hubert Klahr

the following chapter was submitted as a letter to the editor of *Astronomy & Astrophysics*

Context: Gas in protoplanetary disks mostly cools via thermal accommodation with dust particles. Thermal relaxation is thus highly sensitive to the local dust size distribution and the spatial distribution of the grains. So far, the interplay between thermal relaxation and gas turbulence has not been dynamically modeled in hydrodynamic simulations of protoplanetary disks with dust.

Aims: We aim to study the effects of the vertical shear instability (VSI) on the thermal relaxation times and vice-versa. We are particularly interested in the influence of the initial dust grain size on the VSI and whether the emerging turbulence is sustained over long timescales.

Methods: We run three axisymmetric hydrodynamic simulations of a protoplanetary disk including four dust fluids that initially resemble MRN size distributions of different initial grain sizes. From the local dust densities, we calculate the thermal accommodation timescale of dust and gas during the hydrodynamic simulations and use the result as the thermal relaxation time of the gas. We include the effect of dust growth by applying the monodisperse dust growth rate and the typical growth limits.

Results: We find that the emergence of the VSI is strongly dependent on the initial dust grain size. Coagulation also counteracts the emergence of hydrodynamic turbulence in our simulations. Starting a simulation with larger grains (100 µm) generally leads to a less turbulent outcome. While the inner disk regions (within ~ 70 au) develop turbulence in all three simulations, we find that the simulations with larger particles do not develop VSI in the outer disk.

Conclusions: Our simulations with dynamically calculated thermal accommodation times based on the drifting and settling dust distribution show that the VSI, once developed in a disk, can be sustained over long timescales, even if grain growth is occurring. The VSI corrugates the dust layer and even diffuses the smaller grains into the upper atmosphere, where they can cool the gas. Whether the instability can emerge for a specific stratification depends on the initial dust grain sizes and the initial dust scale height. If the grains are initially $\gtrsim 100$ µm and if the level of turbulence is initially assumed to be low, we find no VSI in the outer disk regions.

Author Contributions:

Thomas Pfeil:	numerical simulations, data analysis, figure plotting, manuscript writing
Prof. Til Birnstiel:	scientific discussion, proof reading, project supervision
Prof. Hubert Klahr:	scientific discussion, proof reading, project supervision

5.1 Introduction

Thermal relaxation of temperature perturbations in protoplanetary disks occurs in a two-step process, where collisions thermally couple the slowly cooling gas with the quickly cooling dust grains which then emit or absorb electromagnetic radiation (Malygin et al., 2014; Woitke, 2015; Malygin et al., 2017; Barranco et al., 2018). The local dust size distribution thus plays a crucial role when it comes to the determination of the thermal relaxation time of the gas. Many thermal and hydrodynamic instabilities depend on this timescale (e.g., Convective Overstability, Klahr & Hubbard (2014); Vertical Shear Instability, Urpin & Brandenburg (1998); Nelson et al. (2013); Zombie Vortex Instability, Marcus et al. (2015); etc.). Turbulence resulting from these instabilities can redistribute the dust grains due to aerodynamic drag, altering the cooling timescale itself. Continuous remodeling of the cooling times in hydrodynamic simulation of protoplanetary disks is thus desirable.

In this letter, we present axisymmetric simulations of protoplanetary disks that, for the first time, combine the effects of dust grain growth and the emergence of hydrodynamic turbulence on the cooling times. We are specifically interested in the effect on the vertical shear instability (VSI). Various studies have shown its strong dependence on the thermal relaxation time (e.g., Urpin, 2003; Lin & Youdin, 2015; Manger et al., 2021; Pfeil & Klahr, 2021). VSI requires rapid cooling on a timescale ideally shorter than

$$t_\mathrm{c} \lesssim \frac{H_\mathrm{g}}{R} \frac{|\beta_T|\gamma}{2(\gamma-1)} \left|\frac{z}{H_\mathrm{g}}\right|^{-1} \Omega_\mathrm{K}^{-1}, \tag{5.1}$$

where H_g is the disk's gas pressure scale height, R is the distance from the central star, β_T is the exponent of the radial temperature structure $T \propto R^{\beta_T}$, γ is the heat capacity ratio, z is the distance from the disk midplane, and Ω_K is the Keplerian angular frequency. Urpin (2003) already showed that the VSI's growth rate decreases at thermal relaxation times beyond this limit, which was recently demonstrated in numerical simulations by Klahr et al. (2023).

At the same time, VSI creates mostly meridional gas flows and its ability to vertically corrugate the dust layer has been demonstrated in various simulations (Stoll & Kley, 2016; Lin, 2019; Flock et al., 2020; Schäfer et al., 2020; Schäfer & Johansen, 2022; Fukuhara et al., 2023; Pfeil et al., 2023).

It is however unclear whether the VSI evolves fast enough to avoid the effects of dust settling and maintain a dust layer that is thick enough to provide the necessary fast thermal relaxation times. If the grains are large and the cooling times are long, it would be possible that the VSI is not able to develop in the first place or is not able to counteract the settling

of the grains. Work by Fukuhara et al. (2023) has demonstrated that an equilibrium state might be possible in which the turbulent mixing of the VSI exactly counteracts sedimentation. Their studies are however not self-consistently modeling the dust dynamics and do not take the effect of dust growth into account. As radiative cooling, dust dynamics, and dust coagulation are interdependent processes, they would have to be accounted for in a single simulation. Such a fully self-consistent numerical model of the VSI in protoplanetary disks is currently out of scope. If however, reasonable approximations are made, aspects of this interplay can be studied with much simpler techniques. Here we present hydrodynamic simulations of protoplanetary disks including four dust fluids of evolving grain sizes, to investigate the impact of the VSI-induced turbulence on the cooling times. We omit a full treatment of dust coagulation and only evolve the grain size based on an analytic dust growth model (similar to Birnstiel et al., 2012). Instead of including radiative transfer calculations to model the impact of the evolving dust distribution on the radiative cooling, we relax temperature perturbations on a timescale which is calculated from the local dust size distribution. Although these methods are only approximations, they enable the first simulations of protoplanetary disks in which the time scale for the thermal accommodation of gas and dust is directly linked to the dynamics of the simulated dust fluids.

5.2 Methods

Thermal Relaxation Times

Since thermal relaxation is achieved via thermal accommodation with the dust, we approximate

$$t_{\mathrm{thin}}^{\mathrm{NLTE}} \approx t_{\mathrm{coll}}^{\mathrm{gas}} = \frac{\gamma}{\gamma - 1} \frac{1}{n_{\mathrm{s}} \bar{v}_{\mathrm{gas}} \sigma_{\mathrm{s}}} , \tag{5.2}$$

where $t_{\mathrm{coll}}^{\mathrm{gas}}$ is the thermal accommodation time scale of the gas with the dust due to collisions (Probstein, 1969; Burke & Hollenbach, 1983; Barranco et al., 2018). The thermal accommodation timescale therefore depends on the mean molecular gas velocity $\bar{v}_{\mathrm{gas}}$ and the Sauter mean radius of the dust size distribution (Sauter, 1926)

$$a_{\mathrm{s}} = \frac{\int n(a) a^3 \, \mathrm{d}a}{\int n(a) a^2 \, \mathrm{d}a} , \tag{5.3}$$

from which the number density $n_{\mathrm{s}} = \rho_{\mathrm{d}} / (4/3 \pi \rho_{\mathrm{m}} a_{\mathrm{s}}^3)$ and the collisional cross-section $\sigma_{\mathrm{s}} = \pi a_{\mathrm{s}}^2$ follow. Here, ρ_{m} is the material density of the dust and ρ_{d} is the dust volume density. In most cases, the size distribution of dust in a protoplanetary disk can be approximated as a truncated power law, following

$$n(a) = \frac{n_{\mathrm{tot}} (p+1)}{a_{\mathrm{max}}^{p+1} - a_{\mathrm{min}}^{p+1}} a^p , \tag{5.4}$$

where n_{tot} is the total dust number density and a_{min} and a_{max} are the minimum and maximum grain sizes that truncate the distribution. Typical values of p are in the range of -4 to -2, depending on the physical details of the grain collisions.

Considering a discretized version of the size distribution with bins of size $\Delta a = a_{i+1/2} - a_{i-1/2}$, we can write the same size distribution as

$$n(a) = \sum_{i=1}^{N} \frac{n_i\,(p+1)}{a_{i+1/2}^{p+1} - a_{i-1/2}^{p+1}} a_i^p \Theta(a_{i+1/2} - a)\Theta(a - a_{i-1/2})\,, \tag{5.5}$$

where each bin i contains a total number density of n_i, and the size-grid cell interfaces are $a_{i-1/2} > a_{\min}$ and $a_{i+1/2} < a_{\max}$. Θ denotes the Heaviside step function and truncates every bin at $a_{i+1/2}$ and $a_{i-1/2}$. This assumes that the size distribution is a continuous power law with exponent p in each bin. With these definitions, we can rewrite the numerator of Equation 5.3 as

$$\int n(a) a^3 \,\mathrm{d}a = \frac{p+1}{p+4} \sum_{i=1}^{N} n_i \frac{a_{i+1/2}^{p+4} - a_{i-1/2}^{p+4}}{a_{i+1/2}^{p+1} - a_{i-1/2}^{p+1}} \coloneqq \sum_{i=1}^{N} n_i \chi_i\,.$$

Likewise, we can write the denominator of Equation 5.3

$$\int n(a) a^2 \,\mathrm{d}a = \frac{p+1}{p+3} \sum_{i=1}^{N} n_i \frac{a_{i+1/2}^{p+3} - a_{i-1/2}^{p+3}}{a_{i+1/2}^{p+1} - a_{i-1/2}^{p+1}} \coloneqq \sum_{i=1}^{N} n_i \xi_i\,.$$

If the bin interfaces are fixed in time and if we assume constant p in every bin at all times, ξ_i and χ_i are constants. With these definitions, the Sauter mean of the entire size distribution can be written

$$a_{\mathrm{s}} = \sum_{i=1}^{N} n_i \chi_i \Bigg/ \sum_{i=1}^{N} n_i \xi_i\,. \tag{5.6}$$

The calculation of the Sauter mean radius in hydrodynamic simulation of dust and gas is therefore reduced to the calculation of the dust number density n_i for the given dust size bins. Knowledge of the Sauter mean allows us to calculate $t_{\mathrm{thin}}^{\mathrm{NLTE}}$ from Equation 5.2. If gas and dust are treated through radiative transfer, as in Muley et al. (2023), $t_{\mathrm{thin}}^{\mathrm{NLTE}}$ can be used to dynamically relax the gas and dust temperatures with respect to each other. In a simpler use case, $t_{\mathrm{thin}}^{\mathrm{NLTE}}$ can be used as a dynamically evolving cooling timescale of the gas via

$$T^{(n+1)} = T_{\mathrm{eq}} + (T^{(n)} - T_{\mathrm{eq}}) \exp\left(-\frac{\Delta t}{t_{\mathrm{thin}}^{\mathrm{NLTE}}}\right), \tag{5.7}$$

where T_{eq} is the equilibrium temperature (set by stellar irradiation) and Δt is the current simulation time step. We demonstrate the latter case in hydrodynamic simulations of protoplanetary disks with a focus on the VSI activity in the next section.

Hydrodynamic Simulations

We set up axisymmetric simulations in the r-ϑ plane of a protoplanetary disk in spherical coordinates. Our disk's initial, hydrostatic structure follows the standard accretion disk with mass M_{disk} by Lynden-Bell & Pringle (1974) with a truncated power law in column

Table 5.1: Simulation parameters of the three presented runs. The only difference between the simulations is the initial particle size.

Simulation Parameter	Value
Inner boundary R_{in}	25 au
Outer boundary R_{out}	150 au
Vertical extend $\Delta\vartheta$	$\pm 3 H/R(50\,\mathrm{au})$
Resolution $N_r \times N_\vartheta$	2011×512
Stellar mass M_*	$1\,M_\odot$
Disk gas mass M_{disk}	$0.05\,M_\odot$
Temperature power law β_T	-0.5
Column density power law β_Σ	-0.85
Heat capacity ratio γ	1.4
Disk aspect ratio $H/R(50\,\mathrm{au})$	0.07957
Disk characteristic radius R_{c}	60 au
Minimum particle size a_{min}	0.1 µm
Initial particle sizes a_{ini}	1 µm, 10 µm and 100 µm
Fragmentation velocity v_{frag}	$500\,\mathrm{cm\,s^{-1}}$
Initial dust-to-gas ratio $\varepsilon_0 = \Sigma_{\mathrm{d},0}/\Sigma_{\mathrm{g},0}$	0.01
Size distribution power law p	-3.5
Initial dust diffusivity δ_{ini}	10^{-5}
Dust material density ρ_{m}	$1.67\,\mathrm{g\,cm^{-3}}$

density with exponent β_Σ and characteristic radius R_{c}

$$\Sigma_{\mathrm{g}}(R) = (2+\beta_\Sigma)\frac{M_{\mathrm{disk}}}{2\pi R_{\mathrm{c}}^2}\left(\frac{R}{R_{\mathrm{c}}}\right)^{\beta_\Sigma}\exp\left[-\left(\frac{R}{R_{\mathrm{c}}}\right)^{2+\beta_\Sigma}\right]. \tag{5.8}$$

From this, the vertical disk structure in z follows via

$$\rho_{\mathrm{g}} = \rho_{\mathrm{g,mid}}\exp\left[\left(\frac{H_{\mathrm{g}}}{R}\right)^{-2}\left(\frac{R}{\sqrt{R^2+z^2}}-1\right)\right], \tag{5.9}$$

where we approximate the midplane dust density as $\rho_{\mathrm{g,mid}} \approx \Sigma_{\mathrm{g}}(r)/\sqrt{2\pi}H_{\mathrm{g}}$. The angular frequency in hydrostatic equilibrium follows accordingly as

$$\begin{aligned}\frac{\Omega^2(R,z)}{\Omega_{\mathrm{K}}^2} = &\left(\frac{H_{\mathrm{g}}}{R}\right)^2\left(\beta_T+\beta_\rho-(\beta_\Sigma+2)\left(\frac{R}{R_{\mathrm{c}}}\right)^{\beta_\Sigma+2}\right)\\ &-\frac{\beta_T R}{\sqrt{R^2+z^2}}+\beta_T+1\,,\end{aligned} \tag{5.10}$$

where β_ρ is the power-law exponent of the radial midplane density profile $\rho_{\mathrm{g,mid}} \propto R^{\beta_\rho}\exp\left[-(R/R_{\mathrm{c}})^{\beta_\Sigma+2}\right]$.

For the dust, we initialize the simulation with a Mathis, Rumpl, & Nordsieck (1977) (MRN) distribution with $N = 4$ dust fluids according to Equation 5.5. We conduct simu-

lations with three different initial dust grain sizes $a_{\rm ini}$ =1 µm, 10 µm and 100 µm. As the grains should undergo coagulation, we let the maximum grain size evolve in time following

$$a_{\rm max}(t) = \frac{a_{\rm lim} a_{\rm ini} e^{t\ \varepsilon_0\ \Omega_{\rm K}}}{a_{\rm lim} + a_{\rm ini}\left(e^{t\ \varepsilon_0\ \Omega_{\rm K}} - 1\right)}\,, \tag{5.11}$$

where the limiting particle size $a_{\rm lim} = \min(a_{\rm frag}, a_{\rm frag\text{-}drift})$ is determined by the fragmentation velocity $v_{\rm frag} = 500\,{\rm cm\,s^{-1}}$, the radial pressure gradient, and the level of turbulence, characterized by the α parameter (see Birnstiel et al., 2012, and Section 2.2.2 for definitions). As our simulations are initialized without turbulence, we set this parameter to a very low value of 10^{-5}. The particle growth is thus limited by the drift-fragmentation limit ($\sim$ 1 cm) instead of the turbulent fragmentation limit. The growth rate of the particles depends on the initial dust-to-gas ratio $\varepsilon_0 = {}^{\Sigma_{\rm d,0}}/_{\Sigma_{\rm g,0}}$ via $\dot{a}_{\rm max} = a_{\rm max}\varepsilon_0\Omega_{\rm K}(1 - {}^{a_{\rm max}}/_{a_{\rm lim}})$. We do not change the mass content of the four dust-size bins during the growth. Only the bin interfaces and the respective mass-averaged particle size of each bin change due to growth. Growth therefore also influences the thermal accommodation times. As mass is shifted to larger sizes, fewer small grains are present and thus dust-gas collision rates decrease with time.

The four passive dust fluids are advected using the same technique as in Pfeil et al. (2023) and thus evolve under the influence of settling and radial drift in the terminal velocity approximation. The respective velocity components are calculated from the dust populations' mass-averaged particle size, where an MRN size distribution is assumed within each bin at all times. The bin boundaries are defined to be equidistant in log-space. The size grid is then defined between $a_{\rm min}$ as the lower boundary of the first cell and $a_{\rm max}$ as the upper boundary of the last cell.

The initial dust distribution of each population follows the same vertical structure as the gas but instead of the gas scale height with the dust scale height

$$H_{\rm d} = H_{\rm g}\sqrt{\frac{\delta_{\rm ini}}{\delta_{\rm ini} + {\rm St}_i}}\,, \tag{5.12}$$

where ${\rm St}_i = {}^{\pi a_i \rho_{\rm m}}/_{2\Sigma_{\rm g}}$ is the Stokes number of the respective dust fluid and $\delta_{\rm ini} = \alpha$ is the initially assumed dust diffusivity. Simulations initialized with different particle sizes also have dust layers of different initial heights and cooling times. This can be seen in Figure 5.1, where the top panels show the initial distribution of dust in the inner and outer disk regions as dashed lines. Cooling times increase with height since the dust density decreases with distance from the midplane. We show the cooling times in units of the local, critical cooling time of the VSI. Values above 1 correspond to regions that are not susceptible to linear instability due to the vertical shear.

We run the simulations for 1000 orbital timescales at 50 au, i.e., 353 553 yr and present the simulation parameters in Table 5.1.

5.3 Results

We present the radially-averaged vertical dust distributions and the respective cooling times at the beginning and at the end of the simulation in Figure 5.1, where we distinguish between an inner disk region (30–55 au) and an outer disk region (115–150 au). In Pfeil et al. (2023) (Chapter 4), we conducted simulations with static cooling times and showed that the VSI preferentially develops in the inner disks if the dust is already grown. We observe a qualitatively similar result here. The ongoing dust growth in the new simulations, however, modifies the results and imposes stricter conditions on whether the VSI can emerge. The turbulence is in every case stronger in the inner disk regions, where it maintains a relatively thick dust layer with an almost vertically constant dust-to-gas ratio ε and a stable vertical distribution of cooling times. The outer regions show more settling due to the longer growth timescale of the VSI. Continued settling during the simulation is however of minor importance for the cooling times compared to the coagulation process because thermal relaxation is mostly done by small particles that have very long settling times.

Whether the VSI develops at all, strongly depends on the initial maximum particle size and thus the initial vertical distribution of small dust grains. If the particles are small at the beginning of the simulation, as in the case with $a_{\mathrm{ini}} = 1\,\mu\mathrm{m}$, thermal accommodation times are short almost everywhere in the disk and the VSI develops quickly. The resulting turbulence keeps the dust layer vertically extended and thus maintains the necessary cooling times self-sufficiently. This can also be seen in the first row of Figure 5.2, which shows the dust distribution and the respective cooling times at the end of the simulation. Regions inside of ~ 100 au show the typical filamentary VSI pattern in the dust densities and thus also in the cooling times. The outer regions develop slower and no VSI is present after 350 000 yr of evolution.

The situation is different in the simulation with initially large particles with $a_{\mathrm{ini}} = 100\,\mu\mathrm{m}$. The dust grains are strongly settled at the beginning of the simulation, meaning that the

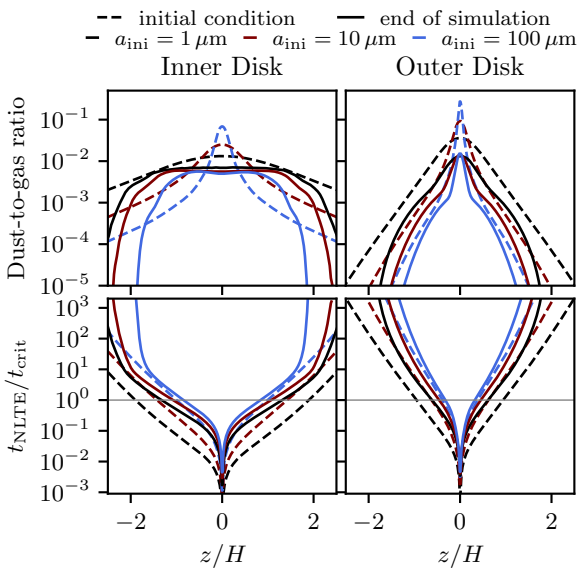

Figure 5.1
Dust-to-gas ratios and thermal relaxation times, radially-averaged over in the 30–55 au inner region and the 115–150 au outer region of our simulations. As the VSI develops, it keeps the dust particle at high altitudes and thus retains the necessary cooling times in the inner disk. The outer regions, however, are mostly sedimenting, as the VSI is not active there, except for the case with the smallest initial particle size.

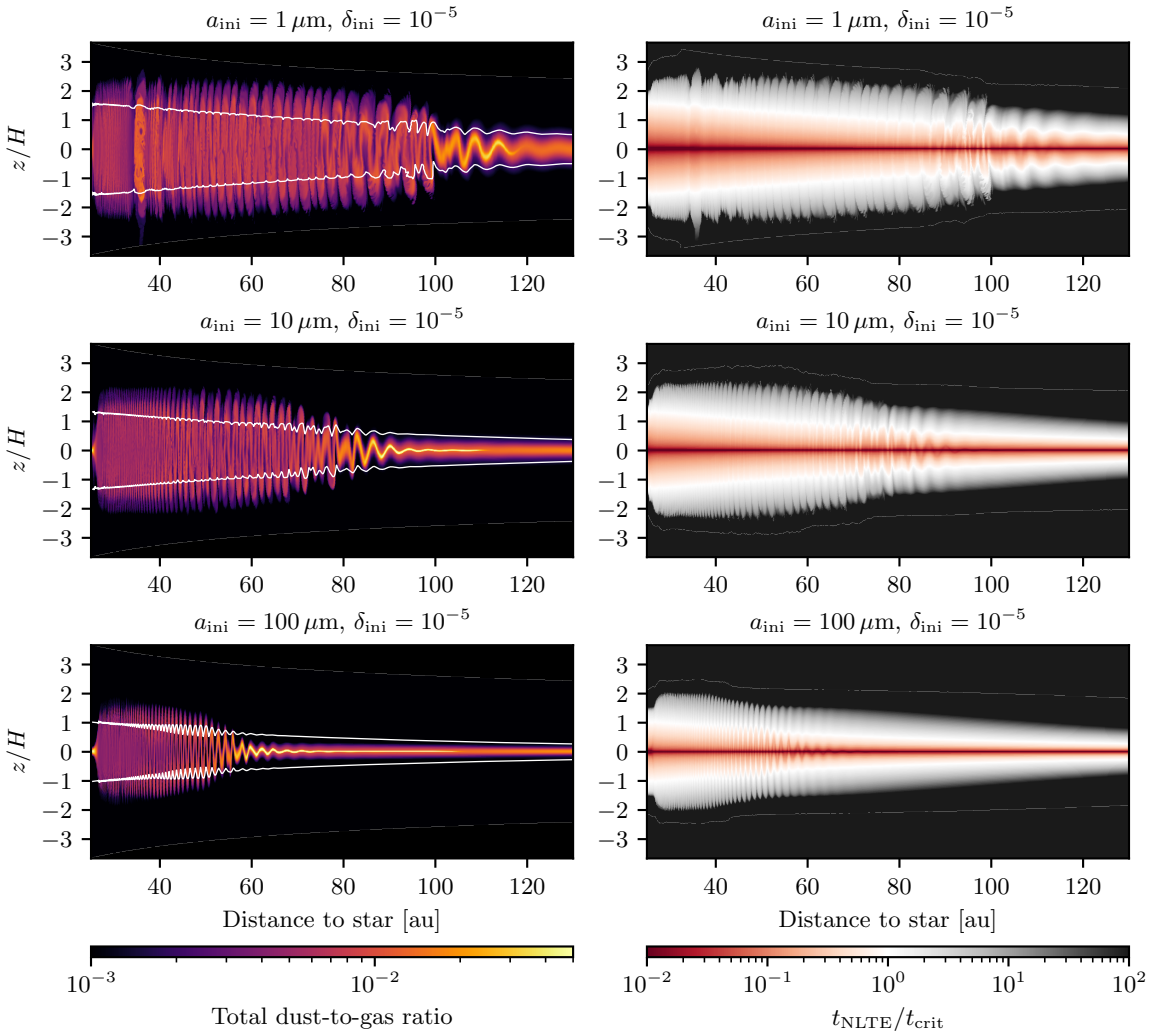

Figure 5.2
Snapshots of our protoplanetary disk simulations with thermal accommodation times calculated from the dust distribution for three different initial particle sizes after ~350 000 yr of evolution. Simulations initialized with larger particles and thus more settled dust layers, are mostly not VSI-active in the outer disk regions. If the VSI can develop in the first place, it can stabilize the dust layer and sustain itself even if grain growth is considered.

cooling times in the upper disk atmosphere are accordingly long. VSI begins to develop in the inner disk at a lower intensity than in the small-particle case. Nonetheless, a sufficiently thick layer of small dust is maintained, thus keeping the cooling times low enough in the inner regions.

The inner disk regions become VSI turbulent in all three cases, however on different timescales and at different intensities. The outer areas evolve differently. For small initial particle sizes, we see that the VSI begins to develop at the end of the simulation. For larger particles, however, the outer disk areas are completely VSI-inactive due to the already long cooling times at the beginning of the simulation. Regions beyond 70 au are not VSI-active

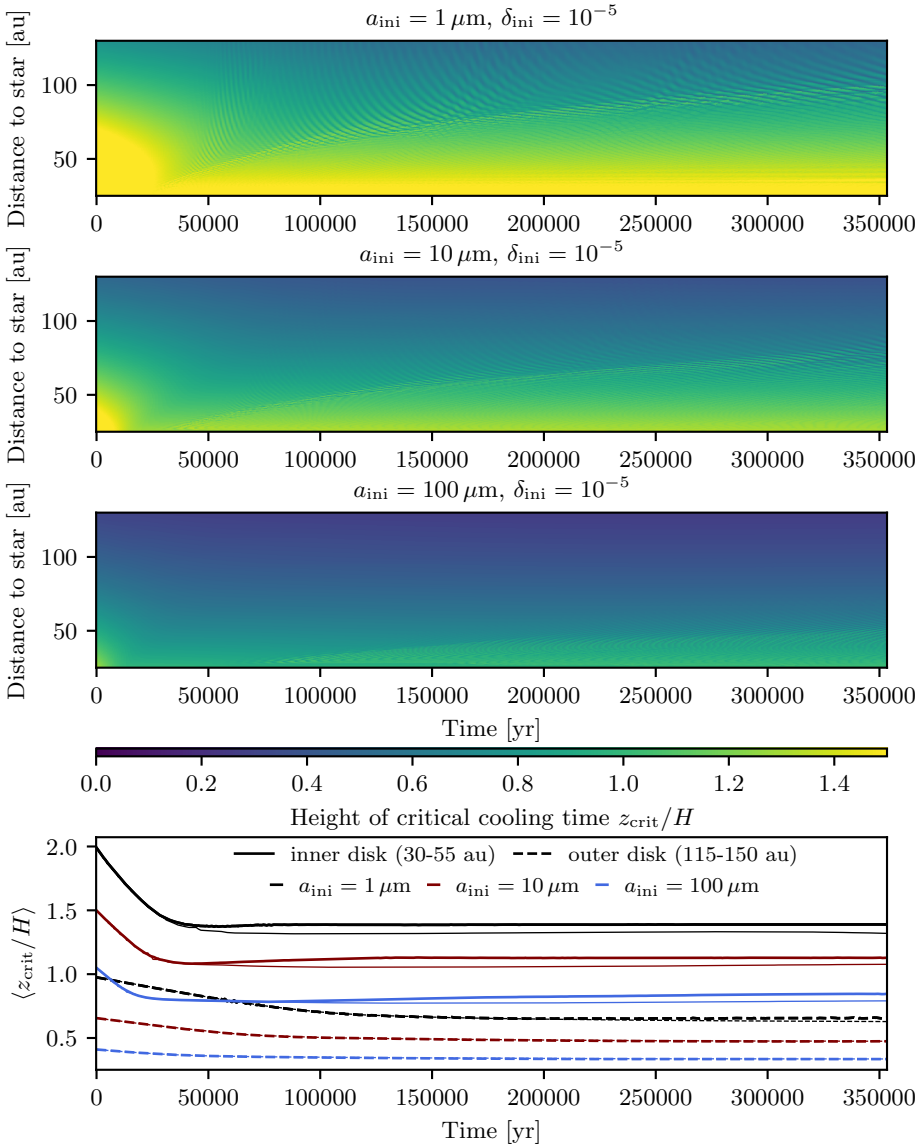

Figure 5.3
Evolution of the vertical extend of the VSI-susceptible region as a function of time and radius. In the inner disk, VSI quickly develops and stabilizes the settling dust layer in less than 50 000 yr. In the outer disk, VSI has not yet developed in our simulations. The thin lines show comparison simulations in which the VSI is artificially suppressed.

for the largest initial particle size of $a_{\mathrm{ini}} = 100\,\mu\mathrm{m}$. For ten times smaller particles, VSI is active up to 90 au at the end of the simulation.

To visualize the impact of the VSI on the cooling times, we plot the height at which the critical cooling time for the VSI is reached (Equation 5.1) as a function of time and radius in Figure 5.3. The beginning of all three simulations is characterized by the growth of the particles and the subsequent settling of the larger grains in the first $\sim 40\,000$ yr. During this time, the surfaces of the VSI-susceptible zone move toward the midplane of the disk. This is mostly due to the coagulation process, which transforms small, not sedimented grains into larger and quickly sedimenting ones. Cooling times are mostly determined by the small grains that remain in the atmosphere and only sediment slowly. The critical surface is thus only moving toward the midplane because mass is transferred from small grains to big grains. During this initial particle growth, the first VSI modes develop in the inner regions of the disk and soon begin to corrugate the dust layer. The emerging VSI turbulence stabilizes the extent of the VSI-susceptible zone and even moves small grains up into the disk atmosphere, thus extending the susceptible region with time in the inner disk. In the simulation with the smallest initial particle size, the critical height reaches a stable value of $\sim 1.5\,H$ in the regions close to the star. If the simulations are initialized with larger, and thus strongly sedimented particles, we see that the initial vertical extent of the susceptible zone is already small. For $a_{\mathrm{ini}} = 10\,\mu\mathrm{m}$, the critical height is stabilized at $\sim 1.2\,H$; for $a_{\mathrm{ini}} = 100\,\mu\mathrm{m}$ at $\sim 0.8\,H$.

In the outer regions, VSI either develops very slowly (in the case of the smallest initial particle size of 1 µm) or not at all during the runtime of our simulations. This is a result of the limited simulation time and could also be a resolution issue, as the fastest growing modes become smaller with longer cooling times. The trend is nonetheless clear: If a hydrodynamic simulation is initialized with large (100 µm), settled particles (here for $\delta_{\mathrm{ini}} = 10^{-5}$), VSI only develops slowly, or possibly not at all during the lifetime of a protoplanetary disk.

If the particles are initially small, or vertically dispersed, VSI can develop quickly and even extend the susceptible region by diffusing small particles to the upper disk layers.

5.4 Discussion

Our studies allow for a first insight into the interplay of VSI and its influence on the cooling times and vice-versa. There are nonetheless various limitations to the presented approach. We only model the size distribution with four dust fluids and assume each size bin to have an MRN particle size distribution. At the beginning of the simulation, the size distribution is continuous. When the dust fluids begin to drift and sediment this changes and the complete size distribution is no longer an MRN distribution. In the future, the coagulation and fragmentation process should be considered when the dust populations evolve. In that way, a meaningful size distribution could be maintained during the simulations. We also set up the initial dust structure in settling-mixing equilibrium at all heights. This is strictly speaking only valid for Stokes numbers $\ll 1$ because the terminal velocity approximation is used in the derivations (Dubrulle et al., 1995). At large distances from the midplane, our initial conditions might thus not be realistic. We model the dust as a passive fluid.

Therefore, back-reaction, which was shown to be able to quench the VSI-activity in the disk midplane, especially if the dust settles, could not be accounted for (Schäfer et al., 2020). The settling however occurs mostly once the dust has grown. We thus do not expect it to be able to hinder the VSI growth in the inner disk.

We have not tested other initial size distribution power laws than the MRN distribution. If initially more small dust were present, the conditions could be more favorable for the VSI. The same is true if the fragmentation velocity is smaller, which counteracts the production of large grains.

Furthermore, we have modeled the dust size as a vertically global quantity. Simulations of coagulation that consider a vertically varying dust size and coagulation at all heights have shown that dust growth can start in the upper layers, where the relative sedimentation velocities are high. This sedimentation-driven coagulation depletes the upper layers of grains, which coagulate, fragment, and sediment continuously (Zsom et al., 2011). A full radial-vertical treatment of coagulation must thus be applied in future studies.

Other sources of cooling have also not been accounted for in our study. Especially in the upper disk atmosphere, cooling through molecular line emission could be the dominant channel of thermal relaxation (Woitke, 2015). These considerations however require thermo-chemical modeling of the different molecular species, which is currently out of scope for the presented work. A future self-consistent study of VSI with realistic thermal relaxation also has to involve the treatment of radiative transfer, ideally in a three-temperature framework as recently presented by Muley et al. (2023). This is especially important when the effects of stellar irradiation and thermal relaxation in the optically thick regime should be included.

One of the caveats in the study of the VSI in protoplanetary disks remains the poorly constrained initial conditions of the simulations. Specifically, the state of the dust size distribution and the initial vertical extent of the dust layer are important for the onset of the VSI because they determine the cooling times. If the dust at the beginning of the disk's lifetime is very small (~1 µm) we would expect the VSI to develop within the first 350 000 yr of disk evolution even in the outer regions. Small dust would be expected if the grains resemble interstellar dust or if an intense source of turbulence during the disk formation process has caused strong fragmentation. The initial phases might be gravitoturbulent which could cause such high initial levels of turbulence (Gammie, 2001; Johnson & Gammie, 2003; Hirose & Shi, 2017; Zier & Springel, 2023). Some observations and studies however hint towards early grain growth, which would cause less favorable conditions for the VSI (Galametz et al., 2019; Bate, 2022)

5.5 Conclusions

We have for the first time conducted hydrodynamic simulations of protoplanetary disks with thermal accommodation times that are consistent with the simulated dust densities and the present grain size. This made it possible to assess the influence of different initial conditions and dust grain growth on the developing VSI. The initial dust distribution is found to have the biggest influence on the resulting spatial distribution of the turbulent gas flows. Coagulation also increases the cooling times and thus counteracts the VSI. This

effect is however not a significant hurdle for the development of hydrodynamic turbulence in the inner regions of protoplanetary disks (inside of 70 au), even if the dust is already large (100 µm) and vertically settled at the beginning of the simulation. VSI can develop during the initial growth phase and even extend the susceptible region by diffusing small grains vertically. In the outer regions of protoplanetary disks (beyond 70 au), the situation is more difficult for the VSI. If the dust is assumed to be big at the beginning of the simulation (100 µm) and is assumed to be in settling-mixing equilibrium (with a low initial diffusivity of $\delta = 10^{-5}$), we find that the potentially VSI-susceptible region is constraint to a small area around the midplane and will probably not develop VSI-induced turbulence during the disk's lifetime.

Note, that although our three simulations only differ in their initial dust grain size and reach identical maximum particle sizes, the resulting spatial distribution of dust and the level of VSI turbulence are vastly different between the three runs. Whether a specific disk stratification will develop VSI turbulence is thus highly dependent on the initial dust size distribution and the initial dust scale height.

Acknowledgments

T.P., H.K., and T.B. acknowledge the support of the German Science Foundation (DFG) priority program SPP 1992 "Exploring the Diversity of Extrasolar Planets" under grant Nos. BI 1816/7-2 and KL 1469/16-1/2. T.B. acknowledges funding from the European Research Council (ERC) under the European Union's Horizon 2020 research and innovation programme under grant agreement No 714769 and funding by the Deutsche Forschungsgemeinschaft (DFG, German Research Foundation) under grants 361140270, 325594231, and Germany's Excellence Strategy - EXC-2094 - 390783311. Computations were conducted on the computational facilities of the University of Munich (LMU) and on the c2pap cluster at the Leibnitz Rechenzentrum under project pn36ta.

CHAPTER 6

TRIPOD: TRI-POPULATION SIZE DISTRIBUTIONS FOR DUST EVOLUTION

COAGULATION IN VERTICALLY INTEGRATED HYDRODYNAMIC SIMULATIONS OF PROTOPLANETARY DISKS WITH PLUTO

Thomas Pfeil, Tilman Birnstiel, and Hubert Klahr,

the following chapter was submitted to *Astronomy & Astrophysics*

Context: Dust coagulation and fragmentation impact the structure and evolution of protoplanetary disks and set the initial conditions for planet formation. Dust grains dominate the opacities, they determine the cooling times of the gas via thermal accommodation in collisions, they influence the ionization state of the gas, and the available grain surface area is an important parameter for the chemistry in protoplanetary disks. Therefore, dust evolution is an effect that should not be ignored in numerical studies of protoplanetary disks. Available dust coagulation models are, however, too computationally expensive to be implemented in large-scale hydrodynamic simulations. This limits detailed numerical studies of protoplanetary disks, including these effects, mostly to one-dimensional models.

Aims: We aim to develop a simple—yet accurate—dust coagulation model that can be easily implemented in hydrodynamic simulations of protoplanetary disks. Our model shall not significantly increase the computational cost of simulations and provide information about the local grain size distribution.

Methods: The local dust size distributions are assumed to be truncated power laws. Such distributions can be fully characterized by only two dust fluids (large and small grains) and a maximum particle size, truncating the power law. We compare our model to state-of-the-art dust coagulation simulations and calibrate it to achieve a good fit with these sophisticated numerical methods.

Results: Running various parameter studies, we achieved a good fit between our simplified three-parameter model and DustPy, a state-of-the-art dust coagulation software.

Conclusions: We present TriPoD, a sub-grid dust coagulation model for the PLUTO code. With TriPoD, we can perform two-dimensional, vertically integrated dust coagulation simulations on top of the hydrodynamics code. Studying the dust distributions in two-dimensional vortices and in planet-disk systems is thus made possible.

Author Contributions:

Thomas Pfeil:	numerical simulations, data analysis, figure plotting, manuscript writing
Prof. Til Birnstiel:	scientific discussion, proof reading, project supervision
Prof. Hubert Klahr:	scientific discussion, proof reading, project supervision

6.1 Introduction

Models of dust coagulation in protoplanetary disks are required to understand the formation of cm-sized pebbles (Brauer et al., 2008; Birnstiel et al., 2009) and km-sized planetesimals (Wetherill & Stewart, 1989; Schlichting & Sari, 2011; Kobayashi et al., 2016; Lau et al., 2022; Drążkowska et al., 2023); they are indispensable for the interpretation of observational data (Birnstiel et al., 2018; Dullemond et al., 2018) and necessary to simulate the assembly of whole planetary systems (Lichtenberg et al., 2021; Emsenhuber et al., 2021). The size of the dust grains also determines their aerodynamic properties and thus sets the timescale at which grains drift towards the central star and collect in local pressure maxima (Whipple, 1972; Weidenschilling, 1977). Furthermore, dust is the dominating source of opacity in circumstellar disks, which means the size distribution of the dust grains has a strong influence on the disks' thermal structure (Muley et al., 2023) and hydrodynamics (Lesur et al., 2023), as well as on the interpretation of observations (Birnstiel et al., 2018; Leiendecker et al., 2022; Bergez-Casalou et al., 2022; Antonellini et al., 2023). In addition, the presence of small grains sets limits to the disks' ionization and is thus also important for studies of magnetohydrodynamic mechanisms like the MRI (Balbus & Hawley, 1991) and magnetized disk winds (Blandford & Payne, 1982) with non-ideal MHD effects (Guillet et al., 2020; Pascucci et al., 2023; Tsukamoto & Okuzumi, 2022). In 2018, observation with the Atacama Large Millimeter/submillimeter Array (ALMA) revealed that a broad variety of substructures exist in the spatial distribution of dust in protoplanetary disks (Andrews et al., 2018). Numerous gaps, spirals, and vortices have since been observed in the dust continuum emission (e.g., Pérez et al., 2018; Baruteau et al., 2019; Tsukagoshi et al., 2022) and also in molecular line observations (see Öberg et al., 2021). The existence of these structures raises questions regarding their origins and how they impact the formation and composition of planetesimals and planets within the disks—which makes hydrodynamic simulations of protoplanetary disks, including dust coagulation models, necessary (Birnstiel et al., 2018; Drążkowska et al., 2019).

Modeling the evolution of the solid content of protoplanetary disks has proven to be an expensive task in computational astrophysics. Many dust evolution models (e.g. Nakagawa et al., 1981; Weidenschilling, 1980; Brauer et al., 2008; Birnstiel et al., 2010; Charnoz & Taillifet, 2012; Drążkowska et al., 2019), numerically solve a discretized form of the Smoluchowski coagulation equation (Smoluchowski, 1916). The coagulation equation's integro-differential nature makes solving it, however, numerically costly. This procedure utilizes a grid of grain sizes, meaning that dozens or hundreds of dust fluids have to be modeled in a single simulation, each representing grains of a different size that interact

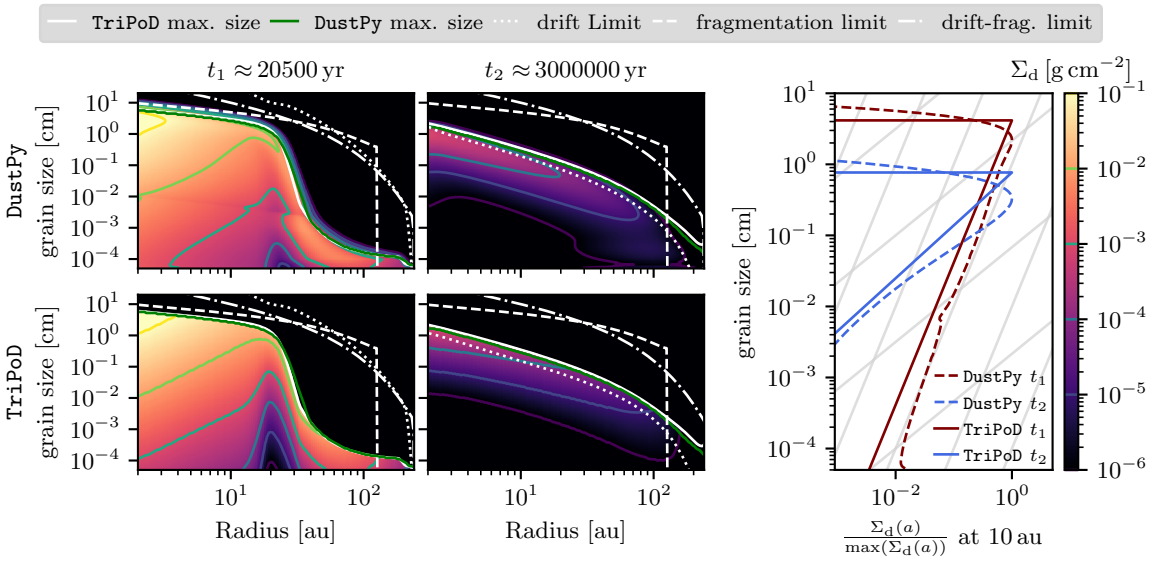

Figure 6.1
Comparison between the full coagulation model `DustPy` (upper row, 171 dust fluids) and our new three-parameter power-law prescription `TriPoD`, which we implemented in the `PLUTO` code (two dust fluids). We show two snapshots of the one-dimensional disk models in the first two panels in each row. The third panel in each row shows the local dust size distribution of the respective model at 10 au for both snapshots. The light grid in the background represents size distribution power laws with $n(a) \propto a^{-3.5}$ and $n(a) \propto a^{-2.5}$.

with every other grain size via collisions. Studies of dust coagulation are often carried out in one-dimensional disk models in either the radial direction (e.g., Lenz et al., 2020; Drążkowska et al., 2021; Pinilla et al., 2021; Gárate et al., 2021; Burn et al., 2022), the vertical direction (e.g, Zsom et al., 2011; Krijt & Ciesla, 2016), or limited two-dimensional studies (Drążkowska et al., 2019).

Therefore, efforts are pursued to solve the coagulation equations more efficiently, e.g., by use of new numerical methods (Lombart et al., 2022), or by applying far-reaching simplifications to the physics of dust coagulation (Birnstiel et al., 2012) that make it possible to implement dust coagulation as a subgrid model in hydrodynamic simulations (Tamfal et al., 2018; Vorobyov et al., 2020). Machine-learning-aided techniques also promise a fast, yet simplified approach to model dust coagulation on top of a hydrodynamic simulation (Pfeil et al., 2022).

Here, we present a semi-analytic model of dust coagulation, which is based on a two-population approach, originally developed by (Birnstiel et al., 2012) and employed in various forms by others (Tamfal et al., 2018; Vorobyov et al., 2018; Vorobyov & Elbakyan, 2019; Vorobyov et al., 2019). This model, however, has the critical disadvantage of not evolving the full dust size distribution but only the maximum particle size. With our new model, we are now able to conduct two-dimensional, vertically integrated hydrodynamics simulations of protoplanetary disks with an evolving dust size distribution at low computational cost. Figure 6.1 shows an example comparison between a full coagulation simulation, conducted with `DustPy` (Stammler & Birnstiel, 2022)—a full-fledged dust coagulation software—and a one-dimensional hydrodynamic simulation with the `PLUTO` code equipped with our new

method. While one-dimensional hydrodynamics simulations do not allow for a direct comparison of performance, due to the different methods to handle the transport (DustPy utilizes an implicit integration scheme and does not solve the equations of hydrodynamics, but an advection-diffusion equation for a Keplerian disk), they allow for detailed tests of the accuracy of our new model.

This article is structured as follows: In Section 6.2, we briefly review the physics of dust dynamics and coagulation. We also give a short description of two-pop-py (Birnstiel et al., 2012), the progenitor of our new model. Section 6.3 introduces our new three-parameter dust coagulation model TriPoD and how it is integrated in the PLUTO hydrodynamics code (Mignone et al., 2007). As TriPoD is a highly simplified prescription of dust coagulation, we have to calibrate it to achieve a good fit with full coagulation models. The respective calibration runs are presented in Section 6.4. In Section 6.5, we present test simulations that demonstrate the accuracy of TriPoD in comparison with DustPy simulations. We also give an example of a two-dimensional simulation of a planet-disk system in which we compare the outcome of our new model to the old two-pop-py model. We discuss the limitations of our approach in Section 6.6 and summarize in Section 6.7.

6.2 Theory

List of General Symbols

Symbol	Description
a	particle size
$\dot{a}$	dust growth rate
a_{drift}	drift-limited particle size
$a_{\text{drift-frag}}$	drift-fragmentation-limited particle size
a_{frag}	total fragmentation-limited particle size
$a_{\text{mon}}, a_{\text{gr}}$	monomer and grown dust size (two-pop-py)
$a_{\text{turb-frag}}$	turbulent-fragmentation-limited particle size
c_{s}	soundspeed
D	dust diffusivity
f_{fric}	aerodynamic friction force
f_{m}	fudge factor (two-pop-py)
G	gravitational constant
H_{g}	gas scale height
H_{d}	dust scale height
k_{B}	Boltzmann constant
L_*	stellar luminosity
m	particle mass
m_{p}	proton mass
M_*	stellar mass
M_{disk}	disk mass
$M_\odot$	solar mass

$n(a), n(m)$	number density size/mass disribution
$\mathcal{N}$	size ratio for drift-induced collisions
R	stellocentric cylindrical radius
R_c	characteristic disk radius
$\mathfrak{Re}$	Reynolds number
p	dust size distribution power-law exponent
p_m	dust mass distribution power-law exponent
P	gas pressure
St	Stokes number
t_fric	stopping time
t_grow	dust growth time scale
T	gas temperature
$\mathbb{T}$	viscous stress tensor
$\overline{v}$	average dust velocity (`two-pop-py`)
$v_{\mathrm{d\text{-}g},R}$	radial relative velocity of dust and gas
v_frag	dust fragmentation velocity
$v_\mathrm{g}, v_\mathrm{d}$	gas and dust velocity
v_K	Keplerian velocity
$v_\mathrm{mon}, v_\mathrm{gr}$	monomer and grown dust vel. (`two-pop-py`)
Δv	relative particle velocity (source in subscript)
z	cylindrical distance from the disk midplane
α	turbulence parameter
β_Σ	double-log. column density gradient
β_T	double-log. temperature gradient
γ	abs. value of the double-log. pressure gradient
δ	dust diffusion parameter (here δ=α)
ε	dust-to-gas ratio
λ_mfp	gas molecule mean free path
μ	mean molecular weight
ν	coagulation kernel index
$\nu_\mathrm{T}, \nu_\mathrm{mol}$	turbulent and molecular viscosity
ξ	fragment size distribution power-law exponent
$\rho_\mathrm{g}, \rho_\mathrm{d}$	gas and dust volume density
$\rho_\mathrm{g,mid}, \rho_\mathrm{d,mid}$	gas and dust midplane volume density
ρ_m	material density of dust
σ_{H_2}	hydrogen molecule collision cross section
σ_SB	Stefan-Boltzmann constant
$\Omega, \Omega_\mathrm{K}$	angular frequency, Keplerian frequency

Dust-Gas Relative Motion

Dust particles moving in gaseous protoplanetary disks experience drag forces due to differences between the equilibrium velocities of dust and gas particles. The gas in a PPD is radially stratified, i.e., the disk has a radial pressure gradient. Consequently, gas moves on

a slightly sub-Keplerian orbit, where hydrostatic equilibrium is given by

$$\Omega^2 = \frac{1}{R\rho_\mathrm{g}}\frac{\partial P}{\partial R} + \Omega_\mathrm{K}^2\,, \tag{6.1}$$

where P and ρ_g are the gas pressure and density respectively, R is the cylindrical, stellocentric radius, and $\Omega_\mathrm{K}^2 = {}^{GM_*}/_{R^3}$ is the Keplerian angular frequency. Conversely, radial pressure forces are negligible for the solid particles, which means their equilibrium orbits would be Keplerian (ignoring the gas drag and additional effects like radiation pressure, etc.). Gas, at velocity $\boldsymbol{v}_\mathrm{g}$ and dust particles, at velocity $\boldsymbol{v}_\mathrm{d}$ are aerodynamically coupled via a friction force density

$$\boldsymbol{f}_\mathrm{fric} = \rho_\mathrm{d}\frac{\boldsymbol{v}_\mathrm{d} - \boldsymbol{v}_\mathrm{g}}{t_\mathrm{fric}}\,, \tag{6.2}$$

where the strength of the coupling can be characterized by the stopping timescale t_fric. In the Epstein regime, the friction time can be written

$$t_\mathrm{fric} = \sqrt{\frac{\pi}{8}}\frac{\rho_\mathrm{m} a}{\rho_\mathrm{g} c_\mathrm{s}}\,, \tag{6.3}$$

where ρ_m is the particles' material density, a denotes the particle radius, and c_s is the sound speed. A useful dimensionless measure of the strength of the coupling between gas and dust particles is the Stokes number $\mathrm{St} \coloneqq t_\mathrm{fric}\Omega_\mathrm{K}$. For $\mathrm{St} \ll 1$, gas and dust particles are well-coupled and the particles quickly adjust to changes in the gas velocity. For $\mathrm{St} \gg 1$ however, particles are decoupled from the gas and the friction force is no longer significant for the trajectories of the dust grains.

The stopping time is the timescale on which the particles and the gas approach a steady state, i.e., force balance. The respective terminal velocities of the grains, i.e., their velocities in force equilibrium, were derived by Nakagawa et al. (1986). Ignoring additional velocity components of the gas, e.g., due to viscous evolution, the respective relative radial velocity between the grains and the gas then follows as

$$v_{\mathrm{d\text{-}g},R} = \frac{\mathrm{St}(1+\varepsilon)}{\mathrm{St}^2 + (1+\varepsilon)^2}\frac{1}{\Omega_\mathrm{K}\rho_\mathrm{g}}\frac{\partial P}{\partial R} \tag{6.4}$$

$$\approx \frac{\mathrm{St}}{\mathrm{St}^2 + 1}\frac{1}{\Omega_\mathrm{K}\rho_\mathrm{g}}\frac{\partial P}{\partial R} \quad \text{for} \quad \varepsilon \ll 1\,, \tag{6.5}$$

where ε is the dust-to-gas density ratio. Thus particles drift towards pressure maxima and reach their maximum terminal velocity at a Stokes number of one.

Dust-Dust Relative Motion

Relative velocities between the gas and dust depend on the aerodynamic properties of the dust. Differently-sized grains therefore experience relative velocities due to gas drag. For small grains, Brownian motion is of importance. Additionally, turbulence causes random variations in the gas velocities that act on the dust particles according to their aerodynamic coupling to differently-sized eddies in the gas.

Brownian Motion Random molecular motion of particles leads to relative velocities that depend on the respective particles' masses (Brauer et al., 2008)

$$\Delta v_{01\,\mathrm{brown}} = \sqrt{\frac{8 k_\mathrm{B} T (m_0 + m_1)}{\pi m_0 m_1}}\,, \tag{6.6}$$

where m_0 and m_1 denote the particles' masses, T is the gas temperature, and k_B is the Boltzmann constant. This effect is only relevant for the smallest particles on micrometer scales.

Relative Drift Velocities For two particles with Stokes numbers St_0 and St_1, the relative drift velocities in the case of low dust-to-gas ratio, are given by Equation 6.5

$$\Delta v_{01\,\mathrm{drift}} = \left| \left(\frac{\mathrm{St}_0}{\mathrm{St}_0^2 + 1} - \frac{\mathrm{St}_1}{\mathrm{St}_1^2 + 1} \right) \frac{1}{\rho_\mathrm{g} \Omega_\mathrm{K}} \frac{\partial P}{\partial R} \right| . \tag{6.7}$$

Relative Settling Velocities Dubrulle et al. (1995) derived the vertical dust distribution in a disk with turbulent diffusion as

$$\rho_\mathrm{d}(z) = \rho_{\mathrm{d,mid}} \exp\left(-\frac{z^2}{2 H_\mathrm{d}} \right) , \tag{6.8}$$

where H_d is the scale height of the dust, given by

$$H_\mathrm{d} = \frac{H_\mathrm{g}}{\sqrt{1 + \frac{\mathrm{St}}{\delta}}}\,, \tag{6.9}$$

(see also Fromang & Nelson, 2009; Binkert, 2023). Here, H_g refers to the gas scale height, and δ denotes the turbulent diffusivity parameter, which for now is assumed to be equal to the turbulent gas viscosity parameter α. Thus, particles of different sizes are, on average, also found at different heights, and thus have different terminal velocities. The average relative velocities between the two particle populations can then be approximated as

$$\Delta v_{01\,\mathrm{set}} = |H_{\mathrm{d}1} \mathrm{St}_1 - H_{\mathrm{d}0} \mathrm{St}_0| \, \Omega_\mathrm{K} . \tag{6.10}$$

Relative Velocities due to Turbulence Ormel & Cuzzi (2007) derived closed-form expressions for the relative particle velocities in different turbulence regimes, which depend on the Stokes numbers, the turbulent gas velocity, and the local Reynolds number

$$\mathfrak{Re} = \frac{\nu_\mathrm{T}}{\nu_\mathrm{mol}} \approx \frac{\alpha c_\mathrm{s} H_\mathrm{g}}{c_\mathrm{s} \lambda_\mathrm{mfp}} = \frac{\alpha H_\mathrm{g} \rho_\mathrm{g} \sigma_{\mathrm{H}_2}}{\mu m_\mathrm{p}}\,, \tag{6.11}$$

where λ_mfp is the mean free path of the gas molecules, μm_p is the mean molecular mass of the gas, and σ_{H_2} is the collisional cross section of two gas molecules (here H_2). The respective derivations assume a Kolmogorov turbulent energy cascade (Kolmogorov, 1941).

We use an implementation of these velocities identical to the one utilized in the full dust coagulation code DustPy.

Dust Coagulation

Dust particles in protoplanetary disks undergo collision since they experience differential velocities due to their interaction with the gas. Surface forces can lead to sticking in such collisions and thus facilitate the growth of dust particles. If collision velocities are too high, they can lead to fragmentation. The Smoluchowski equation describes the evolution of continuous mass (or size) distributions of grains $n(m)$, as a consequence of these processes. In this work, however, we are not rigorously solving the coagulation equation as in full-fledged coagulation models like DustPy (Stammler & Birnstiel, 2022). Instead, we use the results gained with such elaborate numerical methods to construct a simplified, semi-analytic prescription for dust coagulation. For this, it is instructive to have a look at some main results obtained by full coagulation models and simple analytic derivations. One of these simplifying assumptions is a monodisperse size distribution. Kornet et al. (2001) have shown that for such a case, the particle growth rate can be written as

$$\dot{a} = \frac{\rho_\mathrm{d}}{\rho_\mathrm{m}} \Delta v, \tag{6.12}$$

where Δv denotes the relative velocity between the grains. If the relative velocities are assumed to be caused by gas turbulence in the fully-intermediate regime, one finds that the growth of the particles is occurring on a timescale

$$t_\mathrm{grow} = \frac{1}{\varepsilon \Omega_\mathrm{K}} \,. \tag{6.13}$$

However, dust grains can only grow in size as long as their relative velocities due to different aerodynamic properties are not above a critical fragmentation velocity v_frag, i.e., until collisions between grains do not result in destruction instead of coagulation. Another possible outcome of grain collisions is bouncing, as shown by laboratory experiments (Güttler et al., 2010) and studied in numerical models (Zsom et al., 2010; Dominik & Dullemond, 2023). It is possible to derive analytic estimates for the maximum reachable particle size, given a certain fragmentation velocity. Birnstiel et al. (2012) derived the respective maximum particle size in the turbulent fragmentation limit as

$$a_\mathrm{turb\text{-}frag} = \sqrt{\frac{8}{\pi}} \frac{\rho_\mathrm{g}}{3\rho_\mathrm{m}} \frac{v_\mathrm{frag}^2}{\alpha c_\mathrm{s} \Omega_\mathrm{K}} \,. \tag{6.14}$$

Furthermore, dust grains undergo radial drift, which results in relative velocities between grains of different sizes (see Equation 6.5). The resulting collisions can also lead to a drift-fragmentation limit, which is given by

$$a_\mathrm{drift\text{-}frag} = \sqrt{\frac{8}{\pi}} \frac{\rho_\mathrm{g}}{\rho_\mathrm{m}} \frac{v_\mathrm{frag}}{c_\mathrm{s}} \frac{P}{1-\mathcal{N}} \left| \frac{\partial P}{\partial r} \right|^{-1} \,, \tag{6.15}$$

where the constant $\mathcal{N}$ is approximately 0.5 (Birnstiel et al., 2012). Dust particles can thus not reach sizes larger than

$$a_{\mathrm{frag}} = \min(a_{\mathrm{drift\text{-}frag}}, a_{\mathrm{turb\text{-}frag}}) \,. \tag{6.16}$$

In these cases, the typically reached size distributions are approximately power laws with characteristic exponents. Birnstiel et al. (2011) used coagulation simulations and analytical calculations to find these fragmentation-limited size distributions. They derived analytic expressions for the resulting power-law exponent of a mass distribution $n(m) \propto m^{-p_{\mathrm{m}}}$ in three different regimes, translating to the size distribution $n(a) \propto a^p = a^{-3p_{\mathrm{m}}+2}$. If coagulation and fragmentation happen simultaneously, the power-law exponent can be written as

$$p = 2 - \frac{3}{2}(\nu + \xi + 1) \,, \tag{6.17}$$

where ν is a kernel index that depends on the functional form of the relative velocities, i.e., the velocities' dependency on the particle sizes. The parameter ξ determines the typical distribution of fragments in a destructive collision. It is usually set to the canonical value of $11/6$. Birnstiel et al. (2011) determined that in the first regime of turbulence, as derived by Ormel & Cuzzi (2007), where the relative velocities scale linearly with particle size, $\nu = 1$ and thus $p = -3.75$. The same is true for relative drift velocities, which also linearly depend on the difference in Stokes numbers between the colliding particles (as long as $\mathrm{St} \ll 1$). This means that typical size distributions in coagulation-fragmentation equilibrium, with collisions driven by differential drift or the first regime of turbulence, can be approximated as power laws $n(a) \propto a^{-3.75}$, as illustrated in Figure 6.2. This case is thus relevant whenever the particle fragmentation velocity is low and only small particles exist, or if the drift velocities dominate over the turbulent velocities, as in the outer regions of protoplanetary disks.

The other prominent case is relevant whenever turbulence is causing relative velocities between particles in the so-called fully-intermediate regime. Then, $\nu = 5/6$, and one finds that $p = -3.5$, which is equal to the Mathis, Rumpl, & Nordsieck (MRN) distribution. This particular case is relevant in the inner parts of protoplanetary disks, where the particles grow to the largest sizes and where radial drift is less relevant.

Finally, we have the stages of dust growth in which the fragmentation barrier is not yet reached and the largest particles are undergoing a sweep-up growth. In this case, typical size distributions are steeper and we assume $p = -2.5$ in this case (Simon et al., 2022; Birnstiel, 2023).

Radial drift itself also sets a limit to the maximum particle size, which is reached when the radial drift time scale becomes equal to the local growth time scale, i.e.,

$$\begin{aligned} \frac{a_{\mathrm{dr}}}{\dot{a}} &\stackrel{!}{=} \frac{R}{|\dot{R}|} \\ a_{\mathrm{dr}} &= \sqrt{\frac{8}{\pi}} \frac{\rho_{\mathrm{d}}}{\rho_{\mathrm{m}}} \frac{v_{\mathrm{K}}}{c_{\mathrm{s}} \gamma} \,, \end{aligned} \tag{6.18}$$

where v_{K} is the Keplerian velocity and $\gamma = \left| \frac{\mathrm{d} \log P}{\mathrm{d} \log R} \right|$ denotes the absolute value of the radial

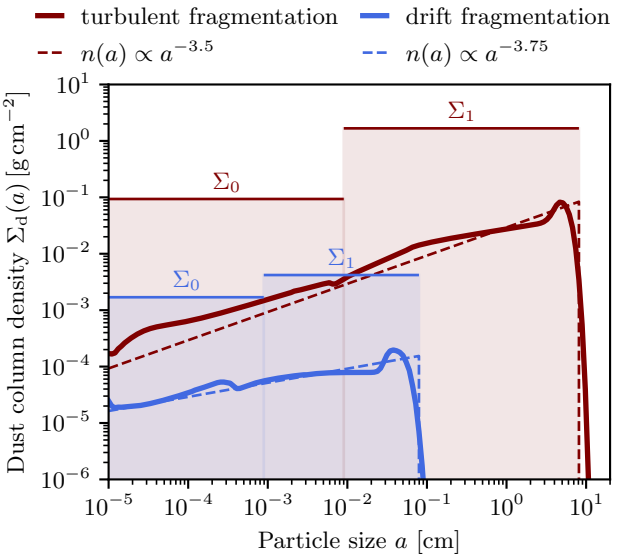

Figure 6.2
Typical Size distributions in regions of a protoplanetary disk model that are either turbulence-dominated (dark red lines) or drift-dominated (blue lines). Both regimes result in distinct power-law exponents of the distribution that we overplot as dashed lines. Assuming a power law as the overall shape of the distribution makes it possible to approximately describe it with only three parameters: The cutoff particle size $a_{\max}$ and the two densities Σ_0 (contained in the size interval $[a_{\min}, \sqrt{a_{\max} a_{\min}})$ and Σ_1 (contained in the size interval $[\sqrt{a_{\max} a_{\min}}, a_{\max}]$). This approximation is the basis of our new dust coagulation model.

double-logarithmic pressure gradient. The drift limit is relevant in the outer regions of protoplanetary disks, where drift can become rapid for large particles. In the drift limit, grains do not undergo fragmentation. Therefore, typical size distributions are sweep-up dominated and accordingly steep. We assume $p = -2.5$, which is a typical value seen in full coagulation simulations.

The `two-pop-py` Model by (Birnstiel et al., 2012)

With `two-pop-py`, Birnstiel et al. (2012) introduced a strongly simplified and very fast method to model the effects of dust coagulation in protoplanetary disks. In this method, dust is realized as a single fluid that drifts relative to the gas. The flux calculation, however, considers two dust species. The small population represents the monomers with fixed size a_{mon} and is assumed to move along with the gas. Larger, grown grains make up the population of size $a_{\text{gr}}(t)$, which is evolving in time, following the monodisperse dust growth rate, which is limited by the above discussed growth barriers

$$a_{\text{gr}}(t) = \min\left[\min(a_{\text{drift}}, a_{\text{turb-frag}}, a_{\text{drift-frag}}), a_{\text{mon}} \exp\left(\frac{t - t_0}{t_{\text{grow}}}\right)\right], \tag{6.19}$$

to simulate the initial phase of coagulation and the growth limits. Both species are associated with a drift velocity according to their Stokes numbers $\text{St}_{0/1} = a_{\text{mon/gr}} \rho_{\text{m}} \pi / 2\Sigma_{\text{g}}$, as

$$v_{\text{mon/gr}} = \frac{v_{\text{gas}}}{1 + \text{St}^2_{\text{mon/gr}}} + \frac{\text{St}_{\text{mon/gr}}}{1 + \text{St}^2_{\text{mon/gr}}} \frac{1}{\rho_{\text{g}} \Omega_K} \frac{\partial P}{\partial r}, \tag{6.20}$$

where the first term takes into account gas velocities arising from viscous disk evolution and the second term is the radial drift velocity derived by Nakagawa et al. (1986) in the limit of small dust-to-gas ratios. The total dust flux velocity follows as a mass average of

both populations, via

$$\bar{v} = (1 - f_\mathrm{m})v_\mathrm{mon} + f_\mathrm{m}v_\mathrm{gr} \,. \tag{6.21}$$

The ratio f_m is dependent on the limiting factor of grain growth: fragmentation-limited, drift-fragmentation-limited, drift-limited, or neither, when the dust is still in the growth phase

$$f_\mathrm{m} = \begin{cases} 0.97 \text{ if } a_\mathrm{drift} < a_\mathrm{frag},\, a_\mathrm{drift\text{-}frag} \\ 0.75 \text{ otherwise.} \end{cases} \tag{6.22}$$

Given the resulting velocity, a flux can be calculated that is used to evolve the dust surface density in time. This method is fast and can be easily implemented in a hydrodynamic simulation. It has however some serious drawbacks:

- Dust growth is always assumed to be limited by an equilibrium of either transport and coagulation, or drift and coagulation. This is mostly true if no substructure is present. In some situations like planetary gaps, however, fluxes and grain sizes are no longer determined by coagulation in the gap but by the supply of small grains that diffuse into the gap and the efficient removal of larger grains. In such cases, grain sizes can be underestimated by `two-pop-py`, which would assume the drift limit.
- Although the maximum grain size is known, no information on the actual size distribution is provided beyond the knowledge whether the distribution is drift-limited or fragmentation-limited.
- The differences between the size distribution in the fragmentation limit and the drift-fragmentation limit are not taken into account. The mass fraction f_m only considers whether the maximum particle size is drift-limited.
- As growth is always assumed to be driven by collisions in the fully-intermediate regime of turbulence, the actual growth timescale can be underestimated (Powell et al., 2019).
- The fragmentation limit is reached instantaneously and not gradually. This is especially problematic if the timescale for dust advection is short.
- The model is only calibrated to reproduce the dust size evolution in protoplanetary disks around $1\,M_\odot$ stars.
- The model overestimated the concentration of dust in pressure bumps due to the treatment of dust being transported as one fluid. Although the flux is calculated in a mass-averaged way that has been determined experimentally, intermediately-sized grains are neglected, which would lead to a wider dust distribution in pressure bumps.

With our new model, `TriPoD`, we aim to mitigate these problems.

6.3 The TriPoD Model

List of Symbols Specific to TriPoD

Symbol	Description
$\dot{a}_{\max}$	growth rate of max. size
a_0, a_1	mass-averaged particle sizes of populations
$a_{\min}, a_{\max}$	minimum and maximum size of distribution
a_{int}	geometric mean of $a_{\min}$ and $a_{\max}$
$a_{\lim}$	lower limit for size reduction in gaps
f_{crit}	critical mass depletion coefficient for shrinking
f_{drift}	drift velocity calibration factor
$f_{\Delta v}$	collision speed parameter
$f_{\Delta v,\,\text{turb}}$	collision speed parameter in turbulence-dominated regime
$f_{\Delta v,\,\text{drift}}$	collision speed parameter in drift-dominated regime
$F^{\text{drift}}_{\Sigma_0,\,i+1/2}$	dust flux due to radial drift (small population)
$F^{\text{drift}}_{\Sigma_1,\,i+1/2}$	dust flux due to radial drift (large population)
$F^{\text{drift}}_{a_{\max}\Sigma_1,\,i+1/2}$	flux of the density-weighted maximum particle size due to radial drift
$F^{\text{diff}}_{\Sigma_0,\,i+1/2}$	dust flux due to radial diffusion (small population)
$F^{\text{diff}}_{\Sigma_1,\,i+1/2}$	dust flux due to radial diffusion (large population)
$F^{\text{diff}}_{a_{\max}\Sigma_1,\,i+1/2}$	flux of the density-weighted maximum particle size due to radial diffusion
$F_{\Sigma_{0/1},\,i\pm1/2}$	total flux of the dust fluids
$F_{a_{\max}\Sigma_1,i\pm1/2}$	total flux of the density-weighted maximum particle size
$\mathcal{F}$	size distribution calibration function
$\tilde{\mathcal{F}}$	vertically integrated size distribution calibration function
H_0, H_1	dust scale height of populations
m_0, m_1	particle masses corresponding to a_0 and a_1
N	number of bins of the reconstructed size distribution
p_{frag}	general fragmentation power-law exponent
$p_{\text{turb.1}}$	fragmentation power-law exponent in turbulence 1 regime
$p_{\text{turb.2}}$	fragmentation power-law exponent in turbulence 2 regime
$p_{\text{drift-frag}}$	drift-fragmentation power-law exponent
p_{sweep}	non-equilibrium power-law exponent
$p_{\text{turb-frag}}$	turbulent-fragmentation power-law exponent
s	steepness parameter of the transition from growth to fragmentation
$v_{\Sigma_{0/1}}$	drift flux velocity for populations
Δv_{01}	relative velocity between grains of sizes a_0 and a_1
Δv_{11}	relative velocity between grains of sizes a_1 and $f_{\Delta v}a_1$
$\Delta v_{\max}$	relative velocity between grains of sizes $a_{\max}$ and $0.5a_{\max}$
$\varepsilon_0, \varepsilon_1$	vertically integrated dust-to-gas ratios of population
ε_{tot}	total dust-to-gas ratio
$\lambda_{\lim}$	flux limiter

Π_{frag}	fragmentation/growth transition function
Π_{sweep}	$1 - \Pi_{\mathrm{frag}}$
Π_{turb}	turbulence-dominated/drift-dominated transition function
Π_{drift}	$1 - \Pi_{\mathrm{turb}}$
$\Pi_{\mathrm{turb.1}}$	turbulence 1/turbulence 2 transition function
$\Pi_{\mathrm{turb.2}}$	$1 - \Pi_{\mathrm{turb.1}}$
$\dot{\rho}_{0\to1}$	"sweep-up" rate
$\dot{\rho}_{1\to0}$	"fragmentation" rate
σ_{01}	collision cross section of grains of size a_0 and a_1
σ_{11}	collision cross section of grains of size a_1 and $f_{\Delta v} a_1$
Σ_0, Σ_1	dust column densities of populations
$\dot{\Sigma}_{0\to1}$	vertically integrated "sweep-up" rate
$\dot{\Sigma}_{1\to0}$	vertically integrated "fragmentation" rate
$\tau_{\mathrm{depletion}}$	dust depletion timescale

Our new three-parameter dust evolution model TriPoD makes use of the knowledge gained from full-fledged coagulation models that are discussed in the previous section. In particular, the power-law prescriptions of the dust size distribution are the basis on which we build our method. TriPoD, describes the power-law size distribution with only three parameters: the dust column densities of a small population Σ_0 and the large population Σ_1, as well as a maximum particle size a_{max} at which the distribution is truncated. The populations are separated at the size $a_{\mathrm{int}} = \sqrt{a_{\mathrm{min}} a_{\mathrm{max}}}$, which then defines the power-law exponent of a full size distribution via

$$p = \frac{\log(\Sigma_1/\Sigma_0)}{\log(a_{\mathrm{max}}/a_{\mathrm{int}})} - 4\,. \tag{6.23}$$

Note, that this formula is in general independent of whether we describe a size distribution in the sense of column densities or volume densities. Although we develop the TriPoD method in this paper for use with vertically integrated size distributions, we could also do so for volume densities. In the following, we will thus oftentimes use the dust-to-gas ratio ε, which can be interpreted as either the vertically integrated, or the local version. Assuming the dust size distribution to follow a truncated power law $n(a) \propto a^p$, we can write the dust-to-gas ratio size distribution as $\varepsilon(a) \propto a^p m \propto a^p a^3$. Normalizing this to the total dust-to-gas ratio $\varepsilon_{\mathrm{tot}}$, we get

$$\varepsilon(a) = \begin{cases} \dfrac{\varepsilon_{\mathrm{tot}}(p+4)}{a_{\mathrm{max}}^{p+4} - a_{\mathrm{min}}^{p+4}} a^{p+3} & \text{for } p \neq -4 \\ \dfrac{\varepsilon_{\mathrm{tot}}}{\log(a_{\mathrm{max}}) - \log(a_{\mathrm{min}})} \dfrac{1}{a} & \text{for } p = -4\,, \end{cases} \tag{6.24}$$

where a_{min} is the minimum particle size and a_{max} is the maximum particle size of the truncated distribution. From this, the dust-to-gas ratio within a given size interval $[a_{\mathrm{I}}, a_{\mathrm{II}}]$

with $a_{\min} \leq a_{\mathrm{I}} < a_{\mathrm{II}} \leq a_{\max}$, can be calculated as

$$\begin{aligned}\varepsilon_{a_{\mathrm{I}}}^{a_{\mathrm{II}}} &\coloneqq \int_{a_{\mathrm{I}}}^{a_{\mathrm{II}}} \varepsilon(a)\,\mathrm{d}a \\ &= \begin{cases} \varepsilon_{\mathrm{tot}} \dfrac{a_{\mathrm{II}}^{p+4} - a_{\mathrm{I}}^{p+4}}{a_{\max}^{p+4} - a_{\min}^{p+4}} & \text{for } p \neq -4 \\ \varepsilon_{\mathrm{tot}} \dfrac{\log(a_{\mathrm{II}}) - \log(a_{\mathrm{I}})}{\log(a_{\max}) - \log(a_{\min})} & \text{for } p = -4\,. \end{cases}\end{aligned} \tag{6.25}$$

Similarly, the mass-averaged particle size of this distribution in the size interval from a_{I} to a_{II} is defined as

$$\begin{aligned}\langle a \rangle_{a_{\mathrm{I}}}^{a_{\mathrm{II}}} &\coloneqq \frac{\int_{a_{\mathrm{I}}}^{a_{\mathrm{II}}} \varepsilon(a)\, a\,\mathrm{d}a}{\int_{a_{\mathrm{I}}}^{a_{\mathrm{II}}} \varepsilon(a)\,\mathrm{d}a} \\ &= \begin{cases} \dfrac{a_{\mathrm{II}} a_{\mathrm{I}}}{a_{\mathrm{II}} - a_{\mathrm{I}}} \log\left(\dfrac{a_{\mathrm{II}}}{a_{\mathrm{I}}}\right) & \text{for } p = -5 \\ \dfrac{p+4}{p+5} \dfrac{a_{\mathrm{II}}^{p+5} - a_{\mathrm{I}}^{p+5}}{a_{\mathrm{II}}^{p+4} - a_{\mathrm{I}}^{p+4}} & \text{for } p \neq -5, -4 \\ \dfrac{a_{\mathrm{II}} - a_{\mathrm{I}}}{\log(a_{\mathrm{II}}) - \log(a_{\mathrm{I}})} & \text{for } p = -4\,. \end{cases}\end{aligned} \tag{6.26}$$

In the TriPoD model, we define two particle populations that together contain the entire dust density of the distribution

$$\begin{aligned}\varepsilon_0 &= \int_{a_{\min}}^{a_{\mathrm{int}}} \varepsilon(a)\,\mathrm{d}a \\ \varepsilon_1 &= \int_{a_{\mathrm{int}}}^{a_{\max}} \varepsilon(a)\,\mathrm{d}a\,.\end{aligned} \tag{6.27}$$

The mass-averaged particle sizes of both populations are then given by $a_0 \coloneqq \langle a \rangle_{a_{\min}}^{a_{\mathrm{int}}}$ and $a_1 \coloneqq \langle a \rangle_{a_{\mathrm{int}}}^{a_{\max}}$ (see Equation 6.26). It can be shown that the two populations ε_0 and ε_1 exactly represent the power-law distribution if a_{int} is defined as the geometric mean of the maximum and minimum size, i.e., $a_{\mathrm{int}} = \sqrt{a_{\max} a_{\min}}$. The power-law exponent p is then given by Equation 6.23. Knowing only ε_0 and ε_1 and the maximum size $a_{\max}$ thus allows us to reconstruct the entire size distribution.

On a size grid with N cells a_i, spanning from $a_{\min}$ to $a_N \geq a_{\max}$, we can write the mass in a single size bin, and likewise the entire size distribution as

$$\varepsilon_i = \begin{cases} \varepsilon_{\mathrm{tot}} \dfrac{a_{i-1/2}^{p+4} - a_{i+1/2}^{p+4}}{a_{\max}^{p+4} - a_{\min}^{p+4}} \theta(a) & \text{for } p \neq -4 \\ \varepsilon_{\mathrm{tot}} \dfrac{\log\left(a_{i-1/2}\right) - \log\left(a_{i+1/2}\right)}{\log(a_{\max}) - \log(a_{\min})} \theta(a) & \text{for } p = -4\,, \end{cases} \tag{6.28}$$

where $a_{i-1/2}$ and $a_{i+1/2}$ denote the cell interfaces on the size grid, $\varepsilon_{\rm tot} = \sum_{i=0}^{N} \varepsilon_i$ is the total dust-to-gas density ratio and $\theta(a) = \Theta(a_i - a_{\rm min})\Theta(a_i - a_{\rm max})$ represents two Heaviside step functions that cut off the distribution at the minimum and maximum particle sizes. This means we can directly compare our model results with full dust coagulation models like `DustPy`, which evolve a large grid of sizes instead of just two fluids in our case. We illustrate this in Figure 6.2, where we overplot the detailed size distributions, obtained with a full coagulation model, with their respective three-parameter size distribution representation. The respective dust column densities Σ_0 and Σ_1 of the two populations are shown as the horizontal bars spanning the respective size ranges.

In the following, we describe how we evolve the three-parameter size distribution (i.e., ε_0, ε_1 and $a_{\rm max}$) in time, using a semi-analytic description of dust coagulation. The prescriptions given in this paper represent the first iteration of our new `TriPoD` model that is derived and calibrated for vertically integrated disk models. Therefore, all calculations include gas and dust column densities instead of volume densities.

Particle Growth (evolution of $a_{\rm max}$)

We model particle growth within the monodisperse approximation (Equation 6.12). The growth limits are realized by comparing a given fragmentation velocity $v_{\rm frag}$ with the velocities between large grains Δv_{11}, given by turbulence, differential settling and drift, and Brownian motion. For this, we modify our growth rate by a sigmoid-like function, which leads to growth for $\Delta v_{\rm max} < v_{\rm frag}$, and decay for $\Delta v_{\rm max} > v_{\rm frag}$, resulting in

$$\dot{a}_{\rm max} = \frac{\Sigma_1 \Delta v_{11}}{\rho_{\rm m}\sqrt{2\pi}H_1} \left(\frac{1 - \left(\frac{v_{\rm frag}}{\Delta v_{\rm max}}\right)^s}{1 + \left(\frac{v_{\rm frag}}{\Delta v_{\rm max}}\right)^s} \right), \tag{6.29}$$

with s being a parameter controlling the steepness of the transition from growth to fragmentation and H_1 being the scale height of large dust grains, and $\Delta v_{\rm max}$ being the relative velocity between grains of size $a_{\rm max}$ and $0.5a_{\rm max}$. Determining Δv_{11} and s is the main task during the calibration of our model with respect to the full coagulation code `DustPy` (see Section 6.4 and the red numbers in Table 6.5).

Fragmentation and Sweep-Up (evolution of Σ_0 and Σ_1)

In our model, two effects account for the evolution of the three-parameter size distribution and the interaction between the populations; fragmentation transfers mass from the large population to the small population, while collisions between larger and smaller particles lead to sweep-up, and thus transfer mass from the small bin to the large bin. Erosion of large particles due to collisions with small grains is not accounted for in our model. We describe the sweep-up process via the collision rates between large and small particles

$$\dot{\rho}_{\rm d,0\to1} = \frac{\rho_{\rm g}^2 \varepsilon_0 \varepsilon_1}{m_0 m_1} \sigma_{01} \Delta v_{01} m_0 \,, \tag{6.30}$$

where m_0 and m_1 are the representative particle masses, Δv_{01} is the representative relative velocity between the large and small particles, and σ_{01} is the representative collision cross section. These quantities are derived from the respective population's mass-averaged particle sizes (see Equation 6.26).

Fragmentation predominantly occurs in collisions between two large grains. The corresponding transfer rate is thus determined by the collision rates between large grains

$$\dot{\rho}_{\mathrm{d},1\to0} = \frac{\rho_\mathrm{g}^2 \varepsilon_1^2}{m_1^2} \sigma_{11} \Delta v_{11} m_1 \mathcal{F} \,. \tag{6.31}$$

Here $\mathcal{F}$ represents a function that regulates the relative effectiveness of sweep-up and fragmentation. It is a function of the grain size, the desired power-law exponent of the size distribution, and the relative velocities Δv_{11}. As we can not model the microphysics of collisions between grains in our simplified framework for dust evolution, we base the functional form of $\mathcal{F}$ on the well-understood results of full coagulation models, which treat the evolution of the size distribution as the result of collisions between grains of all present sizes.

For this first version of our three-parameter model, we are only considering vertically integrated disk models, which means our mass transfer rates are given by

$$\dot{\Sigma}_{0\to1} = \frac{\Sigma_0 \Sigma_1 \sigma_{01} \Delta v_{01}}{m_1 \sqrt{2\pi (H_0^2 + H_1^2)}} \tag{6.32}$$

$$\dot{\Sigma}_{1\to0} = \frac{\Sigma_1^2 \sigma_{11} \Delta v_{11}}{m_1 \sqrt{4\pi H_1^2}} \tilde{\mathcal{F}} \,, \tag{6.33}$$

(see Section 6.B). In order to determine the vertically integrated version of $\mathcal{F}$, named $\tilde{\mathcal{F}}$, we consider the steady state between fragmentation and sweep-up. In this equilibrium, a steady size distribution would be reached. Given $\dot{\Sigma}_{\mathrm{d},0\to1} = \dot{\Sigma}_{\mathrm{d},1\to0}$, we arrive at

$$\tilde{\mathcal{F}} = \sqrt{\frac{2H_1^2}{H_0^2 + H_1^2}} \frac{\sigma_{01}}{\sigma_{11}} \frac{\Delta v_{01}}{\Delta v_{11}} \left(\frac{a_\mathrm{max}}{a_\mathrm{int}} \right)^{-(p+4)} \,, \tag{6.34}$$

where p is the desired power-law exponent of the distribution which will be reached on the dominating collisional timescale.

Mass redistribution due to sweep-up and fragmentation is realized by defining the source terms of both populations in a total-mass-conserving manner as

$$\begin{aligned} \dot{\Sigma}_0 &= \dot{\Sigma}_{1\to0} - \dot{\Sigma}_{0\to1} \\ \dot{\Sigma}_1 &= -\dot{\Sigma}_0 \,. \end{aligned} \tag{6.35}$$

Determining the Size Distribution Power Law

We have summed up the the typical particle size distribution exponents in Section 6.2, which were determined by Birnstiel et al. (2011) for distributions in coagulation-fragmentation

equilibrium. These are given by

$$p_{\text{frag}} = \begin{cases} p_{\text{turb.1}} = -3.75 & \text{small particle turb. regime} \\ p_{\text{turb.2}} = -3.5 & \text{fully-intermediate turb. regime} \\ p_{\text{drift-frag}} = -3.75 & \text{drift-dominated regime} \end{cases}$$
$$p_{\text{sweep}} = -2.5 \quad \text{not in equilibrium (see Birnstiel, 2023)}$$

Our task is now to find a way to smoothly switch between these regimes in our three-parameter coagulation model depending on which regime is prevailing under the given conditions.

Firstly, we can determine whether to apply the equilibrium size distributions p_{frag} or whether the dust has not yet reached coagulation-fragmentation equilibrium and collisions lead predominantly to sticking which results in p_{sweep}. For this, we define a transition function

$$\begin{aligned} \Pi_{\text{frag}} &:= \begin{cases} \to 1 \text{ for } \Delta v_{\text{tot}} \gtrsim v_{\text{frag}} \\ \to 0 \text{ for } \Delta v_{\text{tot}} < v_{\text{frag}} \end{cases} \\ \Pi_{\text{sweep}} &= 1 - \Pi_{\text{frag}} \\ \Rightarrow p &= \Pi_{\text{frag}} \cdot p_{\text{frag}} + \Pi_{\text{sweep}} \cdot p_{\text{sweep}} \,. \end{aligned} \tag{6.36}$$

We now have to determine the equilibrium size distribution exponent p_{frag}. For this, we can again define transition functions. We determine whether the small particle turbulence regime (turb.1) or the fully-intermediate regime (turb.2) dominates the relative turbulent velocities

$$\begin{aligned} \Pi_{\text{turb.1}} &:= \begin{cases} \to 1 \text{ for } \Delta v_{\text{turb.1}} > \Delta v_{\text{turb.2}} \\ \to 0 \text{ for } \Delta v_{\text{turb.1}} < \Delta v_{\text{turb.2}} \end{cases} \\ \Pi_{\text{turb,2}} &= 1 - \Pi_{\text{turb.1}} \\ \Rightarrow p_{\text{turb-frag}} &= \Pi_{\text{turb,1}} \cdot p_{\text{turb,1}} + \Pi_{\text{turb,2}} \cdot p_{\text{turb,2}} \,. \end{aligned} \tag{6.37}$$

Lastly, we must determine whether we are in the turbulence-dominated regime or in the drift-dominated regime. Similar to before, we define

$$\begin{aligned} \Pi_{\text{drift}} &:= \begin{cases} \to 1 \text{ for } \Delta v_{\text{drift}} > \Delta v_{\text{turb}} \\ \to 0 \text{ for } \Delta v_{\text{drift}} < \Delta v_{\text{turb}} \end{cases} \\ \Pi_{\text{turb}} &= 1 - \Pi_{\text{drift}} \\ \Rightarrow p_{\text{frag}} &= \Pi_{\text{drift}} \cdot p_{\text{drift-frag}} + \Pi_{\text{turb}} \cdot p_{\text{turb-frag}} \,, \end{aligned} \tag{6.38}$$

where $p_{\text{turb-frag}}$ comes from Equation 6.37. With this, we have have everything we need to calculate p from Equation 6.36 and we can determine the mass exchange rates from Equation 6.35. The exact form of the transition functions is not of great importance as long as the transition is sufficiently fast, but still smooth enough to not cause issues during numerical integration. The choices that worked best in our tests are listed in Section 6.A.

Passive Dust Fluids (in the PLUTO code)

We use the PLUTO[1] code to solve the equations of hydrodynamics in our calibration and test simulations with TriPoD. The Euler equations, solved by PLUTO, read

$$\frac{\partial \rho_\mathrm{g}}{\partial t} + \boldsymbol{\nabla} \cdot (\rho_\mathrm{g} \boldsymbol{v}) = 0 \tag{6.39}$$

$$\frac{\partial \rho_\mathrm{g} \boldsymbol{v}}{\partial t} + \boldsymbol{\nabla} \cdot (\rho_\mathrm{g}\, \boldsymbol{v} \otimes \boldsymbol{v}) = -\boldsymbol{\nabla} P - \rho_\mathrm{g} \boldsymbol{\nabla} \Phi + \boldsymbol{\nabla} \cdot \mathbb{T}\,, \tag{6.40}$$

where $\boldsymbol{v}$ is the gas velocity vector, Φ is the gravitational potential, and $\mathbb{T}$ is the viscous stress tensor. The ideal equation of state is used as a closure relation, i.e.

$$P = \frac{k_\mathrm{B} T}{\mu m_\mathrm{p}} \rho_\mathrm{g}\,. \tag{6.41}$$

The PLUTO code allows for the treatment of passive tracer fluids, which are simply advected with the gas following

$$\frac{\partial (\rho_\mathrm{g} \varepsilon)}{\partial t} + \boldsymbol{\nabla} \cdot (\varepsilon\, \rho_\mathrm{g}\, \boldsymbol{v}_\mathrm{g}) = 0\,. \tag{6.42}$$

In this work, we consider vertically integrated protoplanetary disks and the advected quantities in our TriPoD model are thus the local dust-to-gas ratios of our two dust populations $\varepsilon_0 = \Sigma_0/\Sigma_\mathrm{g}$ and $\varepsilon_1 = \Sigma_1/\Sigma_\mathrm{g}$. The maximum particle size is defined as a tracer of the large dust population, meaning our third tracer fluid is $a_\mathrm{max}\varepsilon_1$.

The respective tracer fluxes are modified to simulate a dust fluid that is aerodynamically coupled to the gas, i.e., undergoes radial and azimuthal drift in the terminal velocity approximation. To achieve this within PLUTO's tracer prescription, we add a flux component corresponding to the relative velocity between dust and gas

$$\boldsymbol{v}_{\Sigma_{0/1}} = \frac{\mathrm{St}_{\Sigma_{0/1}}}{\mathrm{St}^2_{\Sigma_{0/1}} + 1} \frac{1}{\Omega_\mathrm{K} \rho_\mathrm{g}} \boldsymbol{\nabla} P\,, \tag{6.43}$$

where $\mathrm{St}_{\Sigma_{0/1}}$ is the mass-averaged Stokes number of the respective population. The drift velocities are limited to a fraction of the soundspeed. The third tracer ($a_\mathrm{max}\varepsilon_1$) is given the same drift velocity as the large dust population (ε_1). The tracer fluxes are calculated with the upstream dust density and density-weighted maximum particle size based on the drift velocities at the respective cell interface as

$$\boldsymbol{F}^\mathrm{drift}_{\Sigma_0,\, i+1/2} = \Sigma_{0,\,i}\ \max(0, v_{\Sigma_0,\, i+1/2}) + \Sigma_{0,\,i+1}\ \min(v_{\Sigma_0,\, i+1/2}, 0) \tag{6.44}$$

$$\boldsymbol{F}^\mathrm{drift}_{\Sigma_1,\, i+1/2} = \Sigma_{1,\,i}\ \max(0, v_{\Sigma_1,\, i+1/2}) + \Sigma_{1,\,i+1}\ \min(v_{\Sigma_1,\, i+1/2}, 0) \tag{6.45}$$

$$\begin{aligned}\boldsymbol{F}^\mathrm{drift}_{a_\mathrm{max}\Sigma_1,\, i+1/2} = {} & a_{\mathrm{max},\,i}\Sigma_{1,\,i}\ \max(0, v_{\Sigma_1,\, i+1/2}) \\ & + a_{\mathrm{max},\,i+1}\Sigma_{1,\,i+1}\ \min(v_{\Sigma_1,\, i+1/2}, 0)\,.\end{aligned} \tag{6.46}$$

[1] http://plutocode.ph.unito.it/

Dust diffusion is implemented in a flux-limited manner, where the transport velocity is limited to the turbulent gas velocity $v_{\max} = \frac{\sqrt{\delta} c_\mathrm{s}}{1+\mathrm{St}^2}$. The diffusion flux of the small dust population is given by

$$\boldsymbol{F}^{\mathrm{diff}}_{\Sigma_0, i+1/2} = -\lambda_{\mathrm{lim}} D_{i+1/2} \Sigma_{\mathrm{g}, i+1/2} \boldsymbol{\nabla} \varepsilon_0 \,, \tag{6.47}$$

where λ_{lim} is the flux limiter (see Section 6.C) and $D = \frac{\delta c_\mathrm{s} H}{1+\mathrm{St}}$ is the dust diffusion coefficient that should not be larger than the gas viscosity. In order to account for spatial variation in the maximum particle size, we calculate the diffusion flux of the density-weighted maximum particle size as

$$\boldsymbol{F}^{\mathrm{diff}}_{a_{\max}\Sigma_1, i+1/2} = -\lambda_{\mathrm{lim}} D_{i+1/2} \Sigma_{\mathrm{g}, i+1/2} \boldsymbol{\nabla} (a_{\max} \varepsilon_1) \tag{6.48}$$

In order to keep the particle size a tracer of the large particles, we calculate the diffusion flux of the large population accordingly as

$$\boldsymbol{F}^{\mathrm{diff}}_{\Sigma_1, i+1/2} = \frac{\boldsymbol{F}^{\mathrm{diff}}_{a_{\max}\Sigma_1, i+1/2}}{a_{\max,\, i+1/2}} \,, \tag{6.49}$$

to achieve the same diffusion speed. The drift and diffusion fluxes are added to the advective flux of the dust fluids stemming from the gas motion. We have used this approach in Pfeil et al. (2023), where we also presented some simple test cases of the method. Note that this approach makes use of the terminal velocity approximation and is thus strictly speaking only valid for $\mathrm{St} \ll 1$. The TriPoD model itself, being a local model, is not bound to this form of dust advection scheme and could be implemented in any multi-fluid-capable hydrodynamics code.

Complete Right Hand Side of the Conservation Equations (in the PLUTO code)

All modifications made for our three-parameter dust evolution model can be applied within the framework of PLUTO and without changing the underlying reconstruct-solve-average scheme of the code.

Source terms are added to the right-hand side of the conservative hydrodynamics equations describing the evolution of the three-parameter dust size distribution in the framework of PLUTO. For each dimension and evolving variable, we have the right-hand side of the conservation equation

$$\mathcal{R}_i = -\frac{\Delta t}{\Delta \mathcal{V}_i} \left[(\mathcal{A} F)_{i+1/2} - (\mathcal{A} F)_{i-1/2} \right] + \Delta t \mathcal{S}_i \,, \tag{6.50}$$

where Δt is the timestep, $\Delta \mathcal{V}$, is the cell volume, $\mathcal{A}$ the respective cell surface, F is the flux through the interfaces, determined from advection with the gas plus relative terminal velocity and diffusion fluxes, and $\mathcal{S}_i$ is the source term, given by fragmentation, sweep-up, and growth.

For the two dust fluids, the fluxes are calculated via Equations 6.44 to 6.49, and the

source term of the respective dust fluid is calculated from Equation 6.35

$$F_{\Sigma_{0/1},\,i\pm1/2} = F^{\mathrm{diff}}_{\Sigma_{0/1},\,i\pm1/2} + F^{\mathrm{drift}}_{\Sigma_{0/1},\,i\pm1/2} + F^{\mathrm{adv}}_{\Sigma_{0/1},\,i\pm1/2} \tag{6.51}$$

$$\mathcal{S}_{\Sigma_{0/1},\,i} = \dot{\Sigma}_{0/1,\,i}\,, \tag{6.52}$$

where $F^{\mathrm{adv}}_{\Sigma_{0/1},\,i\pm1/2}$ is the flux component that is calculated by PLUTO for the passive advection of the tracers. The maximum particle size is advected together with a large population as a tracer. The fluxes and growth rate are

$$F_{a_{\max}\Sigma_1,\,i\pm1/2} = F^{\mathrm{diff}}_{a_{\max}\Sigma_{0/1},\,i\pm1/2} + F^{\mathrm{drift}}_{a_{\max}\Sigma_{0/1},\,i\pm1/2} + F^{\mathrm{adv}}_{a_{\max}\Sigma_{0/1},\,i\pm1/2} \tag{6.53}$$

$$\mathcal{S}_{a_{\max}\Sigma_1,\,i} = a_{\max,\,i}\dot{\Sigma}_{1,\,i} + \Sigma_{1,\,i}\dot{a}_{\max,\,i}\,, \tag{6.54}$$

where $F^{\mathrm{adv}}_{a_{\max}\Sigma_{0/1},\,i\pm1/2}$ is the flux component that is calculated by PLUTO for the passive advection of the tracer. The evolution equations are evolved in time with PLUTO's standard third-order Runge-Kutta routine. The timestep is limited by the CFL condition, which we don't have to adjust since the dust drift velocities are limited to a fraction of the speed of sound and the typical growth timescale is much longer than an orbital timescale.

6.4 Calibration

Our model has several free parameters, which have to be calibrated in comparison to full dust coagulation simulations. For the growth rate of the dust (Equation 6.29), the main parameters are s (determining the steepness of the transition from growth to fragmentation), and the parameter $f_{\Delta v}$, which determines the relative velocities Δv_{11} through the size ratio between the grains.

We run a series of one-dimensional simulations for calibration of the model against the full coagulation code DustPy. We set up a 1D disk model similar to the standard DustPy model. We exclude viscous evolution since we are only interested in comparing the dust evolution in both models for the time being. The radial disk structure follows

$$\begin{aligned}\Sigma_{\mathrm{g}}(R) &= (2+\beta_\Sigma)\frac{M_{\mathrm{disk}}}{2\pi R_{\mathrm{c}}^2}\left(\frac{R}{R_{\mathrm{c}}}\right)^{\beta_\Sigma}\exp\left[-\left(\frac{R}{R_{\mathrm{c}}}\right)^{2+\beta_\Sigma}\right]\\ &\coloneqq \Sigma_{\mathrm{g},0}\left(\frac{R}{R_0}\right)^{\beta_\Sigma}\exp\left[-\left(\frac{R}{R_{\mathrm{c}}}\right)^{2+\beta_\Sigma}\right],\end{aligned} \tag{6.55}$$

where we employ the code units $\Sigma_{\mathrm{g},0} = 733.28\,\mathrm{g\,cm^{-2}}$ (derived from a DustPy setup with $M_{\mathrm{disk}} = 0.05\,M_\odot$), $\beta_\Sigma = -0.85$, $\beta_T = -0.5$, and $R_0 = 1\,\mathrm{au}$. In PLUTO, the radial temperature

Table 6.3: Stellar parameter and disk parameter for the simulations presented in this work. Calibration runs are performed for the one-solar-mass case.

M_* [$M_\odot$]	R_* [au]	T_* [K]	M_{disk} [M_*]	R_c [au]	β_Σ	β_T
1.0	3.096	4397	0.05	60.0	-0.85	-0.5
0.9	2.906	4315	"	"	"	"
0.7	2.678	4111	"	"	"	"
0.5	2.458	3849	"	"	"	"
0.3	2.215	3460	"	"	"	"
0.1	1.013	2925	"	"	"	"

Table 6.4: Dust properties for the calibration runs (Section 6.4) and the test simulations with different stellar masses Section 6.5.

Dust Property	Value
Dust-to-gas ratio	0.01
Initial maximum dust size	10^{-4} cm
Minimum dust size	10^{-5} cm
Dust material density	$1.67\,\mathrm{g\,cm^{-3}}$
Dust fragmentation velocity	$100\,\mathrm{cm\,s^{-1}}$

structure is expressed in terms of the speed of sound, which is given by

$$c_s^2 = T_0 \frac{k_B}{\mu m_p} = \left(\frac{0.05 L_*}{4\pi R^2 \sigma_{sb}}\right)^{\frac{1}{4}} \frac{k_B}{\mu m_p} \coloneqq v_0^2 \left(\frac{H_0}{R_0}\right)^2 \left(\frac{R}{R_0}\right)^{\beta_T}, \tag{6.56}$$

with $v_0 = \sqrt{GM_*/R_0}$. In our simulations, this is parameterized by the disk aspect ratio H_0/R_0 at reference radius R_0.

The simulations are initialized with a total dust-to-gas ratio of 1%, and an initial maximum particle size of 1 µm. Particles larger than the initial drift limit are excluded from the initial dust profile in order to avoid an inwards drifting wave of large dust at the beginning of the simulation. The initial dust size distribution in both `DustPy` and `TriPoD` follows a power law with $p = -3.5$. The stellar and disk structure parameters are shown in Table 6.3, the dust properties are shown in Table 6.4, and the parameters for the different calibration runs are shown in Table 6.5.

Calibrating the Growth Rate

Determining the appropriate relative grain velocities to reproduce the full coagulation model with our simplified prescription is the topic of this section.

The particle growth rate in our model can be adjusted by varying the relative velocity Δv prescription in Equation 6.29. This is controlled over the parameter $0 < f_{\Delta v} < 1$, which

Table 6.5: Parameters of the one-dimensional simulations performed to calibrate the three-parameter model to the DustPy simulations. Each simulation in one block is compared to the same DustPy simulation with identical α and δ. The bold red numbers are our final calibrated values used in the following test simulations.

Model Parameters				Physical Parameters	
$f_{\Delta v,\,\mathrm{turb}}$	$f_{\Delta v,\,\mathrm{drift}}$	s	f_{drift}	α_{coag}	δ_{diff}
			Upper row of Figure 6.3		
0.1	0.1	3	-	10^{-3}	no transport
0.2	0.2	"	-	"	"
0.3	0.3	"	-	"	"
0.4	0.4	"	-	"	"
0.5	0.5	"	-	"	"
			Lower row of Figure 6.3		
0.1	**0.2**	3	-	10^{-3}	no transport
0.1	0.3	"	-	"	"
0.1	0.4	"	-	"	"
0.1	0.5	"	-	"	"
			Figure 6.4		
0.1	0.2	2	-	10^{-3}	no transport
"	"	**3**	-	"	"
"	"	4	-	"	"
"	"	5	-	"	"
"	"	6	-	"	"
			Figure 6.5		
0.1	0.2	3	0.5	10^{-3}	10^{-3}
"	"	"	0.6	"	"
"	"	"	**0.7**	"	"
"	"	"	0.8	"	"
"	"	"	0.9	"	"
			Figure 6.11		
0.1	0.2	3	0.5	10^{-3}	0.0
"	"	"	0.6	"	"
"	"	"	**0.7**	"	"
"	"	"	0.8	"	"
"	"	"	0.9	"	"

sets the size ratio between the colliding particles a_1 and $f_{\Delta v} a_1$, i.e., by choosing which particle collision is best reproducing the overall growth rate. Furthermore, the parameter s in Equation 6.29 can be used to adjust the growth rate around the transition from growth to fragmentation, where a small s corresponds to a reduced growth rate close to the fragmentation limit, and a large s corresponds to a steep transition from particle growth to fragmentation-coagulation equilibrium.

In order to characterize the effects in comparison with the full coagulation model DustPy, we measure the rate of change of the mass-averaged particle size in TriPoD and DustPy and determine the respective deviations for the given parameters. We use the mass-

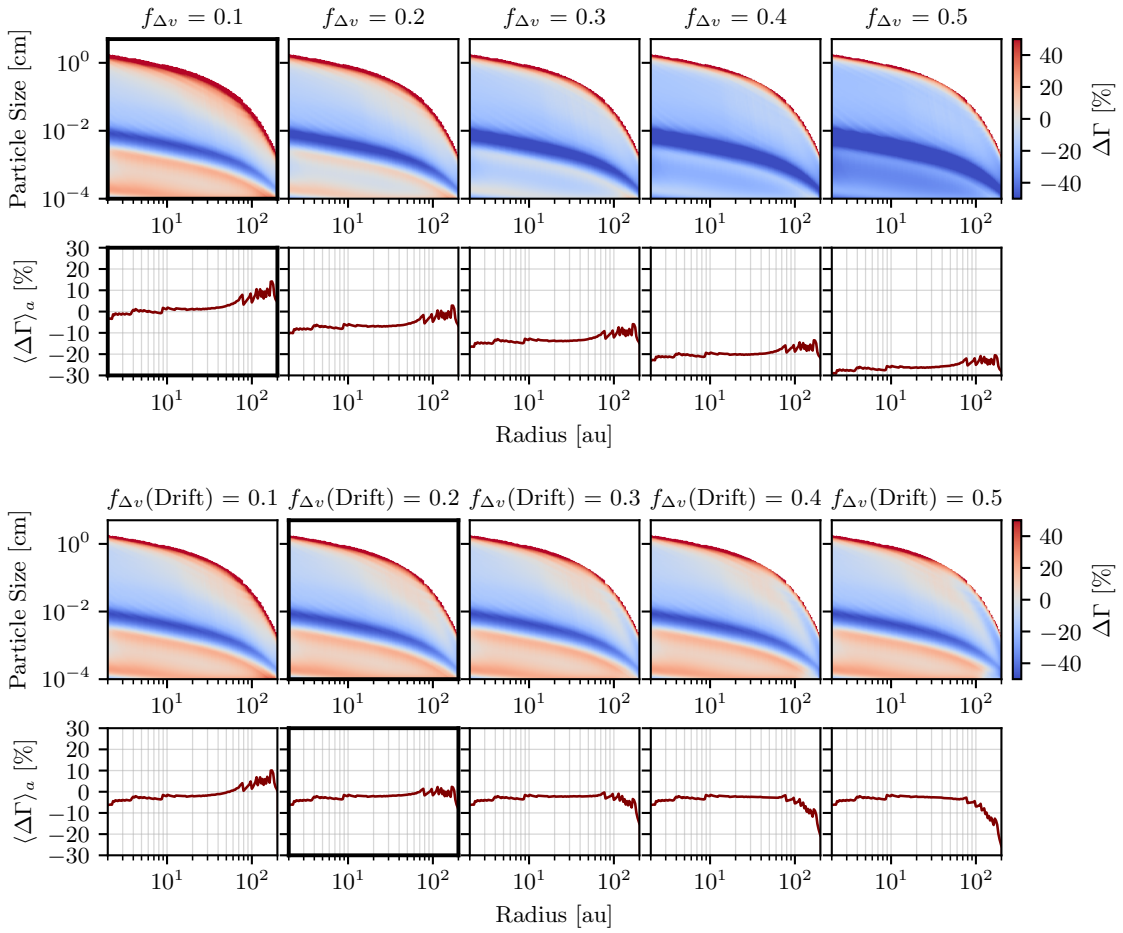

Figure 6.3
Parameter study for the factor $f_{\Delta v}$, which is the most important parameter for the growth rate calibration of our model. For this we calculate the deviation between the mass-averaged particle size's growth rate in `DustPy` and `TriPoD`. In the top row, we show models for different global values of $f_{\Delta v}$. It can be seen that $f_{\Delta v} = 0.1$ seems to fit the dust growth rate best. However, deviations are stronger in the drift-dominated outer disk regions. Therefore, we introduce a transition in $f_{\Delta v}$ from the turbulence-dominated to the drift-dominated regime in the second row, which reduces the error in the outer disk region. We find that a value of $f_{\Delta v} = 0.2$ fits the full coagulation model the best in the drift-dominated regime.

averaged size and not the maximum particle size because it is also a measure of the shape size distribution itself and not just the upper cutoff. To calibrate the growth rate we run `DustPy` and `TriPoD` models without transport (all fluxes are zero). We are, however, still considering the relative drift and sedimentation velocities in the calculation of Δv_{11}. We set up the disk models for a solar-mass pre-main-sequence star with a 0.05 $M_\odot$ gas disk and a dust-to-gas ratio of 1 % (see Table 6.3 and Table 6.4 for details).

First, we run a parameter study for the factor $f_{\Delta v}$, which we vary from 0.1 to 0.5. As can be seen in Figure 6.3, a factor of $f_{\Delta v} = 0.1$ leads to the overall best agreement between the particle growth rate in `TriPoD` and `DustPy`. However, looking at the lower row of the

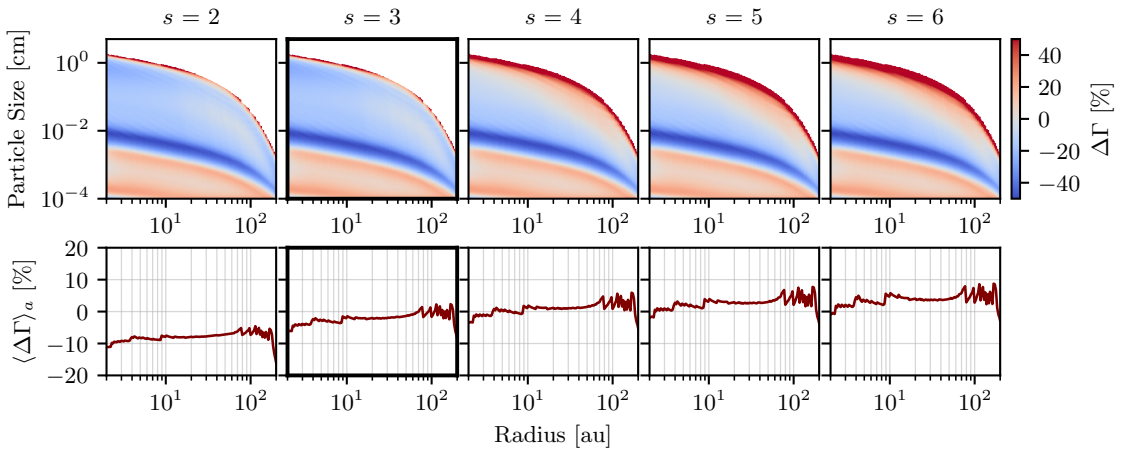

Figure 6.4
Parameter study for the factor s, which determines the steepness of the transition from coagulation to coagulation-fragmentation equilibrium or fragmentation in Equation 6.29. Heat maps show the deviation of the growth rate in TriPoD from the growth rate in DustPy. The lower row shows the average over the size dimension. The influence of a variation in s can be seen around the fragmentation limit, where a larger s corresponds to a steeper transition (fast growth close to the fragmentation limit), while a small s corresponds to a slower transition where growth rates decrease earlier and more slowly. The case of $s = 3$ has the overall best fit with the DustPy model.

upper panel, which shows the averaged deviation, we find that the growth rates disagree in the outer parts of the disk. In these regions, relative drift becomes the more dominant source of relative velocities between the grains. This means the size distribution becomes shallower. In order to bring the growth rates in these regions of the disk into agreement with DustPy, we introduce the transition function from Equation 6.38 to $f_{\Delta v}$, which switches between the drift-dominated and turbulence-dominated regimes. The result for different $f_{\Delta v}$ in the drift-dominated regime can be seen in the lower panel of Figure 6.3. We show that a factor of $f_{\Delta v} = 0.2$ reproduces the growth rate in this case best. Therefore we define

$$f_{\Delta v} = 0.2 \cdot \Pi_{\text{drift}} + 0.1 \cdot \Pi_{\text{turb}} \,. \tag{6.57}$$

The second parameter setting the growth rate is s, which determines the steepness of the transition from growth to fragmentation in Equation 6.29. We run models with values from 2 to 8, which we compare in Figure 6.4. As can be seen, a value of $s = 3$ leads to the best fit between the growth rates close to the fragmentation limit.

Calibrating the Dust Transport

Dust transport is realized by modifying the dust tracer flux (see Section 6.3). For this, the mass-averaged particle size of each dust population is calculated to determine the upstream flux through the respective cell interface. In comparison with a more realistic size distribution, however, the power-law prescription lacks the gradual decrease in mass, shortly before the maximum particle size (visible in the right panels of Figure 6.1). This

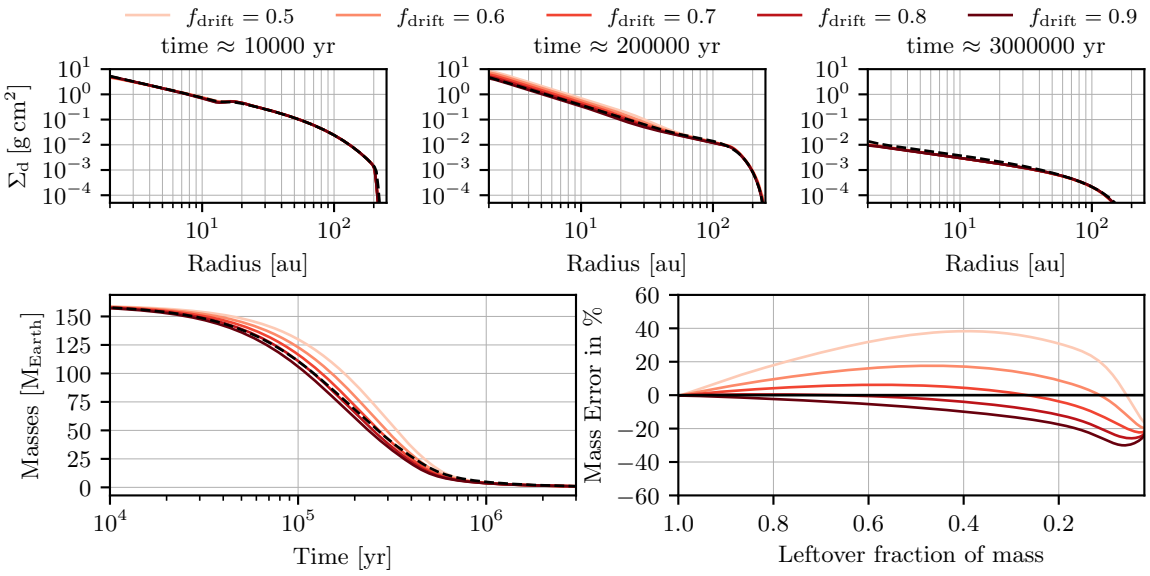

Figure 6.5
Comparison between `DustPy` and our model in a setup with dust diffusion ($\delta = 10^{-3}$) and with different drift calibration factors f_{drift}. The upper row shows a timeseries of the dust column density evolution in three snapshots. In the lower row, we show the mass evolution and the errors with respect to the full coagulation model `DustPy`. For a factor of $f_{\mathrm{drift}} = 0.7$, the mass evolution of the full coagulation model is well reproduced by our three-parameter model.

means that, even if our power-law size distribution reproduces the real size distribution very well, the mass-averaged sizes of both models will not be exactly identical. For this reason, also our dust fluxes will be slightly different from the total flux in `DustPy`. This is generally not a significant effect. We nonetheless try to correct it by using a calibration factor f_{drift} that is multiplied to the calculated mass-averaged particle sizes before the calculation of the dust flux, similar to the fudge factor in the `two-pop-py` model (Birnstiel et al., 2012). For this, we run models for different values of this calibration factor, including dust transport. We neglect any gas transport in these simulations and focus on the dust fluxes, where we conduct one set of simulations with a dust diffusivity of $\delta = 10^{-3}$ (the diffusive runs) and one with $\delta = 0$ (the non-diffusive runs). Except for the inclusion of dust transport, the simulations are identical to the setups used in the growth rate calibration. We apply the best-fitting parameters from the growth rate calibration. We use 150 log-spaced radial grid cells to resolve our simulation domain, which is defined between 2 au and 250 au. This is the same resolution as used in the `DustPy` runs.

For comparison, we plot a time series of the dust column densities in these simulations runs for f_{drift} =0.5, 0.6, 0.7, 0.8 and 0.9 in the upper row of Figure 6.5 (Figure 6.11 depicts the case without diffusion). The lower two panels depict the dust mass evolution (lower left) and the respective deviations from the full coagulation model `DustPy` (lower right). As can be seen, the choice of f_{drift} determines the mass flux throughout the disk's dust evolution. Smaller values of f_{drift} correspond to slower dust velocities and lower fluxes. All values result in deviations of $\lesssim$40 % from the full coagulation model at all times. The value of $f_{\mathrm{drift}} = 0.7$, however, shows the smallest mass error. For this value, the disk's dust mass

only deviates by 10 % from DustPy during most of the mass evolution. The absolute error only increases to $\lesssim 30\,\%$ after 90 % of the mass has already drifted out of the simulation domain. The overall trend in the mass evolution with f_{drift} seems to be independent of the diffusion parameter, as can seen by comparison of Figure 6.5 and Figure 6.11. We therefore chose a value of $f_{\mathrm{drift}} = 0.7$ for all following simulations.

Treatment of Planetary Gaps

Since the particle size in TriPoD can only change due to coagulation/fragmentation, we have to introduce an additional source term that takes into account the reduction of the size distribution's maximum particle size due to the depletion of large particles via transport. The classic example for such a case is a gap carved by a planet. In this case, dust diffusion into the gap from the outer disk, removal of large grains within the gap, and coagulation determine the maximum size of the distribution. As the largest particles are removed from the gap, we reduce the maximum particle size on the respective dust depletion timescale in TriPoD. For this, we set a lower limit for the fraction of large particles at which we begin the size reduction process. We define a hypothetical source term for ε_1, which would set a lower limit to ε_1 in terms of a critical fraction of the total dust density $\frac{\mathrm{d}\varepsilon_1}{\mathrm{d}t} = \frac{f_{\mathrm{crit}}(\varepsilon_0+\varepsilon_1)-\varepsilon_1}{\Delta t}$ where Δt is the current simulation timestep. Since our goal is to reduce the maximum particle size on the depletion timescale, we set $\tau_{\mathrm{depletion}} = \frac{\mathrm{d}\varepsilon_1}{\mathrm{d}t}/\varepsilon_1$ and define the respective size reduction rate

$$\frac{\mathrm{d}a_{\mathrm{max}}}{\mathrm{d}t} = \frac{a_{\mathrm{max}}}{\tau_{\mathrm{depletion}}}\left(1 - \frac{a_{\mathrm{max}}}{a_{\mathrm{lim}}}\right), \tag{6.58}$$

where $a_{\mathrm{lim}} = 1\,\mu\mathrm{m}$ is a minimum size that we define to limit the shrinking to a reasonable value. In order to retain a meaningful power-law exponent for the size distribution during the shrinking process, we set the mass change rate of the large population to

$$\frac{\mathrm{d}\varepsilon_1}{\mathrm{d}t} = \frac{\partial\varepsilon_1}{\partial a_{\mathrm{max}}}\frac{\mathrm{d}a_{\mathrm{max}}}{\mathrm{d}t}\,. \tag{6.59}$$

Here, $\partial\varepsilon_1/\partial a_{\mathrm{max}}$ follows analytically from Equation 6.25. Equation 6.58 and Equation 6.59 are added as source terms to the respective right-hand side of the conservation equations if the condition for size reduction is fulfilled ($\varepsilon_1 < f_{\mathrm{crit}}\varepsilon_{\mathrm{tot}}$). In that way we achieve the following:

- Whenever transport is largely dominating over coagulation, thus removing the large particles, we reduce the maximum particle size on the depletion timescale of the large grain population.
- We thus set a lower limit for the power-law exponent and therefore retain a physically meaningful size distribution, even in planetary gaps.

Determining the critical value of ε_1 at which we begin the size reduction process is an experimental task. The size distribution within a planetary gap is typically not top-heavy due to the efficient removal of the largest grains (e.g., Drążkowska et al., 2019). The large mass bin should thus contain $\lesssim 50\,\%$ of the total dust density in the gap.

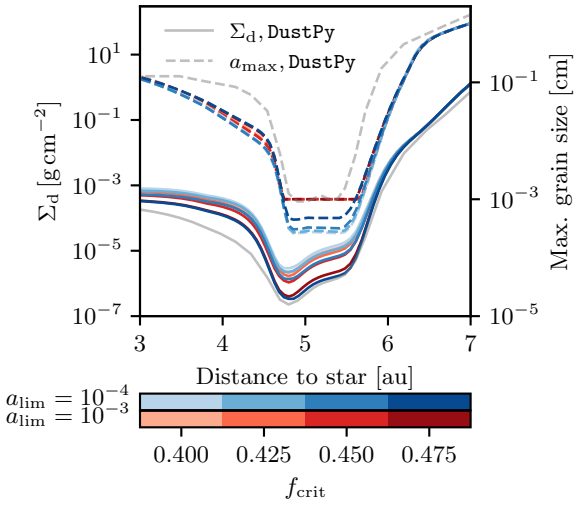

Figure 6.6
Test for the size reduction in planetary gaps. The particle size is reduced on the dust depletion timescale when the large dust population makes up less than the critical fraction f_{crit} of the total dust mass. We run these simulations to determine which value leads to the best agreement with the `DustPy` simulation.

We set up one-dimensional simulation with a gap corresponding to a one Jupiter-mass planet, following the description of Duffell (2020) in `TriPoD` and `DustPy`. The gap is not evolving in time, but pre-defined in the disk's gas structure and the initial dust density structure. We run simulations for several values of the critical mass fraction f_{crit} to determine which values give us the best fit between `TriPoD` and `DustPy` in a planetary gap. For the limiting particle size, we set either 1 µm or 10 µm. The resulting dust column density profiles are shown in Figure 6.6. As can be seen, we reach a reasonably good fit for a value of $f_{\mathrm{crit}} = 0.475$ and a limiting particle size of $a_{\mathrm{lim}} = 1\,\mu\mathrm{m}$. We are therefore choosing these values for all following simulations.

6.5 Test Simulations

Here, we present a series of test cases of our `TriPoD` model for comparison with `DustPy`. Our fiducial model is depicted in Figure 6.1. We set up a smooth protoplanetary disk around a solar-mass star for this. The disk structure is identical to the simulations in the calibration runs. The first two panels in each row show the snapshots of the dust size distributions in `DustPy` (top row) and `TriPoD` after 20 500 yr and 3×10^6 yr of evolution. For this run, gas evolution has been turned off to get a more direct comparison between the dust evolution and transport models. The shape of the size distribution is well reproduced in the drift-limited and fragmentation-limited cases.

Different Stellar Masses

We test the accuracy of our model in simulations of systems with different stellar masses and disk masses. For this, we take the stellar properties of stars with $M_* = 0.1\,M_\odot$, $0.3\,M_\odot$, $0.5\,M_\odot$, $0.7\,M_\odot$ and $0.9\,M_\odot$ from the pre-main-sequence evolution tracks of Baraffe et al. (2015) at $\sim 10^5$ yr of evolution (their first recorded snapshot). We keep the overall disk structure constant for all setups with the values from Table 6.3 and set the disk mass to $0.05\,M_*$. We run the simulations for all stellar masses once with dust diffusion and a

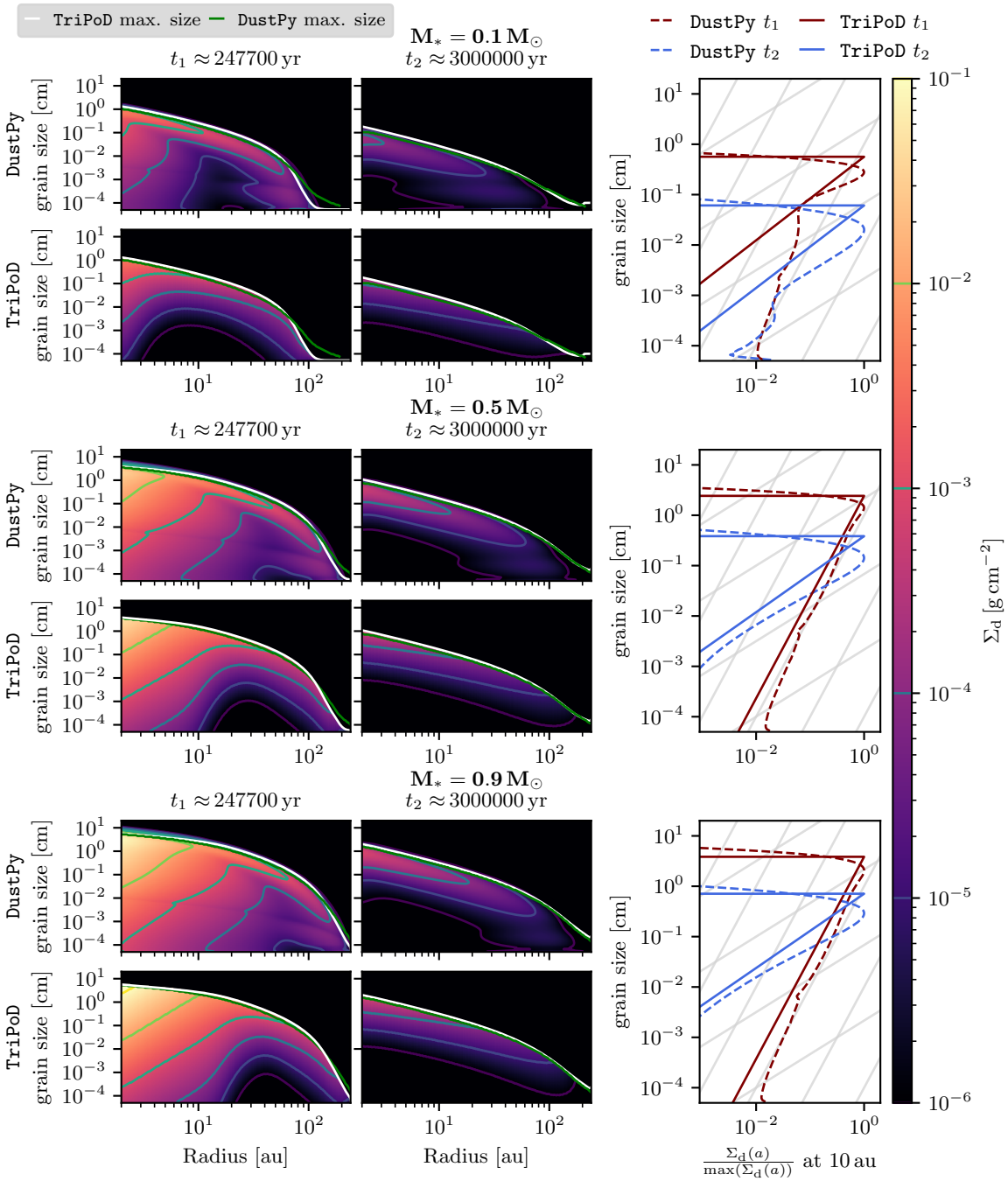

Figure 6.7
Comparison of the dust size distributions in three simulations with different stellar masses and different disk masses. The first row in each group depicts a DustPy simulation (full treatment of coagulation). The lower rows show the respective TriPoD simulations with the PLUTO code. Panels on the right depict the local dust size distributions at 10 au at both snapshots.

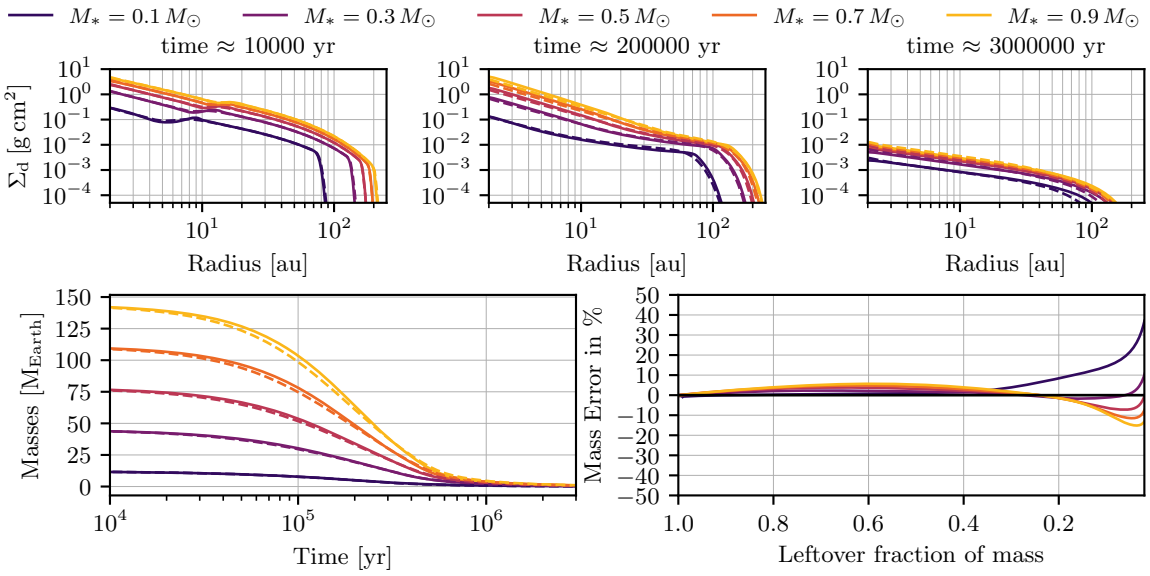

Figure 6.8

Comparison between `DustPy` and our model in setups with different stellar masses. The upper row shows a time series of the dust column density evolution in three snapshots. In the lower row, we show the mass evolution and the errors with respect to the full coagulation model `DustPy`.

diffusion parameter of $\delta = 10^{-3}$ and once without dust diffusion. Gas evolution is turned off in these simulations, as we are for the moment only interested in the accuracy of our dust evolution model. We present three of the simulations with diffusion in Figure 6.7, where the first two panels in each row show snapshots of the simulations. The respective `DustPy` model is shown on top and the `TriPoD` results below. We find that the overall size distribution evolution is well reproduced for most of the simulation domain and runtime. Our model is also able to capture the shape of the size distributions, as can be seen in the right panels. In the early stages of dust evolution (left panel of each row in Figure 6.7), the dust size distribution is in coagulation-fragmentation equilibrium, which results in a typical power-law shape of the distribution with exponent $p = -3.5$. In the case of the $0.1\,M_\odot$ star system, the dust is still in its initial growth phase at the time of the earlier snapshot. Therefore, the distribution has not yet fully reached the equilibrium state and is still more top-heavy—which is typical for the growth phase in which smaller particles are swept-up by bigger particles. In this phase, the distribution is not so well reproduced by a power law. Our three-parameter model nonetheless captures the steeper slope well around the size distribution peak, which contains most of the mass.

We present a more detailed look at the column density and mass evolution in Figure 6.8 (simulations without diffusion can be found in the appendix Figure 6.12). The relative mass error with respect to the full coagulation model is always <10 % until ~90 % of the mass has been accreted. The small errors at the beginning of the simulations are seen to add up in the late stages of disk evolution, where the absolute relative mass error in simulations is $\lesssim$35 % at the end of the simulation when more than 99 % of the mass has drifted out of the simulation domain after 3×10^6 yr. For stellar masses above $0.1\,M_\odot$, the

errors are even smaller. Here, we determine a deviation of less than 10 % until 90 % of the dust mass has drifted out of the simulation domain. Afterward, in the final stages of dust mass evolution, absolute errors increase again and are generally <20 %. Only for the system with the least massive star, we measure of maximum deviation of ~35 % at the very end of the dust mass evolution. One reason for this could be the smaller disk size, which means the dust growth front reaches the outer edge of the disk earlier. This area of strong radial dust-to-gas ratio gradients seems to be the origin of most of the deviations, as can be seen in the upper right panel of Figure 6.8. Overall, the mass evolution in disks around stars of various masses is very well reproduced.

Planetary Gap

As a next test case, we conduct a simulation with a planet-induced gap. For the gap in our one-dimensional DustPy and TriPoD simulations we use the same gap profile as in Section 6.4. Instead of letting the disk viscously evolve, we again turn off gas evolution for these simulations and impose the gap profile immediately on the disk's column density structure. We compare the resulting size distributions in Figure 6.9 with a similar DustPy model in the top row. As can be seen, dust particles collect in the pressure maximum outside of the planetary gap. The gap itself becomes depleted of dust, as the particles

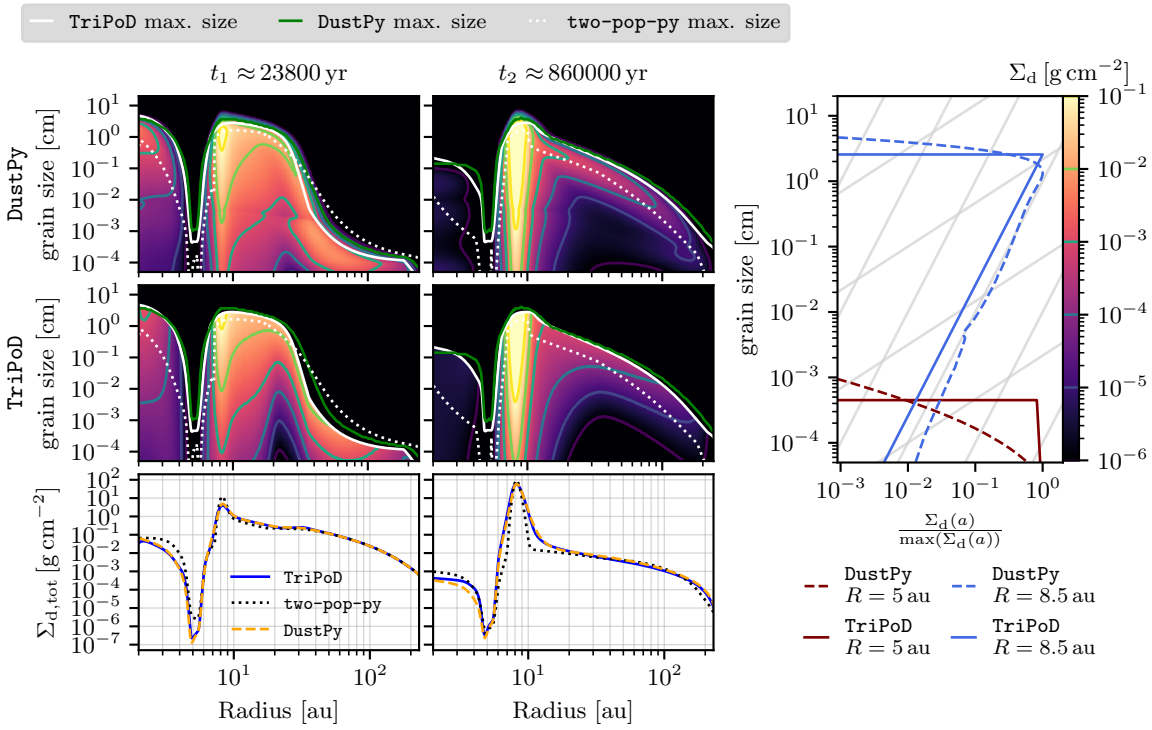

Figure 6.9
Comparison between a DustPy simulation and a PLUTO simulation with our TriPoD dust coagulation model in a protoplanetary disk with a pre-defined gap. We also show the particle sizes and dust column density profiles calculated with the the old two-pop-py model as dotted lines.

drift out and can not be replenished due to the effect of the pressure bump. As a result, the maximum particle size in the full coagulation model is reduced within the gap. As large grains are removed, the maximum particle size is also reduced in `TriPoD`, and thus a reasonable size distribution is retained. In that way, a good fit with the particle size in the gap of the full coagulation model is achieved. The size distribution in the full coagulation model is no longer top-heavy inside the gap but declines toward smaller sizes. The same is achieved in `TriPoD` due to our method of size reduction, as can be seen in the right panels of Figure 6.9. Particles collecting in the pressure bump outside of the gap are fragmentation-limited and can thus grow to larger sizes than in the outer regions, which are drift-limited. Most mass from the outer disk collects around the pressure maximum and does not reach the inner disk.

The size distribution in the regions inside of the gap becomes drift-limited and dust densities decrease significantly due to the decreased inflow from the outer regions. Only diffusion of small particles through the gap maintains some particle flow in the inner disk. For comparison we also show the dust column densities and maximum particle sizes calculated with the old `two-pop-py` method in Figure 6.9. As can be seen, the new method agrees much better with `DustPy`. In the `two-pop-py` simulation, we find a much narrower peak in the dust densities around the pressure maximum due to the lack of a small particle population. Grain sizes are also underestimated in the gap, as `two-pop-py` sets the maximum particle size to the drift limit. This assumes an equilibrium between transport and coagulation which is not given in the gap, where the present particles are diffusing in from the outer edge and large particles are quickly removed by drift.

Two-Dimensional Planet-Disk Simulation

As a last test case, we run a two-dimensional simulation of a protoplanetary disk with a Jupiter-mass planet. We set up a simulation in polar coordinates. The domain is spanning 4–34 au radially and full 2π azimuthally at a resolution of 1024 cells in radial and azimuthal direction. The planet is represented by an additional gravitational potential following

$$\Phi_\mathrm{p} = -\frac{GM_\mathrm{p}}{\sqrt{d^2 + r_\mathrm{sm}^2}}\,, \tag{6.60}$$

where M_p is the planets mass, d is the distance to the planet, and $r_\mathrm{sm} = 0.7\,H_\mathrm{g}$ is the the gravitational smoothing length. The full gravitational potential in our simulation domain is then given as

$$\Phi_\mathrm{tot} = \Phi_* + \Phi_\mathrm{p}\,, \tag{6.61}$$

where Φ_* is the gravitational potential of a Solar-mass star. The disk is set up as a radial power law in column density and temperature with an isothermal equation of state. Details on the disk structure and simulation setup can be found in Table 6.6. We employ a viscosity $\nu_\mathrm{T} = \alpha c_\mathrm{s} H_\mathrm{g}$, with $\alpha = 10^{-3}$. The hydrodynamic equations are solved with the HLL Riemann solver, using the third-order accurate Runge-Kutta scheme for the time integration and piece-wise-polynomial spatial reconstruction scheme to the fifth-order.

For the gas velocities, we use a zero-gradient boundary condition at the inner boundary, where we keep the gas density and the azimuthal velocity fixed to the initial values in the

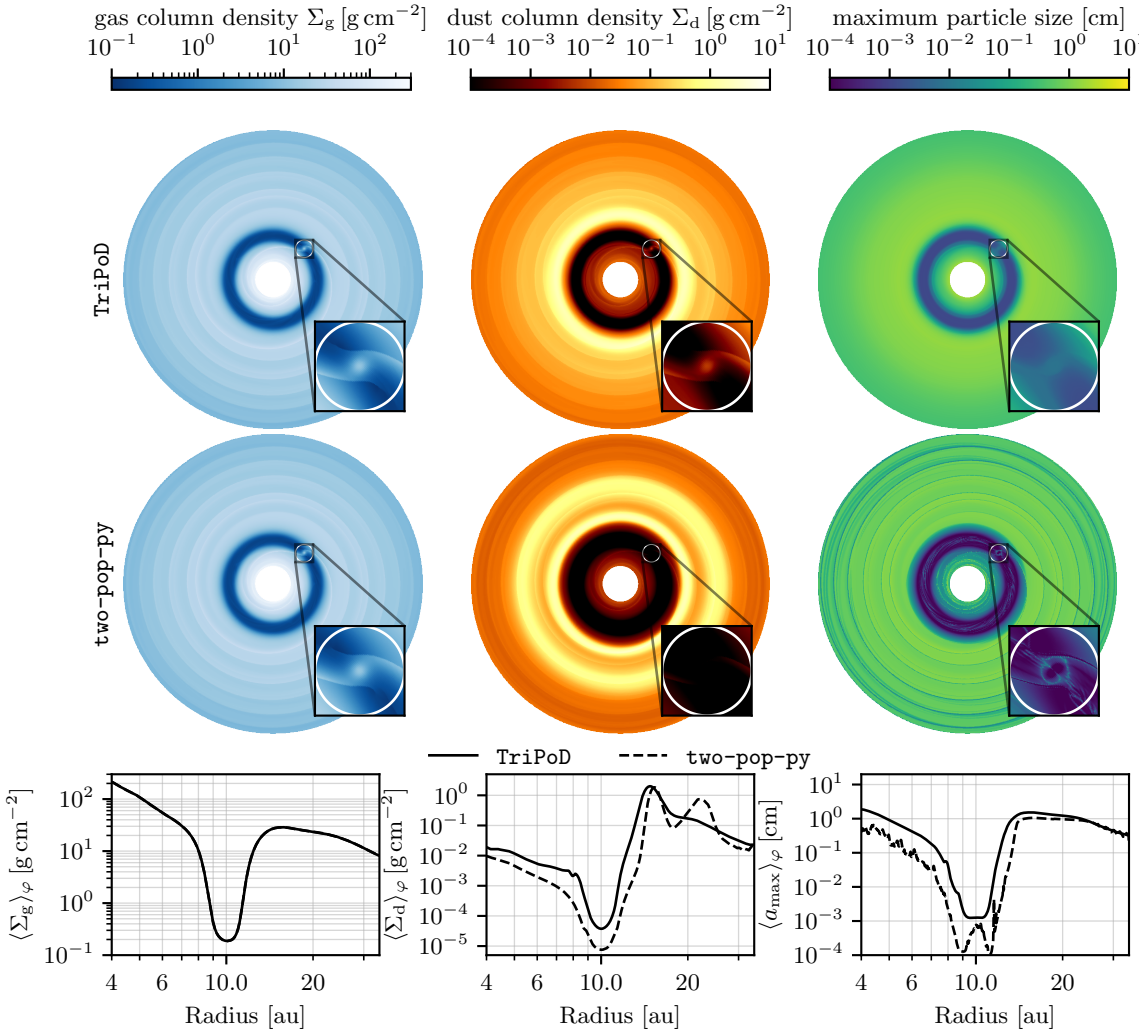

Figure 6.10
Comparison between two-dimensional PLUTO simulations with the TriPoD coagulation model and with the two-pop-py model. The lower panels show the azimuthally-averaged quantities. For the azimuthal averages, we have masked the region around the planet that has been marked with the white circle.

ghost cells. Similar boundary conditions are applied at the outer domain edge, with the difference that we allow for outgoing velocities but not for inflow. The dust densities at the outer boundary are also kept at the initial value for 1000 orbital time scales after which we begin to decrease them exponentially on a timescale of 1000 orbits in order to simulate a reduced dust inflow.

We compare the results to a simulation with the two-pop-py model, which only has one dust fluid. The comparison is presented in Figure 6.10, where the top row shows the TriPoD simulation, and the middle row shows two-pop-py after 2000 planetary orbits of evolution. In the lower panels, we present the respective quantities' azimuthal averages, for which we have masked-out the region around the planet that has been marked with a white circle.

The different grain sizes and the redistribution of mass because of fragmentation and coagulation between the two populations lead to vastly different dust density distributions in the simulation with TriPoD compared to the simulation with two-pop-py. The grains in the two-pop-py simulation collect in two narrowly-peaked overdensities at the pressure maximum outside of the planetary gap and a weak second pressure perturbation. The gap is almost an order of magnitude more depleted than in the simulation with he TriPoD model. Furthermore, dust densities in two-pop-py are strongly enhanced in the weak second pressure perturbation that has almost no visible effect in the simulation with TriPoD. The reason for this is the absence of a small, separately advected grain population in two-pop-py for which the effect of trapping would be much weaker. This is accounted for in the TriPoD simulation, where the smaller dust population broadens the dust peaks significantly due to the weaker trapping of small grains. This also has the effect that more dust can diffuse through the gap, which means that the densities inside and in the gap itself are higher in TriPoD than in two-pop-py.

Inside the gap, TriPoD limits the size distribution exponent to a minimum value of $p \approx 4$ due to the applied size reduction rates, i.e., the distribution is no longer fragmentation-limited but dominated by transport effects. The particles remaining in the gap are accordingly small and the size distributions are no longer top-heavy, as seen in the work by Drążkowska et al. (2019). The two-pop-py model instead simply assumes the drift limit in the gap and inside of it.

Our results are thus qualitatively similar to the conclusions by Drążkowska et al. (2019). Coagulation makes it possible for small grains to pass through the gap via diffusion and coagulate again inside of the planet's orbit. The dust accumulates in the pressure bump, but the peak in the dust density is broader than in a simulation without coagulation due to the presence of small grains, which are constantly produced in our simulation as a result of fragmentation.

6.6 Discussion

Limitations

In its current form in the PLUTO code, our model operates in the terminal velocity approximation. The dust fluids are implemented as passive tracers with modified fluxes. Thus, feedback from the dust on the gas is not included in our two-dimensional test simulation. However, as shown by Drążkowska et al. (2019), the dust feedback in their two-dimensional planet-disk simulation only had a minor effect on the simulation outcome. Effects like the streaming instability (Youdin & Goodman, 2005), can not be simulated with our current version of TriPoD due to this limitation of our very simple dust fluid implementation. Unfortunately, PLUTO does currently not have a multi-fluid feature. A future iteration of the model could be combined with a code that supports dust fluids that are treated more self-consistently, like FARGO3D (Benítez-Llambay & Masset, 2016; Benítez-Llambay et al., 2019) or Athena++ (Stone et al., 2020; Huang & Bai, 2022). The terminal velocity approach also means that effects occurring on timescales shorter than the friction timescale of the particles can not be modeled in the current form of TriPoD. Possible cases could be the effects of shock waves, or spiral density waves.

Table 6.6: Initial conditions for our two-dimensional PLUTO simulation with TriPoD (identical to the initial conditions in Drążkowska et al., 2019).

Simulation Parameter	Value
Gas viscosity parameter (α)	10^{-3}
Gas column density at 1 au	$1700\,\mathrm{g\,cm^{-2}}$
Gas column density exponent (β_Σ)	-1.5
Temperature at 1 au	$195\,\mathrm{K} \Leftrightarrow {}^{H}/_{R}\big\vert_{10\,\mathrm{au}} = 0.05$
Temperature exponent (β_T)	-0.5
Planet mass	$1\,M_{\mathrm{Jupiter}}$
Planet-star distance (circular orbit)	10 au
Dust-to-gas ratio ($\varepsilon_{\mathrm{tot}}$)	0.01
Initial dust size (a_{ini})	10^{-4} cm
Minimum dust size (a_{min})	10^{-5} cm
Dust material density (ρ_{m})	$1.2\,\mathrm{g\,cm^{-3}}$
Dust fragmentation velocity (v_{frag})	$1000\,\mathrm{cm\,s^{-1}}$
Dust diffusion parameter (δ)	10^{-3}

Another shortcoming arises from the way we calculate the dust fluxes. As the maximum particle size changes throughout a simulation domain, neighboring cells usually do not have the same particle sizes. Therefore, the bin interfaces separating Σ_0 and Σ_1 are also different between neighboring cells. Our advection scheme does not take this into account in its current form, where transport is only occurring between the same size bin and not across bins. Due to the smooth variation of a_{max} throughout simulations of protoplanetary disks, neighboring cells will typically still have very similar maximum particle sizes. The effect of this inaccuracy in the advection scheme is therefore likely small. However, one could construct extreme cases in which the error would be large, e.g., if two neighboring cells had vastly different maximum particle sizes. We will have to address this issue in a future version of the model.

Details of the grain size distribution that are modeled in full-fledged coagulation models like DustPy can not be reproduced in our simplified prescription. To still achieve a good fit with such models, our model has several calibration factors that have been adjusted to reach a good fit with DustPy. However, this treatment of dust coagulation can not reproduce the finer details of the coagulation process.

Our model omits particle collisions without mass transfer (bouncing, see, e.g., Dominik & Dullemond, 2023). This effect can lead to a steep, top-heavy size distribution and smaller maximum particle sizes. Bouncing could be implemented in a future version of TriPoD.

TriPoD, as well as DustPy are designed to simulate the dust evolution in vertically integrated models of protoplanetary disks, assuming settling-mixing equilibrium at all times. Effects like sedimentation-driven coagulation (Zsom et al., 2011; Krijt & Ciesla, 2016) can thus not be modeled by DustPy or TriPoD in its current form. This is however not a fundamental limitation of TriPoD, which could easily be adapted to work in three-dimensional setups in a future version.

6.7 Summary and Conclusion

We present TriPoD, an accurate and computationally inexpensive sub-grid model for dust coagulation in vertically integrated hydrodynamic simulations of protoplanetary disks. TriPoD only requires two dust fluids and a tracer for the maximum particle size to model the evolution of a polydisperse dust size distribution. This makes it possible to run inexpensive simulations of planet-disk systems, protoplanetary disks with vortices, etc., and deduce the particle properties and dust densities.

We have implemented our model in the PLUTO code. The workflow of the model during one timestep of a hydrodynamic simulation is as follows:

1. PLUTO calculates the gas fluxes across the cell interfaces with one of the standard Riemann solvers and reconstruction methods that are provided with the code.

2. The dust fluxes and the particle size flux are calculated (Equations 6.44 to 6.46). Flux velocities are calculated from interpolated interface values. The drift flux is then taken upstream depending on the limited dust drift velocity. For dust diffusion, we calculate the limited diffusion flux in a manner identical to the DustPy model (Equations 6.47 to 6.49). The diffusion flux is then added to the total dust flux. (modifications in the PLUTO code made in file `adv_flux.c`)

3. From the mass-averaged particle sizes (Equation 6.26), the relative velocities between grains of sizes a_1 and $f_{\Delta v} a_1$ are calculated. These are used to calculate the particle growth rate (Equation 6.29). The collision speed between particles of sizes $a_{\max}$ and $0.5 a_{\max}$ determines whether the particles are growing or fragmenting.

4. The mass redistribution rates, i.e., the source terms for the large and the small dust fluid, are calculated. These fragmentation and sweep-up rates (Equations 6.32 and 6.33) are then added to the source terms.
   If the large dust population is depleted to less than $f_{\text{crit}} \varepsilon_{\text{tot}}$, we calculate the respective dust depletion time and add the size reduction terms to the source terms in a way that conserves the current power law (Equation 6.58). Mass is shifted accordingly from the small to the large population (Equation 6.59). The source terms of the two dust populations are calculated according to (Equation 6.35) and added to the equations' right-hand side (modification in PLUTO made in file `rhs_source.c`).

5. The array of conserved quantities is advanced by one timestep by PLUTO using a standard time integration scheme provided with the code.

Although TriPoD is a highly simplified model, it can predict the dust mass evolution accurately for millions of years of evolution and simulate the effects of disk sub-structures on the dust size distribution, as demonstrated in our tests and calibration runs. Applications of this first version of TriPoD could include:

- More accurate studies of chemical networks in protoplanetary disks, which are highly dependent on the available grain surface area.

- Better radiative transfer post-processing of simulations, given the knowledge of the grain size distribution.

- Parameter studies of planet-disk systems with dust coagulation, that were so far infeasible due to the high computational cost of full coagulation models.
- Simulations with self-consistently calculated thermal relaxation times.

In the future, we will extend this first version of the model to three-dimensional simulations of protoplanetary disks.

Acknowledgments

T.P., H.K., and T.B. acknowledge the support of the German Science Foundation (DFG) priority program SPP 1992 "Exploring the Diversity of Extrasolar Planets" under grant Nos. BI 1816/7-2 and KL 1469/16-1/2. T.B. acknowledges funding from the European Research Council (ERC) under the European Union's Horizon 2020 research and innovation programme under grant agreement No 714769 and funding by the Deutsche Forschungsgemeinschaft (DFG, German Research Foundation) under grants 361140270, 325594231, and Germany's Excellence Strategy - EXC-2094 - 390783311. Computations were conducted on the computational facilities of the University of Munich (LMU).

6.A Transition Functions

In order to determine the transition functions, we have taken into account the results of local dust coagulation simulations and theoretical models. The transitions should not be too rapid to not cause issues during the numerical integration.

For the transition between the small regime of turbulence and the fully-intermediate regime of turbulence we take the approximate transition criterion from Ormel et al. (2008)

$$f_{\text{turb.1}}^{\text{turb.2}} = \frac{5\,t_\text{s}}{\tau_\text{max}} \begin{cases} > 1 & \text{small particle regime (turb.1)} \\ < 1 & \text{fully-intermediate regime (turb.2),} \end{cases} \tag{6.62}$$

where τ_max is the friction time of the largest particles, and $t_\text{s} = \mathfrak{Re}^{-1/2}\Omega_\text{K}^{-1}$ is the small eddy turnover time. Using the same functional form as for the growth rate Equation 6.29, but now from 0 to 1 instead of -1 to 1, we define

$$\Pi_\text{turb.1} \coloneqq \frac{1}{2}\left(1 - \frac{\left(f_\text{turb.1}^\text{turb.2}\right)^4 - 1}{\left(f_\text{turb.1}^\text{turb.2}\right)^4 + 1}\right). \tag{6.63}$$

This expression is approaching 0 if $\tau_\text{max} < 5t_\text{s}$ and 1 if $\tau_\text{max} > 5t_\text{s}$. We apply a very similar function to the transition from the drift-dominated regime to the turbulence-dominated regime. We define

$$f_\text{drift}^\text{turb} = \frac{\Delta v_\text{turb}}{\Delta v_\text{drift}} \begin{cases} > 1 & \text{turbulence dominated} \\ < 1 & \text{drift dominated,} \end{cases} \tag{6.64}$$

where Δv_{turb} is the turbulent collision velocity and use

$$\Pi_{\mathrm{drift}} \coloneqq \frac{1}{2}\left(1 - \frac{\left(f_{\mathrm{drift}}^{\mathrm{turb}}\right)^6 - 1}{\left(f_{\mathrm{drift}}^{\mathrm{turb}}\right)^6 + 1}\right), \tag{6.65}$$

where we found that a slightly steeper transition fits better with the results of local coagulation simulations. Finally, we have to introduce the transition from growth to fragmentation. For this, we chose a steeper transition, following

$$\Pi_{\mathrm{frag}} = \exp\left[-\left(5\left(\min\left(\frac{\Delta v_{\mathrm{tot}}}{v_{\mathrm{frag}}}, 1.0\right) - 1.0\right)\right)^2\right], \tag{6.66}$$

which ensures that the equilibrium size distribution is reached on a fast enough timescale.

6.B Column Density Formulation

Assuming $\sigma_{01,11}$, $\Delta v_{01,11}$, $m_{0,1}$, and $\mathcal{F}$ to be vertically constant we deduce the vertically integrated mass exchange rates (Equation 6.32 and Equation 6.33)

$$\dot{\Sigma}_{\mathrm{d},0\to1} = \frac{\Sigma_0\Sigma_1\sigma_{01}\Delta v_{01}}{m_1 2\pi H_0 H_1}\int_{-\infty}^{\infty}\exp\left[-\frac{z^2}{2}\left(\frac{H_0^2 + H_1^2}{H_0^2 H_1^2}\right)\right]\mathrm{d}z \tag{6.67}$$

$$= \frac{\Sigma_0\Sigma_1\sigma_{01}\Delta v_{01}}{m_1\sqrt{2\pi(H_0^2 + H_1^2)}} \tag{6.68}$$

$$\dot{\Sigma}_{\mathrm{d},1\to0} = \frac{\Sigma_1^2\sigma_{11}\Delta v_{11}}{m_1 2\pi H_1^2}\tilde{\mathcal{F}}\int_{-\infty}^{\infty}\exp\left[-\frac{z^2}{H_1^2}\right]\mathrm{d}z \tag{6.69}$$

$$= \frac{\Sigma_1^2\sigma_{11}\Delta v_{11}}{m_1\sqrt{4\pi H_1^2}}\tilde{\mathcal{F}} \tag{6.70}$$

Thus, also $\mathcal{F}$ has a modified form in the vertically integrated setup

$$\tilde{\mathcal{F}} = \sqrt{\frac{2H_1^2}{H_0^2 + H_1^2}}\frac{\sigma_{01}}{\sigma_{11}}\frac{\Delta v_{01}}{\Delta v_{11}}\left(\frac{a_{\max}}{a_{\mathrm{int}}}\right)^{-(p+4)}. \tag{6.71}$$

6.C Flux-limited Dust Diffusion

In order to avoid unrealistically large diffusion fluxes in the presence of strong gradients in the dust-to-gas ratio, we introduce a flux limiter that is conceptually identical to the one by Levermore & Pomraning (1981), which was used by Stammler & Birnstiel (2022).

Without the flux limiter, the diffusion flux is given by

$$\boldsymbol{F}_{\mathrm{diff}} = -D_{\mathrm{diff}}\Sigma_{\mathrm{g}}\boldsymbol{\nabla}\varepsilon\,. \tag{6.72}$$

The transport velocity shall however not be larger than the turbulent velocities that drive the diffusion, i.e., the maximum allowed flux is

$$\boldsymbol{F}_{\mathrm{diff,max}} \coloneqq v_{\mathrm{turb}}\varepsilon\Sigma_{\mathrm{g}} = \frac{\sqrt{\delta}c_{\mathrm{s}}}{1+\mathrm{St}^2}\varepsilon\Sigma_{\mathrm{g}}\,. \tag{6.73}$$

The flux limiter is now defined via

$$\lambda_{\mathrm{lim}} = \frac{1+\chi}{1+\chi+\chi^2}\,, \tag{6.74}$$

where

$$\chi = \frac{\boldsymbol{F}_{\mathrm{diff}}}{\boldsymbol{F}_{\mathrm{diff,max}}}\,, \tag{6.75}$$

is the ratio of the diffusion flux and the maximum flux. The limited flux is then given by

$$\boldsymbol{F}_{\mathrm{diff,lim}} = \lambda_{\mathrm{lim}}\boldsymbol{F}_{\mathrm{diff}}\,. \tag{6.76}$$

Note that although the flux is a vector (with components for each direction), all operations here are component-wise. In PLUTO, we define all quantities in the above equations at the cell interfaces.

6.D Calibrations and Test Simulations without Diffusion

Here, we present the same calibration and test simulations shown in the main part of this article, but now without dust diffusion ($\delta = 0$).

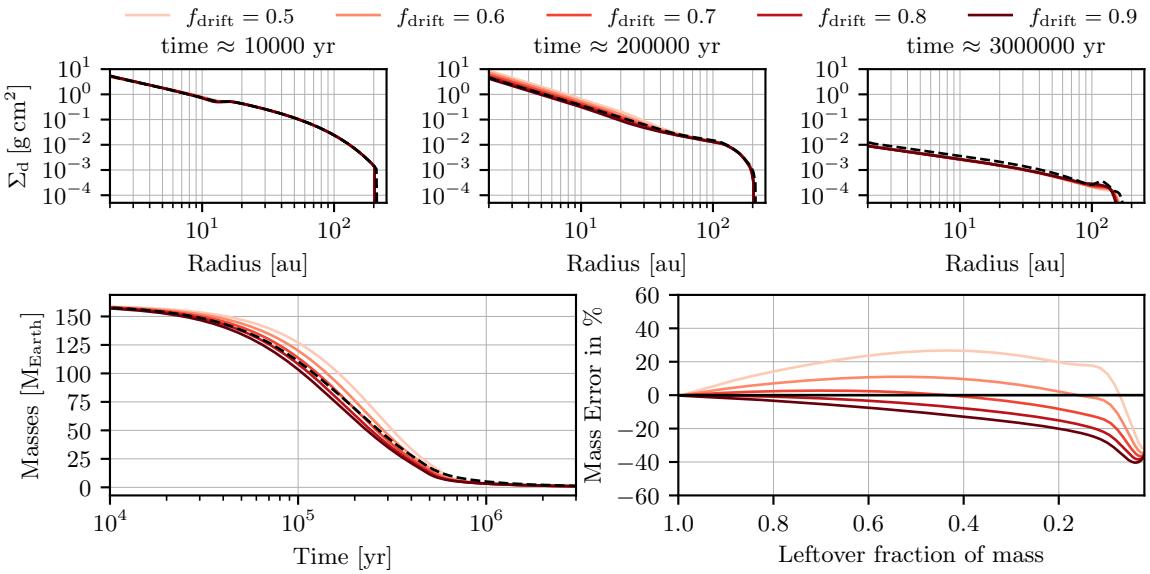

Figure 6.11

Comparison between `DustPy` and our model in a setup without dust diffusion and with different drift calibration factors f_{drift}. The upper row shows a timeseries of the dust column density evolution in three snapshots. In the lower row, we show the mass evolution and the errors with respect to the full coagulation model `DustPy`. For a factor of $f_{\mathrm{drift}} = 0.7$, the mass evolution of the full coagulation model is well reproduced by our three-parameter model.

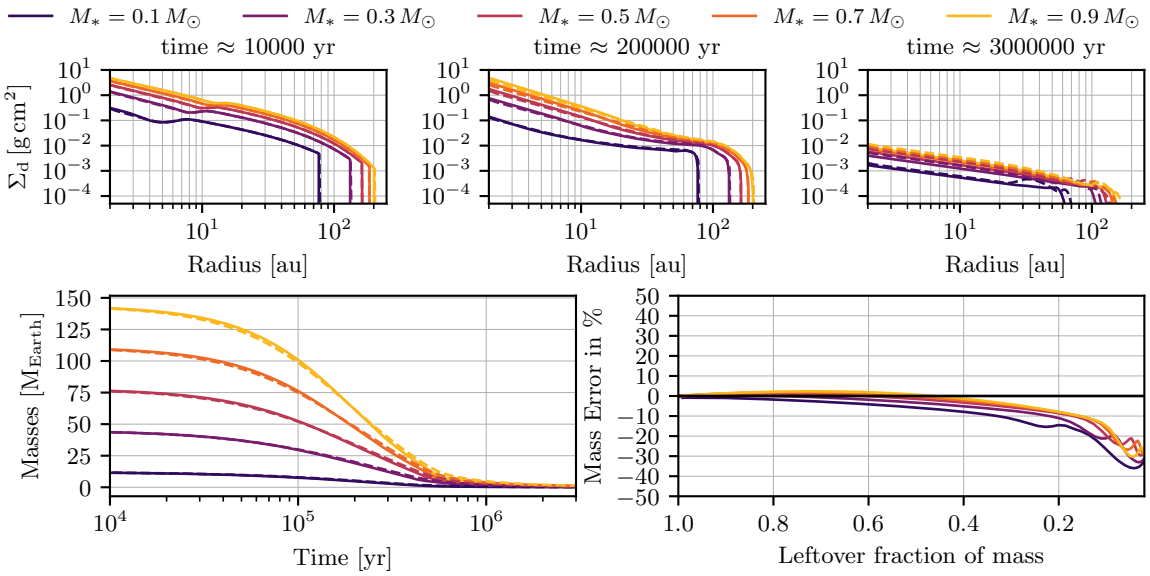

Figure 6.12

Comparison between `DustPy` and our model in setups with different stellar masses without dust diffusion. The upper row shows a time series of the dust column density evolution in three snapshots. In the lower row, we show the mass evolution and the errors with respect to the full coagulation model `DustPy`.

CHAPTER 7

A NEURAL NETWORK MODEL FOR DUST COAGULATION

Thomas Pfeil, Miles Cranmer, Shirley Ho, Philip J. Armitage, Tilman Birnstiel, and Hubert Klahr

the following chapter was published in
Machine Learning and the Physical Sciences Workshop, NeurIPS 2022

Abstract: Planet formation is a multi-scale process in which the coagulation of µm-sized dust grains in protoplanetary disks is strongly influenced by the hydrodynamic processes on scales of astronomical units ($\approx 1.5{\times}10^8$ km). Studies are therefore dependent on subgrid models to emulate the micro physics of dust coagulation on top of a large-scale hydrodynamic simulation. Numerical simulations which include the relevant physical effects are complex and computationally expensive. Here, we present a fast and accurate learned effective model for dust coagulation, trained on data from high-resolution numerical coagulation simulations. Our model captures details of the dust coagulation process that were so far not tractable with other dust coagulation prescriptions with similar computational efficiency.

Author Contributions:

Thomas Pfeil:	numerical simulations, adaptation of the base neural network model and neural network training, data analysis, figure plotting, manuscript writing
Prof. Miles Cranmer:	provision of the base neural network model, scientific discussion, proof reading, project supervision
Prof. Shirley Ho:	scientific discussion, proof reading, project supervision
Prof. Philip J. Armitage:	scientific discussion, proof reading, project supervision
Prof. Til Birnstiel:	scientific discussion, proof reading, project supervision
Prof. Hubert Klahr:	scientific discussion, proof reading, project supervision

7.1 Introduction

After the formation of a protostar, remaining material of its parent molecular cloud core forms a so-called protoplanetary disk around it. About 1 % of the mass of this disk consists of solids in the form of initially µm-sized carbonaceous silicate grains and ices. All solid objects, including the rocky planets, the rocky cores of gas giant planets, comets, and asteroids form out of this material. Subsequent collisions between the grains are caused by gas turbulence and differential aerodynamic drag and lead to the formation of larger aggregates via sticking due to van der Waals forces. Since relative velocities between the grains increase with their sizes, growth is halted at some point, when collisions become too violent for sticking and instead lead to fragmentation (break-up). At this so-called fragmentation barrier, an equilibrium size distribution is reached. Its form is determined by the interior composition of the grains and their size-dependent relative velocities.

Theoretically, these processes are described by the Smoluchowski equation (Smoluchowski, 1916)—an integro-differential equation that gives the mass exchange rates between grains on a continuous spectrum of sizes. Only a few analytically solvable cases exist, which is why most numerical models of dust coagulation rely on solution techniques for the discretized Smoluchowski equation, which is derived by exchanging the continuum of grain sizes by a discreet grid of sizes. Solving the resulting system of ODEs is an elaborate numerically task that requires the size grid to have >100 bins to lead to meaningful results (Brauer et al., 2008; Birnstiel et al., 2009).

An example simulation is shown in the left hand side of Figure 7.1. The model is initialized with a distribution of µm-sized grains. Collisions first lead to an almost exponential growth phase, which, in this case is halted by fragmentation after $\sim 10^4$ yr . The result is a top-heavy equilibrium distribution of up to 2 mm-sized grains.

These multi-bin models are applicable to 0D (local; see Brauer et al., 2008) or 1D (vertically and azimuthally averaged; see Stammler & Birnstiel, 2022) disk models, but due to their high numerical cost, can not be applied in 3D models of protoplanetary disks.

A Power-Law Prescription for Dust Coagulation and the Need for a Machine Learning Approach

We aim to develop an approach in which the dust size distribution is described by a truncated power law, instead of a discretized distribution with hundreds of size bins. Our goal is to make the modeling of dust coagulation on top of large-scale hydrodynamic simulations more feasible. For a given total dust column density $\Sigma_{\rm tot}$, and a minimum particle size $a_{\rm min} = 10^{-5}$ cm, this simplified distribution can be described by only two parameters:

$a_{\rm max}$: The size of the largest particles (truncation size of the power law)

Σ_1 : The column density of particles larger than $a_{\rm int} = \sqrt{a_{\rm max} a_{\rm min}}$.

It can be shown that the exponent of the power-law size distribution $\Sigma(a) \propto a^{p+4}$ is then given by $p = \frac{\log(\Sigma_1/\Sigma_0)}{\log(a_{\rm max}/a_{\rm int})} - 4$, where $\Sigma_0 = \Sigma_{\rm tot} - \Sigma_1$ is the column density of particles smaller than $a_{\rm int}$. In contrast to other approximate models like `two-pop-py` (Birnstiel et al., 2012), this approach makes it possible to retain information about the overall shape of the

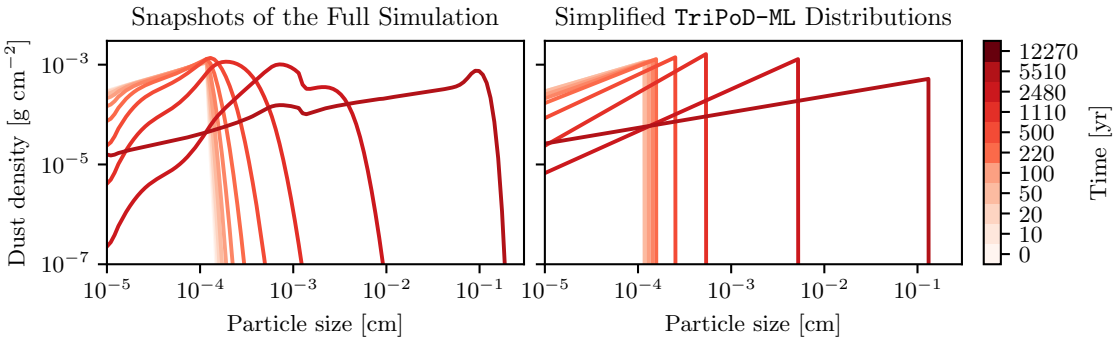

Figure 7.1
Output of a numerical simulation of dust coagulation in a protoplanetary disk (left side). Initially µm-sized grains grow until they reach the fragmentation barrier. On the right-hand side we show the equivalent power-law size distributions derived from the actual simulation results on the left. The simplified time series data is the training data for our machine learning model.

size distribution. It is, however, not trivial to find a mathematical description for the time evolution of the power-law distribution without making strongly simplifying assumptions. We therefore propose a machine-learning-aided power-law model, which predicts the time evolution of the simplified distribution.

7.2 Method

For our method, we trained a Multilayer Perceptron (MLP) on the evolution of power-law grain size distributions derived from detailed multi-bin simulations of dust coagulation. The general workflow of our model is laid out in Figure 7.2. The inputs of our neural network are the size distribution parameters, and the parameters of the protoplanetary disk environment, like gas temperature, gas density, etc. The model's output are the respective time derivatives $\partial_t a_{\max}$ and $\partial_t \Sigma_1$, which are then used as source terms in a numerical integration scheme.
Our simple neural network model therefore makes it possible to simulate the temporal evolution of the physical system, similar to other machine learning approaches explored in recent years Sanchez-Gonzalez et al. (2020); Kidger (2022).
Our MLP consists of 3 hidden layers, each with 100 nodes, 14 nodes in the input layer, and two nodes in the output layer. The layers are fully connected with ReLU activation functions.

Training Data Generation

We create our training data using the `COALA` dust coagulation routine, which was provided by Til Birnstiel and Sebastian Stammler, and which was already used in a hydrodynamic simulation (Drążkowska et al., 2019). `COALA` is a local dust coagulation code, written in FORTRAN that numerically solves the Smoluchowski equation on a mass grid (in our case with 171 bins). 10000 dust coagulation simulations have been created, each with 150 time

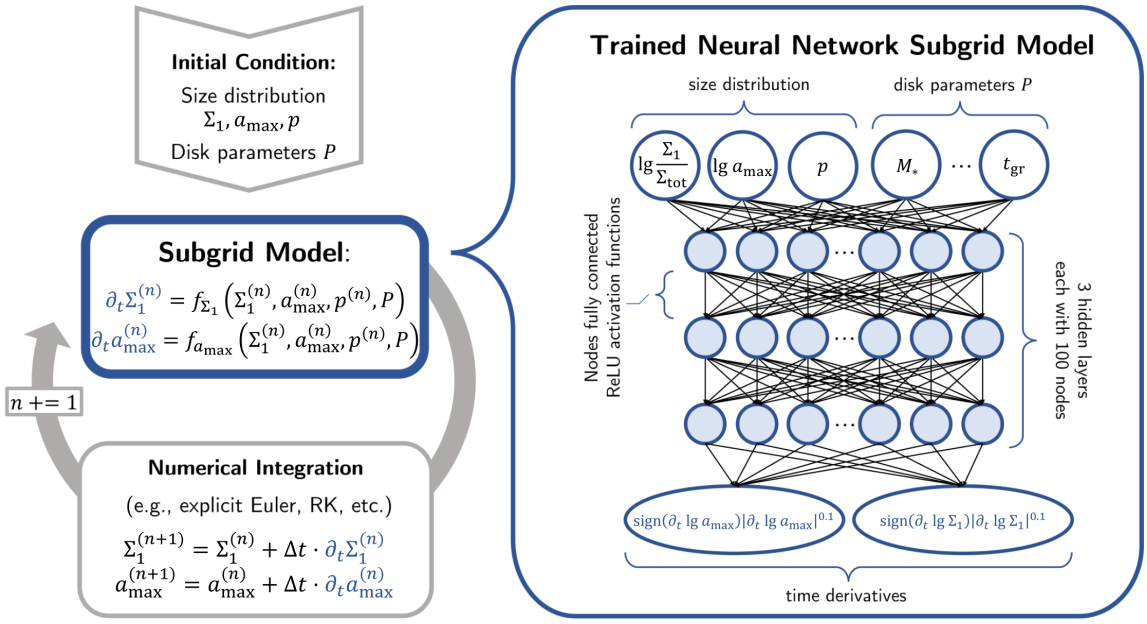

Figure 7.2
General outline of the trained machine learning subgrid model of dust coagulation. An artificial neural network is trained to predict the time derivatives of the size distribution's power-law representation. The resulting source term is used to evolve the distribution in time.

outputs. The dust distributions are evolved over a time corresponding to 50 dust growth time scales, or maximally 10^6 yr to ensure that an equilibrium is reached at the end of each simulation. The initial conditions are chosen randomly from a parameter space that represents the known typical conditions within protoplanetary disks from simulations and observations.

Training Data Pre-Processing

As a first step, we derive the two parameters of the power-law size distributions from the full size distributions with 171 size bins. We define $a_{\max}$ as the particle size for which $\int_{a_{\min}}^{a_{\max}} \Sigma(a)\,\mathrm{d}a/\Sigma_{\text{tot}} = 0.99$ holds, i.e. 99 % of the total mass of the particles has sizes smaller than $a_{\max}$. Σ_1 is then derived by summing up the mass of all bins with sizes larger than $a_{\text{int}} = \sqrt{a_{\max} a_{\min}}$. This results in 10000×150 time series data points for both quantities, from which we derive the respective time derivatives. For training, we scale the data to a range from 0 to 1 and divide the dataset into 8000 training data simulations and 2000 test data simulation. We found that even small deviations from the actual equilibrium states can lead to large errors after time integration with the predicted gradients. Our experiments have shown that the best training results are achieved if we use the tenth root of the time derivatives, multiplied by their sign as the training data. In that way, also small-scale features around the equilibrium states ($\partial_t = 0$) can be learned, leading to the best results during numerical integration and to the correct equilibrium distribution.

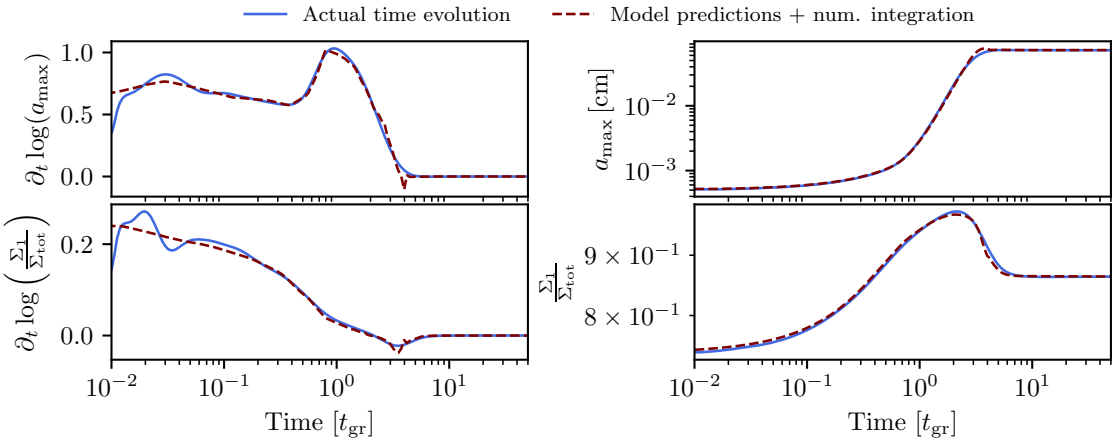

Figure 7.3
Result of a numerical integration with the neural network predictions for the respective time derivatives.

Training Procedure

We train our neural network model within the Pytorch Lightning framework (Paszke et al., 2019; Falcon, 2020), using the Adam optimization algorithm (Kingma & Ba, 2015). The batch size is set to 1000, we apply a learning rate of 3×10^{-4}, and train the model for 1000 epochs. We employ the Mean Absolute Percentage Error (MAPE, de Myttenaere et al., 2016) as a loss function, which also penalized deviations of small absolute value. To avoid division by zero when applying the loss function, we offset the normalized training data by +0.1. Training was conducted on a single Nvidia A100-40GB GPU.

7.3 Results

After training we evaluate the resulting model by using the predicted time derivatives for numerical time integration of the setups from the training data set (see our method in Figure 7.2 and `https://github.com/ThomasPfeil/2popML`). For the tests performed in this work, we utilize an explicit Euler scheme, as shown in Figure 7.2. We limit the time step to ensure numerical stability for the given source terms as

$$\Delta t = C \cdot \min\left(\left|\frac{a_{\max}}{\partial_t a_{\max}}\right|, \left|\frac{\Sigma_1}{\partial_t \Sigma_1}\right|\right), \tag{7.1}$$

with $C = 0.1$. In Figure 7.3, we present an example simulation from the test dataset. The average deviation from the actual time series is about $\sim 4\,\%$. We have conducted this procedure with all 2000 parameter combinations from the test data set. On average, one full integration run takes ≈ 73 ms wall clock time, compared to 791 ms for the full numerical model on the same machine. 11 integrations failed, reaching either negative dust densities or errors larger than 1000 %, resulting in a 99.45 % success rate.

For the 1989 successfully finished test simulations, we plot the distribution of the mean

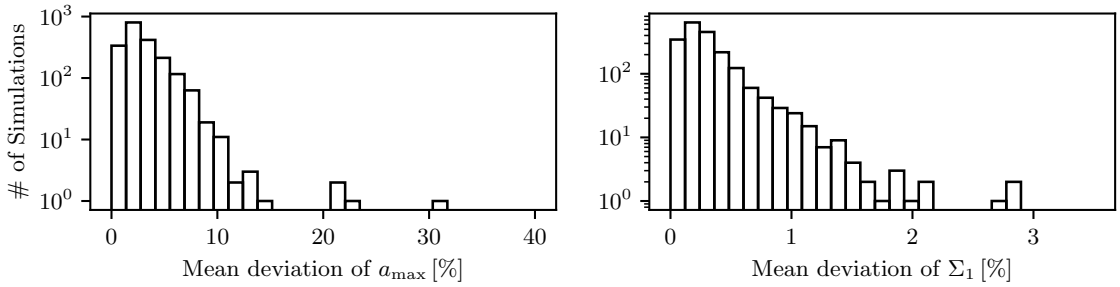

Figure 7.4
Distribution of deviations from the actual simulation time series for the modeled parameters $a_{\max}$ and Σ_1.

relative deviation of each time series to the respective actual time series in Figure 7.4. On average, the deviation between the integration series conducted with the model prediction and the actual data is $\sim 4\,\%$ for the maximum particle size, and $\sim 0.5\,\%$ for the column density of large particles.

7.4 Conclusions and Outlook

Our results strongly suggest that numerical efforts to study the early phases of planet formation can benefit from the use of machine learning techniques. Our neural network model was capable of predicting gradients with high enough precision to allow for time integration of the vast majority of the test data set (99.45 % of the simulations). Our model could therefore be used as a fast and accurate alternative to commonly used full coagulation simulations. Due to its much shorter runtime, it could, for the first time, make large-scale hydrodynamic simulations of protoplanetary disks with dust coagulation feasible.

Since our model is trained on simulation data with various parameter combinations, we expect it to produce accurate results as long as the applied model parameters lie within the ranges used for training. This means, the most important limitation of our model lies in the range of applicable stellar parameters and disk parameters, e.g., stellar mass (varies from 0.01 to $1.4\,M_\odot$), distances to the central star (varied from 0.1 to 100 au), etc.

Further testing is needed for the use of our model in disks with substructure, e.g., disks with planetary gaps and pressure bumps. It is not clear if our model will produce reliable outputs in these environments, since it was trained on parameter combinations derived from simple power-law disks (without substructure).

Testing this requires an implementation of our neural network model as a subgrid model into a hydrodynamics code to simulate gas and dust dynamics in protoplanetary disks. We therefore aim to couple our model to the `PLUTO` code (Mignone et al., 2007). Once a stable run is achieved, we can test our subgrid model in an evolving environment and under the conditions in substructures.

The structural similarity of our approach (Figure 7.2) to semi-analytic physical models could also make it possible to interpret the trained neural network in the future and derive insights into the underlying physics, which could make our results interpretable Cranmer et al. (2020); Kochkov et al. (2021); Stachenfeld et al. (2022).

Acknowledgments

T.P. expresses his gratitude to the Simons Foundation for the opportunity to conduct this project as part of the 2022 Flatiron Machine Learning X Science Summer School. Special thanks goes to the summer school mentors S.H., M.C., and P.A. for their advise and many helpful discussions. T.P., H.K., and T.B. acknowledge the support of the German Science Foundation (DFG) priority program SPP 1992 "Exploring the Diversity of Extrasolar Planets" under grant Nos. BI 1816/7-2 and KL 1469/16-1/2. T.B. acknowledges funding from the European Research Council (ERC) under the European Union's Horizon 2020 research and innovation programme under grant agreement No 714769 and funding by the Deutsche Forschungsgemeinschaft (DFG, German Research Foundation) under grants 361140270, 325594231, and Germany's Excellence Strategy - EXC-2094 - 390783311. All computations were conducted on the VERA cluster of the Max Planck Institute for Astronomy, Heidelberg.

CHAPTER 8

SUMMARY AND OUTLOOK

Hydrodynamic Simulations with Realistic Thermal Relaxation Times from Dust Coagulation Simulations

In Chapter 4 of this thesis, we demonstrated the significance of the dust coagulation process for the vertical shear instability (VSI). VSI drives turbulent gas motions and causes the formation of substructures in protoplanetary disks if the gas is cooled sufficiently fast. Its dependency on thermal relaxation makes it highly sensitive to the dust size distribution because cooling of the gas is achieved via thermal accommodation with the grains. The size distribution is, vice-versa, influenced by the hydrodynamic turbulence created by the VSI. Our axisymmetric hydrodynamic simulations show that the dust coagulation process determines whether and where in protoplanetary disks the VSI can emerge. If small dust grains are depleted because of the coagulation process, thermal accommodation will be inefficient and the VSI will be suppressed. As we show, this effect is mostly important in the outer regions beyond $\sim 70\,\mathrm{au}$. The resulting dichotomy between the turbulent state of the inner regions, and the VSI-inactive state of the outer regions could explain why some protoplanetary disks appear razor-thin in millimeter-wavelength observations (Villenave et al., 2020). These studies, however, have some limitations. The cooling time of the gas, for instance, was calculated from a stationary dust distribution and the redistribution of the dust by the VSI turbulence was thus not taken into account in the simulations.

We therefore conducted hydrodynamic simulations with consistently calculated cooling times, presented in Chapter 5, to assess the influence of the dust dynamics on the cooling times and thus the feedback on the VSI. For this, we took the local dust density distribution into account and calculated the respective dust-gas thermal accommodation timescale in run-time. We found that the initial presence of small grains is one of the important requirements for the growth of VSI. Not only do the small grains provide the fast cooling needed by the VSI, they also settle on very long timescales. This means that, if initially small dust grains are present and if they are vertically dispersed, they can enable cooling over long timescales and thus sustain the emerging VSI turbulence. If however the dust is already grown or strongly settled in the beginning of the simulation, the conditions are hostile to the VSI and the disk remains VSI-inactive. This means that protoplanetary disks with identical gas structure and dust mass can develop vastly different levels of VSI turbulence depending on the initial dust distribution and grain sizes. Note, that after just a few hundred dynamical timescales, when the dust has reached coagulation-fragmentation equilibrium, even the particle sizes in both disks would be similar, yet the level of turbulence would differ. This could be a possible reason for the diverse levels of turbulence observed in protoplanetary disks (Flaherty et al., 2018; Pizzati et al., 2023).

Outlook

Observations show that most protoplanetary disks are not smooth but highly structured (e.g., ALMA-Partnership et al., 2015; Andrews et al., 2018). We are therefore planning to extend our studies from Chapter 4 and Chapter 5 to disks with gaps and pressure bumps. A prominent example of a disk with substructure is HD163296 (see panel 1a in Figure 8.1), which has for instance been studied by Rosotti et al. (2020) and Doi & Kataoka (2021) with focus on the level of turbulence in its rings. Doi & Kataoka (2021) deduced $\alpha/\mathrm{St} > 2.4$ for the inner ring and $\alpha/\mathrm{St} > 0.011$ for the outer ring, hinting towards different levels of turbulence and/or different particle sizes in each ring. In a future study we will fit a combination of dust coagulation and radiative transfer models to the ALMA observations of HD163296 (see panels 1b and 1c of Figure 8.1) to deduce the dust structure of the rings. Given the resulting dust and gas parameters, we want to calculate thermal relaxation times (panel 2 of Figure 8.1) for this disk and run hydrodynamic simulations to investigate whether VSI could be responsible for the turbulence in HD163296's rings.

Furthermore, future studies could continue the development of our method for dynamically evolving thermal relaxation times from Chapter 5. In particular, a combination of this method with the approximate dust coagulation models developed in this thesis would be desirable.

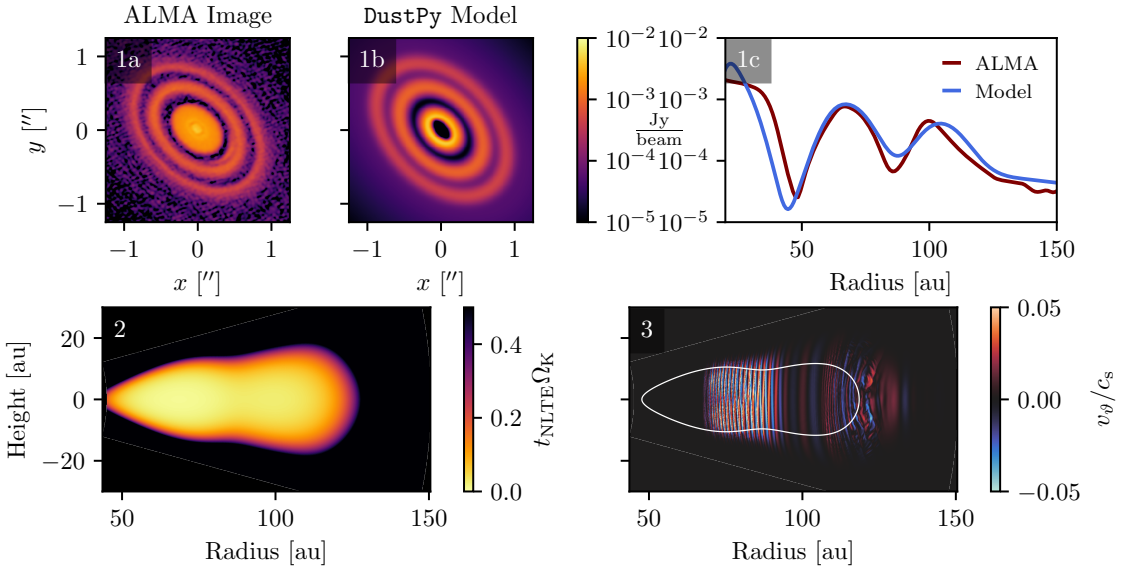

Figure 8.1
Overview of our planned numerical study of turbulence in the protoplanetary disk around HD163296 (see panel 1a, data obtained by Andrews et al., 2018). Dust coagulation models will be directly compared to the ALMA observations of HD163296 via radiative transfer modeling (panels 1b). Once a good fit is achieved between the model and the observations (panel 1c), thermal relaxation times can be calculated from the resulting dust size distributions (panel 2). This will make hydrodynamic simulations of HD163296 possible that could help us to determine whether the VSI plays a role in the generation of turbulence in the rings of this disk (panel 3).

New Methods for Dust Coagulation in Hydrodynamic Simulations of Protoplanetary Disks

Although our studies in Chapter 4 and Chapter 5 allowed us to gain some insight into the effects of dust growth and dynamics on the generation of hydrodynamic turbulence in protoplanetary disks, they omitted the simulation of the dust coagulation process. Implementing full-fledged dust coagulation models in hydrodynamic simulations comes at enormous computational cost (see Drążkowska et al., 2019). The second half of this thesis therefore dealt with the development of fast, approximate methods for dust coagulation. In Chapter 6, we introduced our new three-parameter dust coagulation model `TriPoD`. This model relies on the treatment of the dust size distribution as a truncated power law and thus only requires the time evolution of three parameters—the density of small particles Σ_0, the density of large particles Σ_1 and the maximum particle size $a_{\max}$. By calibrating our model to the full coagulation code `DustPy`, we achieved very good agreement of our fast approximate model with full-fledged dust coagulation simulations. The simplicity of the model allowed us to implement it into the `PLUTO` code for use in vertically integrated hydrodynamic simulations of protoplanetary disks. We demonstrated the accuracy of our model in comparison with full coagulation models in one-dimensional hydrodynamic simulations. We have shown that `TriPoD` produces much better results than the old `two-pop-py` model in a two-dimensional simulation of a protoplanetary disks that is perturbed by the gravitational potential of a Jupiter-mass planet.

A potential alternative to the semi-analytic `TriPoD` model was investigated in Chapter 7. Instead of calibrating the method to full coagulation models by hand, an artificial neural network was trained on local dust coagulation simulations. The result was a fast and accurate local dust coagulation model based on the same power-law size distribution prescription as `TriPoD`. The machine learning model is so far not tested in combination with transport and thus not as readily applicable to studies of protoplanetary disks as the semi-analytic `TriPoD`. Our work nonetheless demonstrates the potential of machine-learning techniques for future numerical studies of planet-forming disks.

Outlook

The `TriPoD` model will be applied to a number of topics in future studies. One possible application will be larger parameter studies of planet-disk systems with dust coagulation that were so far not feasible with full coagulation models. In particular it will be interesting to investigate the filtering efficiency of a planetary gap for various planetary masses and possibly also including the effect of planet migration.

As `TriPoD` is computationally relatively inexpensive, it could be tried to couple it with a simple chemical network, e.g., to track the evolution of ices on grain surfaces throughout the disk's evolution.

In its current form, `TriPoD` is developed for the use in vertically integrated simulations of protoplanetary disks. However, as discussed in the first half of this thesis, many processes in protoplanetary disks are inherently three-dimensional, such as turbulence, planet-disk interactions, etc. The next step in the development of the `TriPoD` model will thus be a version of the model that is applicable to three-dimensional setups. `TriPoD`'s local

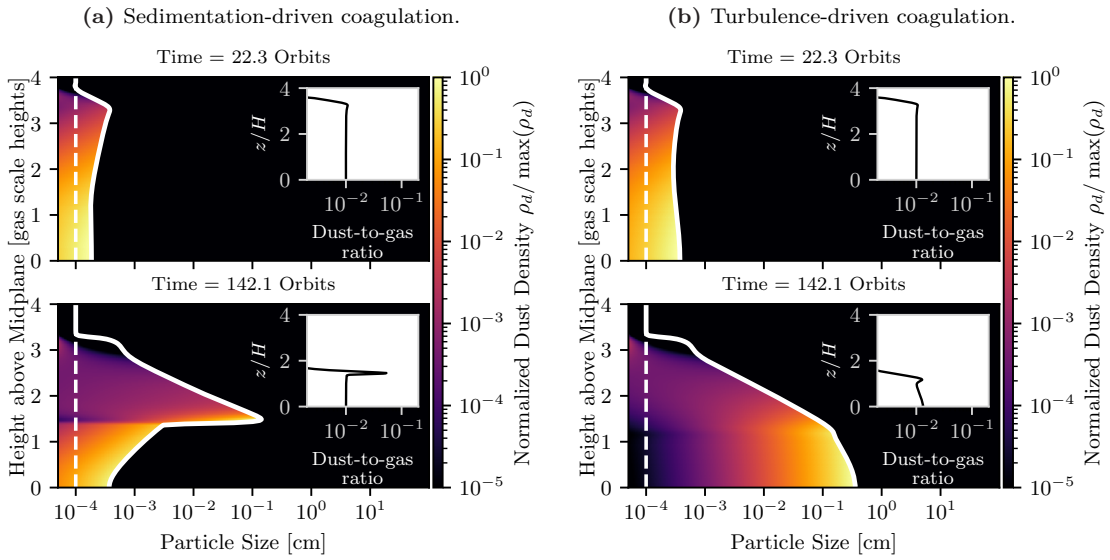

Figure 8.2
A first version of a three-dimensional `TriPoD` model. Shown here is a vertical slice through an axisymmetric, radial-vertical simulation with `PLUTO`.

character should make this transition relatively simple and some first test runs have already been conducted, as shown in Figure 8.2. These simulations depict a radial-vertical slice of a protoplanetary disk with an initially constant dust-to-gas ratio of 1 %. The initial particle size was set to 1 µm and then evolved in time under the three-parameter prescription. Figure 8.2a depicts two snapshots of a simulation without any assumed turbulence, i.e., particle collisions are only driven by sedimentation and drift. Particles from the upper layers settle towards the disk midplane and coagulate with other particles on their way. A wave of large particles rains out into the disk midplane and forms a thin layer. Figure 8.2b shows the same simulation setup but with an assumed turbulence of $\alpha = 10^{-3}$. In this setup dust grows fastest in the disk's midplane, where the highest densities are present. Although `TriPoD` is easily extendable to a three-dimensional version, the lack of full dust coagulation models in three dimensions to calibrate the model to will make testing its accuracy difficult.

The machine-learning-aided three-parameter model `TriPoD-ML` requires further testing and especially implementation into a one-dimensional dust transport scheme to allow for benchmarking against `DustPy`. Furthermore, different neural network architectures could be tested in the future and a more adequate hyperparameter search must be conducted to find the ideal setup. As a next step, a neural network model for the entire dust size distribution could be conceived, which models a size distribution at high resolution instead of the three-parameter approach.

Final Remarks

The unprecedented advancements in radio astronomy of the past decade have shed new light and raised more questions about the dust and gas evolution in protoplanetary disks and its role in the formation of large-scale substructures and, ultimately, planets. We are challenged by a large amount of observational data, whose interpretation requires more and more complexity from our theoretical models. Novel techniques to simulate the interplay of gas and dust must go beyond the aerodynamic coupling of gas and dust and include the effects on coagulation, thermal relaxation and turbulence arising from it. The required methods must not only be reasonably accurate, but also computationally feasible.

In this thesis, we have discussed two possible paths towards the development of such methods. Although our models are approximate and still in development, we hope that they will become valuable tools for the theoretical study of protoplanetary disks and planet formation. The study of flow instabilities and turbulence that depend on the interplay of dust coagulation, hydrodynamics, and thermal relaxation could be a possible field of application, as laid out in the first half of this thesis. If we learn how instabilities like the VSI drive large-scale structure formation and interact with the dust in protoplanetary disks, we can advance our interpretations of observations and better understand the initial conditions for planet formation.

BIBLIOGRAPHY

Aitken, D. K., Roche, P. F., Smith, C. H., James, S. D., & Hough, J. H. 1988, Monthly Notices of the Royal Astronomical Society, 230, 629, doi: 10.1093/MNRAS/230.4.629

Alexiades, V., Amiez, G., & Gremaud, P. A. 1996, Communications in Numerical Methods in Engineering, 12, 31, doi: 10.1002/(SICI)1099-0887(199601)12:1<31::AID-CNM950>3.0.CO;2-5

ALMA-Partnership, Brogan, C. L., Pérez, L. M., et al. 2015, Astrophysical Journal Letters, 808, doi: 10.1088/2041-8205/808/1/L3

Andrews, S. M., Wilner, D. J., Hughes, A. M., Qi, C., & Dullemond, C. P. 2009, Astrophysical Journal, 700, 1502, doi: 10.1088/0004-637X/700/2/1502

Andrews, S. M., Huang, J., Pérez, L. M., et al. 2018, The Astrophysical Journal, 869, L41, doi: 10.3847/2041-8213/aaf741

Antonellini, S., Kamp, I., & Waters, L. B. 2023, Astronomy and Astrophysics, 672, A92, doi: 10.1051/0004-6361/202244773

Appelgren, J., Lambrechts, M., & Van Der Marel, N. 2023, Astronomy and Astrophysics, 673, A139, doi: 10.1051/0004-6361/202245252

Armitage, P. J. 2011, Annual Review of Astronomy and Astrophysics, 49, 195, doi: 10.1146/annurev-astro-081710-102521

—. 2020, Astrophysics of Planet Formation (Cambridge University Press), doi: 10.1017/9781108344227

Avenhaus, H., Quanz, S. P., Garufi, A., et al. 2018, The Astrophysical Journal, 863, 44, doi: 10.3847/1538-4357/aab846

Bae, J., & Zhu, Z. 2018, The Astrophysical Journal, 859, 118, doi: 10.3847/1538-4357/aabf8c

Bae, J., Isella, A., Zhu, Z., et al. 2023, in Protostars and Planets VII, ed. S.-i. Inutsuka, Y. Aikawa, T. Muto, K. Tomida, & M. Tamura, Vol. 534 (San Francisco: ASPCS), 423, doi: 10.48550/ARXIV.2210.13314

Balbus, S. A., & Hawley, J. F. 1991, The Astrophysical Journal, 376, 214, doi: 10.1086/170270

Bally, J. 1982, The Astrophysical Journal, 261, 558, doi: 10.1086/160366

Baraffe, I., Homeier, D., Allard, F., & Chabrier, G. 2015, Astronomy and Astrophysics, 577, doi: 10.1051/0004-6361/201425481

Barge, P., & Sommeria, J. 1995, Astronomy and Astrophysics, 295, L1, doi: 10.48550/ARXIV.ASTRO-PH/9501050

Barker, A. J., & Latter, H. N. 2015, Monthly Notices of the Royal Astronomical Society, 450, 21, doi: 10.1093/mnras/stv640

Barranco, J. A., Pei, S., & Marcus, P. S. 2018, The Astrophysical Journal, 869, 127, doi: 10.3847/1538-4357/aaec80

Baruteau, C., Barraza, M., Pérez, S., et al. 2019, Monthly Notices of the Royal Astronomical Society, 486, 304, doi: 10.1093/mnras/stz802

Bate, M. R. 2022, Monthly Notices of the Royal Astronomical Society, 514, 2145, doi: 10.1093/mnras/stac1391

Batten, P., Clarke, N., Lambert, C., & Causon, D. M. 1997, SIAM Journal on Scientific Computing, 18, 1553, doi: 10.1137/S1064827593260140

Beckwith, S. V. W., Sargent, A. I., Chini, R. S., & Guesten, R. 1990, Astronomical Journal, 99, 924, doi: 10.1086/115385

Bell, K. R., & Lin, D. N. C. 1994, The Astrophysical Journal, 427, 987, doi: 10.1086/174206

Benítez-Llambay, P., Krapp, L., & Pessah, M. E. 2019, The Astrophysical Journal Supplement Series, 241, 25, doi: 10.3847/1538-4365/ab0a0e

Benítez-Llambay, P., & Masset, F. S. 2016, The Astrophysical Journal Supplement Series, 223, 11, doi: 10.3847/0067-0049/223/1/11

Bergez-Casalou, C., Bitsch, B., Kurtovic, N. T., & Pinilla, P. 2022, Astronomy and Astrophysics, 659, A6, doi: 10.1051/0004-6361/202142490

Bhandare, A., Kuiper, R., Henning, T., et al. 2020, Astronomy and Astrophysics, 638, 86, doi: 10.1051/0004-6361/201937029

—. 2018, Astronomy and Astrophysics, 618, 95, doi: 10.1051/0004-6361/201832635

Biele, J., Grott, M., Zolensky, M. E., Benisek, A., & Dachs, E. 2022, International Journal of Thermophysics, 43, 1, doi: 10.1007/s10765-022-03046-5

Binkert, F. 2023, Monthly Notices of the Royal Astronomical Society, 000, 1, doi: 10.1093/MNRAS/STAD2471

Birnstiel, T. 2018, dsharp_opac: Revised Release of Package, doi: 10.5281/ZENODO.1495277

—. 2023, Annual Reviews of Astronomy and Astrophysics. https://arxiv.org/abs/2312.13287

Birnstiel, T., & Andrews, S. M. 2014, The Astrophysical Journal, 780, 153, doi: 10.1088/0004-637X/780/2/153

Birnstiel, T., Dullemond, C. P., & Brauer, F. 2009, Astronomy and Astrophysics, 503, 5, doi: 10.1051/0004-6361/200912452

—. 2010, Astronomy and Astrophysics, 513, 79, doi: 10.1051/0004-6361/200913731

Birnstiel, T., Klahr, H., & Ercolano, B. 2012, Astronomy and Astrophysics, 539, 148, doi: 10.1051/0004-6361/201118136

Birnstiel, T., Ormel, C. W., & Dullemond, C. P. 2011, Astronomy and Astrophysics, 525, 11, doi: 10.1051/0004-6361/201015228

Birnstiel, T., Dullemond, C. P., Zhu, Z., et al. 2018, The Astrophysical Journal, 869, L45, doi: 10.3847/2041-8213/aaf743

Bjorkman, J. E., & Wood, K. 2001, The Astrophysical Journal, 554, 615, doi: 10.1086/321336

Blaes, O. M., & Balbus, S. A. 1994, The Astrophysical Journal, 421, 163, doi: 10.1086/173634

Blanco, D., Ricci, L., Flock, M., & Turner, N. 2021, The Astrophysical Journal, 920, 70, doi: 10.3847/1538-4357/ac15fa

Blandford, R. D., & Payne, D. G. 1982, Monthly Notices of the Royal Astronomical Society, 199, 883, doi: 10.1093/mnras/199.4.883

Blum, J. 2000, Space Science Reviews, 92, 265, doi: 10.1023/a:1005251414391

—. 2018, Space Science Reviews, 214, 1, doi: 10.1007/s11214-018-0486-5

Blum, J., Schrapler, R., Davidsson, B. J. R., & Trigo-Rodriguez, J. M. 2006, The Astrophysical Journal, 652, 1768, doi: 10.1086/508017

Bohren, C. F., & Huffman, D. R. 1998, Absorption and scattering of light by small particles (Nashville, TN: John Wiley & Sons)

Bonnor, W. B. 1956, Monthly Notices of the Royal Astronomical Society, 116, 351, doi: 10.1093/mnras/116.3.351

Boss, A. P. 1997, Science, 276, 1836, doi: 10.1126/science.276.5320.1836

Boussinesq, J. 1877, Essai sur la théorie des eaux courantes, Impr. nationale (Paris). https://gallica.bnf.fr/ark:/12148/bpt6k56673076

Brauer, F., Dullemond, P., & Henning, T. 2008, Astronomy and Astrophysics, 480, 859, doi: 10.1051/0004-6361:20077759

Burke, J. R., & Hollenbach, D. J. 1983, The Astrophysical Journal, 265, 223, doi: 10.1086/160667

Burn, R., Emsenhuber, A., Weder, J., et al. 2022, Astronomy and Astrophysics, 666, doi: 10.1051/0004-6361/202243262

Cameron, A. G. 1978, The Moon and the Planets, 18, 5, doi: 10.1007/BF00896696

Chamberlin, T. C., & Moulton, F. R. 1909, The development of the planetesimal hypothesis, doi: 10.1126/science.30.775.642

Chambers, J. 2018, The Astrophysical Journal, 865, 30, doi: 10.3847/1538-4357/aada09

Chapman, S., & Cowling, T. G. 1991, Cambridge mathematical library: The mathematical theory of non-uniform gases: An account of the kinetic theory of viscosity, thermal conduction and diffusion in gases (Cambridge, England: Cambridge University Press)

Charnoz, S., & Taillifet, E. 2012, Astrophysical Journal, 753, 119, doi: 10.1088/0004-637X/753/2/119

Chevance, M., Krumholz, M. R., McLeod, A. F., et al. 2023, in Protostars and Planets VII, ed. S.-i. Inutsuka, Y. Aikawa, T. Muto, K. Tomida, & M. Tamura, Vol. 534 (San Francisco: ASPCS), 717, doi: 10.48550/ARXIV.2203.09759

Chiang, E. I., & Goldreich, P. 1997, The Astrophysical Journal, 519, 279, doi: 10.1086/307351

Clarke, C., & Carswell, B. 2007, Principles of Astrophysical Fluid Dynamics, 1, doi: 10.1017/CBO9780511813450

Courant, R., Friedrichs, K., & Lewy, H. 1928, Mathematische Annalen, 100, 32, doi: 10.1007/BF01448839

Cox, D. P., & Reynolds, R. J. 1987, Annual Review of Astronomy and Astrophysics, 25, 303, doi: 10.1146/annurev.aa.25.090187.001511

Cranmer, M., Sanchez-Gonzalez, A., Battaglia, P., et al. 2020, Advances in Neural Information Processing Systems, 2020-Decem. https://arxiv.org/abs/2006.11287

Cui, C., & Latter, H. N. 2022, Monthly Notices of the Royal Astronomical Society, 512, 1639, doi: 10.1093/mnras/stac279

Cuzzi, J. N., Dobrovolskis, A. R., & Champney, J. M. 1993, Icarus, 106, 102, doi: 10.1006/icar.1993.1161

D'Alessio, P., Calvet, N., & Hartmann, L. 2001, The Astrophysical Journal, 553, 321, doi: 10.1086/320655

D'Alessio, P., Canto, J., Calvet, N., & Lizano, S. 1998, The Astrophysical Journal, 500, 411, doi: 10.1086/305702

Davidson, P. 2015, Turbulence: An Introduction for Scientists and Engineers, 2nd edn. (London, England: Oxford University Press)

Davidson, P. A. 2010, Turbulence in Rotating, Stratified and Electrically Conducting Fluids, 1, doi: 10.1017/CBO9781139208673

de Myttenaere, A., Golden, B., Le Grand, B., & Rossi, F. 2016, Neurocomputing, 192, 38, doi: 10.1016/j.neucom.2015.12.114

Delage, T. N., Gárate, M., Okuzumi, S., et al. 2023, Astronomy and Astrophysics, 674, A190, doi: 10.1051/0004-6361/202244731

Desch, S. J. 2004, The Astrophysical Journal, 608, 509, doi: 10.1086/392527

Dohnanyi, J. S. 1969, Journal of Geophysical Research, 74, 2531, doi: 10.1029/JB074I010P02531

Doi, K., & Kataoka, A. 2021, The Astrophysical Journal, 912, 164, doi: 10.3847/1538-4357/abe5a6

Dominik, C., & Dullemond, C. 2023, Astronomy and Astrophysics, forthcomin, doi: 10.1051/0004-6361/202347716

Dominik, C., & Tielens, A. G. G. M. 1997, The Astrophysical Journal, 480, 647, doi: 10.1086/303996

Dong, R., & Fung, J. 2017, The Astrophysical Journal, 835, 146, doi: 10.3847/1538-4357/835/2/146

Dong, R., Liu, S.-y., Eisner, J., et al. 2018, The Astrophysical Journal, 860, 124, doi: 10.3847/1538-4357/aac6cb

Drazin, P. G., & Reid, W. H. 2004, Hydrodynamic Stability Second Edition (Cambridge University Press), 605. https://books.google.com/books/about/Hydrodynamic_Stability.html?hl=de&id=GDDhso7XjngC

Drążkowska, J., Li, S., Birnstiel, T., Stammler, S. M., & Li, H. 2019, The Astrophysical Journal, 885, 91, doi: 10.3847/1538-4357/ab46b7

Drążkowska, J., Stammler, S. M., & Birnstiel, T. 2021, Astronomy and Astrophysics, 647, 15, doi: 10.1051/0004-6361/202039925

Drazkowska, J., Windmark, F., & Dullemond, C. P. 2013, Astronomy and Astrophysics, 556, A37, doi: 10.1051/0004-6361/201321566

Drążkowska, J., Windmark, F., & Dullemond, C. P. 2014, Astronomy and Astrophysics, 567, doi: 10.1051/0004-6361/201423708

Drążkowska, J., Bitsch, B., Lambrechts, M., et al. 2023, in Protostars and Planets VII, ed. S.-i. Inutsuka, Y. Aikawa, T. Muto, K. Tomida, & M. Tamura, Vol. 534 (San Francisco: ASPCS), 717–759. https://arxiv.org/abs/2203.09759

Dubrulle, B., Morfill, G., & Sterzik, M. 1995, Icarus, 114, 237, doi: 10.1006/icar.1995.1058

Duffell, P. C. 2020, The Astrophysical Journal, 889, 16, doi: 10.3847/1538-4357/ab5b0f

Dullemond, C. P., Ziampras, A., Ostertag, D., & Dominik, C. 2022, Astronomy and Astrophysics, 668, 105, doi: 10.1051/0004-6361/202244218

Dullemond, C. P., Juhasz, A., Pohl, A., et al. 2012, ascl, ascl:1202.015. https://ui.adsabs.harvard.edu/abs/2012ascl.soft02015D/abstract

Dullemond, C. P., Birnstiel, T., Huang, J., et al. 2018, The Astrophysical Journal, 869, L46, doi: 10.3847/2041-8213/aaf742

Ebert, R. 1955, Zeitschrift fur Astrophysik, 37, 217. http://adsabs.harvard.edu.ep.fjernadgang.kb.dk/abs/1955ZA.....37..217E

Eddington, A. S. 1926, Cambridge science classics: The internal constitution of the stars (Cambridge, England: Cambridge University Press)

Einstein, A. 1905, Annalen der Physik, 322, 549, doi: 10.1002/ANDP.19053220806

Emsenhuber, A., Mordasini, C., Burn, R., et al. 2021, Astronomy and Astrophysics, 656, 69, doi: 10.1051/0004-6361/202038553

Epstein, P. S. 1924, Physical Review, 23, 710, doi: 10.1103/PhysRev.23.710

Falcon, W. A. 2020, Lightning: Deep learning framework to train, deploy, and ship AI products Lightning fast. https://github.com/Lightning-AI/lightning

Flaherty, K. M., Hughes, A. M., Teague, R., et al. 2018, The Astrophysical Journal, 856, 117, doi: 10.3847/1538-4357/aab615

Flock, M., Ruge, J. P., Dzyurkevich, N., et al. 2015, Astronomy and Astrophysics, 574, A68, doi: 10.1051/0004-6361/201424693

Flock, M., Turner, N. J., Nelson, R. P., et al. 2020, The Astrophysical Journal, 897, 155, doi: 10.3847/1538-4357/ab9641

Flores-Rivera, L., Flock, M., & Nakatani, R. 2020, Astronomy and Astrophysics, 644, 50, doi: 10.1051/0004-6361/202039294

Forgan, D. H., Hall, C., Meru, F., & Rice, W. K. 2018, Monthly Notices of the Royal Astronomical Society, 474, 5036, doi: 10.1093/MNRAS/STX2870

Fricke, K. 1968, Zeitschrift fur Astrophysik, 68, 317. https://ui.adsabs.harvard.edu/abs/1968ZA.....68..317F/abstract

Fromang, S., & Nelson, R. P. 2009, Astronomy and Astrophysics, 496, 597, doi: 10.1051/0004-6361/200811220

Fukuhara, Y., Okuzumi, S., & Ono, T. 2021, The Astrophysical Journal, 914, 132, doi: 10.3847/1538-4357/abfe5c

—. 2023, Publications of the Astronomical Society of Japan, 75, 233, doi: 10.1093/pasj/psac107

Galametz, M., Maury, A. J., Valdivia, V., et al. 2019, Astronomy and Astrophysics, 632, doi: 10.1051/0004-6361/201936342

Gammie, C. F. 2001, The Astrophysical Journal, 553, 174, doi: 10.1086/320631

Gárate, M., Delage, T. N., Stadler, J., et al. 2021, Astronomy and Astrophysics, 655, 18, doi: 10.1051/0004-6361/202141444

Garaud, P., Barriere-Fouchet, L., & Lin, D. N. C. 2004, The Astrophysical Journal, 603, 292, doi: 10.1086/381385

Gerbig, K., Murray-Clay, R. A., Klahr, H., & Baehr, H. 2020, The Astrophysical Journal, 895, 91, doi: 10.3847/1538-4357/ab8d37

Godunov, S. K. 1959, Mat. Sb., 47, 271. https://hal.science/hal-01620642https://hal.science/hal-01620642/document

Goldreich, P., & Schubert, G. 1967, The Astrophysical Journal, 150, 571, doi: 10.1086/149360

Goldreich, P., & Tremaine, S. 1978, The Astrophysical Journal, 222, 850, doi: 10.1086/156203

Goldreich, P., & Ward, W. R. 1973, The Astrophysical Journal, 183, 1051, doi: 10.1086/152291

Gonzalez, J. F., Laibe, G., & Maddison, S. T. 2017, Monthly Notices of the Royal Astronomical Society, 467, 1984, doi: 10.1093/mnras/stx016

Guillet, V., Hennebelle, P., Pineau Des Forêts, G., et al. 2020, Astronomy and Astrophysics, 643, 17, doi: 10.1051/0004-6361/201937387

Güttler, C., Blum, J., Zsom, A., Ormel, C. W., & Dullemond, C. P. 2010, Astronomy and Astrophysics, 513, A56, doi: 10.1051/0004-6361/200912852

Haisch, K. E. J., Lada, E. A., & Lada, C. J. 2001, The Astrophysical Journal, 553, L153, doi: 10.1086/320685

Harris, C. R., Millman, K. J., van der Walt, S. J., et al. 2020, Nature, 585, 357, doi: 10.1038/s41586-020-2649-2

Harten, A., Lax, P. D., & van Leer, B. 1983, SIAM Review, 25, 35, doi: 10.1137/1025002

Hartmann, L., Calvet, N., Gullbring, E., & D'Alessio, P. 1998, The Astrophysical Journal, 495, 385, doi: 10.1086/305277

Hawley, J. F., Balbus, S. A., & Stone, J. M. 2001, The Astrophysical Journal, 554, L49, doi: 10.1086/320931

Held, L. E., & Latter, H. N. 2018, Monthly Notices of the Royal Astronomical Society, 480, 4797, doi: 10.1093/mnras/sty2097

Hirose, S., & Shi, J. M. 2017, Monthly Notices of the Royal Astronomical Society, 469, 561, doi: 10.1093/mnras/stx824

Holton, J. R., & Hakim, G. J. 2012, An Introduction to Dynamic Meteorology: Fifth Edition, 9780123848, 1, doi: 10.1016/C2009-0-63394-8

Huang, J., Andrews, S. M., Dullemond, C. P., et al. 2018, The Astrophysical Journal, 869, L42, doi: 10.3847/2041-8213/aaf740

Huang, P., & Bai, X.-N. 2022, The Astrophysical Journal Supplement Series, 262, 11, doi: 10.3847/1538-4365/ac76cb

Hunter, J. D. 2007, Computing in Science and Engineering, 9, 90, doi: 10.1109/MCSE.2007.55

Jaeger, C., Mutschke, Begemann, B., Dorschner, J., & Henning, T. 1994, Astronomy and Astrophysics, 292, 641. https://ui.adsabs.harvard.edu/abs/1994A%26A...292..641J/abstract

Jankovic, M. R., Owen, J. E., Mohanty, S., & Tan, J. C. 2021, Monthly Notices of the Royal Astronomical Society, 504, 280, doi: 10.1093/mnras/stab920

Johansen, A., Oishi, J. S., Low, M. M. M., et al. 2007, Nature, 448, 1022, doi: 10.1038/nature06086

Johnson, B. M., & Gammie, C. F. 2003, The Astrophysical Journal, 597, 131, doi: 10.1086/378392

Kawasaki, Y., & Machida, M. N. 2023, Monthly Notices of the Royal Astronomical Society, 522, 3679, doi: 10.1093/mnras/stad1241

Keppler, M., Benisty, M., Müller, A., et al. 2018, Astronomy and Astrophysics, 617, A44, doi: 10.1051/0004-6361/201832957

Kidger, P. 2022, PhD thesis, University of Oxford, doi: 10.13039/501100000266

Kimura, H., Wada, K., Senshu, H., & Kobayashi, H. 2015, Astrophysical Journal, 812, 67, doi: 10.1088/0004-637X/812/1/67

Kingma, D. P., & Ba, J. L. 2015, 3rd International Conference on Learning Representations, ICLR 2015 - Conference Track Proceedings. https://arxiv.org/abs/1412.6980

Klahr, H., Baehr, H., & Fuksman, J. D. M. 2023, The Astrophysical Journal, in press. https://arxiv.org/abs/2305.08165

Klahr, H., & Hubbard, A. 2014, Astrophysical Journal, 788, 21, doi: 10.1088/0004-637X/788/1/21

Klahr, H., & Schreiber, A. 2020, The Astrophysical Journal, 901, 54, doi: 10.3847/1538-4357/abac58

Klahr, H. H., & Bodenheimer, P. 2003, The Astrophysical Journal, 582, 869, doi: 10.1086/344743

Kobayashi, H., Tanaka, H., & Okuzumi, S. 2016, The Astrophysical Journal, 817, 105, doi: 10.3847/0004-637x/817/2/105

Kochkov, D., Smith, J. A., Alieva, A., et al. 2021, Proceedings of the National Academy of Sciences of the United States of America, 118, e2101784118, doi: 10.1073/PNAS.2101784118

Kolmogorov, A. N. 1941, Doklady AN SSSR, 30, 299

Kornet, K., Stepinski, T. F., & Rózyczka, M. 2001, Astronomy and Astrophysics, 378, 180, doi: 10.1051/0004-6361:20011183

Krijt, S., & Ciesla, F. J. 2016, The Astrophysical Journal, 822, 111, doi: 10.3847/0004-637x/822/2/111

Landau, L., & Lifschitz, E. 1987, Fluid Mechanics, Landau and Lifshitz: Course of Theoretical Physics, Volume 6, 2nd edn. (Pergamon), doi: 10.1016/C2013-0-03799-1

Larson, R. B. 1969, Monthly Notices of the Royal Astronomical Society, 145, 271, doi: 10.1093/mnras/145.3.271

Latter, H. N., & Papaloizou, J. 2018, Monthly Notices of the Royal Astronomical Society, 474, 3110, doi: 10.1093/mnras/stx3031

Lau, T. C. H., Drążkowska, J., Stammler, S. M., Birnstiel, T., & Dullemond, C. P. 2022, Astronomy and Astrophysics, 668, 170, doi: 10.1051/0004-6361/202244864

Leiendecker, H., Jang-Condell, H., Turner, N. J., & Myers, A. D. 2022, The Astrophysical Journal, 941, 172, doi: 10.3847/1538-4357/aca32d

Lenz, C. T., Klahr, H., Birnstiel, T., Kretke, K., & Stammler, S. 2020, Astronomy and Astrophysics, 640, doi: 10.1051/0004-6361/202037878

Lesur, G., Flock, M., Ercolano, B., et al. 2023, in Protostars and Planets VII, ed. S.-i. Inutsuka, Y. Aikawa, T. Muto, K. Tomida, & M. Tamura, Vol. 534 (San Francisco: ASPCS), 465. https://ui.adsabs.harvard.edu/abs/2023ASPC..534..465L/abstract

Levermore, G. D., & Pomraning, G. C. 1981, The Astrophysical Journal, 248, 321. https://ui.adsabs.harvard.edu/abs/1981ApJ...248..321L/abstract

Lichtenberg, T., Drążkowska, J., Schönbächler, M., Golabek, G. J., & Hands, T. O. 2021, Science, 371, 365, doi: 10.1126/science.abb3091

Lin, D. N. C., & Papaloizou, J. 1980, Monthly Notices of the Royal Astronomical Society, 191, 37, doi: 10.1093/mnras/191.1.37

Lin, M. K. 2019, Monthly Notices of the Royal Astronomical Society, 485, 5221, doi: 10.1093/MNRAS/STZ701

Lin, M. K., & Youdin, A. N. 2015, Astrophysical Journal, 811, doi: 10.1088/0004-637X/811/1/17

Lin, M.-K., & Youdin, A. N. 2017, The Astrophysical Journal, 849, 129, doi: 10.3847/1538-4357/aa92cd

Liu, X. D. 1994, Journal of Computational Physics, 115, 200, doi: 10.1006/jcph.1994.1187

Lodders, K. 2003, The Astrophysical Journal, 591, 1220, doi: 10.1086/375492

Lombart, M., Hutchison, M., & Lee, Y. N. 2022, Monthly Notices of the Royal Astronomical Society, 517, 2012, doi: 10.1093/mnras/stac2232

Lovelace, R. V. E., Li, H., Colgate, S. A., & Nelson, A. F. 1999, The Astrophysical Journal, 513, 805, doi: 10.1086/306900

Lüst, R. 1952, Zeitschrift fur Naturforschung - Section A Journal of Physical Sciences, 7, 87, doi: 10.1515/zna-1952-0118

Lynden-Bell, D., & Pringle, J. E. 1974, Monthly Notices of the Royal Astronomical Society, 168, 603, doi: 10.1093/mnras/168.3.603

Lyra, W. 2014, The Astrophysical Journal, 789, 77, doi: 10.1088/0004-637X/789/1/77

Lyra, W., & Mac Low, M. M. 2012, The Astrophysical Journal, 756, 62, doi: 10.1088/0004-637X/756/1/62

Lyra, W., & Umurhan, O. M. 2019, Publications of the Astronomical Society of the Pacific, 131, 072001, doi: 10.1088/1538-3873/aaf5ff

Magg, E., Bergemann, M., Serenelli, A., et al. 2022, Astronomy and Astrophysics, 661, 140, doi: 10.1051/0004-6361/202142971

Malygin, M. G., Klahr, H., Semenov, D., Henning, T., & Dullemond, C. P. 2017, Astronomy and Astrophysics, 605, 30, doi: 10.1051/0004-6361/201629933

Malygin, M. G., Kuiper, R., Klahr, H., Dullemond, C. P., & Henning, T. 2014, Astronomy and Astrophysics, 568, 91, doi: 10.1051/0004-6361/201423768

Manara, C. F., Ansdell, M., Rosotti, G. P., et al. 2023, in Protostars and Planets VII, ed. S.-i. Inutsuka, Y. Aikawa, T. Muto, K. Tomida, & M. Tamura, Vol. 534 (San Francisco: ASPCS), 539, doi: 10.48550/ARXIV.2203.09930

Manger, N., & Klahr, H. 2018, Monthly Notices of the Royal Astronomical Society, 480, 2125, doi: 10.1093/MNRAS/STY1909

Manger, N., Pfeil, T., & Klahr, H. 2021, Monthly Notices of the Royal Astronomical Society, 508, 5402, doi: 10.1093/mnras/stab2599

Marcus, P. S., Pei, S., Jiang, C.-H., & Barranco, J. A. 2016, The Astrophysical Journal, 833, 148, doi: 10.3847/1538-4357/833/2/148

Marcus, P. S., Pei, S., Jiang, C. H., et al. 2015, The Astrophysical Journal, 808, 87, doi: 10.1088/0004-637X/808/1/87

Marcus, P. S., Pei, S., Jiang, C. H., & Hassanzadeh, P. 2013, Physical Review Letters, 111, doi: 10.1103/PhysRevLett.111.084501

Masunaga, H., & Inutsuka, S. 2000, The Astrophysical Journal, 531, 350, doi: 10.1086/308439

Masunaga, H., Miyama, S. M., & Inutsuka, S. 1998, The Astrophysical Journal, 495, 346, doi: 10.1086/305281

Mathis, J. S., Rumpl, W., & Nordsieck, K. H. 1977, The Astrophysical Journal, 217, 425, doi: 10.1086/155591

Mayor, M., & Queloz, D. 1995, Nature, 378, 355, doi: 10.1038/378355a0

Meyer, F., & Meyer-Hofmeister, E. 1982, Astronomy and Astrophysics, 106, 34. https://ui.adsabs.harvard.edu/abs/1982A&A...106...34M/abstract

Mie, G. 1908, Annalen der Physik, 330, 377, doi: 10.1002/andp.19083300302

Mignone, A., Bodo, G., Massaglia, S., et al. 2007, The Astrophysical Journal Supplement Series, 170, 228, doi: 10.1086/513316

Mignone, A., Plewa, T., & Bodo, G. 2005, The Astrophysical Journal Supplement Series, 160, 199, doi: 10.1086/430905

Min, M. 2015, EPJ Web of Conferences, 102, doi: 10.1051/epjconf/201510200005

Miotello, A., Kamp, I., Birnstiel, T., et al. 2023, in Protostars and Planets VII, ed. S.-i. Inutsuka, Y. Aikawa, T. Muto, K. Tomida, & M. Tamura, Vol. 534 (San Francisco: ASPCS), 501, doi: 10.48550/ARXIV.2203.09818

Miyake, K., & Nakagawa, Y. 1993, Icarus, 106, 20, doi: 10.1006/icar.1993.1156

Moll, R. 2012, Astronomy and Astrophysics, 548, 76, doi: 10.1051/0004-6361/201118249

Morbidelli, A., & Raymond, S. N. 2016, Journal of Geophysical Research: Planets, 121, 1962, doi: 10.1002/2016JE005088

Mordasini, C., Alibert, Y., & Benz, W. 2009, Astronomy and Astrophysics, 501, 1139, doi: 10.1051/0004-6361/200810301

Muley, D., Fuksman, J. D. M., & Klahr, H. 2023, Astronomy and Astrophysics, 678, A162, doi: 10.1051/0004-6361/202347101

Musiolik, G., & Wurm, G. 2019, The Astrophysical Journal, 873, 58, doi: 10.3847/1538-4357/ab0428

Nakagawa, Y., Nakazawa, K., & Hayashi, C. 1981, Icarus, 45, 517, doi: 10.1016/0019-1035(81)90018-X

Nakagawa, Y., Sekiya, M., & Hayashi, C. 1986, Icarus, 67, 375, doi: 10.1016/0019-1035(86)90121-1

Nelson, R. P., Gressel, O., & Umurhan, O. M. 2013, Monthly Notices of the Royal Astronomical Society, 435, 2610, doi: 10.1093/mnras/stt1475

Nesvorný, D., Li, R., Youdin, A. N., Simon, J. B., & Grundy, W. M. 2019, Nature Astronomy, 3, 808, doi: 10.1038/s41550-019-0806-z

Noebauer, U. M., & Sim, S. A. 2019, Living Reviews in Computational Astrophysics 2019 5:1, 5, 1, doi: 10.1007/S41115-019-0004-9

Öberg, K. I., Guzmán, V. V., Walsh, C., et al. 2021, The Astrophysical Journal Supplement Series, 257, 1, doi: 10.3847/1538-4365/ac1432

O'dell, C. R., Wen, Z., & Hu, X. 1993, The Astrophysical Journal, 410, 696, doi: 10.1086/172786

Ogilvie, G. I., & Lubow, S. H. 2002, Monthly Notices of the Royal Astronomical Society, 330, 950, doi: 10.1046/j.1365-8711.2002.05148.x

Ohashi, S., & Kataoka, A. 2019, The Astrophysical Journal, 886, 103, doi: 10.3847/1538-4357/ab5107

Ohtsuki, K., Nakagawa, Y., & Nakazawa, K. 1990, Icarus, 83, 205, doi: 10.1016/0019-1035(90)90015-2

Ormel, C. W., & Cuzzi, J. N. 2007, Astronomy and Astrophysics, 466, 413, doi: 10.1051/0004-6361:20066899

Ormel, C. W., Cuzzi, J. N., & Tielens, A. G. G. M. 2008, The Astrophysical Journal, 679, 1588, doi: 10.1086/587836

Otto, E., & Fissan, H. 1999, Advanced Powder Technology, 10, 1, doi: 10.1016/S0921-8831(08)60453-7

Paneque-Carreño, T., Izquierdo, A. F., Teague, R., et al. 2023, Astronomy and Astrophysics, submitted. https://arxiv.org/abs/2312.04618

Pascucci, I., Cabrit, S., Edwards, S., et al. 2023, in Protostars and Planets VII, ed. S.-i. Inutsuka, Y. Aikawa, T. Muto, K. Tomida, & M. Tamura (San Francisco: ASPCS), 567–604. https://arxiv.org/abs/2203.10068

Paszke, A., Gross, S., Massa, F., et al. 2019, Advances in Neural Information Processing Systems, 32. https://arxiv.org/abs/1912.01703

Pavlyuchenkov, Y. N., Tutukov, A. V., Maksimova, L. A., & Vorobyov, E. I. 2020, Astronomy Reports, 64, 1, doi: 10.1134/S1063772920010060

Pérez, L. M., Carpenter, J. M., Chandler, C. J., et al. 2012, Astrophysical Journal Letters, 760, 17, doi: 10.1088/2041-8205/760/1/L17

Pérez, L. M., Benisty, M., Andrews, S. M., et al. 2018, The Astrophysical Journal, 869, L50, doi: 10.3847/2041-8213/aaf745

Persson, M. V. 2013, PhDT, 106, doi: 10.5281/ZENODO.28797

Petersen, M. R., Julien, K., & Stewart, G. R. 2007a, The Astrophysical Journal, 658, 1236, doi: 10.1086/511513

Petersen, M. R., Stewart, G. R., & Julien, K. 2007b, The Astrophysical Journal, 658, 1252, doi: 10.1086/511523

Pfeil, T., Birnstiel, T., & Klahr, H. 2023, The Astrophysical Journal, 959, 121, doi: 10.3847/1538-4357/ad00af

Pfeil, T., Cranmer, M., Ho, S., et al. 2022, in Machine Learning and the Physical Sciences workshop, NeurIPS. https://arxiv.org/abs/2211.04160

Pfeil, T., & Klahr, H. 2019, The Astrophysical Journal, 871, 150, doi: 10.3847/1538-4357/aaf962

—. 2021, The Astrophysical Journal, 915, 130, doi: 10.3847/1538-4357/ac0054

Pinilla, P., Lenz, C. T., & Stammler, S. M. 2021, Astronomy and Astrophysics, 645, 70, doi: 10.1051/0004-6361/202038920

Piqueux, S., Vu, T. H., Bapst, J., et al. 2021, Journal of Geophysical Research: Planets, 126, doi: 10.1029/2021JE007003

Pizzati, E., Rosotti, G. P., & Tabone, B. 2023, Monthly Notices of the Royal Astronomical Society, 524, 3184, doi: 10.1093/mnras/stad2057

Pollack, J. B., Hollenbach, D., Beckwith, S., et al. 1994, The Astrophysical Journal, 421, 615, doi: 10.1086/173677

Pope, S. B. 2000, Turbulent Flows (Cambridge University Press), doi: 10.1017/CBO9780511840531

Powell, D., Murray-Clay, R., Pérez, L. M., Schlichting, H. E., & Rosenthal, M. 2019, The Astrophysical Journal, 878, 116, doi: 10.3847/1538-4357/ab20ce

Prandtl, L. 1925, ZAMM - Journal of Applied Mathematics and Mechanics / Zeitschrift für Angewandte Mathematik und Mechanik, 5, 136, doi: 10.1002/zamm.19250050212

Probstein, R. 1969, in Problems of Hydrodynamics and Continuum Mechanics: Contributions in Honor of the Sixtieth Birthday of Academician L. I. Sedov, ed. M. Lavrent'ev (Philadelphia: Society for Industrial and Applied Mathematics), 568–583. https://books.google.de/books?id=oaO7AAAAIAAJ

Raettig, N., Lyra, W., & Klahr, H. 2021, The Astrophysical Journal, 913, 92, doi: 10.3847/1538-4357/abf739

Rafikov, R. R. 2002, The Astrophysical Journal, 572, 566, doi: 10.1086/340228

Rayleigh, L. 1879, The London, Edinburgh, and Dublin Philosophical Magazine and Journal of Science, 8, 261, doi: 10.1080/14786447908639684

—. 1917, Proceedings of the Royal Society of London. Series A, Containing Papers of a Mathematical and Physical Character, 93, 148, doi: 10.1098/rspa.1917.0010

Reynolds, O. 1895, Philosophical Transactions of the Royal Society of London. (A.), 186, 123, doi: 10.1098/RSTA.1895.0004

Ricci, L., Robberto, M., & Soderblom, D. R. 2008, The Astronomical Journal, 136, 2136, doi: 10.1088/0004-6256/136/5/2136

Richard, S., Nelson, R. P., & Umurhan, O. M. 2016, Monthly Notices of the Royal Astronomical Society, 456, 3571, doi: 10.1093/mnras/stv2898

Roe, P. L. 1981, Journal of Computational Physics, 43, 357, doi: 10.1016/0021-9991(81)90128-5

Ros, K., & Johansen, A. 2013, Astronomy and Astrophysics, 552, A137, doi: 10.1051/0004-6361/201220536

Rosotti, G. P. 2023, New Astronomy Reviews, 96, 101674, doi: 10.1016/j.newar.2023.101674

Rosotti, G. P., Teague, R., Dullemond, C., Booth, R. A., & Clarke, C. J. 2020, Monthly Notices of the Royal Astronomical Society, 495, 173, doi: 10.1093/mnras/staa1170

Rüdiger, G., Arlt, R., & Shalybkov, D. 2002, Astronomy and Astrophysics, 391, 781, doi: 10.1051/0004-6361:20020853

Rybicki, G. B., & Lightman, A. P. 1985, Radiative Processes in Astrophysics (Nashville, TN: John Wiley & Sons)

Safronov, V. S. 1969, Evolution of the Protoplanetary Cloud and Formation of the Earth and the Planets (Moskow: Nauka)

Saito, E., & Sirono, S. I. 2011, The Astrophysical Journal, 728, 20, doi: 10.1088/0004-637X/728/1/20

Sanchez-Gonzalez, A., Godwin, J., Pfaff, T., et al. 2020, 37th International Conference on Machine Learning, ICML 2020, PartF16814, 8428. https://arxiv.org/abs/2002.09405

Sano, T., & Miyama, S. M. 1999, The Astrophysical Journal, 515, 776, doi: 10.1086/307063

Sauter, J. 1926, VDI-Verlag, Forschungsarbeiten auf dem Gebiete des Ingenieurwesens, 279. https://books.google.de/books?id=5pcinQEACAAJ&redir_esc=y

Schäfer, U., & Johansen, A. 2022, Astronomy and Astrophysics, 666, doi: 10.1051/0004-6361/202243655

Schäfer, U., Johansen, A., & Banerjee, R. 2020, Astronomy and Astrophysics, 635, doi: 10.1051/0004-6361/201937371

Schlichting, H. E., & Sari, R. 2011, The Astrophysical Journal, 728, 68, doi: 10.1088/0004-637X/728/1/68

Schreiber, A., & Klahr, H. 2018, The Astrophysical Journal, 861, 47, doi: 10.3847/1538-4357/aac3d4

Semenov, D., Henning, T., Helling, C., Ilgner, M., & Sedlmayr, E. 2003, Astronomy and Astrophysics, 410, 611, doi: 10.1051/0004-6361:20031279

Shakura, N. I., & Sunyaev, R. A. 1973, Astronomy and Astrophysics, 24, 337. https://ui.adsabs.harvard.edu/abs/1973A%26A....24..337S/abstract

Shu, F. H. 1992, The physics of astrophysics: Gas dynamics v. 2 (Sausalito, CA: University Science Books)

Sierra, A., Pérez, L. M., Zhang, K., et al. 2021, The Astrophysical Journal Supplement Series, 257, 14, doi: 10.3847/1538-4365/ac1431

Silk, J., & Takahashi, T. 1979, The Astrophysical Journal, 229, 242, doi: 10.1086/156949

Simon, J. B., Blum, J., Birnstiel, T., & Nesvorný, D. 2022, accepted for publication in Comets III. https://arxiv.org/abs/2212.04509

Smoluchowski, M. 1916, Physik. Z., 17, 557. https://ui.adsabs.harvard.edu/abs/1916ZPhy...17..557S/abstract

Squire, J., & Hopkins, P. F. 2018a, Monthly Notices of the Royal Astronomical Society, 477, 5011, doi: 10.1093/mnras/sty854

—. 2018b, The Astrophysical Journal, 856, L15, doi: 10.3847/2041-8213/aab54d

Stachenfeld, K., Fielding, D. B., Kochkov, D., et al. 2022, ICLR 2022 - 10th International Conference on Learning Representations. https://arxiv.org/abs/2112.15275

Stammler, S. M., & Birnstiel, T. 2022, The Astrophysical Journal, 935, 35, doi: 10.3847/1538-4357/ac7d58

Stoll, M. H., & Kley, W. 2016, Astronomy and Astrophysics, 594, 57, doi: 10.1051/0004-6361/201527716

Stoll, M. H., Kley, W., & Picogna, G. 2017, Astronomy and Astrophysics, 599, 6, doi: 10.1051/0004-6361/201630226

Stone, J. M., Tomida, K., White, C. J., & Felker, K. G. 2020, The Astrophysical Journal Supplement Series, 249, 4, doi: 10.3847/1538-4365/ab929b

Svanberg, E., Cui, C., & Latter, H. N. 2022, Monthly Notices of the Royal Astronomical Society, 514, 4581, doi: 10.1093/mnras/stac1598

Takeuchi, T., & Lin, D. N. C. 2002, The Astrophysical Journal, 581, 1344, doi: 10.1086/344437

Tamfal, T., Drążkowska, J., Mayer, L., & Surville, C. 2018, The Astrophysical Journal, 863, 97, doi: 10.3847/1538-4357/aad1f4

Tassoul, J. L. 1978, Theory of rotating stars (Princeton University Press), 528

Tazaki, R., & Dominik, C. 2022, Astronomy and Astrophysics, 663, A57, doi: 10.1051/0004-6361/202243485

Tazzari, M., Testi, L., Ercolano, B., et al. 2016, Astronomy and Astrophysics, 588, 53, doi: 10.1051/0004-6361/201527423

Terebey, S., Shu, F. H., & Cassen, P. 1984, The Astrophysical Journal, 286, 529, doi: 10.1086/162628

Toomre, A. 1964, The Astrophysical Journal, 139, 1217, doi: 10.1086/147861

Toro, E. F. 1999, Riemann Solvers and Numerical Methods for Fluid Dynamics (Springer Berlin Heidelberg), doi: 10.1007/978-3-662-03915-1

Toro, E. F., Spruce, M., & Speares, W. 1994, Shock Waves, 4, 25, doi: 10.1007/BF01414629

Tsukagoshi, T., Nomura, H., Muto, T., et al. 2022, The Astrophysical Journal, 928, 49, doi: 10.3847/1538-4357/ac5111

Tsukamoto, Y., & Okuzumi, S. 2022, The Astrophysical Journal, 934, 88, doi: 10.3847/1538-4357/ac7b7b

Urpin, V. 2003, Astronomy and Astrophysics, 404, 397, doi: 10.1051/0004-6361:20030513

Urpin, V., & Brandenburg, A. 1998, Monthly Notices of the Royal Astronomical Society, 294, 399, doi: 10.1111/j.1365-8711.1998.01118.x

Villenave, M., Ménard, F., Dent, W. R., et al. 2020, Astronomy and Astrophysics, 642, doi: 10.1051/0004-6361/202038087

Villenave, M., Stapelfeldt, K. R., Duchêne, G., et al. 2022, The Astrophysical Journal, 930, 11, doi: 10.3847/1538-4357/ac5fae

Villenave, M., Podio, L., Duchêne, G., et al. 2023, The Astrophysical Journal, 946, 70, doi: 10.3847/1538-4357/acb92e

Virtanen, P., Gommers, R., Oliphant, T. E., et al. 2020, Nature Methods, 17, 261, doi: 10.1038/s41592-019-0686-2

Vorobyov, E. I., Akimkin, V., Stoyanovskaya, O., Pavlyuchenkov, Y., & Liu, H. B. 2018, Astronomy and Astrophysics, 614, 98, doi: 10.1051/0004-6361/201731690

Vorobyov, E. I., & Basu, S. 2005, The Astrophysical Journal, 633, L137, doi: 10.1086/498303

Vorobyov, E. I., & Elbakyan, V. G. 2019, Astronomy and Astrophysics, 631, doi: 10.1051/0004-6361/201936132

Vorobyov, E. I., Matsukoba, R., Omukai, K., & Guedel, M. 2020, Astronomy and Astrophysics, 638, A102, doi: 10.1051/0004-6361/202037841

Vorobyov, E. I., Skliarevskii, A. M., Elbakyan, V. G., et al. 2019, Astronomy and Astrophysics, 627, A154, doi: 10.1051/0004-6361/201935438

Wada, K., Tanaka, H., Okuzumi, S., et al. 2013, Astronomy and Astrophysics, 559, A62, doi: 10.1051/0004-6361/201322259

Wagner, K., Apai, D., & Kratter, K. M. 2019, The Astrophysical Journal, 877, 46, doi: 10.3847/1538-4357/ab1904

Wasson, J. T. 1974, Minerals and Rocks, Vol. 10, Meteorites (Berlin, Heidelberg: Springer Berlin Heidelberg), doi: 10.1007/978-3-642-65863-1

Weidenschilling, S. J. 1977, Monthly Notices of the Royal Astronomical Society, 180, 57, doi: 10.1093/MNRAS/180.2.57

—. 1980, Icarus, 44, 172, doi: 10.1016/0019-1035(80)90064-0

Weingartner, J., & Draine, B. 2001, The Astrophysical Journal, 548, 296, doi: 10.1086/318651

Weizsäcker, C. F. 1943, Zeitschrift fur Astrophysik, 22, 319. https://ui.adsabs.harvard.edu/abs/1943ZA.....22..319W

—. 1948, Zeitschrift fur Naturforschung - Section A Journal of Physical Sciences, 3, 524, doi: 10.1515/zna-1948-8-1118

Wetherill, G. W. 1990, Icarus, 88, 336, doi: 10.1016/0019-1035(90)90086-O

Wetherill, G. W., & Stewart, G. R. 1989, Icarus, 77, 330, doi: 10.1016/0019-1035(89)90093-6

Whipple, F. 1972, in From Plasma to Planet, ed. A. Evlius (New York: Wiley Interscience Division), 211. https://ui.adsabs.harvard.edu/abs/1972fpp..conf..211W/abstract

Windmark, F., Birnstiel, T., Güttler, C., et al. 2012, Astronomy and Astrophysics, 540, A73, doi: 10.1051/0004-6361/201118475

Woitke, P. 2015, EPJ Web of Conferences, 102, doi: 10.1051/epjconf/201510200011

Woitke, P., Kamp, I., & -F. Thi, W. 2009, Astronomy and Astrophysics, 501, 383, doi: 10.1051/0004-6361/200911821

Wolff, S. G., Duchêne, G., Stapelfeldt, K. R., et al. 2021, The Astronomical Journal, 161, 238, doi: 10.3847/1538-3881/abeb1d

Wurm, G., Blum, J., & Colwell, J. E. 2001, Physical Review E - Statistical Physics, Plasmas, Fluids, and Related Interdisciplinary Topics, 64, 9, doi: 10.1103/PhysRevE.64.046301

Yang, C. C., & Johansen, A. 2014, The Astrophysical Journal, 792, 86, doi: 10.1088/0004-637X/792/2/86

Youdin, A. N., & Goodman, J. 2005, The Astrophysical Journal, 620, 459, doi: 10.1086/426895

Youdin, A. N., & Lithwick, Y. 2007, Icarus, 192, 588, doi: 10.1016/j.icarus.2007.07.012

Youdin, A. N., & Shu, F. H. 2002, The Astrophysical Journal, 580, 494, doi: 10.1086/343109

Zagaria, F., Clarke, C. J., Booth, R. A., Facchini, S., & Rosotti, G. P. 2023, ApJL, 959, L15, doi: 10.3847/2041-8213/ad0c54

Zhu, Z., Stone, J. M., Rafikov, R. R., & Bai, X. N. 2014, The Astrophysical Journal, 785, 122, doi: 10.1088/0004-637X/785/2/122

Zier, O., & Springel, V. 2023, Monthly Notices of the Royal Astronomical Society, 520, 3097, doi: 10.1093/mnras/stad319

Zormpas, A., Birnstiel, T., Rosotti, G. P., & Andrews, S. M. 2022, Astronomy and Astrophysics, 661, A66, doi: 10.1051/0004-6361/202142046

Zsom, A., Ormel, C. W., Dullemond, C. P., & Henning, T. 2011, Astronomy and Astrophysics, 534, A73, doi: 10.1051/0004-6361/201116515

Zsom, A., Ormel, C. W., Güttler, C., Blum, J., & Dullemond, C. P. 2010, Astronomy and Astrophysics, 513, A57, doi: 10.1051/0004-6361/200912976

Zucker, C., Goodman, A. A., Alves, J., et al. 2022, Nature, 601, 334, doi: 10.1038/s41586-021-04286-5

LIST OF FIGURES

LIST OF TABLES

PUBLICATIONS

Refereed First Author Publications:

- **Thomas Pfeil**, Til Birnstiel, and Hubert Klahr, "Dust Coagulation Reconciles Protoplanetary Disk Observations with the Vertical Shear Instability. I. Dust Coagulation and the VSI Dead Zone", 2023, *The Astrophysical Journal*, Volume 959, Number 2, `http://doi.org/10.3847/1538-4357/aaf962`

- **Thomas Pfeil**, Miles Cranmer, Shirley Ho, Philip J. Armitage, Tilman Birnstiel, and Hubert Klahr, "A Neural Network Subgrid Model of the Early Stages of Planet Formation", accepted contribution to the *Machine Learning and the Physical Sciences Workshop*, NeurIPS 2022, `https://ml4physicalsciences.github.io/2022/files/NeurIPS_ML4PS_2022_2.pdf`, (This work is the result of an eight week stay at the Flatiron Institute, New York City, as a part of the *2022 Flatiron Machine Learning X Science Summer School).*

Submitted First Author Publications:

- **Thomas Pfeil**, Til Birnstiel, and Hubert Klahr, "Vertical shear instability with dust evolution and consistent cooling times. Settling and mixing of dust do not erase the initial condition.", submitted as a letter to the editor of *Astronomy & Astrophysics*

- **Thomas Pfeil**, Til Birnstiel, and Hubert Klahr, "`TriPoD`: Tri-Population size distributions for Dust evolution. Coagulation in vertically-integrated hydrodynamic simulations of protoplanetary disks with `PLUTO`.", submitted to *Astronomy & Astrophysics*

ACKNOWLEDGMENTS

I would like to thank Prof. Til Birnstiel, for giving me the opportunity to work in his group for the last 3 1/2 years. He gave me the freedom and trust to work on the topics I was most interested in and even to spend 2 1/2 months in New York City, to pursue a project that was not originally planned to be a part of my work. His advice and enthusiasm for my projects always motivated me to further advance the work that led to this thesis. Thank you for everything, Til!

I would like to thank everyone in Til's group for the time we spend together in countless group meetings and *Fancy Friday* lunches.

For my time at the *Center for Computational Astrophysics* (CCA) at the *Flatiron Institute* in New York City, I am very grateful for my supervisors Prof. Shirley Ho, Prof. Miles Cranmer, and my future supervisor Prof. Phil Armitage. He encouraged me to apply for the *2022 Flatiron Machine Learning X Science Summer School* in the first place. Although I had no previous experience in the field of Machine Learning, they gave me the opportunity to work on the project that I continued in Munich and that led to Chapter 7 of this thesis. I am very much looking forward to joining Prof. Armitage's Exoplanet Group at CCA in April 2024!

Special thanks goes to Prof. Hubert Klahr from MPIA in Heidelberg. His seminar on planet formation first sparked my interest in the field. Thank you for encouraging me throughout my journey, for the many meetings we had together with Til, and for acting as the secondary supervisor to this thesis!

I would also like to thank the other members of my thesis committee, Prof. Paola Caselli, Prof. Ilka Brunner, and Prof. Barbara Ercolano for agreeing to examine my thesis.

The time I spend in Munich got infinitely more enjoyable when we were finally allowed to return to our offices and I met my amazing office mates after one year of remote working. From *Cake Wednesday* to *Glühwein Thursday* and our *Star Trek Evenings*, I had a great time with you guys. I even got a few of you to watch Godzilla with me! Thank you Adi, Christiane, Daniel, Elena, Fabian, Luca, Ludwig, Peter, Sophie, Stefan, and Tommy. I will never forget the two-week trip to *Protostars and Planets VII* in Japan with Christiane, Fabian, Luca, and Tommy. This was a real highlight and it wouldn't have been the same without you.

I also want to thank Stefan, Ludwig, and Elena for proofreading parts of this thesis.

Ohne die Unterstützung und Ermutigung meiner Familie hätte ich diese Arbeit nicht schreiben können. Auch wenn ich nicht mehr so oft in der Heimat bin, ich denke an Euch und bin Euch sehr dankbar für Alles!

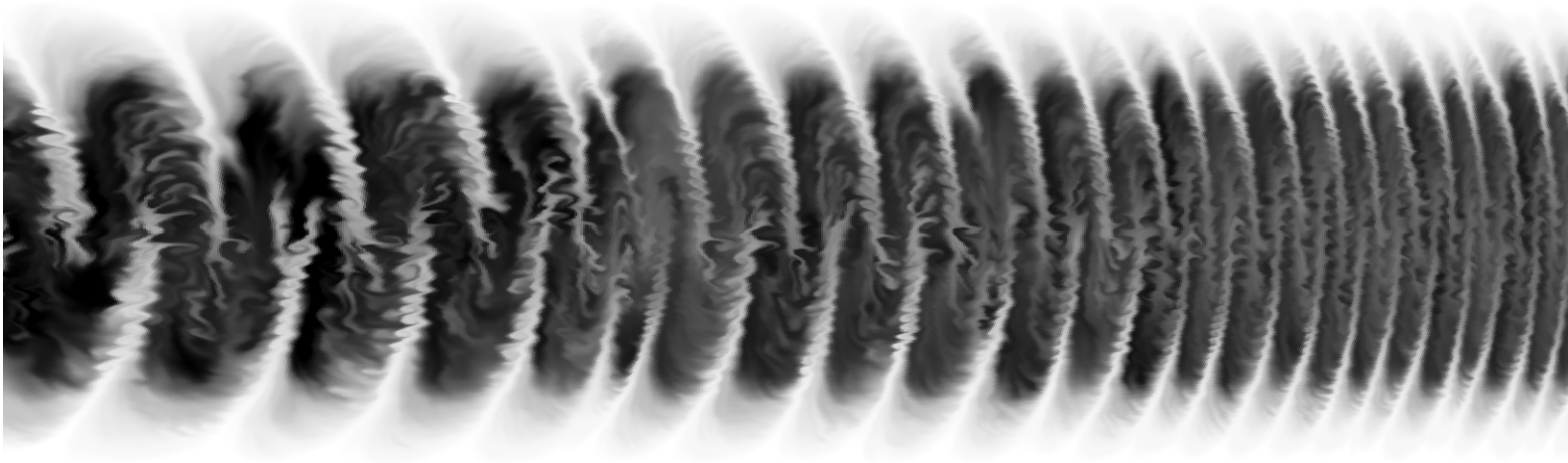

"Though I sweep and sweep,
Everywhere my garden path,
Though invisible
On the slim pine needles still
Specks of dirt may yet be found"

—Sen no Rikyū